Earthquake Resilient Bridge Columns Utilizing Damage Resistant Hybrid Fiber Reinforced Concrete

By

William Dean Trono

A dissertation submitted in partial satisfaction of the

requirements for the degree of

Doctor of Philosophy

in

Engineering – Civil and Environmental Engineering

in the

Graduate Division

of the

University of California, Berkeley

Committee in charge:

Professor Claudia P. Ostertag, Chair
Assistant Professor Marios Panagiotou
Professor John Strain

Spring 2014

Abstract

Earthquake Resilient Bridge Columns Utilizing Damage Resistant Hybrid Fiber Reinforced Concrete

by

William Dean Trono

Doctor of Philosophy in Civil and Environmental Engineering

University of California, Berkeley

Professor Claudia Ostertag, Chair

Modern reinforced concrete bridges are designed to avoid collapse and to prevent loss of life during earthquakes. To meet these objectives, bridge columns are typically detailed to form ductile plastic hinges when large displacements occur. California seismic design criteria acknowledges that damage such as concrete cover spalling and reinforcing bar yielding may occur in columns during a design-level earthquake.

The seismic resilience of bridge columns can be improved through the use of a damage resistant hybrid fiber reinforced concrete (HyFRC). Fibers delay crack propagation and prevent spalling under extreme loading conditions, and the material resists many typical concrete deterioration mechanisms through multi-scale crack control.

Little is known about the response of the material when combined with conventional reinforcing bars. Therefore, experimental testing was conducted to evaluate such behaviors. One area of focus was the compression response of HyFRC when confined by steel spirals. A second focus was the tensile response of rebar embedded in HyFRC. Bridge columns built with HyFRC would be expected to experience both of these loading conditions during earthquakes.

The third focus of this dissertation was the design, modeling, and testing of an innovative damage resistant HyFRC bridge column. The column was designed to rock about its foundation during earthquakes and to return to its original position thereafter. In addition to HyFRC, it was designed with unbonded post-tensioning, unbonded rebar, and headed rebar which terminated at the rocking plane. Because of these novel details, the column was not expected to incur damage or residual displacements under earthquake demands exceeding the design level for ordinary California bridges. A sequence of scaled, three dimensional ground motion records was applied to the damage resistant column on a shaking table. An equal scale reinforced concrete reference column with conventional design details was subjected to the same motions for direct comparison.

Compression tests showed that the ductility of HyFRC is superior to concrete in the post-peak softening branch of the response. HyFRC achieved a stable softening response and had

significant residual load capacity even without spiral confinement. Concrete required the highest tested levels of confinement to achieved comparable post-peak ductility. Tension tests showed that HyFRC provides a substantial strength enhancement to rebar well beyond their yield point. Interesting crack localization behavior was observed in HyFRC specimens and appeared to be dependent on the volumetric ratio of rebar.

The damage resistant HyFRC bridge column attained its design objectives during experimental testing. It exhibited pronounced reentering behavior with only light damage under earthquake demands 1.5 to 2.0 times the design level. It accumulated only 0.4% residual drift ratio after seven successive ground motions which caused a peak drift ratio of 8.0%. The conventional reinforced concrete column experienced flexural plastic hinging with extensive spalling during the same seven motions. It accumulated 6.8% residual drift ratio after enduring a peak drift ratio of 10.8%.

Table of Contents

Dedication

I humbly dedicate this research to my incredible wife, Kati. Her empathy, advice, encouragement, and generous acceptance of “PhD life” were all paramount to this achievement. I dedicate the final manuscript to our daughter, Lena. Her laughs and smiles ease the burden of all life’s challenges, including putting my dissertation on paper.

Acknowledgements

A number of people deserve recognition for their contributions to my research. My advisor, Professor Claudia Ostertag, provided generous financial support during my studies. Her expertise in the field of fiber reinforced concrete was crucial to building and shaping this thesis. Professor Marios Panagiotou guided the design and modeling of bridge columns; his support in that arena was very helpful. Grants from the Pacific Earthquake Engineering Research Center funded a large portion of this research and I am grateful for their contribution.

My colleague and collaborator, Gabriel Jen, offered constructive advice and discussion on all aspects of my research and devoted countless mornings and afternoons to concrete mixing and casting. Matt Schoettler organized the shake table tests and volunteered valuable time to aid in column construction. Additional thanks go to graduate students Rotana Hay, Yosuke Ishihara, Alexander Lin, and Will Nguyen and engineers/technicians Clement Barthe, Matt Cataleta, Jeff Higginbotham, Nate Knight, Dave MacLam, Russ Middleton, Wes Neighbour, and Phil Wong for their assistance with lab work and testing.

Finally, I thank my family, who ultimately provided the foundation for my success. My mother, Carol, and father, Ruben, have always encouraged and supported my academic pursuits, and I am forever grateful. I must also thank my older brother, Mike, for always letting me tag along (well into adulthood).

List of Figures

List of Tables

List of Symbols and Abbreviations

Chapter 2

A_{cc}	area of core material, mm^2
A_{cov}	area of cover material, mm^2
A_g	gross cross-sectional area, mm^2
A_s	area of longitudinal reinforcement, mm^2
A_{sp}	area of spiral reinforcement, mm^2
D	specimen width or diameter, *mm*
d_b	diameter of longitudinal reinforcement, *mm*
d_f	diameter of fibers, *mm*
d_s	center-to-center diameter of spiral, *mm*
E_c	modulus of elasticity of concrete, *MPa*
f_c'	compressive strength of concrete, *MPa*
f_{cc}'	compressive strength of confined concrete, *MPa*
f_t	tensile strength of concrete, *MPa*
F_u	ultimate load of the bare rebar, *kN*
f_{ul}	ultimate strength of longitudinal reinforcement, *MPa*
f_y	yield strength of longitudinal reinforcement, *MPa*
f_f	strength of fibers, *MPa*
f_{yt}	yield strength of transverse reinforcement, *MPa*
H	specimen height, mm
K_0	initial stiffness of unconfined specimens, *kN/mm*
K_{avg}	average initial stiffness of confined specimens, *kN/mm*
K_{cc}	initial stiffness of confined specimens, *kN/mm*
K_{sg}	initial stiffness of confined specimens with strain gages, *kN/mm*
L	gage length of compression specimens, *mm*
L_f	length of fibers, *mm*
L_{sg}	gage length of strain gaged specimens, *mm*
n	modular ratio of steel to concrete, E_s/E_c
P	applied load, *kN*
P_{max}	maximum specimen load, *kN*
P_y	strength of uncracked specimen before strain hardening, *kN*
r_1	residual load factor at 1% strain
r_2	residual load factor at 2% strain
s	spiral spacing, *mm*
T_1	toughness at 1% strain, *kN-mm*

T_2	toughness at 2% strain, *kN-mm*
V_f	volumetric ratio of fibers, %
w	crack opening, *mm*
δ	axial displacement, *mm*
δ_{pp}	post-peak axial displacement, *mm*
ε	axial strain, *%*
ε_c	concrete compressive strain, *%*
ε_{c0}	strain of unconfined concrete at peak stress, *%*
ε_{cc}	strain of confined concrete at peak stress, *%*
$\varepsilon_{s,y}$	yield strain of spiral reinforcement, *%*
ε_t	concrete tensile strain, *%*
ε_y	yield strain of longitudinal reinforcement, *%*
ρ_l	longitudinal reinforcement ratio, *%*
ρ_s	spiral reinforcement ratio, *%*
ρ_t	transverse reinforcement ratio, *%*
σ_c	concrete compressive stress, *MPa*
σ_t	concrete tensile stress, *MPa*

ACI	American Concrete Institute
CI	confinement index
ECC	engineered cementitious composite
H, HyFRC	Hybrid fiber reinforced concrete
HPFRCC	high performance fiber reinforced cementitious composite
FRC	fiber-reinforced concrete
LVDT	linear variable displacement transducers
NC	normal concrete
PVA	polyvinyl alcohol
R/C	reinforced concrete
RI	reinforcement index
SCC	self-consolidating concrete
SCHa, SCHb, SC-HyFRC	self-consolidating hybrid fiber reinforced concrete
SP	superplasticizer
UTM	universal testing machine
VMA	viscosity modifying admixture

Chapter 3

θ	drift ratio, *%*
θ_y	yield drift ratio, %
λ	recentering parameter
λ_c	ratio of the unloading slope to initial slope (*Concrete03*)
μ_D	column displacement ductility demand
μ_r	predicted displacement ductility of columns (Japan Road Association)
a_1, a_2, a_3, a_4	isotropic hardening parameters (*Steel02*)
A_{pt}	area of post-tensioning, mm^2

A_{sp}	area of compression spring, mm^2
b	strain hardening ratio, E_p/E (*Steel02*)
c	neutral axis depth, *mm*
c_1, c_2	parameters controlling change in R with cyclic loading (*Steel02*)
D	column width or diameter in direction of loading, *mm*
E	initial tangent (*ElasticPPGap*)
E	Young's modulus, *MPa* (*Steel02*)
E_{pt}	elastic modulus of post-tensioning, *MPa*
f_c'	concrete compressive strength, *MPa*
f_{cu}	crushing strength, *MPa* (*Concrete03*)
f_t	tensile strength of concrete, *MPa* (*Concrete03*)
f_{t1}	tensile stress at transition to linear softening, *MPa* (*Concrete03*)
F_y	stress when material reaches plastic state (*ElasticPPGap*)
f_y	yield stress of energy dissipaters, *MPa*
H	height to centroid of inertial mass, *mm*
K_0	initial axial stiffness of column, *kN/mm*
L_{pt}	length of post-tensioning, *mm*
L_{sp}	length of compression spring, *mm*
M / VD	shear span ratio
M_d	moment contribution of energy dissipaters, *kN-mm*
M_N	moment contribution of gravity load, *kN-mm*
M_{pt}	moment contribution of post-tensioning, *kN-mm*
$P / f_c'A_g$	axial load ratio, *%*
$P_t / f_c'A_g$	total axial load ratio including post-tensioning, *%*
P_{exc}	earthquake probability of exceedance
P_{pt}	post-tension force, *kN*
r	bilinear factor (Japan Road Association)
R	exponent controlling transition at yield point (*Steel02*)
V	column shear force, *kN*
$V_{4.2}$	shear force at 4.2% drift ratio, *kN*
$V_{8.3}$	shear force at 8.3% drift ratio, *kN*
V_{max} / A_g	ratio of maximum shear force to gross cross-sectional area, *MPa*
V_{max}	maximum shear force, *kN*
W	weight of inertial mass, *kN*
α_1	ratio of crushing strain to strain at peak stress (*Concrete03*)
α_2	ratio of crushing stress to peak stress (*Concrete03*)
β	exponent of the tension softening curve (*Concrete03*)
Δ_{up}	column uplift, *mm*
ε_0	initial strain (*InitStrainMaterial*)
ε_0	strain at peak compressive stress (*Concrete03*)
$\varepsilon_{c,max}$	maximum compression strain, *%*
$\varepsilon_{d,max}$	maximum strain in unbonded bars, *%*
$\varepsilon_{max,\ pt}$	maximum strain in post-tensioning, *%*
ε_{t1}	tensile strain at transition from nonlinear to linear softening (*Concrete03*)
ε_{tu}	tensile strain at zero tensile stress (*Concrete03*)
ε_u	strain at crushing strength (*Concrete03*)

$\varepsilon_{y,\,pt}$	yield strain of post-tensioning, %
ρ_b	reinforcement ratio of bonded rebar not cross the rocking plane, %
ρ_d	reinforcement ratio of energy dissipaters, %
ρ_{pt}	reinforcement ratio of post-tensioning, %
ρ_t	transverse reinforcement ratio, %
σ_i	initial stress in post-tensioning, *MPa*

COV	coefficient of variation
FEMA	Federal Emergency Management Agency
FRC	fiber-reinforced concrete
FRP	fiber-reinforced polymer
JRA	Japan Road Association
MCE	maximum considered earthquake
NRHA	nonlinear response history analysis
PT HyFRC	post-tensioned hybrid fiber reinforced concrete
R/C	reinforced concrete
SDC	Seismic Design Criteria (Caltrans)
SDOF	single degree of freedom

Chapter 4

f_{su}	ultimate stress of steel spiral, rebar, or strands, *MPa*
f_y	yield stress of steel spiral, rebar, or strands, *MPa*
L	length scale factor
T_1, T_2, T_3	modal periods
u/u_0	ratio of column displacement to initial displacement in free vibration test
α_t	total axial force ratio, %
ε_{su}	ultimate strain of steel spiral, rebar, or strands, *MPa*
ε_y	yield strain of steel spiral, rebar, or strands, *MPa*
ζ	damping ratio, %
θ_B	base rotation, %
$\theta_{M=0}$	drift ratio at zero moment after unloading, %

(variables not explicitly listed were defined in Chapter 3)

ASTM	American Society for Testing and Materials
GM	ground motion
PSRP	plane sections remain plane
RMS	root mean square
SRSS	square root of the sum of squares

1 Introduction

Reinforced concrete (R/C) bridges in seismic regions are designed to prevent collapse when strong ground shaking occurs during earthquakes; still, moderate damage is anticipated under design-level demands. Capacity design concepts are typically employed to avoid catastrophic failure of the most critical regions, such as the joints between beams and columns. Such capacity-protected elements are designed so that their overall damage is minimal when adjoining components reach their maximum possible load capacity. Thus, damage is concentrated in the adjoining elements as they accommodate the inelastic displacement demands. Bridges in California are designed according to this approach. Columns are detailed such that ductile plastic hinges can develop in their end regions to avoid damage in joints or other capacity-protected regions (Caltrans 2010).

Plastic hinge damage in conventional R/C bridge columns may consist of cover spalling and yielding of longitudinal reinforcing bars (rebar) under design-level demands. Larger demands may cause more severe damage. If transverse reinforcement fractures as a result of shear and the expansion of confined concrete, longitudinal rebar can suffer inelastic buckling in compression. Subsequent loading might lead to longitudinal rebar fracture as a result of reversing cycles of plastic strain. Nonetheless, the ductility of modern code compliant bridge columns has been adequate in cyclic and dynamic tests, despite the presence of these local failure modes. Such columns will indeed prevent bridge collapse and loss of life during design-level earthquakes.

Unfortunately, the continued functionality of bridges is not guaranteed by code provisions. Extensive repairs or complete replacement of concrete bridge components may be required after earthquakes. In the past, it has been more cost effective to demolish bridges with permanent displacements rather than to attempt to return the bridge columns to their plumb position. Regardless of the scope of repairs, such processes are time consuming and costly, especially for critical infrastructure. In addition, the condition of bridges in the United States is declining and investment in upgrades, retrofits, and replacements remains inadequate. The American Society of Civil Engineers (2013) estimates that $6.8 billion would be required to repair or replace all structurally deficient bridges in California (including non-R/C bridges), yet only $500 million was received in federal funds in 2008. Furthermore, over 8,300 California bridges have exceeded their expected service life of 50 years (Shoup et al. 2013).

With these facts in mind, there is clearly a need for new bridges to be earthquake resilient and have longer service lives to remain cost effective in the long term. This dissertation aims to improve bridge longevity using two general approaches. The first focuses on improving the damage resistance of bridge components using high-performance fiber-reinforced cement-based composites (HPFRCC's). Their performance is investigated under monotonic tension and compression since bridge columns are exposed to both these loading conditions during earthquakes. The second involves the design, modeling, and testing of an innovative damage resistant bridge column made with HPFRCC. The column was designed to reduce earthquake damage and to maintain continuous post-earthquake functionality.

Renewed interest has been generated in fiber-reinforced concrete (FRC) in recent years, owing mainly to the development of HPFRCC materials. These materials exhibit tensile strain hardening rather than strain softening. They are a damage resistant alternative to normal concrete for seismic design. HPFRCC's that utilize fiber hybridization (i.e. incorporate both micro- and macro-fibers) can reduce concrete deterioration processes via multi-scale crack control. Such materials restrict and confine the expansive products formed by corrosion of rebar (Grupp et al. 2007, Jen and Ostertag 2012), alkali-silica reaction (ASR) (Yi and Ostertag 2005), and other processes such as sulfate attack. Significant research has been directed toward material characterization of HPFRCCs, but few studies have investigated the performance of the material when combined with conventional rebar under seismic loading conditions. In this dissertation, tests were performed on an HPFRCC known as hybrid fiber-reinforced concrete (HyFRC) which was developed previously at UC Berkeley.

The damage resistant bridge column was designed to have zero downtime following severe earthquakes. It was tested on a shaking table to verify the anticipated performance. Past research has shown that R/C structures designed to rock about their foundation can achieve the same displacement ductility as conventional designs while incurring less damage. Post-tensioning tendons are often used to encourage hysteretic recentering—that is, the tendency of the structure's force-deformation response to unload through the origin. Internal or external devices that yield and dissipate energy are also common in past rocking column designs. Two novel components of the column proposed herein were headed reinforcing bars and HyFRC. These details were intended to increase the column's damage resistance in compression.

The results of small scale compression and tension tests on HyFRC members containing conventional steel reinforcement are presented in Chapter 2. Specimens with variable amounts of transverse reinforcement were tested in compression to investigate the effect of confinement on the load capacity and ductility of HyFRC. Tension tests on reinforcing bars embedded in HyFRC prisms were performed to evaluate the magnitude and extent of rebar stiffening and strengthening provided by the material.

The design and modeling of the damage resistant column are presented in Chapter 3. The column was designed to eliminate residual displacements after earthquakes and the response was predicted using a nonlinear analytical column model. A parametric study was performed to optimize the design parameters given a specific set of performance objectives.

Chapter 4 presents the results of a shake table test conducted on the damage resistant column. The test column was subjected to a sequence of earthquake ground motion records on a shaking table, and the response was compared to a reference column with conventional ductile design details tested in the same manner. The dynamic column response predicted by the analytical model was in strong agreement with the experimental test response.

Current design practices result in bridges that will perform adequately during earthquakes; however, the research herein will show that ductile HPFRCC materials and rocking and/or recentering column design techniques can improve bridge resilience during earthquakes. As aging bridges are replaced in seismic regions like California, these solutions should be considered as viable alternatives to conventional R/C design.

2 Confinement and Tension Stiffening Effects in Reinforced HyFRC Composites

2.1 Introduction

Reinforced concrete (R/C) structures designed for seismic loading conditions typically contain transverse reinforcement in the form of steel hoops, ties, or spirals. The purpose of such reinforcement is to confine concrete contained within the core of the member. Confinement increases concrete strength and ductility capacity.

Designers are required to provide a level of confinement sufficient to avoid abrupt loss of load capacity (i.e. brittle failure) after the unconfined cover concrete spalls away from the core. The seismic criteria of the American Concrete Institute (2010) specifies confinement requirements for buildings structures (e.g. special moment frames), while confinement requirements for bridge structures in California are provided by Caltrans (2010).

Prior research has shown that adequate confinement detailing indeed prevents brittle failure in members such as bridge columns; however, spalling of unconfined concrete cover is still unavoidable under large demands. Spalled concrete must be repaired to protect exposed steel reinforcement from corrosion or other environmental attack. Repairs such as patching with grout or epoxy injection can be both costly and time consuming. Therefore, preventing or reducing spalling in ductile concrete members could reduce repair requirements following large earthquakes.

Fiber-reinforced concrete can be combined with traditional steel hoops, ties, or spirals to reduce spalling in compression members. The fibers prevent spalling by bridging cracks that form between the cover and core material. Furthermore, they offer a uniformly distributed resistance to core concrete dilation rather than only at the heights of transverse reinforcement. HyFRC members may ultimately require lower levels of confinement to obtain the same level of ductility as concrete members with the added benefit of reducing spalling.

Fibers can also influence a second phenomenon in R/C structures known as the tensioning stiffening effect. Tension stiffening refers to the increase in tensile stiffness afforded to reinforcing bars when they are embedded in concrete. Fibers can carry loads across cracks and may stiffen (and strengthen) the rebar to larger deformations than in concrete with no fibers. Unique cracking mechanisms and rebar-fiber-crack interaction may occur after the rebar yields.

This chapter presents a series of tests of reinforced compression and tension members with and without fibers to investigate the above phenomena. A series of compression tests were conducted on cylindrical column specimens made of HyFRC, a self-consolidating HyFRC (SC-HyFRC), and an engineered cementitious composite (ECC). The longitudinal rebar was the same for all columns but the ratio of transverse steel reinforcement was varied. Columns were also cast using normal concrete (NC) and self-consolidating concrete (SCC) for comparison.

Second, a series of tension tests were conducted on HyFRC, SC-HyFRC, and NC specimens containing a single rebar. Specimens were tested with two different reinforcement ratios. The reinforcing bar was loaded in tension and the force-deformation and cracking characteristics of the specimens were observed. Strain gage measurements were taken on the embedded rebar to characterize the rebar strain distribution and relate it to the observed surface crack pattern.

The results of these testing programs will show that the compression and tension behavior of reinforced HyFRC composites is markedly different than the behavior of typical R/C. These differences should be considered when designing structures using such materials.

2.2 Properties of HyFRC

HyFRC was developed at UC Berkeley as a tensile strain hardening, deflection hardening composite material containing steel macrofibers and polymer microfibers. The material was initially developed for lightly reinforced concrete structures. The flexural performance criterion was to delay dominant macrocrack formation up to a tensile strain equal to the yield strain of mild steel of 0.2% (Blunt and Ostertag 2009).

Fiber hybridization modifies cracking on two scales. Polyvinyl alcohol (PVA) microfibers resist crack initiation by strengthening the fracture process zone at the crack tip. Steel macrofibers resist opening of the crack wake through fiber bridging, pullout, yielding, or fracture. Synergistic effects between the fibers can occur, such as the tendency of the microfiber-reinforced matrix to increase the pullout resistance of the macrofibers.

HyFRC is part of the broad classification of materials known as HPFRCC’s. These materials are different from conventional FRC composites because their tensile response is strain hardening rather than strain softening as explained in Figure 1 (Naaman and Reinhardt 2005). Under bending stresses, a tensile strain hardening material will exhibit deflection hardening behavior. HPFRCC’s typically have volumetric ratios of fibers in excess of 2%.

Blunt and Ostertag (2009) observed that this deflection hardening effect can enhance post-cracking flexural stiffness of beams with reinforcing bars. Reinforced HyFRC beams with 0.3% longitudinal rebar by volume showed greater stiffness and strength than conventional R/C beams with the same reinforcement ratio in the post-cracking regime.

The fiber volume fraction of 0.015 in HyFRC reduces the workability, thus inhibiting its use in densely reinforcement structures. This drawback motivated the development of a self-consolidating HyFRC (SC-HyFRC). SC-HyFRC was intended to be used for seismically-designed reinforced concrete structures where flow through dense reinforcement cages would be required. SC-HyFRC was used in the confinement and tensioning stiffening tests included in this Chapter as well as in the columns tested by Kumar et al. (2011).

The bulk of this dissertation is devoted to the testing and analysis of structures built using HyFRC. Slight variations of the original material proportions were made for each unique application (e.g. SC-HyFRC). The primary goal was to understand how HyFRC interacts with conventional steel reinforcing bars in structures subjected to seismic loads.

Several researchers have investigated the use of other HPFRCC's for seismic applications in recent years. Parra-Montesinos (2005) provides an excellent overview of previous work, noting the benefits of using HPFRCC's in shear-critical members such as beam-column joints, squat walls, and couplings beams or in flexural members subjected to large shear stress reversals. Post-tensioned columns made of ductile fiber-reinforced cement composites (DFRCC) test by Billington and Yoon (2004) maintained their integrity considerably better than normal concrete under high compressive loads. Aviram et al. (2010) tested an HPFRCC bridge column and found that under cyclic loading, the HPFRCC column had improved damage tolerance, shear strength, and energy dissipation compared to conventionally reinforced concrete columns. A performance-based earthquake engineering design methodology was applied to this column and found that the HPFRCC material provided both economic and structural benefits.

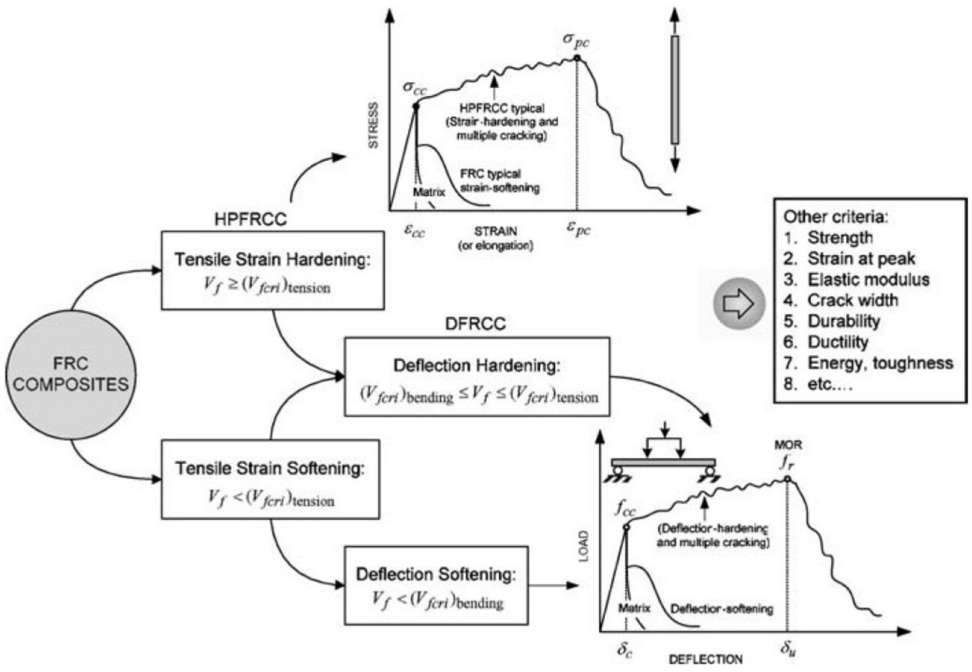

Figure 1. Classification of FRC composites based on tensile response (Naaman and Reinhardt 2006)

2.3 Confinement of HyFRC composites

2.3.1 Background and previous experimental studies

Previous research has proven that the unidirectional behavior of concrete is improved when lateral confining stresses are present. In early studies, Richart et al. (1928) actively confined concrete specimens using pressurized oil then loaded the specimens in one direction. These tests showed that triaxial confining stresses restrict concrete dilation and stabilize deformations when the concrete is loaded to failure in a single direction. The result is greater stress and strain capacity in the direction of loading and an improved softening response.

Practical situations where concrete is actively confined are limited but can include situations where concrete is under strong soil or hydrostatic pressures (e.g. deep foundations, underwater structures).

Passive confinement is much more common for R/C structures, and early investigations of this type were also conducted by Richart et al. (1929). Passive implies that confining stresses are only activated after compression loads are applied. Loading causes core concrete to dilate and expand, and tensile stresses are subsequently induced in discretely spaced reinforcing bars or external jackets. The reinforcement surrounds the core and, when stressed, provides passive confinement.

Numerous experimental studies have investigated the behavior of passively confined concrete. Sheik (1982) provides a comprehensive summary of confinement tests through the 1980's and a comparison of several early analytical models. Most analytical models predict the stress-strain response of confined concrete based on the transverse reinforcement properties (primarily ρ_t and f_{yt}). One notable study for R/C columns under seismic loading conditions was conducted by Mander et al. (1988a,b). A constitutive stress-strain model for confined concrete based on those tests has been widely adopted for modern seismic analysis of R/C components.

The effect of passive confinement on conventional FRC's (i.e. FRC's that strain-soften after crack initiation) has been investigated in several prior test programs. A summary of the characteristics of those tests is provided in Table 1. The geometric properties (width, D, and height, H) of the specimens in each test are given, as well as the volumetric ratios of longitudinal and transverse reinforcement (ρ_l and ρ_t), the yield strength of the transverse reinforcement (f_{yt}), the compressive strength of the FRC material (f_c'), the volume fraction of fibers (V_f), the fiber length (L_f), the fiber aspect ratios (L_f/d_f), and the fiber types (see footnote *a*). Multiple transverse reinforcement ratios were tested in each study, and specimens at each ratio were cast with each of the fiber volume fractions (V_f) listed in the table. In all cases, only one type of fiber was used as is typical of conventional FRC's.

The studies listed in Table 1 focused on conventional FRC materials with only one type of fiber. In all five studies, confinement by spirals or ties caused greater gains in stress and strain capacity in FRC than in equally confined concrete. The softening response of the confined FRC was also superior to confined concrete. Confinement tests of FRC columns on the scale of the R/C column tests by Mander et al. (1988a,b) have not been undertaken. In the FRC studies presented here, ρ_l ranged from 0.1% to 3.8%, f_c' ranged from 20 to 88 MPa, and H/D ranged from 2 to 5. The width (diameter) of specimens was less than 200 mm in all cases.

Empirical analytical models which define the stress-strain relationship of confined FRC's were proposed in the studies. However, as shown in Table 1, a unique combination of confinement and fiber properties was considered in each investigation. Therefore, a given model might be highly accurate for the specimens considered yet less accurate for other possible combinations of fibers and confinement steel. All five models were applied to the HyFRC specimens considered in this study and compared with tested performance. None of the models were found to be particularly accurate and thus the comparison was not included in this Chapter.

Table 1. Summary of selected confinement studies of FRC specimens.

Reference	*Cross section*	*D mm*	*H mm*	*ρ_l %*	*ρ_t %*	*f_{yt} MPa*	*f_c' MPa*	*V_f, %*	*L_f mm*	*L_f/d_f*	*Fiber type* [a]
Ganeson and Murthy (1990)	square	200	1000	2.0	0.6 0.8 1.6 2.4	469	20	1.5	np	70	S
Hsu and Hsu (1994)	circular	76	152	np	0.4 0.6 1.2	456	83	0.5, 0.75, 1.0	np	60	S, H
Campione et al. (1999)	circular	100	200	np	1.3 2.6	550	70	1.5, 2.0	20	26	C
Foster and Attard (2001)	square	155	650	3.8	0.4 0.8 1.7	600	88	0.6	36	84	S, H
		200	900	2.3	1.4 2.8	470	67, 73				
Ramesh et al. (2003)	square	150	300	0.2	0.8[b] 1.1[b]	350	23	0.3, 0.6, 0.9, 1.2	38	75	S
				0.1	0.6[b] 0.9[b]	448	37				

np = not provided
[a] *S = steel; C = carbon; H = hooked ends;*
[b] *calculated as volume of transverse reinforcement divided by gross specimen volume (rather than volume of confined core as in all other cases)*

Studies in Table 1 which investigated the performance of normal strength steel fiber-reinforced concrete (SFRC) columns with transverse spirals include those of Ganeson and Murthy (1990) and Ramesh et al. (2003). The former considered ρ_t between 0.6% and 2.4% and V_f of steel fibers was 1.5%. The latter considered ρ_t between 0.6% and 1.1% and V_f varied between 0.3% and 1.2%. The analytical stress-strain model by Ramesh et al. was dependent on a reinforcing index (*RI*) for fibers and a confinement index (*CI*) for transverse steel. The reinforcing index is the product of the weight fraction of fibers and the aspect ratio of fibers; the confinement index is a function of ρ_t, the prism dimensions, and the spacing and type of transverse reinforcement. This model provided a strong correlation with their test data.

Studies that have focused on columns made with high strength SFRC include those of Hsu and Hsu (1994) and Foster and Attard (2001). The intent of these studies was to investigate whether a combination of fibers and transverse confinement could reduce the brittleness of high strength columns compared to those with transverse confinement alone. The values of ρ_t ranged from 0.4% to 2.8% and V_f ranged from 0.6% to 1.0%. However, f_c' of the SFRC exceeded 67 MPa. As in prior studies, Hsu and Hsu (1994) noted higher strains at peak load in confined SFRC compared to confined concrete. They attributed this phenomenon to an increased amount of entrapped air in the SFRC resulting from the reduction in workability caused by the addition of fibers. Foster and Attard (2001) found that steel fibers arrested early spalling of concrete cover. They applied both concentric and eccentric compression loads.

The remaining study listed in Table 1 involved high strength carbon fiber-reinforced concrete (CFRC) with V_f = 1.5% and 2.0% and transverse steel ties at ρ_t = 1.3% or 2.6% (Campione et al. 1999). One interesting observation in this study was that CFRC specimens with the lower level of confinement (ρ_t = 1.3%) had lower strength than the same material with no confinement.

Only a few studies have investigated confinement of tensile strain-hardening HPFRCC materials (see below) and no studies have yet been conducted on HyFRC. Triaxial compression tests with varying levels of active confinement (using pressurized oil) were conducted on HPFRCC's by Fantilli et al. (2011a,b). They tested two HPFRCC materials; one had steel and polyethylene fibers at equal volume fractions 0.75%, while the other had the same fibers at equal volume fractions of 1.0%. The polyethylene fibers had $L_f = 6$ mm and $d_f = 0.012$ mm, while the steel fibers had $L_f = 32$ mm and $d_f = 0.33$ mm. They found that the HPFRCC materials with no active confinement achieved similar post-peak ductility as normal and self-consolidating concrete with 1 MPa (0.15 ksi) of triaxial confining pressure. These tests showed that the level of external confinement required to promote ductile behavior in HPFRCC's is less than for both normal and self-consolidating concrete.

2.3.2 Testing program

The confinement tests presented in this chapter were conducted on several different HyFRC materials. In addition, tests were performed on a second type of HPFRCC known as engineered cementitious composite (ECC). No prior tests have been conducted on passively confined specimens of these materials.

The experimental investigation was performed at the Concrete Testing Laboratory of the Civil and Environmental Engineering Department at UC Berkeley. A total of 54 confined column specimens were built and tested to large strains (greater than 2%) in uniaxial compression. The materials, specimens, and the test configuration are described in this section.

2.3.2.1 *Materials*

The mix proportions for the materials are provided in Table 2 and fiber properties are provided in Table 3. HyFRC was composed of water, type I/II Portland cement, class F fly ash (SC-HyFRC only), fine aggregate with a fineness modulus of 3.2, coarse aggregate with a 9.5 mm maximum aggregate size, and a small amount of superplasticizer (SP). HyFRC contained S2 and S1 hooked-end steel fibers and PVA1 straight polyvinyl alcohol fibers. The volumetric ratios of these fibers were 0.008, 0.005, and 0.002, respectively.

SC-HyFRC had a higher ratio of cement paste to aggregate compared to HyFRC. The fibers consisted of only S1 fibers at a volume ratio of 0.013 and PVA1 fibers at a volume ratio of 0.002. The material had higher proportions of superplasticizer (SP) to increase flowability and viscosity modifying admixture (VMA) to control segregation.

ECC was developed based on a micromechanics concept (Li 1992). It consisted of a mortar matrix reinforced by PVA2 fibers at a volume ratio of 0.02. The mortar matrix consisted of water, type II/V Portland cement, class F fly ash, silica sand with a 0.13 mm particle size, SP, and VMA.

Reference specimens were cast using normal vibrated concrete (NC) or self-consolidating concrete (SCC) with no fibers. The matrix constituents (water, cement, aggregates) were the same as for HyFRC and SC-HyFRC. SCC was proportioned to have similar workability as SC-HyFRC using fly ash, SP, and VMA. Mix proportions for the materials without fibers are also given in Table 2.

Table 2. Material mix proportions for confinement tests (SSD condition)

HPFRCC	proportions by mass					fraction of binder mass		volume fraction			
material	Cement	Fly Ash	Water	Sand	Gravel	SP	VMA	PVA1	PVA2	S1	S2
NC	1	-	0.45	1.67	1.61	-	-	-	-	-	-
SCC	0.75	0.25	0.45	2.03	0.81	0.0046	0.0222	-	-	-	-
HyFRC	1	-	0.45	1.67	1.53	0.0016	-	0.002	-	0.005	0.008
SC-HyFRC	0.75	0.25	0.45	1.97	0.79	0.0046	0.0222	0.002	-	0.013	-
ECC	0.45	0.55	0.26	0.36	-	0.0050	0.0011	-	0.02	-	-

Table 3. Fiber properties

Fiber	*L, mm)*	*D, mm)*	*F_u, MPa*	*E, GPa*
PVA1	8	0.04	1600	43
PVA2	12.7	0.04	1600	43
S1	30	0.55	1100	200
S2	60	0.75	1050	200

2.3.2.2 *Description of test specimens*

The geometry and reinforcement of the confined test specimens is shown in Figure 2(a). The specimens had a height to diameter ratio of two and diameters of 152 mm. Longitudinal and transverse reinforcement details in the test specimens were chosen to be similar to typical R/C columns in terms of reinforcing ratios. Scaling of the fibers was not possible because fibers small enough for these specimens do not exist.

The longitudinal reinforcement ratio of the specimens was ρ_l = 1.6%, consisting of four 9.5 mm diameter (No. 3) deformed mild steel bars with an average tensile yield strength of 372 MPa. The spiral reinforcement was black annealed steel wire with a diameter of 3.4 mm and an average yield stress and strain (determined by the 0.2% offset method) of f_{yt} = 256 MPa and ε_y = 0.30%. Three coupons of each material were tested in tension to determine their stress-strain response (Figure 3).

Specimens were fabricated with spiral pitches (s) of 76, 51, 25, and 13 mm for transverse reinforcement ratios of ρ_s = 0.3%, 0.5%, 1.0%, and 1.9%, respectively. The ratios of spiral spacing to bar diameter (s/d_b) were 8.0, 5.3, 2.7, and 1.3—sufficient to resist bar buckling. The transverse reinforcement ratio was calculated using [2.1], where A_{sp} is the cross sectional area of the spiral and d_s is the diameter of the confined core. ACI 318 (2005) defines d_s as the out-to-out diameter of the spiral, while [2.1] takes d_s as the center-to-center diameter of the spiral as in Mander et al. (1988b).

$$\rho_s = \frac{4A_{sp}}{d_s s} \qquad [2.1]$$

The design clear cover over the spiral was 3 mm in all specimens, although it likely varied from 3 to 6 mm. Several spirals were bunched near the ends of the specimens [see Figure 2(a)] to provide higher confinement and encourage damage to occur only over the gage length in the center of the specimen.

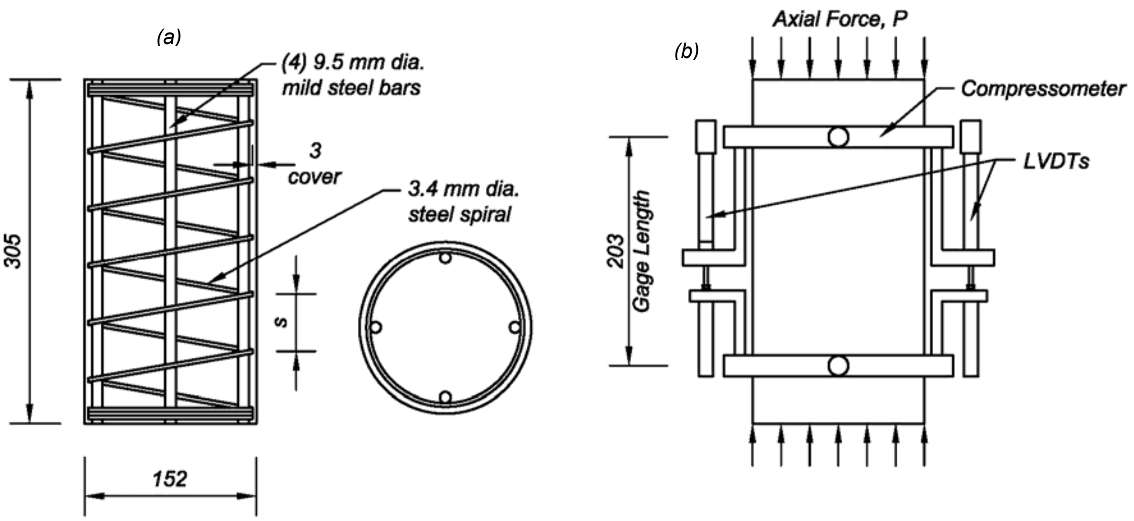

Figure 2. Compression specimen details; (a) cross sections, (b) test configuration

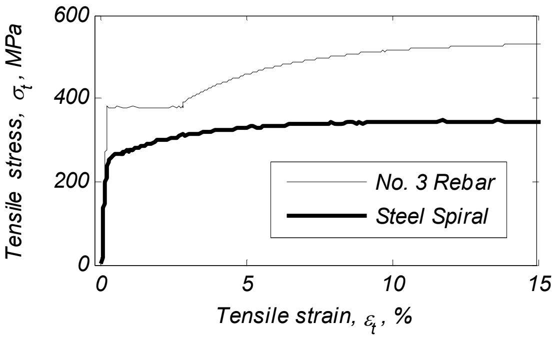

Figure 3. Measured stress-strain response of longitudinal bars and spiral

2.3.2.3 *Test configuration*

All specimens were tested under monotonically increasing axial compression in a 1300 kN servo-controlled universal testing machine (UTM). Load was measured by the UTM and displacement was measured by external linear variable displacement transducers (LVDT's). Each test was stopped when the LVDT's reached their maximum stroke or when damage in the specimen caused the displacement measurements to be inaccurate.

The UTM actuator was not displacement controlled, but the load rate was slow enough to capture the softening response of the confined specimens. The recorded strain rate was on the order of 10^{-5} strain per second between 10% and 90% of the maximum load. As specimens approached the maximum load, the strain rate increased and was typically on the order of 10^{-4} strain per second. These rates were consistent except when specimens had a sudden, abrupt loss of load resistance. In those cases, instantaneous drops in load were accompanied by a sudden increase in strain rate. The strain rate then restabilized as displacements continued.

The compressometer fixture is shown in Figure 2(b). The two LVDT's were attached to opposite sides of a compressometer frame which was then tightened against the surface of the specimen using screws. Strain was calculated using the average of the two LVDT measurements. The gage length was 203 mm for all confined specimens. The length at the ends of the specimen outside the gaged region was 51 mm. This length was insufficient to provide full development of the longitudinal bars in compression (discussed in Section 2.3.4.1).

Two different sizes of unconfined samples were tested for stress-strain properties. Unconfined samples that had a 152 mm diameter used the test configuration in Figure 2(b). Unconfined specimens with a diameter of 102 mm used a similar compressometer fixture but had a gage length of only 102 mm.

Finally, some specimens had four or eight strain gages attached to the spiral at mid-height. The gages were separated by 90 degrees circumferentially and were located on consecutive spirals in specimens with eight gages. The compressometer frame in Figure 2(b) was not used for strain gaged specimens because they were tested up to 10% shortening. Instead, two LVDT's were positioned on either side between the load platens. The deformation was measured over the full specimen height and the recorded response had an abnormally low initial stiffness as the load platens settled when load was first applied. Therefore, the load-displacement curves were modified to have a stiffness, K_{sg}, equivalent to the stiffness between 20% and 40% of the maximum load to account for this effect (i.e. to remove the initial "soft" portion of the curve).

Furthermore, the gage length for calculating strain was estimated for each strain-gaged specimen by [2.2], where L is the LVDT gage length (203 mm) and K_{avg} is the average stiffness of the identical non-strain-gaged specimens (for displacement measured over L). This correction resulted in similar load-strain responses for the gaged specimens and non-gaged specimens.

$$L_{sg} = \frac{K_{avg}L}{K_{sg}} \qquad [2.2]$$

2.3.3 Test results

2.3.3.1 *Unconfined material properties*

Table 4 provides a summary of the measured mechanical properties of each of the tested materials. It includes the compressive strength, f_c', the strain at the compressive strength, ε_{c0}, and the elastic modulus, E_c. SC-HyFRC and ECC were cast in two separate batches each (*a* and *b*), while specimens of the other materials were cast in a single batch.

In conventional concrete, the level of confinement required for ductile behavior is directly proportional to concrete compressive strength (ACI 2011). Therefore, similar strengths were targeted in all materials to isolate the effects of different fiber and spiral reinforcement combinations.

The compressive strengths of the NC, SCC, HyFRC, and SC-HyFRC materials varied moderately, despite the fact that these materials all had equivalent water to binder ratios of 0.45. This water to binder ratio was chosen to produce a design compressive strength of 38 MPa. Strength could have been affected by differences in casting technique (mechanical vibration for HyFRC and NC versus no vibration for SC-HyFRC or SCC), variability in the types and proportions of fibers and aggregates, and the use of fly ash as a cement replacement material. A single root cause could not be identified. These specimens were wet-cured for seven days then cured under ambient conditions. Testing was conducted after 28 to 42 days of curing.

ECC specimens, which had a water-to-binder ratio of 0.26, were cured for seven days then tested immediately in order to have target compressive strength similar to the other materials. The ECC material presented in this study typically has a 28 day compressive strength on the order of 55 to 65 MPa.

Table 4. Summary of unconfined compression properties.

Material (abbr.)	Diameter, mm	No. of samples	$f_c'^{\,a}$, MPa	$\varepsilon_{c0}^{\,a}$, %	$E_c^{\,a}$, MPa	$n = E_s/E_c^{\,a,b}$
NC	102	2	46.5	0.33	26300	8.2
SCC	152	2	39.3	0.27	24200	9.4
HyFRC (H)	102	1	33.6	0.27	22900	10.3
SC-HyFRCa (SCHa)	102	2	40.3	0.56	20100	9.3
SC-HyFRCb (SCHb)	152	2	31.4	0.34	18400	9.3
ECCa	152	3	41.0	0.35	20300	7.2
ECCb	152	3	38.8	0.34	20300	7.8

[a] *properties averaged over all samples*

[b] *E_s = 188550 MPa based on longitudinal bar tensile test*

2.3.3.2 *Unconfined material stress-strain response*

The compressive stress strain response of a single unconfined sample of each material is shown in Figure 4. The recorded test data for each material is shown by the solid lines. The servo-controlled test machine could not capture the softening response for materials that were brittle after the peak load (NC, SCC, and ECC).

SCHb was the only HyFRC material where a continuous, stable softening response could be recorded. The others (HyFRC and SCHa) had 2/3 the height and diameter of the SCHb samples (see Table 4). Damage outside the gaged region in the smaller test specimens tended to invalidate the LVDT displacement measurements. Still, the load did not drop abruptly when the peak stress was reached.

The load-displacement curve of the the core material for the confined specimens was calculated by subtracting the estimated cover load curve from each specimen's total load curve. The cover load-displacement curve was estimated using the unconfined stress-strain response of each material and the cover area. Therefore, if the unconfined stress-strain response ended abruptly or had discontinuities, those discontinuities would also appear in the response of the confined core. A continuous loading and unloading stress-strain curve (with no instantaneous drops in load) was required for each material to avoid those discontinuities. Therefore, assumptions were made regarding the softening curves of all materials except for SCHb (dashed lines). A steep linear softening branch with a slope of $-E_c/2$ was assumed for the brittle materials (NC, SCC, ECCa, and ECCb). This assumption resulted in a complete loss of stress capacity ($\sigma_c = 0$) at strains between 0.5% and 0.8%.

The assumption made for H and SCHa was that the softening branch was identical to that of the SCHb specimen. The portion of the SCHb curve from the maximum stress onward was translated to the point of maximum stress in the H and SCHa samples. In the absence of reliable measured data, this approximation was assumed to be reasonable because the recorded H and SCHa data points measured after the maximum load (solid lines) tend toward the softening curve estimated by this procedure (dashed lines). All three materials had the same total volume of steel and polymer fibers so it is likely that they would have similar post-peak behavior. The differences in strength between materials may have caused variation in their softening responses; however, strength was neglected in creating the curves.

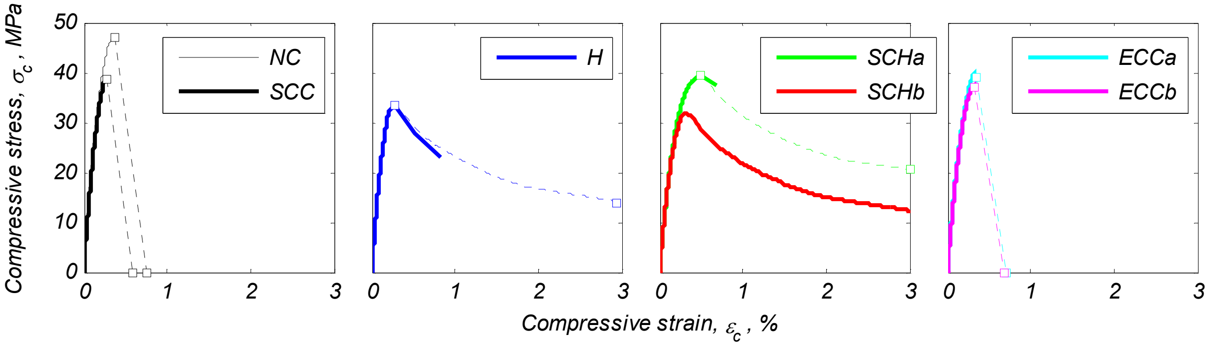

Figure 4. *Measured unconfined compression stress-strain response of materials.*

2.3.3.3 *Measured response of confined specimens*

Figure 5 shows the measured axial load-displacement response of the confined HPFRCC specimens at different transverse reinforcement ratios. Axial strains over the 203 mm gage length are given on the top horizontal axis. Figure 5 also shows the estimated response of the unconfined cover material of each specimen. The load carried by the cover was estimated as the product of A_{cov} and the stress obtained from the unconfined material stress-strain response (Figure 4). The area of cover material (A_{cov}) was defined as the area outside the centerline of the spiral and made up 11.9% of the gross cross sectional area (A_g).

Specimens with fiber hybridization (H, SCHa, and SCHb) tended to show stable linear or bilinear softening after the peak load. The response of specimens with ρ_s = 0.3% and 0.5% was similar, and modest increases in the maximum load were observed in specimens with ρ_s = 1.0%.

ECC specimens tended to be brittle after reaching their maximum load. In most cases a sudden loss of load resistance was followed by a period of constant load with increasing axial displacement. The maximum load and the load resistance in the stable region tended to increase as the transverse reinforcing ratio increased. Again, there was practically no difference in the response of specimens with ρ_s = 0.3% and 0.5%.

The axial load-displacement response of the control specimens without fibers is shown in Figure 6. The maximum load of these specimens increased as ρ_s increased, and a distinct difference in maximum load was observed even at the lowest ratios of ρ_s = 0.3% and 0.5%. Abrupt parabolic softening occurred after the peak load in most specimens, except for a single SCC specimen at ρ_s = 1.9%. After this abrupt portion, the softening slope increased but was not as flat as the ECC specimens. Higher ρ_s resulted in a more gradual softening slope.

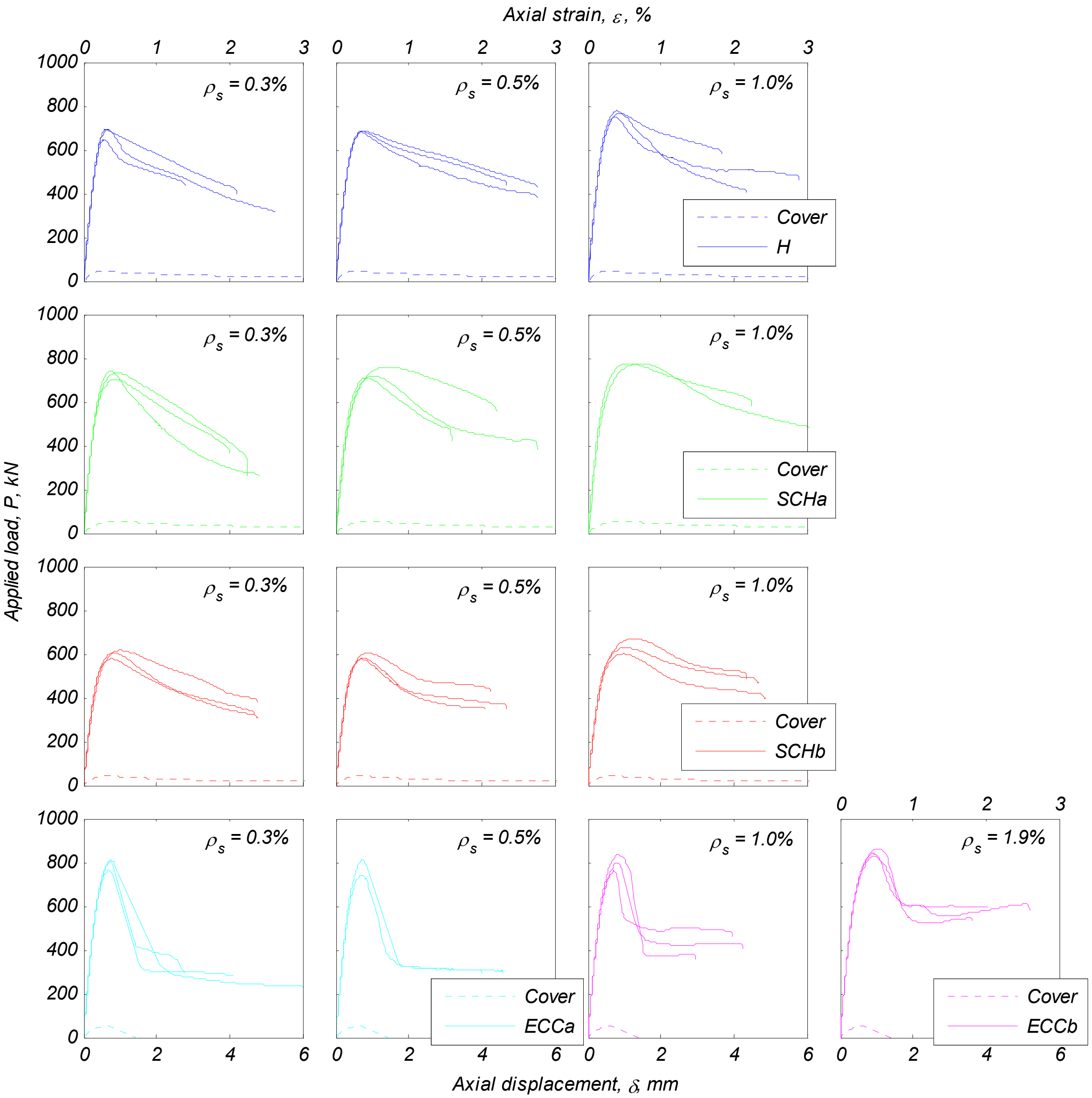

Figure 5. Measured axial force-displacement response of confined HPFRCC specimens at different transverse reinforcement ratios.

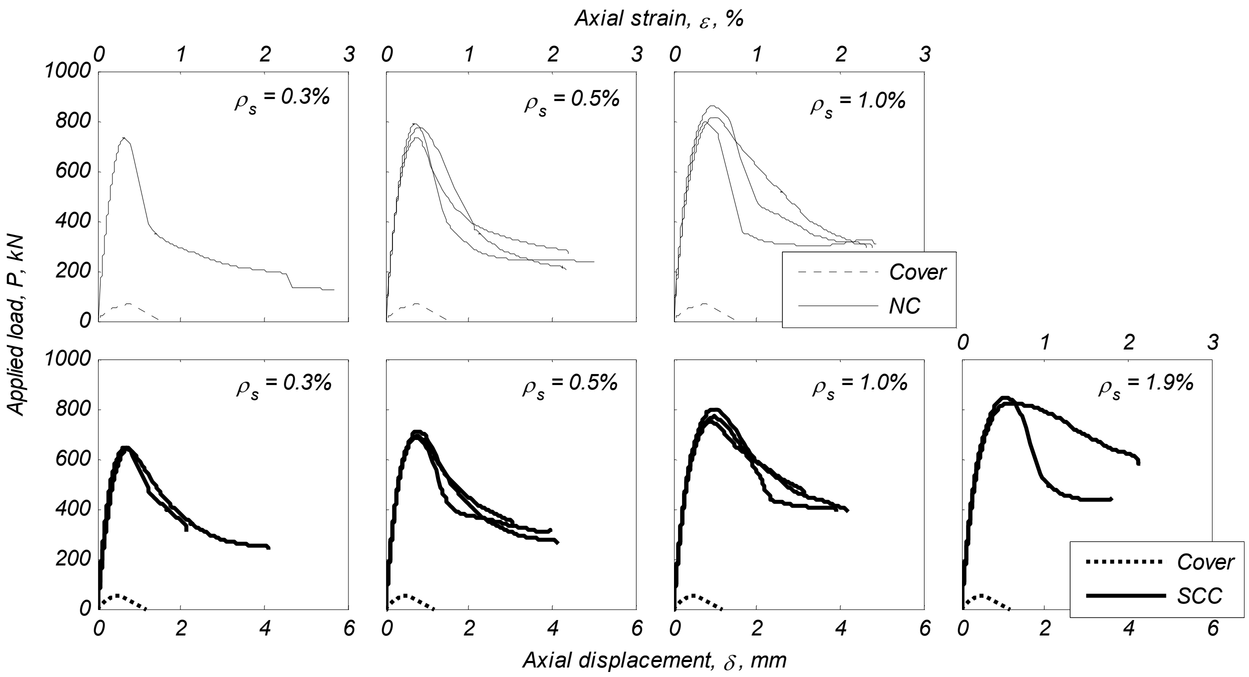

Figure 6. Measured axial force-displacement response of confined NC and SCC specimens at different transverse reinforcement ratios.

Table 5 provides a summary of key response parameters for all of the specimens in Figure 5 and Figure 6. Each specimen name contains the material abbreviation, the transverse ratio, and an identifier to differentiate duplicate specimens (separated by dashes). For example, specimen H-03-sg4 would be a HyFRC specimen with ρ_s = 0.3% and four spiral strain gages.

Parameters in Table 5 include the maximum load (P_{max}), the strain at the maximum load (ε_{cc}), and the ratios f_{cc}'/f_c' and K_{cc}/K_0. The unconfined compressive strength (f_c') is the value in Table 4 and the confined concrete strength (f_{cc}') was calculated as the maximum specimen load minus the estimated cover load at ε_{cc}, divided by the area of the confined core concrete (A_{cc}). This area was obtained as $A_{cc} = (1-\rho_l)A_g - A_{cov}$. The confined specimen stiffness (K_{cc}) is the initial slope of the force-displacement response of each confined specimen based on displacements taken over the 203 mm gage length, and the gross specimen stiffness (K_0) was calculated as $K_0 = \frac{E_c A_g}{L}$, where E_c is from Table 4.

Table 5 also provides the specimen toughness (T_1 and T_2) and the residual load ratio (r_1 and r_2) at 1% or 2% strain as indicated by the subscript. The toughness was calculated as the area under the axial load-displacement curve up to the indicated strain level (or up to the end of the test if it was stopped prior to reaching those strains). The residual load ratios are defined as the residual load in the specimen at the indicated strain divided by the peak specimen load; a dash indicates the test did not reach that strain.

Table 5. Summary of key response parameters of confined test specimens.

Specimen	P_{max}, *kN*	ε_{cc}, *%*	f_{cc}'/f_c'	K_{cc}/K_0	T_1 *, kN-mm*	T_2 *, kN-mm*	r_1	r_2
H-03-a	689	0.32	1.16	0.92	1179	2195	0.84	0.62
H-03-b	648	0.27	1.08	0.94	1042	1394	0.76	-
H-03-sg4	696	0.29	1.18	0.93	1096	1968	0.72	0.51
H-05-a	682	0.36	1.16	0.87	1172	2288	0.86	0.71
H-05-b	686	0.39	1.17	0.87	1197	2351	0.89	0.75
H-05-sg4	681	0.35	1.15	0.87	1140	2137	0.81	0.64
H-10-a	766	0.43	1.32	0.91	1319	2358	0.88	-
H-10-b	776	0.40	1.34	0.96	1283	2270	0.74	0.55
H-10-sg4	749	0.36	1.28	0.93	1208	2270	0.76	0.67
SCHa-03-a	704	0.43	0.99	1.04	1224	2184	0.83	-
SCHa-03-b	732	0.46	1.04	1.08	1266	2334	0.87	0.56
SCHa-03-sg4	740	0.38	1.06	1.06	1185	1969	0.68	0.40
SCHa-05-a	711	0.42	1.01	1.04	1207	1799	0.81	-
SCHa-05-b	759	0.72	1.10	0.91	1312	2687	0.98	0.80
SCHa-05-sg4	717	0.48	1.01	0.98	1227	2237	0.84	0.62
SCHa-10-a	776	0.57	1.11	1.04	1350	2735	0.94	0.82
SCHa-10-sg4	774	0.67	1.12	0.95	1337	2626	0.95	0.72
SCHb-03-a	616	0.51	1.11	0.94	1079	2067	0.90	0.67
SCHb-03-b	604	0.41	1.07	0.99	1033	1860	0.79	0.60
SCHb-03-c	577	0.38	1.02	1.05	998	1795	0.81	0.59
SCHb-05-a	578	0.37	1.02	0.92	971	1775	0.74	0.66
SCHb-05-b	604	0.43	1.08	0.95	1042	1999	0.83	0.74
SCHb-05-c	577	0.34	1.01	1.01	952	1714	0.72	0.61
SCHb-10-a	600	0.49	1.07	0.90	1033	1976	0.85	0.72
SCHb-10-b	628	0.53	1.13	0.96	1114	2181	0.91	0.79
SCHb-10-sg8	668	0.63	1.22	0.93	1148	2281	0.93	0.78
ECCa-03-a	805	0.35	1.15	1.09	1067	1330	0.48	-
ECCa-03-b	811	0.37	1.17	1.12	1192	1737	0.41	0.31
ECCa-03-sg8	765	0.35	1.09	1.12	989	1591	0.39	0.37
ECCa-05-a	811	0.36	1.16	1.12	1078	1691	0.40	-
ECCa-05-sg8	742	0.35	1.05	1.08	985	1616	0.43	0.41
ECCb-10-a	762	0.35	1.16	1.08	1078	2026	0.64	-
ECCb-10-b	795	0.39	1.24	1.05	1108	1979	0.54	0.54
ECCb-10-sg8	835	0.42	1.31	1.11	1146	1498	0.45	-
ECCb-19-a	829	0.47	1.33	1.06	1320	2518	0.73	-
ECCb-19-b	840	0.46	1.34	1.09	1315	2479	0.72	0.69
ECCb-19-sg8	861	0.52	1.40	1.08	1341	2182	0.62	-
NC-03-sg4	735	0.30	0.86	0.87	888	1344	0.38	0.26
NC-05-a	775	0.40	0.92	0.85	1218	1756	0.49	0.29
NC-05-b	735	0.37	0.85	0.82	1072	1749	0.54	0.39
NC-05-sg4	791	0.34	0.93	0.84	1012	1529	0.37	0.31
NC-10-a	859	0.47	1.06	0.88	1354	2119	0.55	0.37
NC-10-b	813	0.49	1.01	0.80	1317	2233	0.75	0.41
NC-10-sg4	799	0.34	0.94	0.84	1046	1674	0.40	0.40
SCC-03-a	642	0.36	0.96	0.77	932	967	0.54	-
SCC-03-c	646	0.33	0.95	0.93	1001	1584	0.58	0.39
SCC-05-a	689	0.38	1.05	0.90	1088	1490	0.64	-
SCC-05-b	688	0.36	1.03	0.88	1005	1657	0.54	-
SCC-05-c	711	0.39	1.09	0.91	1091	1740	0.58	0.39
SCC-10-a	749	0.44	1.17	0.86	1239	1805	0.78	-
SCC-10-b	768	0.48	1.22	0.84	1252	2052	0.71	-
SCC-10-sg8	800	0.47	1.28	0.85	1303	2270	0.73	0.50
SCC-19-b	843	0.53	1.37	0.88	1331	2050	0.60	-
SCC-19-sg8	822	0.61	1.34	0.85	1421	2824	0.96	0.75

2.3.3.4 *Damage observed in confined specimens*

Photos of the damage incurred by HyFRC, SC-HyFRC, and normal concrete specimens during testing are shown in Figure 7, Figure 8, and Figure 9, respectively. In each figure, the load-displacement response of the strain-gaged specimen of each material is plotted, and the triangles mark the points during the response when the photos were taken. The axial strains are shown on the top horizontal axis. Each row of photos corresponds to a single specimen.

Surface cracking initiated in HyFRC and SC-HyFRC at the maximum load (Figure 7 and Figure 8). The internal fibers slowed crack growth and coalescence and led to diffuse crack propagation after the peak. Cover spalling was eliminated and spiral fracture/bar buckling were delayed when compared to ECC, NC, and SCC specimens. Cracks were wider in HyFRC and SC-HyFRC specimens with $\rho_s = 0.3\%$ than at the higher transverse ratios at equal displacement levels.

Cracks also formed on the surface of NC specimens in the direction of loading as the maximum load was reached (Figure 9). This cracking coalesced into a dominant diagonal shear crack at an angle between 45 and 60 degrees from the horizontal in all three specimens when the strain was approximately 1% (for specimen NC-10-sg4, the crack is only partially in the frame). Shear cracks were the primary cause for loss of load capacity but were not observed in the specimens with fibers. Spalling was prominent along the shear cracks. Shear propagation occurred faster in specimens with low transverse reinforcing ratios since less spiral reinforcement was available to resist the shear deformation. Ultimate failure occurred when the spiral fractured, leading to localized buckling of the longitudinal bars due to loss of lateral support. Buckled bars can be observed in specimens NC-03-sg4 and NC-05-sg4 at strains of approximately 1.8%.

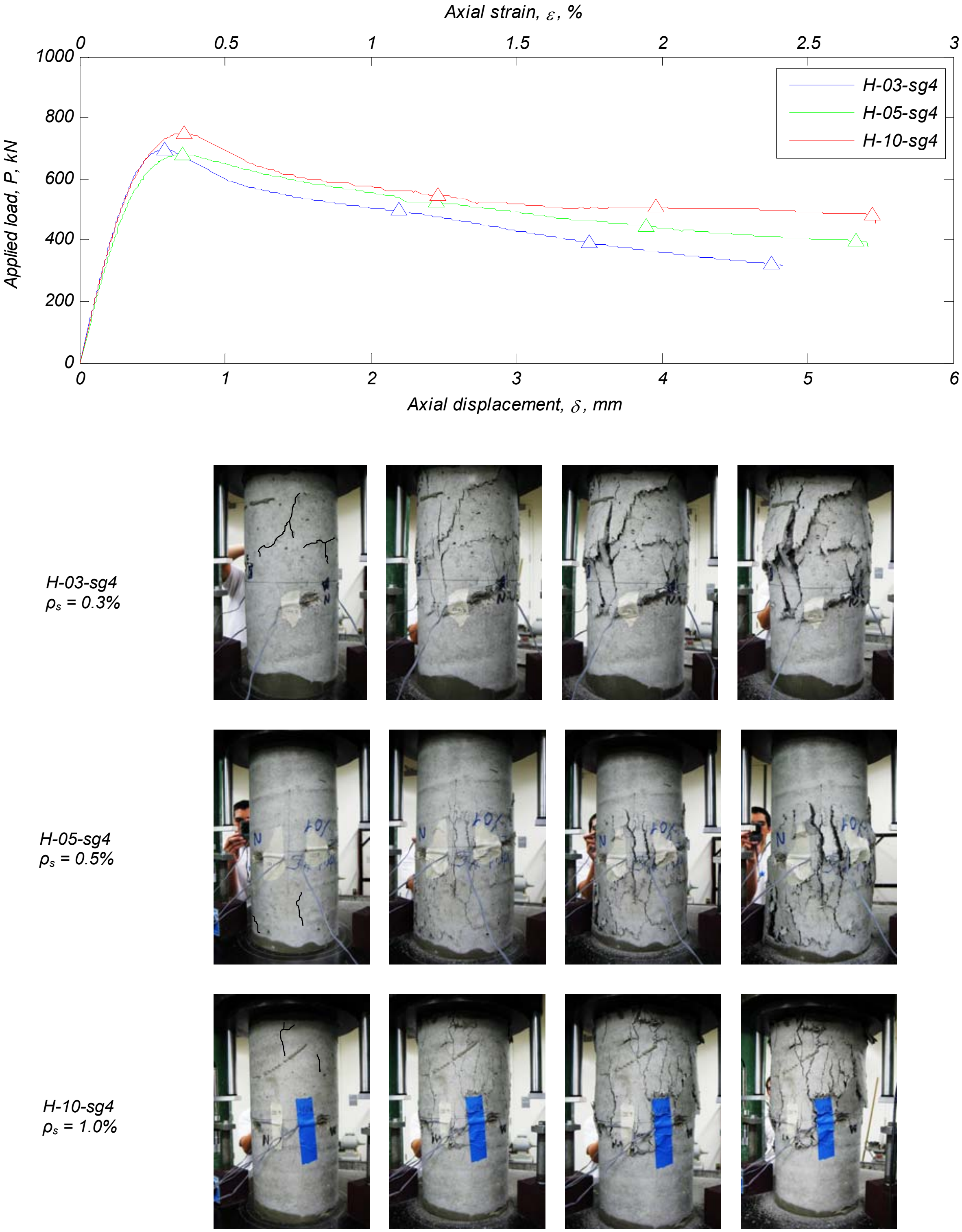

Figure 7. Damaged incurred during testing in HyFRC specimens at each transverse reinforcement ratio (cracks at peak load traced with black lines for clarity).

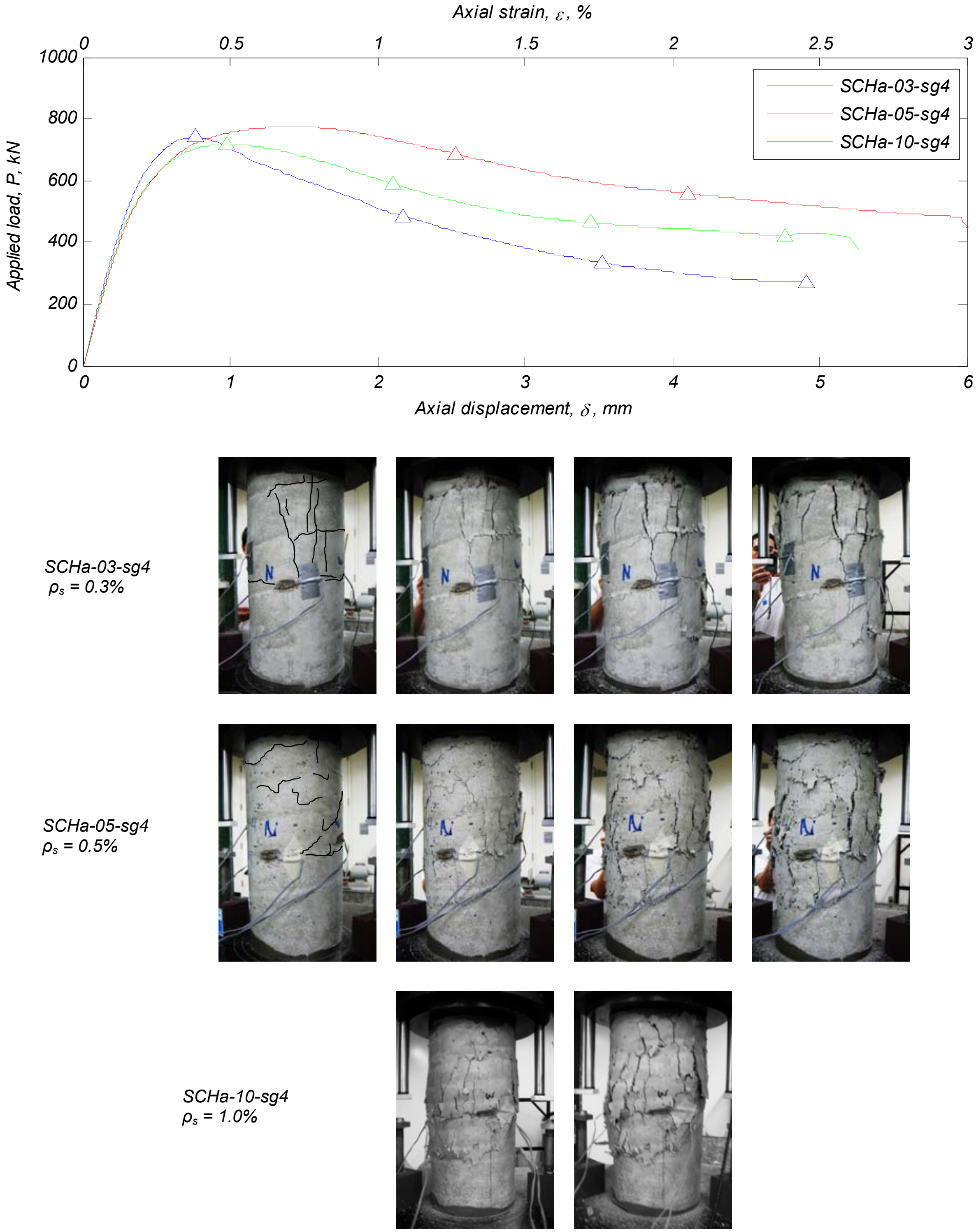

Figure 8. Damaged incurred during testing in SC-HyFRC specimens at each transverse reinforcement ratio (cracks at peak load traced with black lines for clarity).

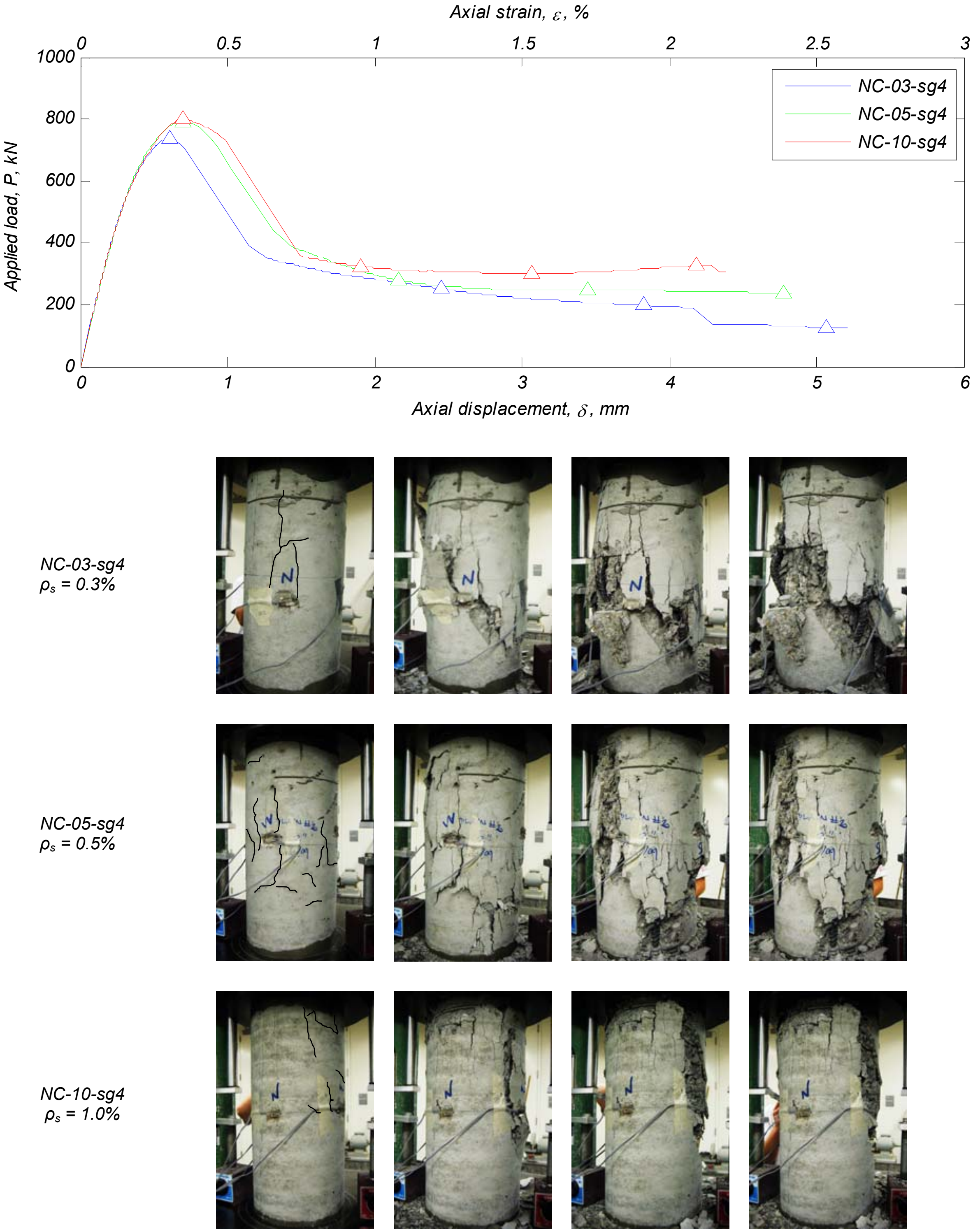

Figure 9. Damaged incurred during testing in NC specimens at each transverse reinforcement ratio (cracks at peak load traced with black lines for clarity).

2.3.3.5 *Strain in the spiral reinforcement*

Passively confined concrete relies on dilation perpendicular to loading to initiate stress in the transverse reinforcement. One hypothesis investigated in the confinement tests was whether the internally distributed fibers in HPFRCC's would delay dilation of the confined core material compared to normal concrete. The PVA microfibers are known to delay microcrack initiation and coalescence in flexural specimens, but their influence on the pure compressive response of materials is rarely studied. A delay in microcrack initiation would result in a steeper ascending branch of the load-displacement response. If outward dilation is more restricted in HPFRCC's, higher loads might be necessary to develop confining stresses in transverse reinforcement. At the same time, the required quantity of transverse reinforcement might be reduced if an internally distributed field of confining stresses was provided by the fibers.

Strain gage measurements of the spiral reinforcement were used to investigate the dilation of the confined core and are shown in Figure 10 for each gaged specimen. The strain measurements (four or eight per specimen) are normalized by the spiral yield strain, $\varepsilon_{s,y} = 0.30\%$, and are plotted against the ratio of applied load to peak load, P/P_{max}. After the peak load, damage and spiral strains often occurred away from the location where the strain gages were attached so the strains are shown only up to the peak load.

In specimens both with and without fibers, strains tended to increase at a constant rate (as a function of applied load) up to approximately 60% of the peak load. At that point, the maximum recorded spiral strain was less than 25% of $\varepsilon_{s,y}$ in all specimens. After that point, the rate of straining in the spiral increased due to the onset of internal microcracking. The point when the peak load was reached coincided with yielding of the spiral (measured by at least one gage) in all specimens. The confining stresses are maximized when the spiral yields; therefore, the fact that higher loads could not be sustained after spiral yielding was not surprising.

No appreciable difference in spiral strain behavior was observed between HyFRC and SC-HyFRC specimens compared to the specimens without fibers (NC, SCC). In addition, the spiral strains tended to increase at approximately the same rate between different transverse reinforcement ratios (ratios increase left to right in Figure 10– see specimen names).

Strain in the spiral was lower in the ECC specimens than all other specimens prior to the peak. A change in the rate of spiral strain did not occur until approximately 75% of the peak load. This difference may be attributed to the fact that ECC contains ten times the amount of PVA fibers (2.0% by volume) compared to the HyFRC and SC-HyFRC specimens (0.2% by volume) and those fibers would have the most influence on internal microcracking and dilation. However, ductility after the peak load was poor in ECC due to the lack of steel macrofibers which restrict and slow crack propagation.

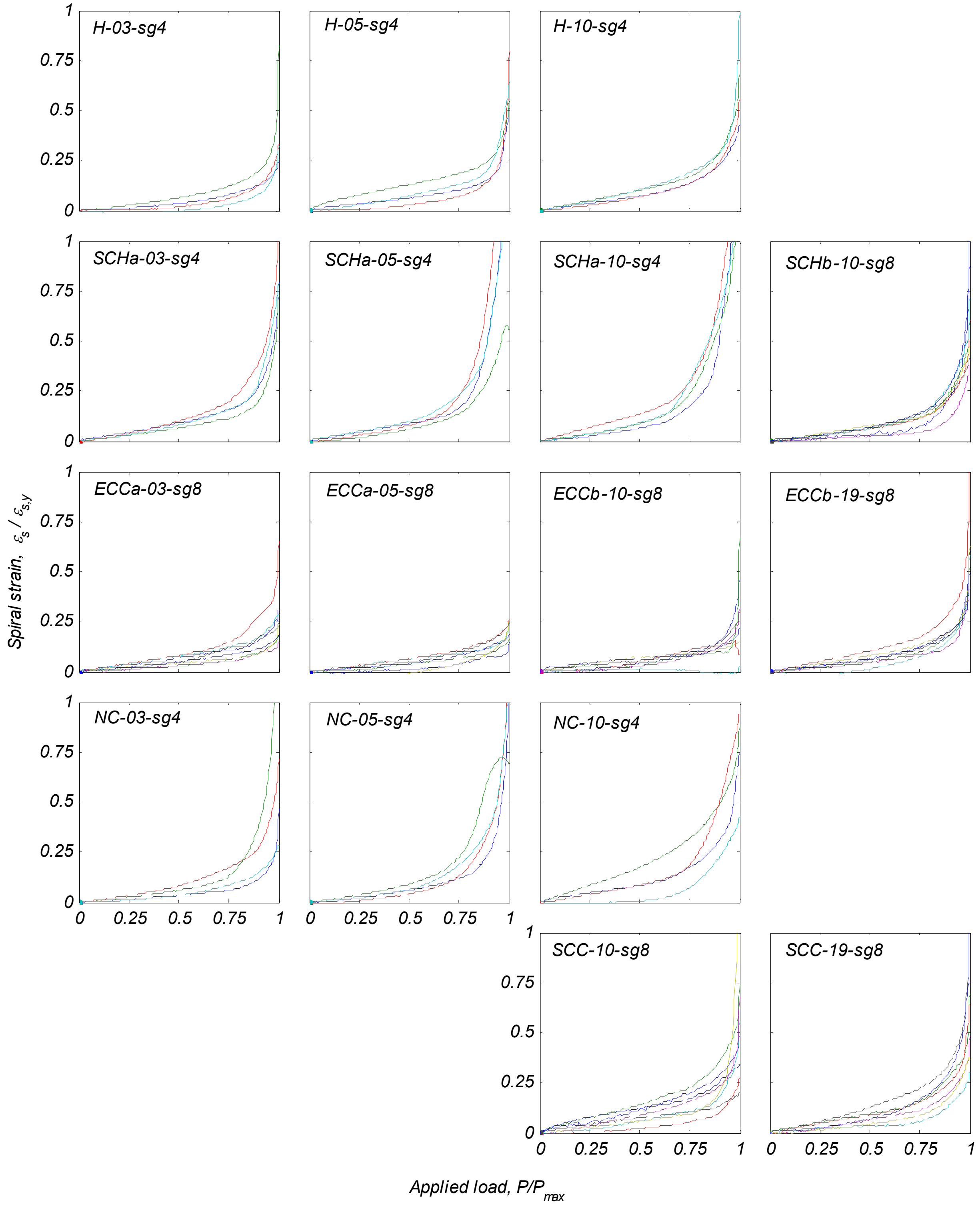

Figure 10. Spiral strain gage measurements.

2.3.4 Confined material strength and ductility characteristics

Empirical stress strain models for confined concrete typically predict that the maximum confined concrete stress exceeds the unconfined strength by an amount proportional to the lateral stress provided by transverse spirals, hoops, or ties. Researchers must separate the loads carried by the unconfined cover, the confined core, and any vertical reinforcement in the cross section to obtain the maximum confined concrete stress. The procedures used for such analyses are rarely reported in the literature, although they significantly affect the final result. For example, in short specimens, the load in longitudinal bars may be variable along the region where displacement is measured since load develops through bond, end loading, or a combination of the two.

One reason the tests by Mander et al. (1988a) are widely accepted for seismic design is because they considered full-scale column specimens (500 mm diameter) tested at high strain rates (up to 0.0167 strain per second). The ends of the columns (outside the instrumented region) were heavily confined and were long enough to develop a constant compression (over height) in the longitudinal bars. However, even in these tests, an assumption of “zero-slip” was made between the longitudinal bars and the concrete in the instrumented region. They did not take any direct measurement of the bar strains.

In this section, the stress-strain characteristics of the confined specimens were deduced, approximately, from the measured test data using a procedure similar to Mander et al. (1988a). The “zero-slip” assumption was not assumed and a discussion of the treatment of longitudinal bars is included in Section 2.3.4.1. The confined material stress-strain curves are presented and a discussion of the effects of confinement on strength, toughness, and residual load capacity follows.

2.3.4.1 *Consideration of the longitudinal rebar*

The load carrying ability of the longitudinal rebar was neglected when deducing the stress-strain response of the confined materials. The entire load was assumed to be carried by the cover and core material. The following list of considerations will show that this assumption is more appropriate than a “zero-slip’ assumption used in prior investigations:

1. The load from the testing machine was not passed directly from the load platen into the longitudinal rebar (i.e. the bars were not directly end-loaded). Rather, the load was passed through the layer of sulfur capping compound (several millimeters thick) at the top and bottom of the specimen. There were then several additional millimeters of cement paste above and below the ends of the rebar.

2. Observations of the specimen caps at the ends of the tests showed that the longitudinal bars penetrated into the capping compound during the test. Thus, slip must have occurred between the concrete or HPFRCC and the rebar during testing. Slip would result in lower strains in the bars than were measured by the external LVDT’s. Slip also indicates that compression in the rebar was forced to develop through bond rather than direct axial end loading.

3. The initial stiffness of the confined specimens was lower than the stiffness estimated for an unreinforced specimen of the same size as evidenced by the ratio K_{cc}/K_0

provided in Table 5. If the bars were attaining equal strains as the confined material, a plane-sections-remain-plane “zero-slip” model of the concrete and longitudinal bars in parallel could be used to estimate the confined specimen axial stiffness as in [2.3]:

$$K_{cc} = \frac{E_c A_c + E_s A_s}{L} = \frac{E_c(1-\rho_l)A_g + nE_c\rho_l A_g}{L} = (1-\rho_l+n\rho_l)\frac{E_c A_g}{L} = (1-\rho_l+n\rho_l)K_0 \qquad [2.3]$$

where $n = E_s/E_c$. Thus, for $\rho_l = 0.01556$ and n between 7.2 and 10.3 (see Table 4), the ratio K_{cc}/K_0 would be expected to range from 1.10 to 1.14. The ratios measured during testing were in many cases below 1.0, with the exception of the ECC specimens. It is hypothesized that the high cement content and high volume of microfibers in ECC improved the bond and decreased slip between the bar and surrounding concrete. Thus, for ECC, neglecting the bar contribution may have caused the confined concrete stress (presented in Section 2.3.4.2) to be overestimated.

4. According to ACI 318 Section 12.3.2 (2008), the development length for the longitudinal bars in compression would be calculated as the larger of $0.02\frac{f_y}{\sqrt{f_c'}}d_b$ or $0.0003 f_y d_b$, with an additional 25% reduction due to the spiral reinforcement. This would result in $12d_b$ (114 mm) of required length. Only 51 mm was provided outside the gage length; hence, there was not enough to develop a constant compression in the bars in the gaged region. Demands on the core material were therefore higher near the specimen ends, and, not surprisingly, cracking initiated in those regions.

5. No strain measurements were taken from the longitudinal rebar so stresses could not be deduced directly and any other estimate would be highly uncertain.

2.3.4.2 *Confined material stress-strain response*

The stress in the confined material was calculated by first finding the difference between the total applied specimen load and the cover load, both of which are shown in Figure 5 and Figure 6. The core stress was then calculated as the core load divided by A_{cc} for all data points.

The cover and core stress-strain responses are compared in Figure 11 and Figure 12 for HPFRCC materials and the materials with no fibers, respectively. Figure 11 shows that the softening response of the unconfined and confined HyFRC and SC-HyFRC was practically identical. Increasing ρ_s has the effect of slightly increasing the slope of the softening branch in some specimens (SCHa and SCHb, $\rho_s = 1.0\%$); however, at $\rho_s = 0.3\%$ and $\rho_s = 0.5\%$ the difference was negligible. This result supports the notion that the inclusion of fibers can result in a ductile softening response even in the absence of passive confinement reinforcement. After the peak load, the dominant failure mode is compression-shear macrocracking and the steel fibers therefore play a significantly larger role compared to the PVA fibers. The PVA fibers lose effectiveness when macrocracks form and likely only affect the ascending branch (to a small degree) during microcracking.

The stress strain response of the confined ECC specimens was more ductile than the unconfined specimens. A sudden drop in stress occurred in most of the confined specimens immediately after the peak load regardless of ρ_s. Increasing ρ_s tended to increase the load during the “plastic” portion for cases of $\rho_s = 1.0\%$ and $\rho_s = 1.9\%$.

The NC and SCC specimens showed incremental improvements in stress capacity and softening behavior with increasing ρ_s as shown in Figure 12. Still, the softening curve of *unconfined* HyFRC and SC-HyFRC was still superior to *confined* NC and SCC. The NC and SCC specimens had negligible strength enhancement at $\rho_s = 0.3\%$ since that ratio is quite low.

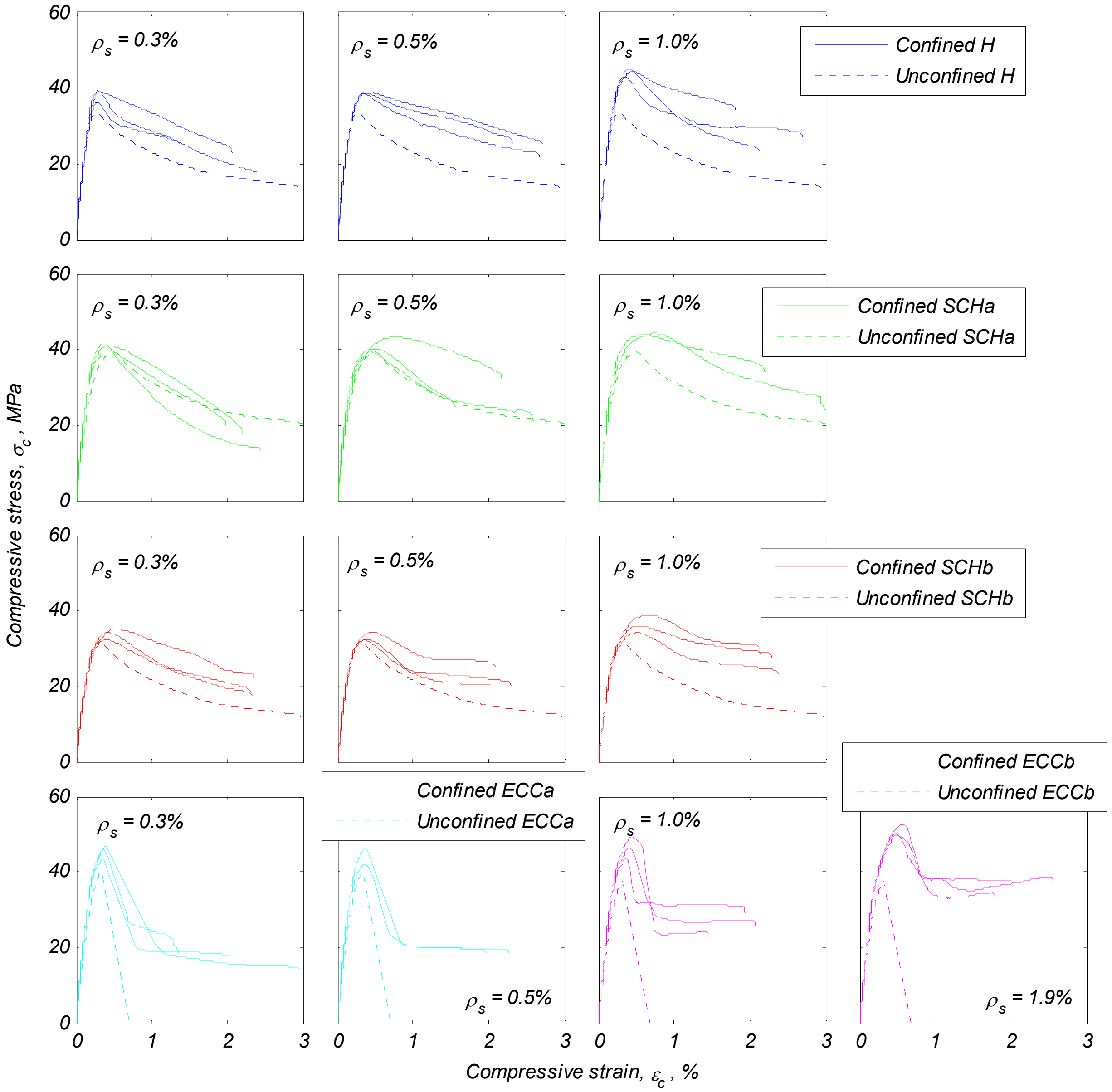

Figure 11. Comparison of unconfined and confined compression stress-strain responses for HPFRCC materials.

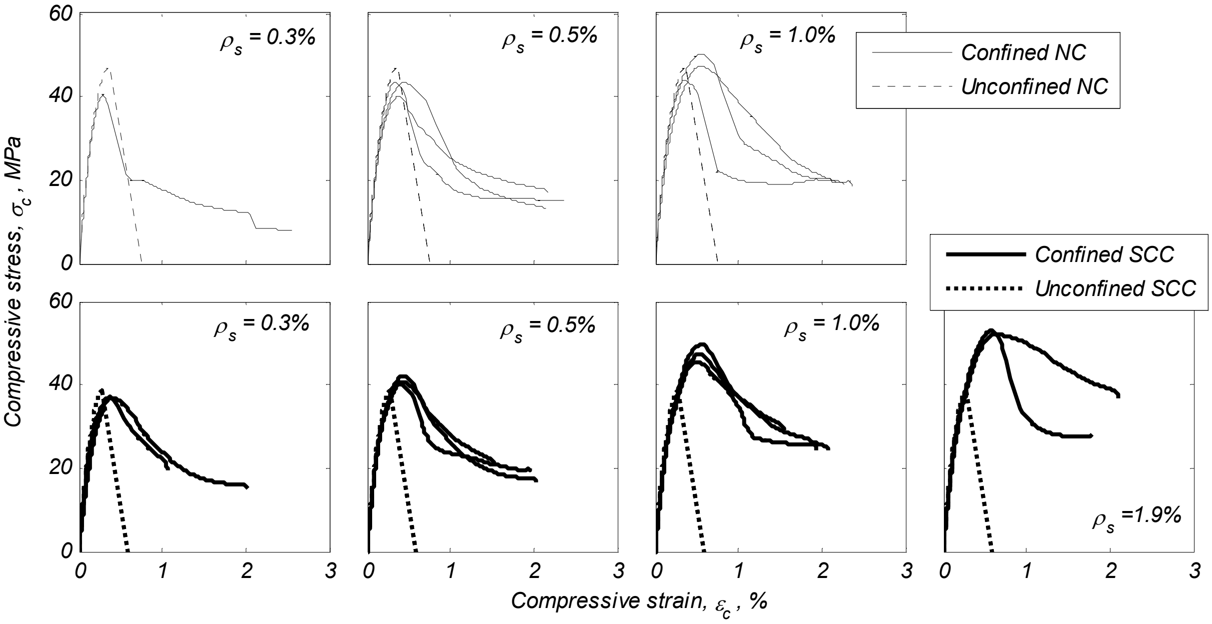

Figure 12. *Comparison of unconfined and confined compression stress-strain responses for NC and SCC materials.*

2.3.4.3 *Effect of confinement on peak strength*

Figure 13 plots the mean and individual confined strength ratios against ρ_s for the specimens of each material. All of the specimens had a greater mean confined strength ratio as the transverse reinforcing ratio increased above $\rho_s = 0.5\%$.

For the specimens with fibers (HyFRC, SC-HyFRC, and ECC), the variability of individual specimen results at $\rho_s = 0.3\%$ and 0.5% indicates that ρ_s had little effect on the confined concrete strength at such low ratios. The HyFRC, SC-HyFRC, and ECC specimens had mean values of f_{cc}'/f_c' that ranged between 1.03 and 1.36 over all values of ρ_s. HyFRC at $\rho_s = 1.0\%$ and ECC at $\rho_s = 1.9\%$ consistently had f_{cc}'/f_c' over 1.30.

NC and SCC specimens had mean values of f_{cc}'/f_c' between 0.86 and 1.36. The mean values were < 1 for all NC at $\rho_s = 0.3\%$ and 0.5% and for all SCC at $\rho_s = 0.3\%$. Increasing levels of transverse reinforcement in the specimens without fibers caused appreciable increases in f_{cc}'/f_c' with less variability between specimens than for the HPFRCC specimens. The fact that specimens without fibers had $f_{cc}' < f_c'$ might have been related to additional voids and/or defects caused by the reinforcement in confined specimens.

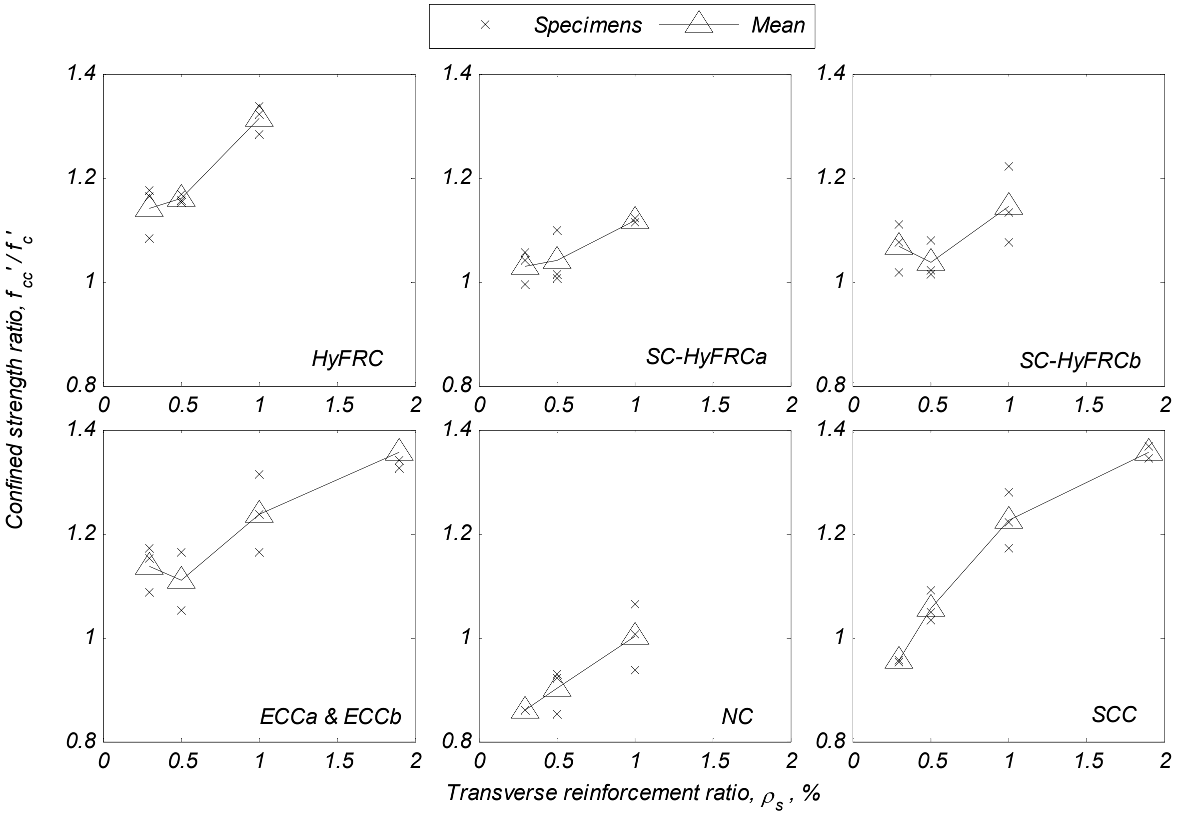

Figure 13. Mean and individual confined strength ratios of specimens at different transverse reinforcement ratios.

2.3.4.4 *Effect of confinement on softening and residual load ratios*

The post-peak residual load resistance is a better metric than confined material stress-strain curves for evaluating seismic performance. First, "strain" measurements after the peak are essentially a smeared average of localized cracking. Furthermore, the load in the longitudinal bars was more significant following the peak because of specimen damage, so the "stress" in the softening portion of the confined stress strain curves is highly approximate.

Considering these facts, the confined material stress-strain curves in Section 2.3.4.2 (Figure 11 and Figure 12) are unique to this specimen size and test configuration (in particular, gage length) and care should be taken if they are used for nonlinear modeling. Degrading stress-strain curves are often used for concrete fibers in R/C moment-curvature analysis. When the reported stress-strain results are used for such modeling, they would need to be scaled using fracture energy principles based on element length to accurately predict deformations. HPFRCC's are also characterized by discrete cracking rather than uniform strain behavior so care must be taken when using stress-strain curves in nonlinear analysis. Such discrete cracking occurs at higher deformations than in concrete without fibers, hence use of such curves is more appropriate for HPFRCC's than for conventional R/C.

Figure 14 and Figure 15 plot only the softening portion of each specimen's load-displacement response (see Figure 5 and Figure 6). Residual load ratio is given on the ordinate and the post-peak displacement, δ_{pp}, is shown on the abscissa. The residual load ratio is defined as the load in the specimen normalized by the maximum load (P/P_{max}) while the post-peak displacement is displacement occurring after the peak load was reached. Axial shortening (dimensionless) is also shown on the top horizontal axis, calculated as the post-peak displacement normalized by the LVDT gage length.

As shown in Figure 14, most of the HyFRC and SC-HyFRC specimens softened linearly at a constant rate up to 4 mm of post-peak displacement (2% post-peak shortening). They retained over 70% of their peak load at 2 mm post-peak displacement (1% post-peak shortening) and over 60% of their peak load at 4 mm post-peak displacement (2% post-peak shortening). Some of the SCHb specimens had a more bilinear softening curve. ECC specimens showed a very abrupt softening response. For ρ_s = 0.3% and 0.5%, they immediately lost roughly 60% of load capacity after the peak. For higher ρ_s , the load loss was still abrupt but the residual capacity increased.

Figure 15 shows the same data for the NC and SCC specimens. The softening curves were less abrupt than for ECC and parabolic in shape. The specimens at ρ_s = 0.3% and 0.5% lost over 50% of their load capacity by 2 mm of post-peak displacement. For higher ρ_s the magnitude of load loss decreased only marginal except for one SCC specimen at ρ_s = 1.9%. Although the confined concrete strength of NC and SCC seemed to be highly dependent on ρ_s, the shape of the softening curves was not. Like the HyFRC specimens, NC and SCC softened at about the same rate, independent of ρ_s.

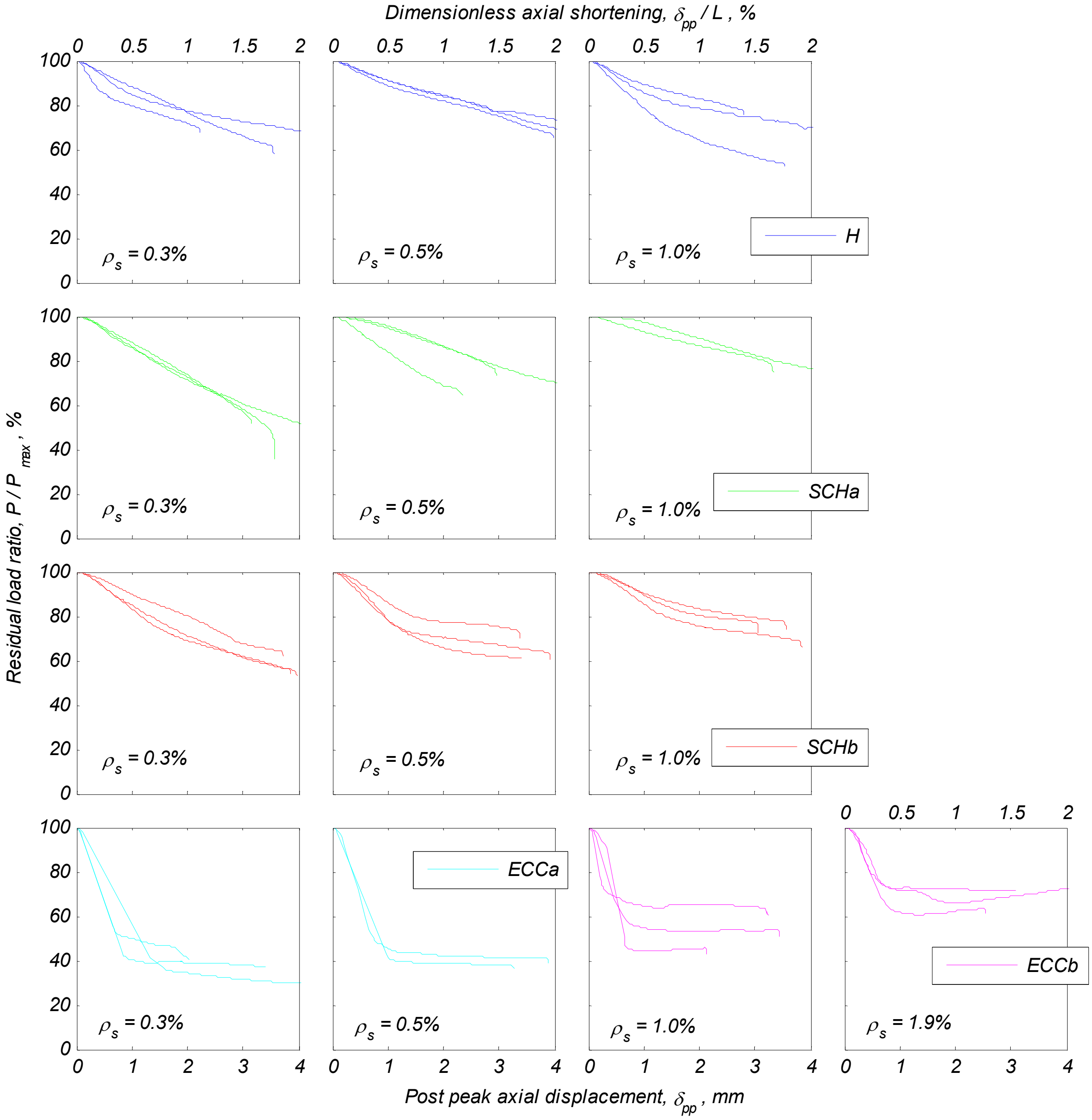

Figure 14. Softening response of HPFRCC specimens at varying transverse reinforcement ratios.

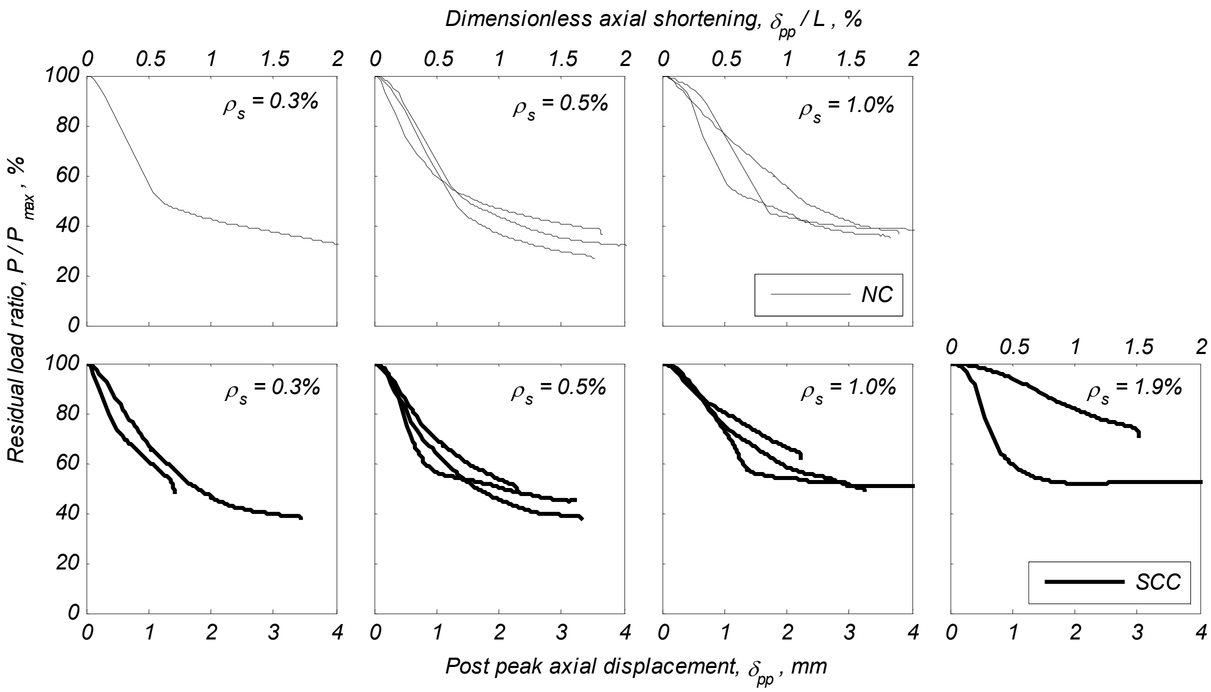

Figure 15. Softening response of NC and SCC specimens at varying transverse reinforcement ratios.

Figure 16 plots the residual load ratios, r_1 and r_2, for all the confined materials as well as the mean value at each transverse reinforcement ratio. These factors were defined as the fraction of peak load at 1% or 2% strain during testing and were listed in Table 5. Specimens with $r_2 = 0$ due to early test termination are not shown and were not included in the mean value calculation.

The residual load factors at both 1% and 2% strain were substantially higher for HyFRC and SC-HyFRC than for the other materials. The mean r_1 exceeded 0.76 for all values of ρ_s. The mean r_2 exceeded 0.57 for all ρ_s except SCHa at $\rho_s = 0.3\%$, which was abnormally low compared to the other specimens. The mean values of r_1 and r_2 were independent of ρ_s for HyFRC and SC-HyFRC.

The mean residual load factors for ECC, NC, and SCC were generally lower than HyFRC or SC-HyFRC, but they were more likely to increase with increasing ρ_s. For ECC, there was practically no difference between r_1 and r_2 since the response was nearly plastic after the initial loss of load. The mean values ranged between 0.42 and 0.69 over the range of ρ_s. For NC, mean r_1 values ranged between 0.38 and 0.57 while the mean r_2 did not exceed 0.39. SCC samples had mean r_1 values that ranged from 0.56 to 0.78 and mean r_2 values that ranged from 0.39 to 0.75. One NC sample at $\rho_s = 1.0\%$ and one SCC sample at $\rho_s = 1.9\%$ attained significantly more residual strength than the others.

The overall greater level of residual strength capacity in specimens with fiber hybridization (HyFRC, SC-HyFRC) is indicative of the toughness improvement provided by the steel fibers. The length of the steel fibers allows them to affect crack behavior even at large crack openings. Although the PVA microfibers are effective in arresting microcracks, the failure of specimens in compression causes an abrupt formation of macrocracks and hence the PVA fibers quickly became ineffective. HyFRC and SC-HyFRC attained a high degree of residual load capacity at compressive strains of 2% (r_2) regardless of the transverse reinforcement ratio. This level of residual capacity was attainable only at the highest reinforcement ratios in a limited number of ECC, NC, and SCC specimens.

These results show that the capacity of HyFRC members after cracking/crushing may be substantially greater than for concrete members. This behavior can improve the performance of bridge columns when they experience high compression forces in the plastic hinge. The improved softening response of HyFRC provides an additional safeguard against brittle failure if/when seismic forces exceed the crushing strength of the confined core.

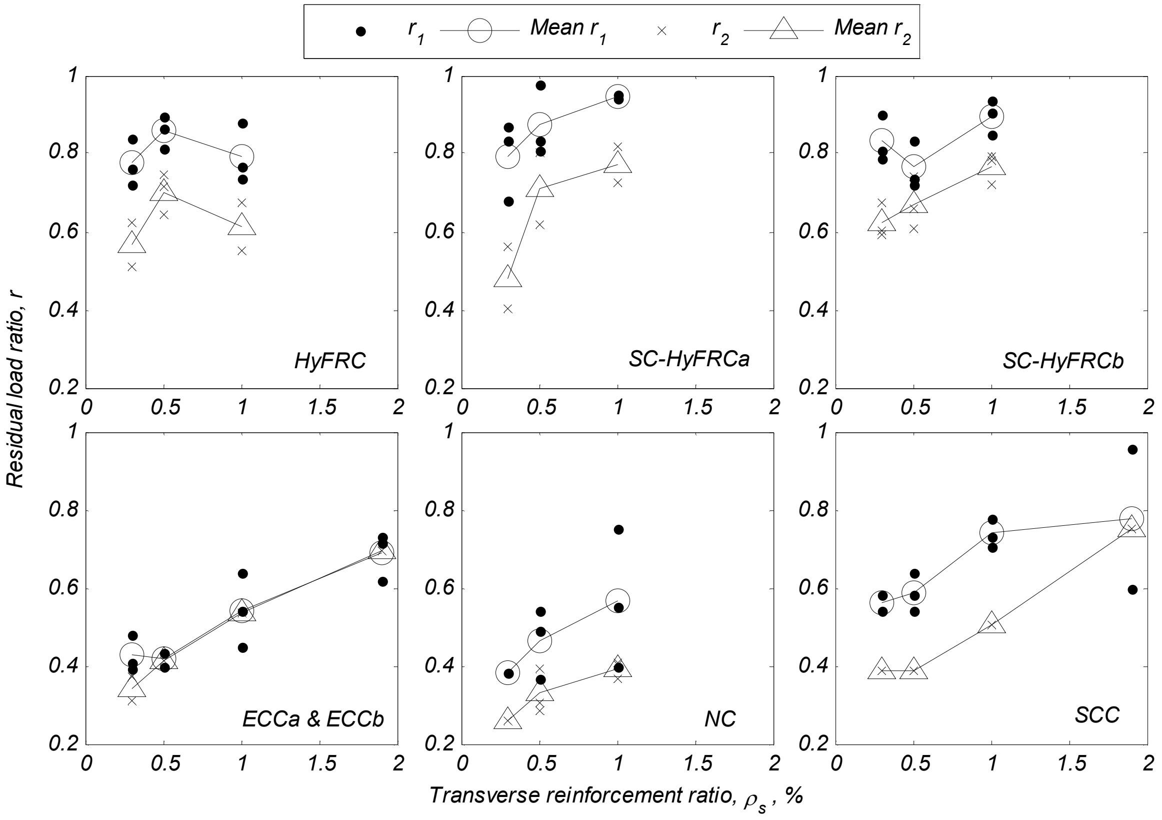

Figure 16. Mean and individual residual strength ratios of specimens at different transverse reinforcement ratios.

2.3.4.5 *Effect of confinement on compression toughness*

Figure 17 shows the calculated mean and individual toughness against ρ_s for all the confined materials. Variations in peak load and the softening slope among the different materials affected the magnitude of T_1 and T_2. The slope of the HyFRC and SC-HyFRC softening branches was greater than that of ECC, NC, and SCC specimens. However, the values of T_1 (i.e. area under the load-displacement curve up to 1% strain) were similar for all materials because only a small amount of softening occurred before 1% strain. Variations in peak load had a smaller effect on toughness since the proportion of total energy dissipated prior to reaching the peak load is generally small.

The toughness of HyFRC, SC-HyFRCa and SC-HyFRCb specimens up to 2% strain was generally greater than that of ECC, NC, and SCC, especially at ρ_s of 0.3% and 0.5%. The latter group saw noticeable increases in T_2 as ρ_s increased, while the former group attained similar toughness regardless of ρ_s. For HyFRC and SC-HyFRCa there was more variability among the specimens at ρ_s = 0.3% and 0.5% than at 1.0%.

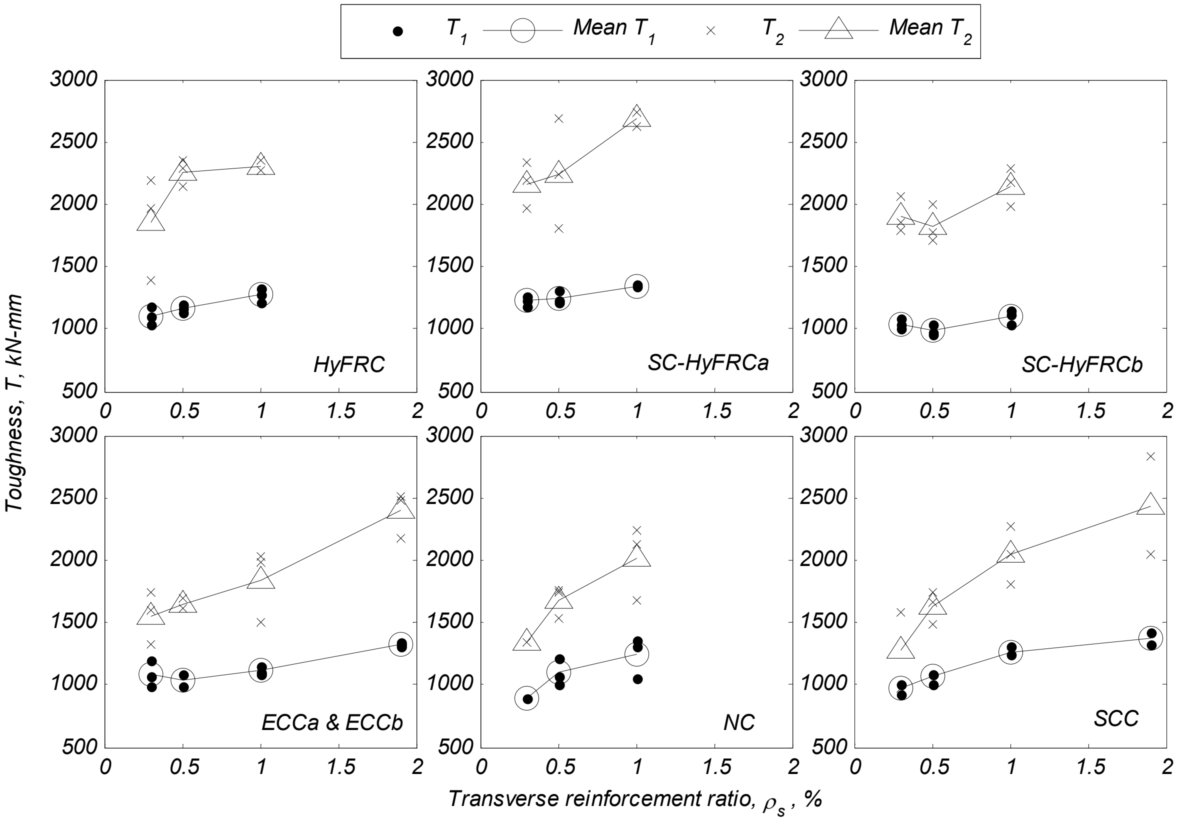

Figure 17. Mean and individual toughness values of specimens at different transverse reinforcement ratios.

2.3.4.6 *Effect of different fiber combinations on confined specimen behavior*

The results presented in this section showed that the HyFRC and SC-HyFRC specimens with minimal confinement (or no confinement at all) had a superior softening response compared to NC or SCC specimens with higher levels of confinement. This improved softening was a result of the steel macrofibers and their ability to resist propagation of compression and compression-shear cracks. The fibers did not seem to affect the strength enhancement; it was primarily a function of the level of confinement for all materials. The PVA microfibers are ineffective at resisting large macrocracks and had little effect on the softening response of HyFRC and SC-HyFRC specimens.

The ECC specimens contained only PVA microfibers and showed very poor softening behavior. Their initial stiffness, however, was noticeably higher than the other specimens, potentially due to a delay in microcrack initiation during the ascending branch. The lower spiral strains in the ECC specimens during the ascending branch suggest a reduction in dilation and also support the hypothesis that microcracks were delayed by the high proportion of PVA microfibers (2% by volume).

2.4 Tension stiffening in HyFRC composites

The first part of this section will review the existing literature on tension stiffening effects in fiber-reinforced concrete. Then, results from uniaxial tension tests of prismatic HyFRC members reinforced with a single conventional reinforcing bar are presented and analyzed. In total, 20 specimens were fabricated and tested to investigate the tension stiffening response of HyFRC and SC-HyFRC materials. The results are compared with identical members cast with normal concrete and the pertinent conclusions are summarized and discussed.

2.4.1 Background and previous experimental studies

Tension stiffening effects arise when reinforcing bars are embedded in concrete and subjected to tension. Before the concrete cracks, strains/deformations are uniformly distributed (plane sections remain plane) and the member stiffness is the aggregated stiffness of the steel and concrete in parallel. After cracking, the concrete between cracks enhances the overall member rigidity and thus must be considered in estimations of member deflection and crack widths under service loads. Still, tension stiffening in R/C with no fibers is typically exhausted at low strains and well before the rebar yield strain; hence, concrete is typically assumed to carry no tension when designing members. The degree of tension stiffening is a function of several characteristics of the member including the relative proportions of concrete and rebar (i.e. the reinforcing ratio), the rebar diameter, the tensile strength of concrete, and the length of the cracked region (since concrete can continue to stiffen the rebar response between cracks after they form).

The tension stiffening effect in concrete with fibers is markedly different. The fibers can bridge cracks thereby increasing the stiffness in their vicinity. Several prior experimental investigations have supported this conclusion, and the characteristics of specimens in those investigations are summarized in Table 6. These include the cross section dimensions, the specimen height (H), the longitudinal bar diameter (d_b), the longitudinal reinforcement ratio (ρ_l), the bar yield strength (f_y), the compressive strength of FRC (f_c'), the volume fraction of fibers (V_f), and the fiber length (L_f), aspect ratio (L_f/d_f), and type. In all of these studies, the specimens were tested by applying load to the embedded rebar. Load developed in the FRC through steel-concrete bond.

Table 6. Summary of selected tension stiffening studies on FRC specimens.

Reference	*Cross section*	*H mm*	*d_b mm*	*ρ_l %*	*f_y MPa*	*f_c', MPa*	*V_f, %*	*L_f, mm*	*L_f/d_f*	*Fiber type* [a]
Abrishami and Mitchell (1997)	rectangular, 95x170 mm	1500	16	1.2	480	30.8 74.6	1.0	30	60	S, H
Fischer and Li (2002)	square, 175x175 mm 125x125 mm	500	25	1.5 1.8	420	80	1.5	-	-	PE
Bischoff (2003)	square, 100x100 mm	1100	16 19	2.0 3.1	421 442	62.4	0.8	50	100	S, H
Yuguang et al. (2009)	square, 50x50 mm	700	10	3.1	530	130	0.8 1.6	13 13, 20, 6	81 81, 67, 38	S

[a] *S = steel; H = hooked-end; PE = polyethylene*

Specimens ranged from 500 to 1500 mm in length and ρ_l varied between 1.2% and 3.1%. Fiber quantities ranged from $V_f = 0.8\%$ to 1.6%. The study by Fischer and Li considered a tensile strain hardening HPFRCC with polyethylene fibers while the other studies considered conventional FRC's with steel fibers.

All tests showed that specimens with fibers had higher strength after cracking than specimens with no fibers at equivalent levels of elongation. The fibers continued to carry load even after the rebar yielded, while specimens with no fibers followed the load-displacement response of a bare reinforcing bar after yielding (Abrishimi and Mitchell 1997, Bischoff 2003, Yuguang et al. 2009). However, prior to cracking, the stiffening effect in specimens both with and without fibers was nearly identical.

Abrishimi and Mitchell (1997) observed both transverse and splitting cracks in concrete specimens, while FRC specimens showed transverse cracking only with a shorter crack spacing. Bischoff (2003) also observed a shorter crack spacing in FRC specimens compared to concrete specimens. Yuguang et al. (2009) found that in FRC specimens, yielding was localized to one crack whereas in concrete specimens yielding occurred at three points along specimen length. Incremental increases in fiber content from 0% to 0.8% to 1.6% reduced crack spacing from 56 mm to 23 mm to 14 mm. The lack of splitting cracks in FRC specimens, shorter crack spacing, and localized yielding at a single crack are indicative of greater FRC-rebar bond compared to normal concrete. Such phenomena could result in more strain localization and earlier fracture in reinforcing bars under large seismic demands.

All the tests on steel FRC specimens were terminated at average composite strains of less than 0.5%. In R/C structures subjected to seismic loading, significantly higher tension strains might develop in flexural plastic hinges and therefore one purpose of the tests presented in this chapter was to investigate the response at large strains (> 1%). Fischer and Li (2002) found that HPFRCC specimens with polyethylene fibers at $V_f = 2.0\%$ maintained strain compatibility with the rebar (through closely spaced microcracks) up to strains of 4.5%.

2.4.2 Testing program

Eight specimens were cast using HyFRC and four were cast with SC-HyFRC. Eight additional specimens were cast with normal concrete as reference specimens. Two different specimen cross sections were considered resulting in longitudinal reinforcement ratios of ρ_l = 1.2% and 0.6%. All specimens contained a single deformed reinforcing bar through which external load was applied. Tension was transferred from the bar to the surrounding matrix through the bond between the materials. This section of the report contains pertinent details of the test specimens, test setup, and test results. The results presented here were part of a larger collaborative test program, fully detailed in Moreno et al. (2014).

2.4.2.1 *Description of test specimens*

The tensions stiffening tests were performed on large prismatic specimens with a 127x127 mm or 178x178 mm square cross section and a height of 1041 mm. The single rebar located at the centroid of each specimen was deformed mild steel with a 16 mm diameter (No. 5). Two bare rebar samples were tested in tension and the average yield strength and strain at onset of yielding were f_y = 439 MPa and ε_y = 0.25%. The longitudinal reinforcing ratios were either ρ_l = 1.2% or ρ_l = 0.6% depending on the cross section. HyFRC, SC-HyFRC, and normal concrete specimens were tested. Four specimens with 127x127 mm cross sections were tested for each material. Four additional specimens with 178x178 mm cross section were tested for both NC and HyFRC. A cross section of the specimens is shown in Figure 18(a).

Material mix proportions for SC-HyFRC were identical to those used in the confinement tests. A small change was made to the water to cement ratio for HyFRC and normal concrete, increasing from 0.45 to 0.54. The proportions of aggregate were also increased to maintain the aggregate+fiber to cement paste ratio. The fiber content was kept the same as the confinement tests. The proportions used in the tension stiffening experiments are given in Table 7, and properties of the three fiber types were the same as were used for the confinement tests (Table 3).

Table 7. Material mix proportions for tension stiffening tests (SSD condition).

	proportions by mass					*fraction of binder mass*		*volume fraction*		
Material	*Cement*	*Fly Ash*	*Water*	*Sand*	*Gravel*	*SP*	*VMA*	*PVA1*	*S1*	*S2*
HyFRC	1	-	0.54	1.95	1.77	0.0016	-	0.002	0.005	0.008
SC-HyFRC	0.75	0.25	0.45	1.91	0.77	0.0093	0.0222	0.002	0.013	-
Concrete	1	-	0.54	2.06	1.75	-	-	-	-	-

2.4.2.2 *Test configuration*

Tensile load was applied through 25 mm diameter threaded rods extended from the end of the specimen as in Figure 18(a) and Figure 18(b). Prior to casting the specimens, these rods were threaded into female couplers which were friction welded to the ends of the rebar. A steel wire cage was used to reinforce the end region where the threaded rod and rebar are coupled in order to prevent pullout failure of the rebar. The ends of the specimens with 178x178 mm cross sections were also reinforced with carbon fiber-reinforced polymer (CFRP) wrapping to prevent rebar pullout at the ends [Figure 18(b)] since they had a higher load capacity.

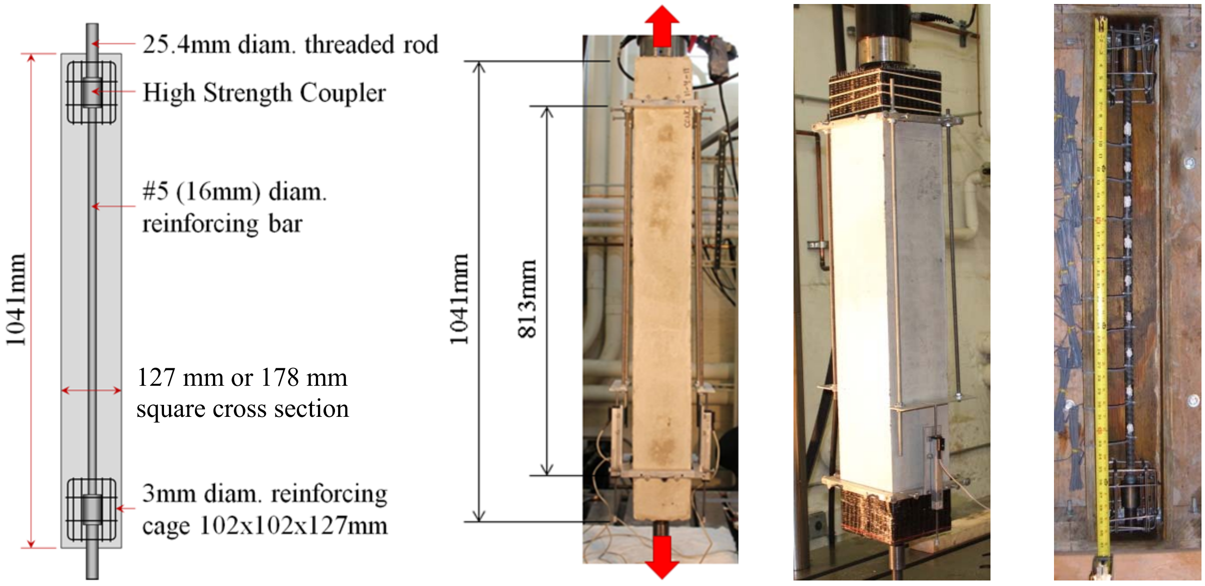

(a) Cross section *(b) Test setup* *(c) Strain gages*

Figure 18. Tension specimen details; (a) cross section, (b) test setup, and (c) strain gages (based on Moreno et al. 2014).

The test setup is shown in Figure 18(b). Displacements were measured over a gage length of 813 mm over the center of the specimen using displacement transducers. Applied load was measured by the testing machine. Loading was displacement-controlled at a constant rate of 0.6 mm/min to accurately capture the inelastic response of the specimens.

Nine strain gages were fixed to the rebar in one specimen of each size and material type to measure the distribution of strain in the rebar along the specimen length. Gages were spaced at 75 mm intervals extending outward from the center of the specimen. Care was taken to minimize the area of bar covered by the gages to preserve as much bond as possible. A gaged specimen is shown in Figure 18(c) prior to casting.

2.4.2.3 *Material properties*

The compressive and tensile strengths of the materials are given in Table 8. The compressive strengths were obtained by averaging three 102x203 mm cylinders. The tensile strengths were obtained from the reinforced specimens using [2.4], assuming compatible strains between the material and the rebar at first cracking. In [2.4], P_{cr} is the specimen load at first cracking, A_s is the area of the rebar, $f_s(\varepsilon_{cr})$ is the rebar stress (from the bare rebar stress-strain curve) at the strain corresponding to first cracking of the specimen, and A_g is the gross cross-sectional area.

$$f_t = \frac{P_{cr}-A_s f_s(\varepsilon_{cr})}{A_g-A_s} \qquad [2.4]$$

Table 8. *Compressive and tensile strength of tested materials.*

Material	*f_c', MPa*	*f_t, MPa*
HyFRC	31	1.90
SC-HyFRC	40	1.80
Concrete	44	1.40

The tensile stress-strain characteristics of the HyFRC and SC-HyFRC materials are shown in Figure 19. These curves were obtained from unreinforced dogbone specimens with the dimensions shown in Figure 19(a). In direct tension, the materials had a brief period of tensile strain hardening, followed by a short period of plastic strain (SC-HyFRC) and then softening. The HyFRC sample had a small loss of load (due to cracking) prior to the plastic strain occurring.

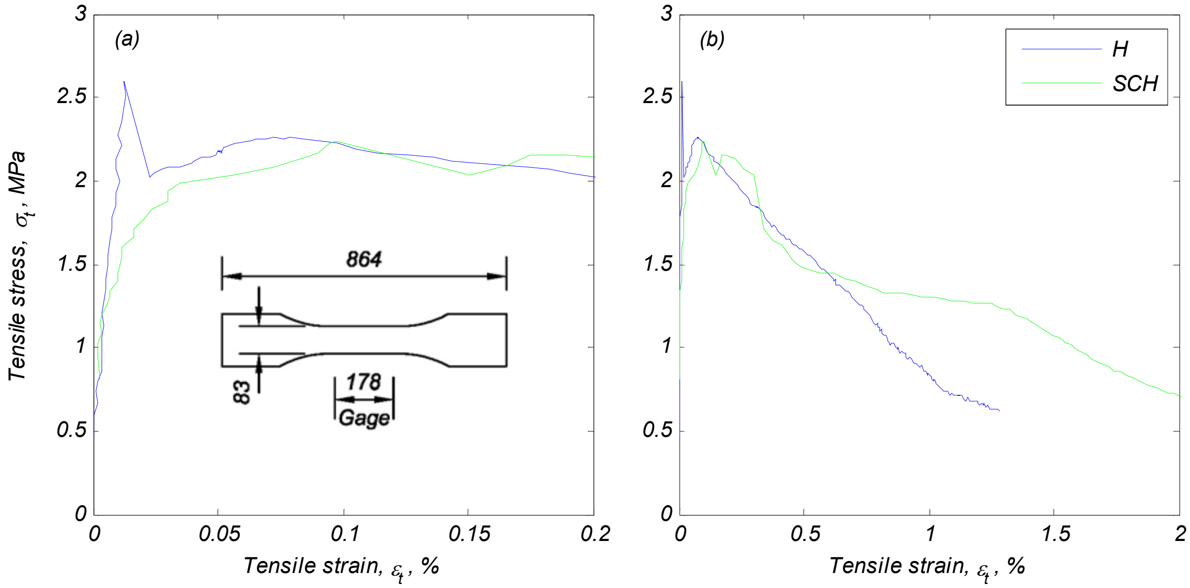

Figure 19. *Tensile-stress strain curve of HyFRC and SC-HyFRC; (a) to 0.2% strain and (b) to 2.0% strain.*

2.4.3 Test results

Tension stiffening tests showed that the HyFRC and SC-HyFRC materials provided both stiffness and strength enhancements to the response of the bare rebar alone. The stiffness enhancement occurs in the early portion of the response prior to crack localization in the HyFRC. The strength enhancement continued well beyond yield of the rebar. In normal concrete specimens, there was a stiffness enhancement initially; however, once cracking occurred, the specimens followed the response of the plain rebar. When the rebar yielded, there was practically no remaining strength enhancement from the concrete and the rebar behavior dominated the composite response.

2.4.3.1 *Measured load-displacement response*

The axial load-displacement response of the HyFRC, SC-HyFRC, and normal concrete specimens are shown in Figure 20, Figure 21, and Figure 22, respectively. The naming convention for specimens begins with a material designation (H, SCH, NC) followed by the reinforcement ratio (06 or 12) and then the cross section width (127 or 178), but identical specimens are not differentiated in these figures. The figures also show the load-strain response of the bare rebar.

As seen in Figure 20(a) and Figure 21(a), the HyFRC and SC-HyFRC specimens stiffened the response upon initial loading while the material was still elastic. As cracking initiated, the stiffness of the specimens reduced to the stiffness of the steel rebar. The strength contribution of the material to the composite response did not degrade. For the H-12-127 and SCH-12-127 specimens, the peak load at rebar yielding was roughly 1.3 times that of the bare rebar. This enhancement continued well beyond the yield strain of the rebar (0.25%) due to the post-cracking resistance of the fibers. Because of the larger cross section, the peak load of the H-06-178 specimens at rebar yielding was approximately 1.6 times higher than the H-12-127 specimens and two times that of the rebar alone. The rebar pulled out of one of the H-06-178 specimens hence the early failure; see Figure 20(a).

Figure 20(b) and Figure 21(b) show the response of the fiber-reinforced specimens up to failure. Failure occurred in all tests when the rebar necked and ultimately fractured. Fracture occurred at composite strains between $\varepsilon = 5\%$ and 8% for the H-12-127 specimens. For the H-06-178 specimens, fracture occurred between composite strains of $\varepsilon = 3\%$ and 4%. Fracture typically occurred at composite strains lower than the fracture strain of the bare bar; however, local strains in the embedded rebar were higher than the composite strain at fracture.

The H-06-178 specimens reached their peak load when the rebar yielded. Subsequent displacements resulted in a reduction in load capacity due to the loss of fiber bridging ability as the crack opened. Localization occurred because the cracked section remained weaker than the uncracked sections even when the rebar strain hardened at the initial crack. The H-12-127 and SCH-12-127 specimens also reached their peak load when the rebar yielded, but additional displacements resulted in an increase in load resistance and opening of multiple cracks as the rebar strain hardened at multiple crack locations.

Figure 22(a) shows that both the NC-12-127 and NC-06-178 specimens showed an enhanced initial stiffness while the concrete was elastic. The stiffness was temporarily less than that of the bare reinforcing bar while load (and strain) redistributed from the concrete to the rebar after cracking. The specimen response converged to the bare bar response after redistribution occurred. The remaining load resistance of all the NC specimens was controlled primarily by the rebar.

A greater initial peak load (prior to cracking) was obtained for the NC-06-178 specimens compared to the NC-12-127 specimens because the cross section was larger. Furthermore, the larger specimens reloaded after initial cracking at a higher apparent stiffness than the bare rebar. Concentrated deformations occurred in the rebar at the crack location and, averaged over the full specimen height, resulted in low strains and higher stiffness.

Figure 22(b) shows the full response of the normal concrete specimens, which tended to follow the bar rebar response up to ultimate load. No load is transferred across cracks in the concrete and minimal load develops in the concrete through bond after the embedded rebar yields. The larger NC specimens failed between $\varepsilon = 7\%$ and 8% whereas the smaller specimens failed between $\varepsilon = 10\%$ and 12%. The load carried by NC-06-178 is greater than the bare rebar in Figure 22(b) at equal strains due to the fact that strains were localized in the large specimen compared to the bare rebar.

The reinforcing ratio affected the fracture strains of both HyFRC and NC specimens. The higher reinforcing ratio of 1.2% resulted in 1.5 to 2.0 times the ductility (in terms of composite fracture strains) compared to the lower ratio of 0.6% (fracture strains of 5-8% vs. 3-4% for HyFRC, fracture strains of 10-12% vs. 7-8% for NC). A possible explanation of this effect in HyFRC is proposed in the next section. For NC, the larger concrete section of the specimens at 0.6% provides better confinement to the rebar, reducing splitting cracks and unbonding and leading to more localized strains at the cracks.

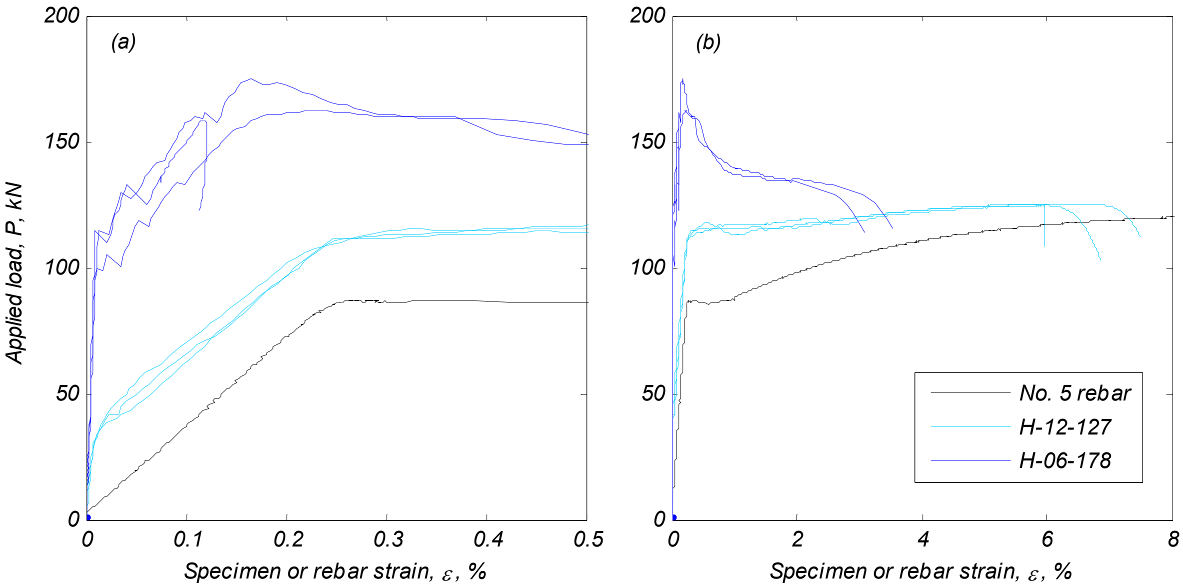

Figure 20. Load-displacement response of HyFRC specimens; (a) to 0.5% strain and (b) to 8% strain.

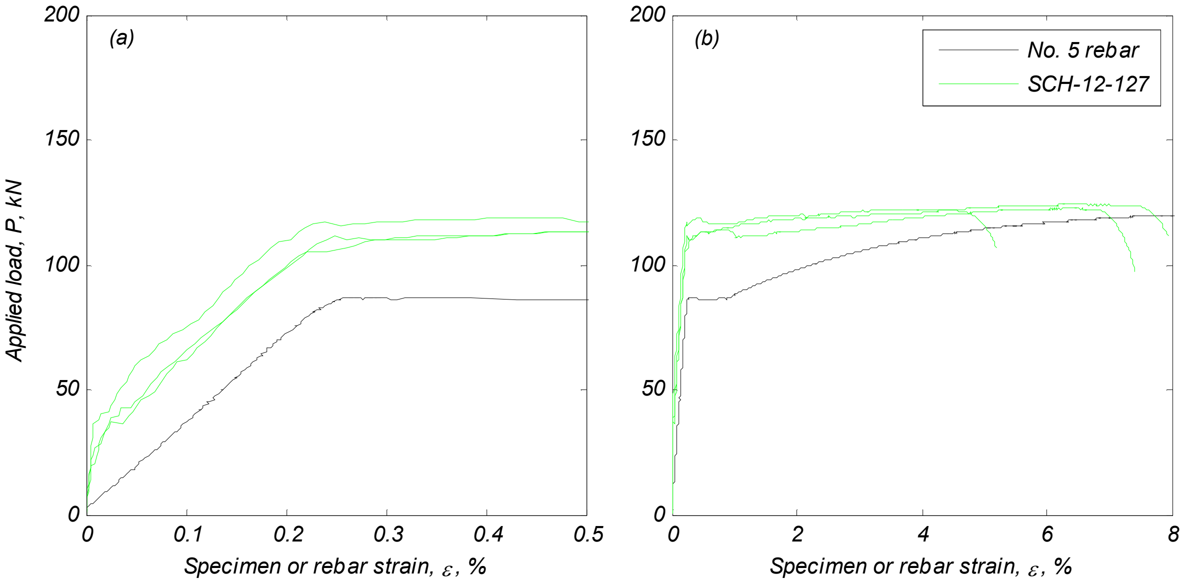

Figure 21. Load-displacement response of SC-HyFRC specimens; (a) to 0.5% strain and (b) to 8% strain.

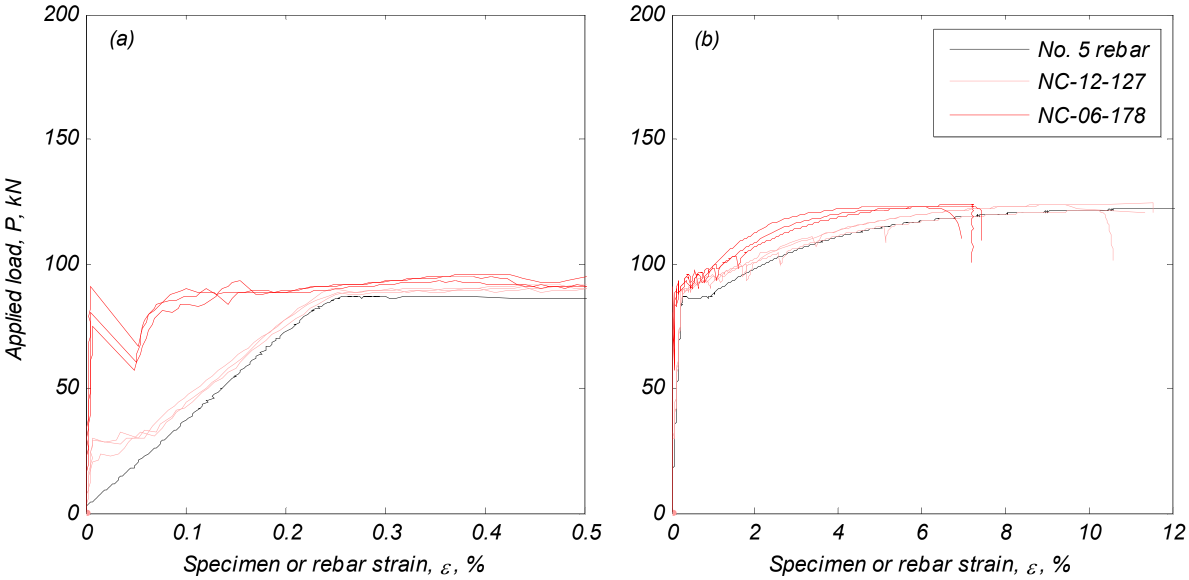

Figure 22. Load-displacement response of NC specimens; (a) to 0.5% strain and (b) to 12% strain.

2.4.3.2 *Crack formation and rebar strain distribution*

The load-strain responses of the five specimens with strain gages are shown Figure 23. The rebar strain distribution and photos of the response were studied at the strain levels represented by the vertical dashed lines ($\varepsilon = 0.25\%$, 1.0%, 2.0%, and 4.0%). The first level corresponds to the yield strain of the rebar. The others were arbitrarily chosen to investigate the crack localization behavior of the specimens. The strain gage distributions and photos of associated cracking are provided in Figure 24 through Figure 28 for each specimen. Early cracks are marked with black pen in the photos but the opening of cracks is discernable at large strains.

All five specimens had a constant distribution of strain gage measurements close to the rebar yield strain when the composite strain was $\varepsilon = 0.25\%$ (blue strain distribution lines). By the time the composite strains reached $\varepsilon = 1.0\%$, strain gages measured localized strains in excess of 2% at crack locations. For composite strains beyond 1%, the distribution of strain in the bar varied for HyFRC and NC specimens and for different ρ_l. The differences among specimens at large composite strains are discussed below.

The localization of strain in specimen SCH-12-127-sg (Figure 24) first occurred near the gage -225 mm from specimen mid-height. That gage measured strains of 4% and 7% at composite strain of $\varepsilon = 1\%$ and 2%, and the opening of a crack near that gage is evident in the photos. Surprisingly, a second localization of gage strain occurred at +225 mm from mid-height sometime after a composite strain of $\varepsilon = 2\%$. At $\varepsilon = 4\%$, the gages at -225 mm and +225 mm both recorded strains in excess of 6%, although the upper gage had recorded only minimal strain before then. Secondary opening of the upper crack is also evident in the photos.

The localization of strain in H-12-127-sg (Figure 25) occurred near the gage at +300 mm from mid-height which recorded strains of 3% when the composite strain was $\varepsilon = 1\%$. Photos show that this crack opened as the composite strain increased. Between composite strains of $\varepsilon =$ 1% and 4%, two additional cracks opened—one at mid-height and one at -150 mm. Opening of these cracks is evident in the photos as well. At $\varepsilon = 4\%$ composite strain, the gage at the bottom crack measured a strain of over 8%.

Only one localization occurred in H-06-178-sg (Figure 26) and the behavior was substantially different than the smaller HyFRC specimen. The gage at -300 mm recorded strains of 5% and over 10% at composite strains of $\varepsilon = 1\%$ and 2%. At a composite strain of $\varepsilon = 2\%$, only the bottom two gages had exceeded the rebar yield strain. The rebar fractured prior to $\varepsilon =$ 4% composite strain.

Localization in the NC specimens was generally less severe than in the HyFRC specimens. NC-12-127-sg had a relatively constant distribution of strain in the gages through the duration of testing (Figure 27). At composite strain of $\varepsilon = 2\%$, the gage strain distribution was practically constant (~2.5% strain) and splitting cracks branch from all of the transverse cracks. Based on the photos, all of the cracks in NC-12-127-sg open at about the same rate.

The larger NC-06-178-sg had slightly more localization than NC-12-127-sg (Figure 28). In the uncracked regions the strains never exceeded the yield strain (+300, -75, -300 mm from midheight). Gage strain measurements exceeded 2% and 4% at the crack locations -225 mm and +150 mm when the composite strain was $\varepsilon = 1\%$ and 2%, respectively.

Transverse tensile and splitting cracks occurred in both HyFRC and NC specimens but at different composite strain levels. The occurrence of splitting cracks in both materials led to more distributed strains along the bar. For NC reinforced at $\rho_l = 1.2\%$, splitting cracks resulted in a near-constant strain distribution in the bar since bond between the concrete and rebar was essentially zero. Therefore, the specimen load-displacement response was equivalent to the bare rebar response as shown in Figure 23. The lower reinforcement ratio of $\rho_l = 0.6\%$ in NC reduced the bond deterioration. Away from the cracks the concrete still carried some load (Figure 23) and the response was improved over the specimen with higher ρ_l.

For HyFRC reinforced at $\rho_l = 1.2\%$, an interesting phenomena occurred due to the fibers ability to bridge the cracks and contribute strength. In these specimens (SCH-12-127-sg, H-12-12-sg), the load resistance at the first localized crack consisted of the yield load of the rebar and the load carried by bridging fibers. As that crack opened, the fiber contribution presumably remained approximately the same but the rebar began to strain harden and hence the composite load resistance increased above the load at first rebar yielding (Figure 24, Figure 25). The increase in load resistance forced the rebar to strain harden at other cracks as well to maintain load equilibrium. This simultaneous processes of degrading fiber load resistance (due to crack opening) and increasing rebar load resistance (due to strain hardening) resulted in strain localization at several cracks and delayed fracture to composite strains of 5 to 8% over all specimens.

The HyFRC specimen reinforced at $\rho_l = 0.6\%$ did not display this level of ductility and the fracture strains were much lower. At the lower reinforcing ratio, strain hardening of the rebar at the first localized crack cannot result in a load resistance greater than the uncracked sections or the cracked sections where the fibers still have more load carrying ability. Hence, localization was much more severe as shown in Figure 26 and fracture occurred at lower composite strains.

A strength criterion was proposed to describe this effect in [2.5]; if the expression is satisfied, multiple crack localizations/openings would be expected for a given fiber reinforced tension stiffening specimen. In [2.5], P_y is the load resistance at secondary cracks (prior to rebar strain hardening) and is a function of the tensile strength of the material (f_t), the longitudinal steel ratio (ρ_l), the yield strength of the longitudinal reinforcement (f_y), the volume fraction of fibers (V_f), the strength of fibers (f_f), and the crack opening (w). F_u is the ultimate load of the bare rebar and is a function of ρ_l and the ultimate strength of the rebar (f_{ul}).

For multiple crack opening/localization:

$$P_y = f\left(f_t, \rho_l, f_y, V_f, f_f, w\right) \quad < \quad F_u = f(\rho_l, f_{ul}) \qquad [2.5]$$

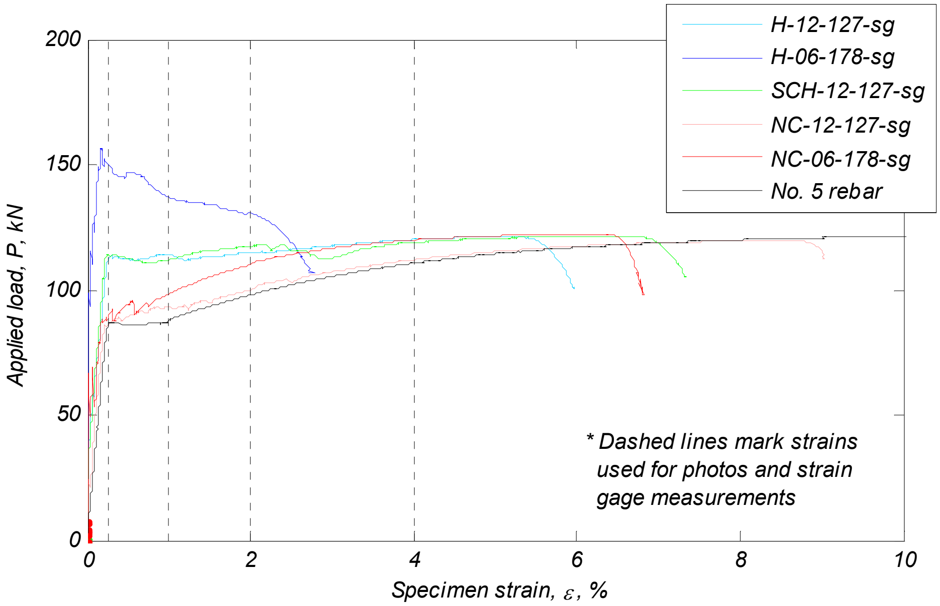

Figure 23. Load-displacement response of specimens with strain gages.

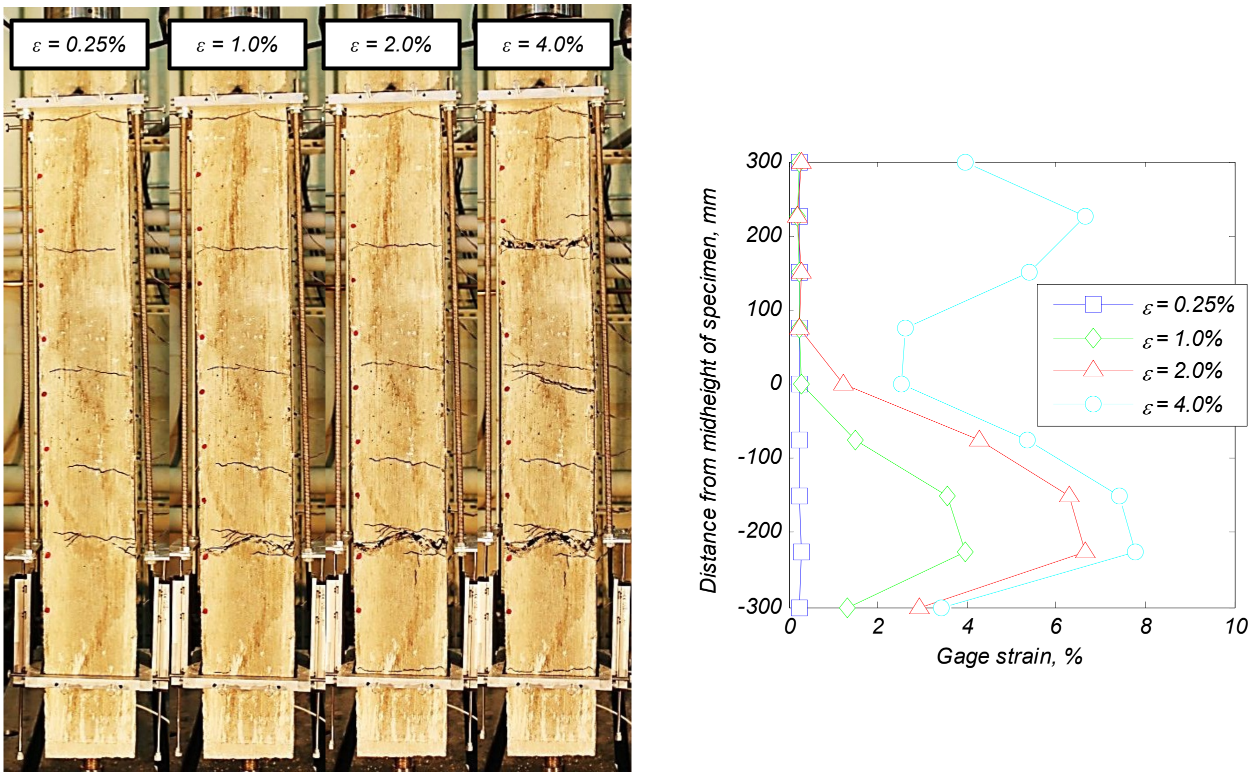

Figure 24. Cracking and strain distribution in specimen SCH-12-127-sg

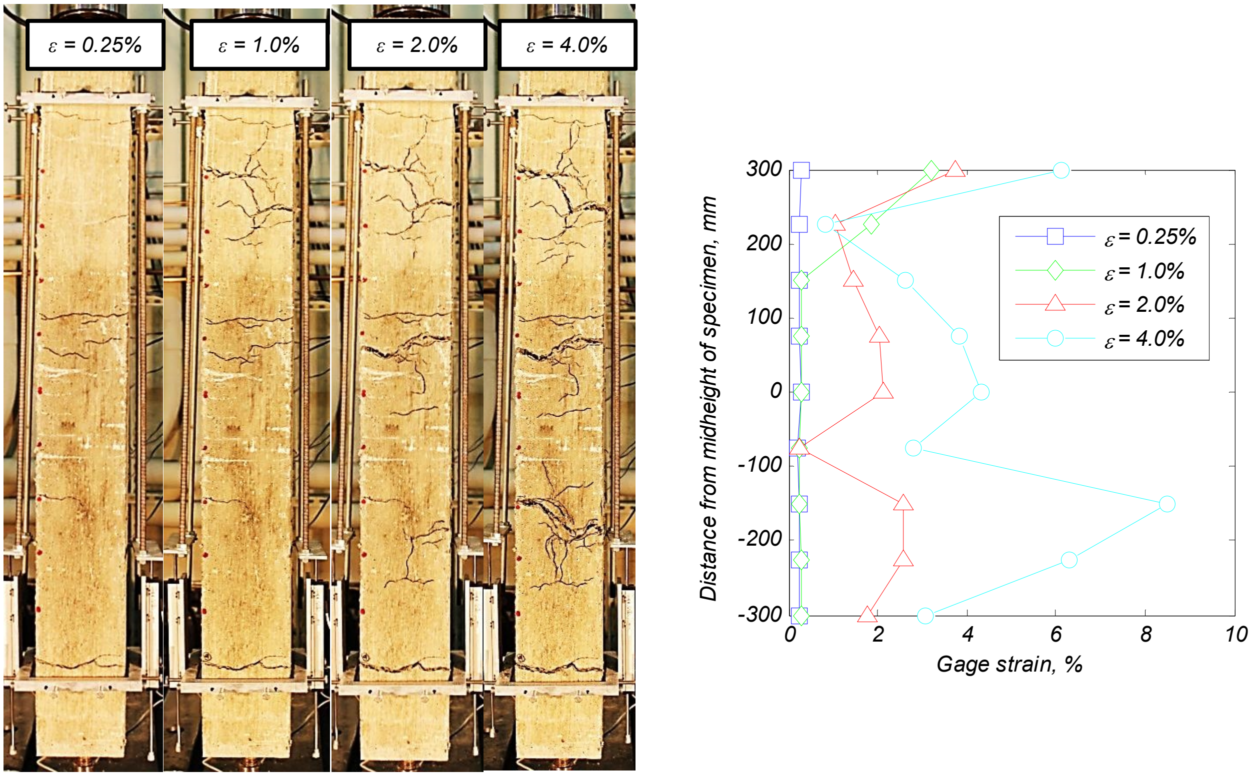

Figure 25. Cracking and strain distribution in specimen H-12-127-sg

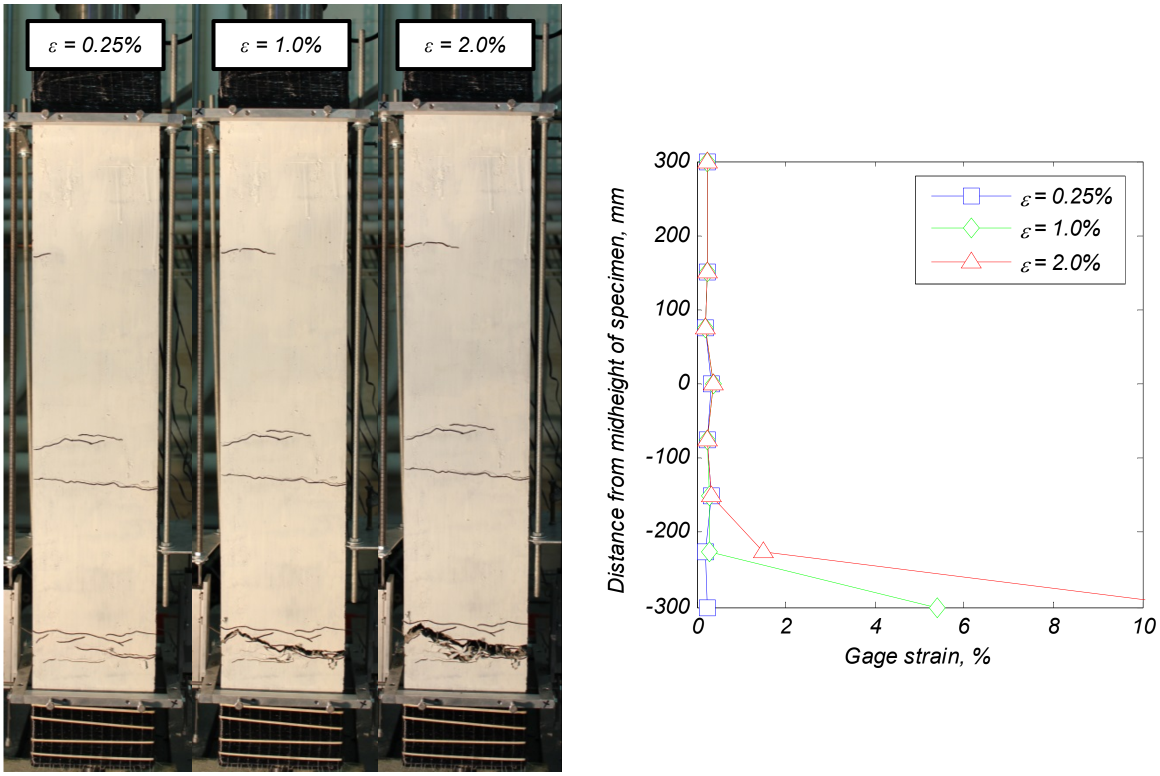

Figure 26. Cracking and strain distribution in specimen H-06-178-sg.

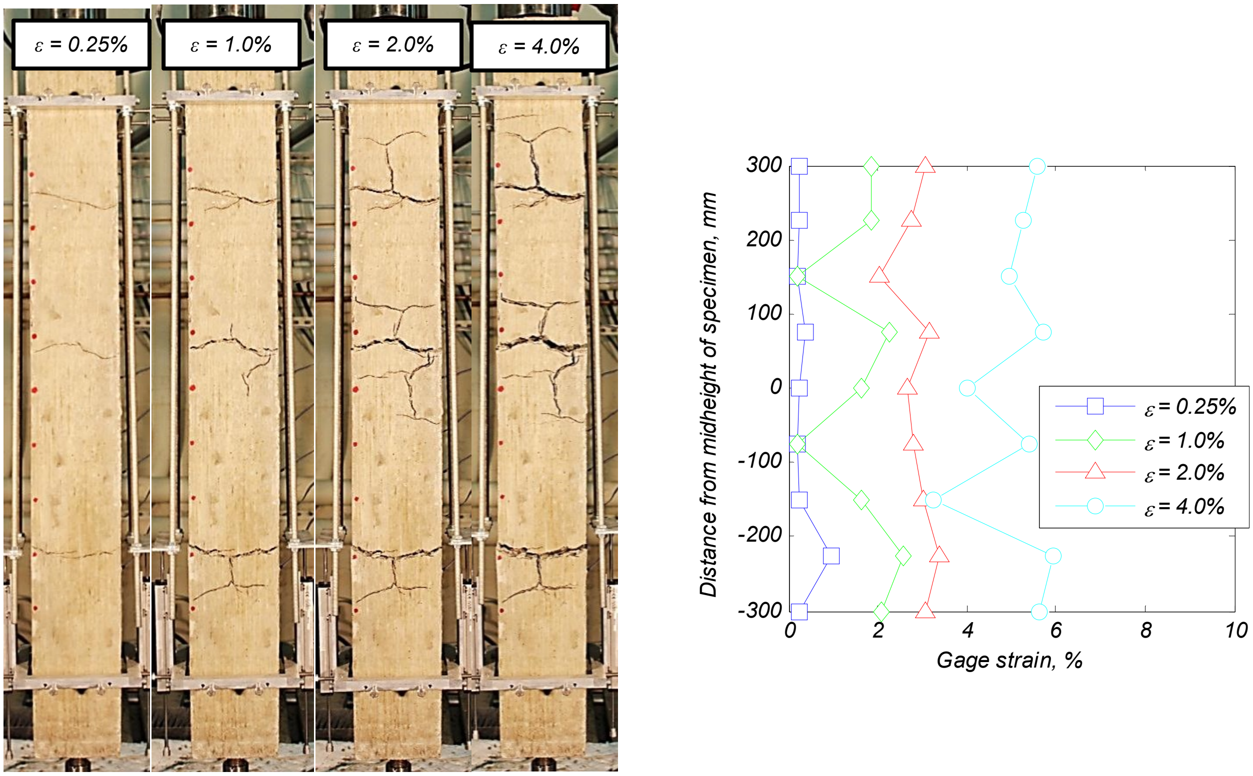

Figure 27. Cracking and strain distribution in specimen NC-12-127-sg

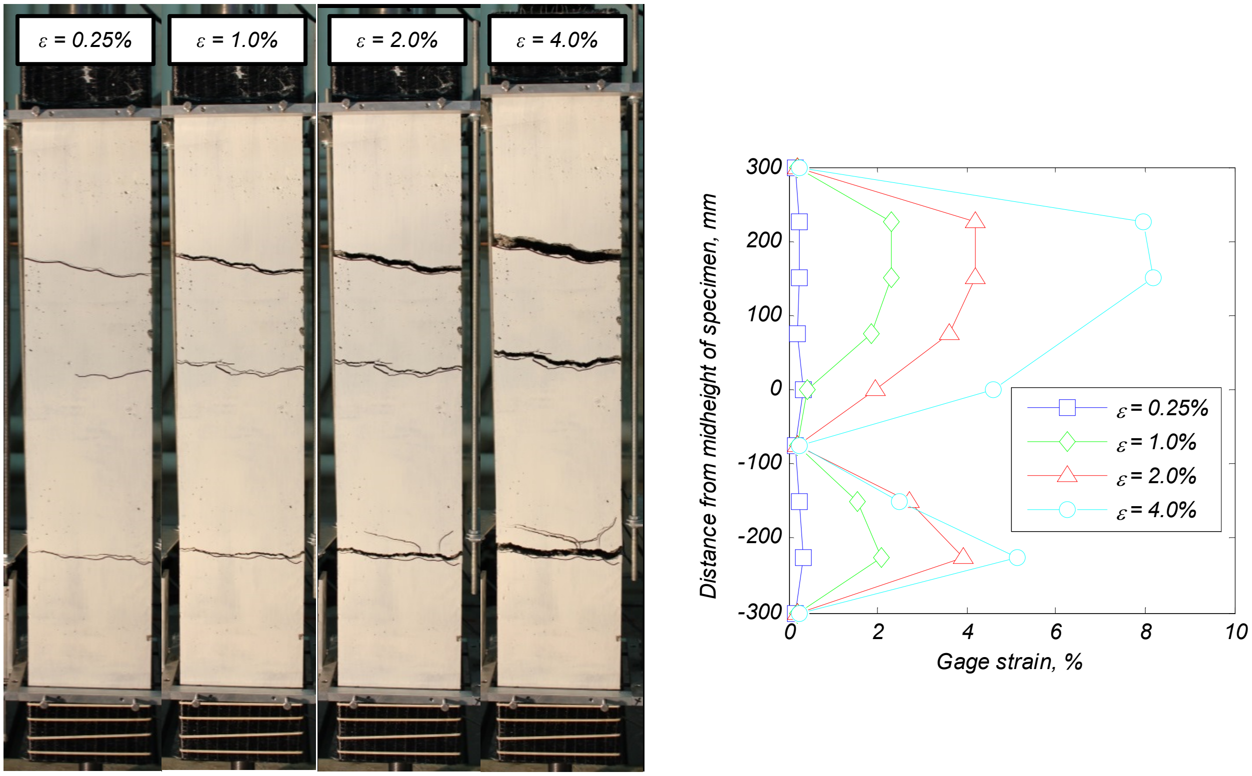

Figure 28. Cracking and strain distribution in specimen NC-06-178-sg.

2.5 Summary

HPFRCC specimens containing conventional steel reinforcing bars and spirals were tested in compression and tension. The confinement effect was evaluated first by testing 54 transversely-reinforced specimens at four different ratios, both with and without fibers. The second part investigated the tensioning stiffening effect in 20 longitudinally-reinforced prismatic specimens with varying cross-sections, reinforcement ratios, and HPFRCC materials.

The confinement tests showed that spiral-reinforced HPFRCC materials exhibit a markedly different response compared to equally confined concrete with no fibers. Results supported several of the hypotheses discussed in the introduction. The following is a summary of key findings from these tests:

- No spalling or noticeable bar buckling occurred in HyFRC and SC-HyFRC specimens for strains up to 3%, regardless of the transverse reinforcement ratio.

- A distributed crack pattern occurred in HyFRC and SC-HyFRC; no dominant shear crack plane developed.

- Formation of a dominant shear crack and initiation of spalling occurred in NC specimens at a strain of approximately 1%.

- The peak load of all specimens coincided with yielding of the spiral, regardless of the transverse reinforcement ratio.

- The un-gaged end length of the longitudinal bars was insufficient for development. Slip occurred between the bars and matrix material. Thus, the bars' load-carrying contribution at the peak load was neglected.

- The unconfined stress-strain curve had the same shape as the confined stress-strain curves for HyFRC and SC-HyFRC after the peak stress.

- HyFRC, SC-HyFRC, and ECC specimens had average confined strength ratios ranging from 1.03 to 1.36. NC and SCC had ratios ranging from 0.86 to 1.36 (NC and SCC with ρ_s of 0.5% or less had ratios less than one).

- No difference was observed in the confined strength of specimens with fibers (HyFRC, SC-HyFRC, ECC) when ρ_s did not exceed 0.5%.

- Confined strength in the specimens with no fibers (NC, SCC) was proportional to ρ_s at all ratios.

- HyFRC and SC-HyFRC specimens had nearly linear softening, while NC and SCC had more abrupt parabolic softening.

- HyFRC and SC-HyFRC specimens retained over 76% of their peak load at 1% strain when averaged at each transverse reinforcing ratio (mean $r_l > 0.76$).

- NC and SCC specimens retained between 38% and 78% of their peak load at 1% strain when averaged at each transverse reinforcing ratio.

- ECC specimens had substantially more abrupt softening behavior due to the lack of steel macrofibers which were utilized in HyFRC and SC-HyFRC specimens.

- ECC specimens had lower initial spiral strains and higher initial stiffness compared to all other specimens. These results were indicative of less core dilation in the ascending branch compared to HyFRC and SC-HyFRC. PVA fibers are effective at delaying microcrack initiation and ECC had 10 times the volume compared to HyFRC or SC-HyFRC.

The tensile response of rebar embedded in HyFRC or SC-HyFRC was found to be distinctly different than for bars embedded in concrete. Differences were most obvious in the post-cracking and post-yielding phases of the load-displacement envelope. The following is a summary of the key findings from the tension stiffening tests:

- The pre-cracking portion of the load-displacement responses was similar for all materials. Fibers did not noticeable enhance the initial loading stiffness in specimens with equal cross-sectional areas due to the low fiber volume fractions.

- HyFRC and SC-HyFRC specimens had significantly higher strength than the bare rebar after cracking occurred. The strength enhancement continued well into the inelastic range of the rebar response.

- The strength of NC specimens did not exceed the ultimate strength of the rebar after cracking.

- The strain distribution in all specimens was constant when the rebar yielded.

- HyFRC and SC-HyFRC specimens at a longitudinal ratio of $\rho_l = 1.2\%$ showed localized deformations at several cracks, often at different points in the load-displacement response. This phenomenon was attributed to the simultaneous effects of rebar strain hardening and fiber degradation at crack locations.

- Fracture occurred at composite strains between 5% and 8% for HyFRC and SC-HyFRC specimens with $\rho_l = 1.2\%$.

- Only a single localization occurred in HyFRC specimens at $\rho_l = 0.6\%$. In these specimens, the rebar+fiber resistance at cracks away from the localized crack exceeded the resistance at the localized crack.

- Fracture occurred at composite strains between 3% and 4% for HyFRC specimens with $\rho_l = 0.6\%$.

- NC specimens at $\rho_l = 1.2\%$ had significant splitting cracking and the associated rebar bond degradation resulted in a nearly uniform strain distribution. Fracture occurred at composite strains between 10% and 12% for these specimens.

- NC specimens at $\rho_l = 0.6\%$ had less rebar bond degradation due to the larger cross section. Hence, large rebar strains were concentrated near cracks. Fracture occurred at composite strains between 7% and 8% for these specimens.

3 Design and Modeling of a Low Damage Post Tensioned HyFRC Bridge Column

3.1 Introduction

In California, reinforced concrete (R/C) bridges are designed according to the seismic design criteria (SDC) of the California Department of Transportation. These provisions are intended to prevent bridge collapse and do so by balancing the ductility capacity of bridge components with the corresponding seismic demands (Caltrans 2010). Recent shake table tests of a full-scale bridge column designed in this manner showed that current provisions are effective for collapse prevention and result in ductile inelastic behavior (Schoettler et al. 2012). However, such columns will still incur damage (by design) during maximum considered earthquakes, and repairs and/or retrofits are expensive and time consuming. Long-term bridge closure or even bridge demolition can result when R/C bridges are permanently offset from their original position (i.e. residual displacements occur).

Any loss of bridge serviceability would be highly detrimental for congested California urban areas where highways are critical lifelines for post-earthquake disaster response. Therefore, the design of critical R/C bridges should include some assessment of the residual displacement hazard. Unfortunately, there are two major sources of uncertainty in such assessments. First, complicated inelastic damage mechanisms such as cracking and spalling in concrete and/or buckling, bond-slip, and strain penetration of rebar have significant effects on the magnitude of residual displacements but are difficult to model accurately (Sakai and Mahin 2004, Lee and Billington 2009). Forty-one blind predictions of residual displacements by academic researchers and engineering professionals based on the full-scale column test performed by Schoettler et al. (2012) varied significantly from the actual results as shown in Figure 29.

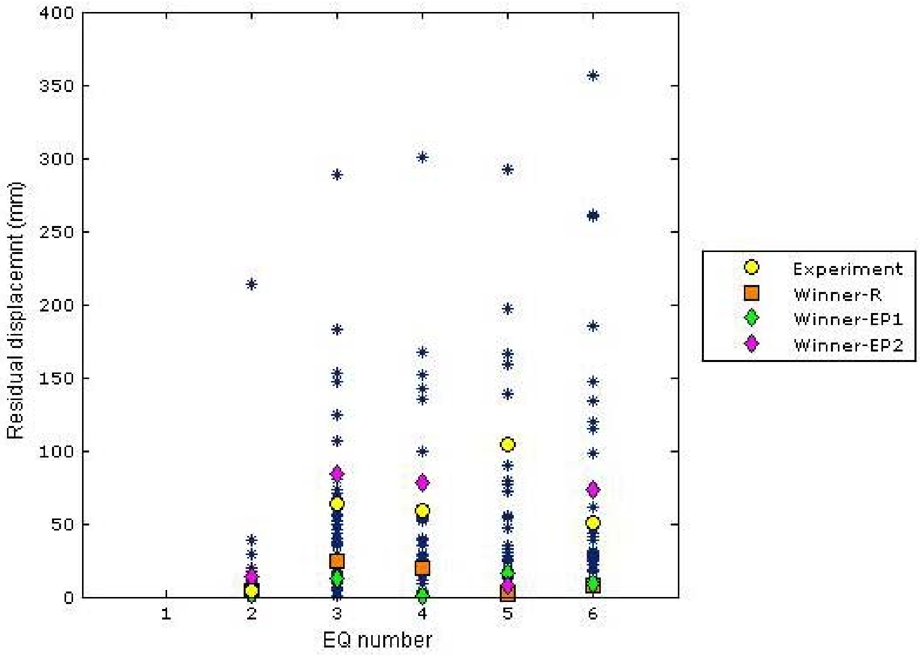

Figure 29. Blind prediction of residual displacements in full-scale R/C column shake table test (PEER 2010).

The second source of uncertainty is that residual displacements are known to be highly dependent on the characteristics of individual ground motions. For instance, near-fault, pulse-like ground shaking has been shown to induce large displacement demands in bridges, leading to more severe damage and a greater residual displacement hazard (Phan et al. 2007, Choi et al. 2007, Choi et al. 2010, Antonellis and Panagiotou 2013, Ardakani and Saiidi 2013).

Despite the difficulty in assessment, code provisions do exist which address residual displacements in bridges. One example is the Japanese *Design Specification of Highway Bridges* (Japan Road Association 2002). Explicit requirements for residual displacements are not currently included in U.S. codes, although they are mentioned in the structural performance levels defined by *FEMA 356* (FEMA 2010).

The Japanese specification incorporated a residual displacement limit for bridges following the 1995 Kobe earthquake. That earthquake caused residual drift ratios exceeding 1.75% in over 100 reinforced concrete bridge columns (Kawashima et al. 1998). Those columns were demolished and replaced rather than undergoing difficult realignment. In response, Kawashima et al. developed a residual displacement response spectrum for bridges. It was based on the analysis of bilinear SDOF oscillators with varying hysteretic characteristics subjected to 63 different ground motions. The resulting amplitude of the spectrum was found to be most dependent on the bilinear factor of the oscillators, r (the ratio of post-yield stiffness to initial stiffness). Consequently, the residual displacement prediction equation in the specification is dependent on both r and the predicted displacement ductility response of the bridge column(s), μ_r. The maximum allowable residual drift ratio of important bridges is 1%. Sakai and Mahin (2004) calculated that R/C columns designed using Caltrans SDC with a diameter of 1.8 m, aspect ratios ranging from 3 to 10, and μ_r ranging from 3 to 6 had residual drift ratios ranging from 0.7% to 3.9% using the JRA equation.

Performance-based design criteria for critical R/C bridges might include a continuous functionality requirement for low-probability earthquakes (e.g. P_{exc} = 2% in 50 years; 2475 year return period). Designers commonly choose alternative design techniques to meet such requirements because of the uncertainty in predicting damage and residual displacements of R/C bridge components. Seismic isolation is one widely accepted technique which essentially eliminates any risk of residual displacements (Buckle et al. 2006). Elastomeric or friction pendulum bearings isolate the response of the bridge superstructure from the support structure, concentrating the deformation demands in the isolation plane. The bearings are designed to remain elastic and to recenter upon loading. Although this technique has been employed in existing R/C bridges, its cost prohibits widespread use.

A less common (albeit less expensive) strategy for eliminating residual displacements is to design structural members to rock at joint interfaces during ground shaking (e.g. foundation-soil, column-foundation, column-superstructure). This technique avoids damage caused by inelastic deformation of the structure itself (e.g. plastic hinging in concrete structures). Furthermore, rocking structures can have lateral stiffness and strength characteristics similar to conventional reinforced concrete structures. Seismic design methods have been proposed for rocking bridge components in the literature (Mander and Cheng 1997, Palermo 2004). One of the first bridge structures to actually incorporate rocking elements was the South Rangitikei Rail Viaduct in New Zealand (Beck and Skinner 1974). It had piers designed to uplift and "step" during large seismic excitation.

The research contained in this chapter focuses on the design and modeling of a new damage resistant, recentering, post-tensioned HyFRC (PT HyFRC) bridge column which aimed to reduce or eliminate residual displacements. The column accommodates displacement demands by rocking at the foundation and bent cap joints. Post-tensioning resists overturning and encourages recentering force-displacement hysteresis. Unbonded rebar is used to provide hysteretic energy dissipation equivalent to that of conventional R/C columns. Furthermore, the end region of the column is precast with HyFRC and contains headed rebar to resist damage in compression.

The use of post-tensioning to encourage column recentering is not new and has been investigated in many studies. Many columns also incorporated some type of energy dissipaters, either externally or within the column cross section. The key components of this column which differentiate it from prior studies are the use of headed rebar and HyFRC in addition to post-tensioning and energy dissipaters. Headed bars have been used for similar purposes by Belleri et al. (2013) in post-tensioned rocking shear walls and by Guerrini and Restrepo (2013a) in a precast post-tensioned dual steel shell column. HyFRC has been used in several columns recently tested at UC Berkeley (Kumar et al. 2011, Nguyen et al. 2014), but not in post-tensioned columns.

The first part of this chapter summarizes previous experimental and analytical studies involving post-tensioned rocking columns. In addition, it includes a summary of quasi-static cyclic tests performed on HyFRC columns by the author and others. The second part explains the design objectives of the proposed bridge column and the approaches used to achieve them. An analytical model is proposed in the third part to predict the strength and deformation response characteristics of the rocking column. A parametric study was conducted on the three dimensional model using the OpenSEES software framework with existing nonlinear material, element, and analysis objects. Analyses were performed on a model representing the scaled test specimen (presented in Chapter 4) subjected to cyclic lateral displacements.

3.2 Previous studies of post-tensioned rocking bridge columns

Over the past 20 years, a number of experimental and analytical studies have been conducted on post-tensioned R/C columns designed to rock at end connections. These columns commonly consist of one or more precast column segments connected to the footing and bent cap by unbonded post-tensioned tendons. Some studies have also focused on post-tensioned columns that incorporate internal or external reinforcement for hysteretic energy dissipation. Fiber-reinforced concrete materials, external column jackets, and other armoring details such as steel plates have been employed to prevent damage near the highly stressed rocking joints. These prior studies are reviewed in this section.

3.2.1 Experimental studies

A summary of the parameters of previous rocking column tests is compiled in Table 9, including the test method, the column width (or diameter) in the direction of loading (*D*), the shear span ratio (*M/VD)*, the total axial load ratio including the post-tension force ($P_t / f_c' A_g$), and the volumetric steel ratios for post-tensioning (ρ_{pt}), hysteretic energy dissipaters (ρ_d), bonded rebar not crossing the rocking planes (ρ_b), and transverse reinforcement (ρ_t). The initial post-tension stress (σ_i) and the dissipater yield stress (f_y) are also reported. The ratio of the maximum recorded shear force to the gross cross sectional area (V_{max} / A_g) is provided for comparison of the section strengths.

The peak drift ratio, the corresponding damage observed, and the subsequent residual drift ratio are described for each column specimen in Table 9. Drift ratio, θ, is the lateral displacement at the load point (or the centroid of inertial mass) divided by the height of that point. The residual drift ratio is the ratio after unloading to zero lateral force (or moment) for cyclic tests or the drift ratio at the end of the ground motion for shake table tests.

Precast monolithic columns made of conventional R/C have been considered in several prior tests. Mander and Cheng (1997) tested precast post-tensioned R/C columns with armored steel end plates but no energy dissipating devices and R/C columns by Marriott et al. (2008) had steel end plates in addition to external energy dissipating devices. Steel angles were used around the perimeter at the base of the columns by Palermo et al. (2007) along with unbonded internal dissipaters. The top surface of the foundation was reinforced with a solid steel plate in all three of these tests and concrete confinement consisted of internal steel spiral or hoop reinforcement. These columns rotate about their toe rather than about a deeper neutral axis due to the rigid steel-on-steel rocking plane. The plate-armored columns were not tested beyond 4.5% drift ratio. Hollow precast segmental post-tensioned R/C columns were tested by Yamashita and Sanders (2006), while Jeong et al. (2008) tested cast in place post-tensioned R/C columns with bonded or unbonded internal dissipaters.

Several past studies also considered post-tensioned columns with steel or fiber-reinforced polymer (FRP) jackets providing external confinement. These include segmental columns with steel jackets and external dissipaters (Chou and Chen 2006) or no dissipaters (Hewes and Priestley 2002) and segmental columns with FRP jackets only (El Gawady et al. 2010). Monolithic columns with steel jackets and internal dissipaters (Jeong et al. 2008, Guerrini and Restrepo 2013a) have also been tested.

FRC has also been used in several post-tensioned column tests. Solberg et al. (2009) tested a column having unbonded internal energy dissipaters, steel plates, and a combination of 1% crimped steel fibers and extra rebar in the end region. Billington and Yoon (2004) tested columns with 2% polyethylene fibers by volume and no energy dissipaters. Finally, Haraldsson et al. (2013) incorporated HyFRC into the shell of a precast, prestressed column with internal energy dissipaters.

The common advantage gained by rocking column designs is a reduction in column damage and residual displacement. This advantage is clearly evident in all of the tests presented in Table 9. Rocking results in large concentrated rotations at the column base and reduces the curvature demand over the height of the column, especially under large displacement demands. For peak drift ratios below 4%, the residual drift ratio in these tests was negligible (< 0.5%) and only minor damage was observed. For peak drift ratios above 5%, moderate to heavy spalling of concrete cover was observed in R/C specimens that did not have jackets or FRC and residual drift ratios exceeded 2% in some cases.

Clearly, most of the previous post-tensioned columns eliminated residual displacements for displacement demands that might be incurred during a California design-level earthquake (e.g. P_{exc} = 10% in 50 years; 475 year return period). Larger drift ratios could be imposed by a lower-probability maximum considered earthquake (MCE) in California (e.g. P_{exc} = 2% in 50 years; 2475 year return period). Such an earthquake could cause significant damage to many prior post-tensioned rocking column designs, particularly those made of conventional R/C.

Table 9. *Summary of previous tests of recentering post-tensioned rocking bridge columns*

Author (year)	*Test method* [a]	*D, mm (shape)*	*M/VD*	*Specimen type*	$P_t/f_c'A_g$ [b] *%*	ρ_{pt} *%*	σ_i *MPa*	ρ_d *%*	f_y *MPa*	ρ_b *%*	ρ_t *%*	V_{max}/A_g *MPa*	*Peak drift ratio* [c]*, %*	*Residual drift ratio* [c]*, %*	*Damage sustained after peak drift ratio*
Mander and Cheng (1997)	Uniaxial static	610 (sq.)	4.2	RC, M	10.4	0.3	669	-	-	1.2	1.0	0.73	4.5	< 0.5	Minor flexural cracking
Hewes and Priestley (2002)	Uniaxial static	610 (circ.)	6	RC, S, J RC, S, J	25.0 20.3	0.9	1009 801	-	-	0.4	0.6	0.74 0.71	3.0 4.0	< 0.5 < 0.5	Minor spalling above and crushing below jackets
Billington and Yoon (2004)	Uniaxial static	200 (sq.)	3.4	RC, S FRC, S FRC, S	10.5 10.4 10.5	0.5	756	-	-	0.3	0.5	1.16 1.18 1.37	16.0 16.0 16.0	2.0 1.0 1.0	Heavy cover spalling (RC); minor flexural cracking (FRC)
Chou and Chen (2006)	Uniaxial static	500 (circ.)	4.9	RC, S, J RC, S, J, ED	22.7 23.2	1.4	889 926	- 0.1	- 248	-	-	1.02 1.07	6.0 6.0	< 0.5 0.6	Minor crushing below jackets
Yamashita and Sanders (2006)	Uniaxial dynamic	457 (rect.)	4.0	RC, S, H	24.6	0.7	1100	-	-	0.5	0.5	1.24	9.7	< 0.5	Heavy cover spalling; strand anchorage failure
Palermo et al. (2007)	Uniaxial static	350 (sq.)	4.6	RC, M RC, M RC, M, UID RC, M, UID	3.0 4.5 3.0 4.5	0.2 0.3 0.2 0.3	1010 758 1010 758	- - 0.7 0.4	- - 304 586	1.0	1.4	0.41 0.24 0.45 0.61	3.5 4.0 3.0 3.5	< 0.5 < 0.5 1.4 0.9	Minor flexural cracking
Jeong et al. (2008)	Biaxial dynamic	406 (circ.)	6.0 6.2 6.2 6.2 6.2	RC, M, BID RC, M, BID RC, M, UID RC, M, UID RC, M, J, UID	12.4 10.8 10.7 13.9 11.0	0.6 0.7 0.7 0.7 0.7	479 230 216 362 226	0.7	476	-	0.8	0.50 0.48 0.48 0.51 0.50	13.2 10.7 11.1 10.0 9.8	4.4 2.1 2.3 0.9 0.6	Moderate to heavy cover spalling; rebar buckling
Marriott et al. (2008)	Uniaxial static	350 (circ.)	4.6	RC, M RC, M, ED RC, M, ED	3.7	0.3	758 758 758	- 0.3 0.3	- 450 450	1.0	1.4	0.37 0.53 0.61	3.5 3.5 3.5	< 0.5 < 0.5 < 0.5	Minor flexural cracking; fracture of dissipaters
Solberg et al. (2009)	Biaxial static	400 (sq.)	5.3	FRC, M, UID	10.1	n/a	n/a	0.1	n/a	1.0	2.5	0.77	5.5	< 0.5	Minor flexural cracking
El Gawady et al. (2010)	Uniaxial static	203 (circ.)	8.1	RC, M, J RC, S, J	37.0 37.0	1.7	301 301	-	-	-	-	0.61 0.59	15.3 15.4	2.5 6.8	Minor crushing below jackets
Guerrini and Restrepo (2013)	Triaxial dynamic	406 (circ.)	6.0	RC, M, H, J, UID	12.1	2.0	282	0.7	862	0.7	-	1.49	8.5	< 0.5	Minor cracking of mortar at base; buckling and fracture of dissipaters
Haraldsson et al. (2013)[d]	Triaxial dynamic	406 (oct.)	6.0	FRC, M, BID	12.9	0.3	986	0.8	n/a	-	0.9	0.79	9.7	1.3	Minor cover spalling

RC = reinforced concrete; FRC = fiber-reinforced concrete; M = monolithic; S = segmental; H = hollow; J = steel or FRP jacket; UID = unbonded internal energy dissipaters; BID = bonded internal energy dissipaters; ED = external energy dissipaters

[a] All dynamic tests were conducted on a shake table; [b] Reported f_c' values between 32 and 70 MPa, except in El Gawady et al. (2010) where f_c' = 13 MPa; [c] Peak and residual drift ratios are the maximum in any direction; [d] Column by Haraldsson et al. (2013) had strands prestressed prior to concrete casting

3.2.2 Analytical studies

The column proposed in this dissertation contains a combination of unbonded post-tensioning and unbonded internal energy dissipaters. This type of detailing was evaluated by several of the experiments summarized in the previous section and is sometimes referred to as a "hybrid" post-tensioned column. The hybrid concept was integrated into precast building systems under the PRESSS program (Priestley et al. 1999) and later extended to bridge pier systems (Palermo et al. 2005). The concept of "controlled rocking" in such systems is a result of the combination of self-centering and energy dissipating mechanisms. Typically, a flag-shaped hysteretic loop is targeted.

Analytical analyses by Palermo et al. (2005) show that combining different types of energy dissipaters (e.g. elastoplastic, friction, viscoelastic) with self-centering mechanisms (e.g. axial force, post-tensioning) can result in unique hybrid hysteretic responses. The shape of the hysteretic response considering elastoplastic dissipaters (e.g. unbonded rebar) and post-tensioning is a function of the relative contributions of unbonded post-tensioning and energy dissipaters. The net effect can be described using the parameter λ given by [3.1], where M_{pt}, M_N, and M_d are the overturning moment resistance provided by the post-tensioning, the axial load, and the energy dissipaters, respectively.

$$\lambda = \frac{M_{pt}+M_N}{M_d} \qquad [3.1]$$

As a hybrid post-tensioned column unloads, the combined moment caused by the axial force and post-tensioning must exceed the moment resisted by the yielded dissipaters as they reload in compression. Therefore, the column must have $\lambda > 1$ to recenter after the dissipaters yield. Higher λ values are associated with greater recentering tendencies at the expense of energy dissipation, while columns with $\lambda < 1$ likely would not recenter. The parametric analysis presented later in this chapter shows the effect of varying λ on the hysteretic response of the rocking post-tensioned HyFRC column.

Analytical models of varying complexity were developed to capture the response of many of the experimental studies listed in Table 9. Other analytical studies have been performed by several research groups. Kwan and Billington (2003a,b) performed cyclic and dynamic model analyses on post-tensioned bridge pier systems utilizing unbonded rebar for internal energy dissipaters. In a similar study, Sakai and Mahin (2004) conducted a series of quasi-static model analyses for 256 post-tensioned columns with rebar for internal energy dissipation. They varied the unbonded length of the strand, the magnitude of the post-tension force, and the total amounts of post-tensioning and rebar. They recommend that for small residual displacements, the total steel ratio, $\rho_{pt} + \rho_d$, should be larger than about 0.7%, but ρ_d should be less than 0.6% and the axial force ratio from post-tensioning alone should be between 5% and 10%. Higher levels of confinement reinforcement (e.g. external jackets) and greater unbonded lengths in the dissipaters had the effect of reducing residual drift ratios.

Lee and Billington (2009) applied PEER's performance based earthquake engineering (PBEE) assessment methodology to bridge columns having both unbonded post-tensioning and HPFRCC and compared them to conventional R/C columns. By comparing the initial costs of three systems (R/C, post-tensioning only, post-tensioning plus HPFRCC or steel jacket) with anticipated repair costs, they concluded that the system with post-tensioning only was optimal in terms of minimizing repair costs and downtime under severe earthquakes. However, the bridge with post-tensioning and HPFRCC was expected to have essentially no downtime compared to the R/C system.

3.3 Previous studies of bridge columns built with HyFRC

Three bridge column specimens containing HyFRC have been built and tested by research groups at UC Berkeley. Two columns were built monolithically with the same SC-HyFRC material described in Chapter 2 and had unique detailing of the longitudinal reinforcement (Panagiotou et al. 2014). One column had unbonded mild steel rebar, while the second contained bonded, highly ductile stainless steel rebar. The third column was designed for accelerated bridge construction. It consisted of a precast hollow HyFRC shell and was designed to be field-installed and to serve as permanent formwork for the core, which could be cast with low-strength, low-cost concrete. The HyFRC used in the shell had no coarse aggregate (like mortar), higher strength, and a higher fiber content (2.0% by volume) than the SC-HyFRC material.

All three columns were tested quasi-statically and subjected to unidirectional cyclic lateral loading with a constant vertical load. Full details of these tests can be found in Kumar et al. (2011) and Nguyen et al. (2014). A fourth column containing HyFRC was tested by Haraldsson et al. (2013) and details of that test are provided in Table 9. This section of the report provides details of the three UC Berkeley columns and the observed and measured performance. Emphasis is placed on the improvements in damage resistance compared to conventional R/C columns.

3.3.1 Description of HyFRC columns

The two monolithic columns with SC-HyFRC were designated TS-1 and TS-2. TS-1 was designed to rock at the base by unbonding the longitudinal steel in the typical plastic hinge region. No post-tensioning was provided, so the column had $\lambda < 1$ and complete recentering was not expected. TS-2 was designed to form a plastic hinge with bonded stainless steel reinforcing bars which have a more ductile inelastic response than mild steel. Both columns employed only one half of the required amount of confining steel based on SDC requirements (Caltrans 2010). The precast shell column also contained unbonded reinforcing bars.

The precast HyFRC shell used for the third column contained all of the column reinforcement, including the spiral and the longitudinal rebar. Like TS-1, the longitudinal rebar was unbonded over the typical plastic hinge region. The thickness of the shell was 3/16 of the diameter which allowed space for 30 mm fibers. The inside wall of the shell consisted of a corrugated steel pipe which effectively transferred shear between the shell and the core concrete.

All three columns had a diameter of 406 mm and a height of 1708 mm (to the point of load application) for a shear span ratio, M/VD, of 4.2. The design axial load ratio, $P/f_c'A_g$, was 10% for all columns (for design f_c' = 34.5 MPa). All columns contained the same quantity of longitudinal steel reinforcement with ρ_l = 1.2%. TS-1 and TS-2 had a spiral reinforcement ratio of $\rho_t = 0.4\%$ (W3.5 @ 64 mm), while the HyFRC shell column had $\rho_t = 0.9\%$ (W4 @ 32 mm). Elevations and cross sections of TS-1 and TS-2 are provided in Figure 30(a) and Figure 30(b), respectively. An elevation and cross section of the HyFRC shell column is provided in Figure 30(c). Plan and global views of the test configuration for all three columns are shown in Figure 31. The two horizontal actuators pushed and pulled in the W-E direction.

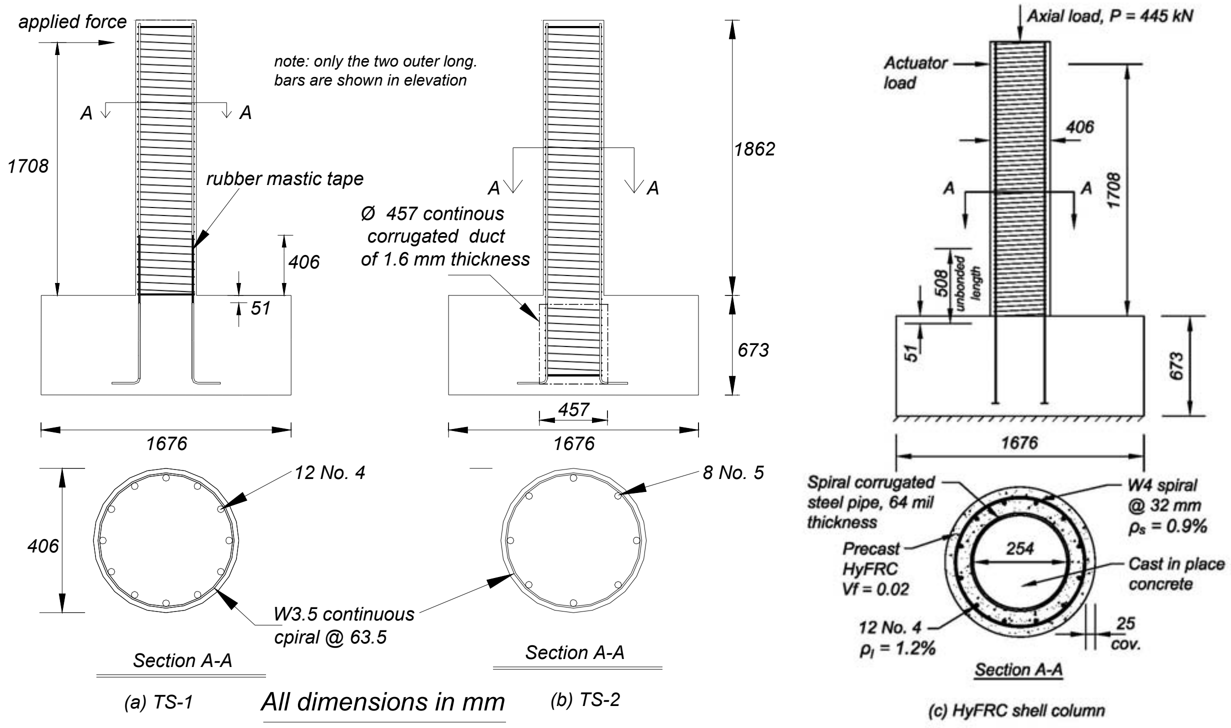

Figure 30. HyFRC column elevations and cross sections; (a) TS-1, (b) TS-2 (Panagiotou et al. 2014), and (c) HyFRC shell column.

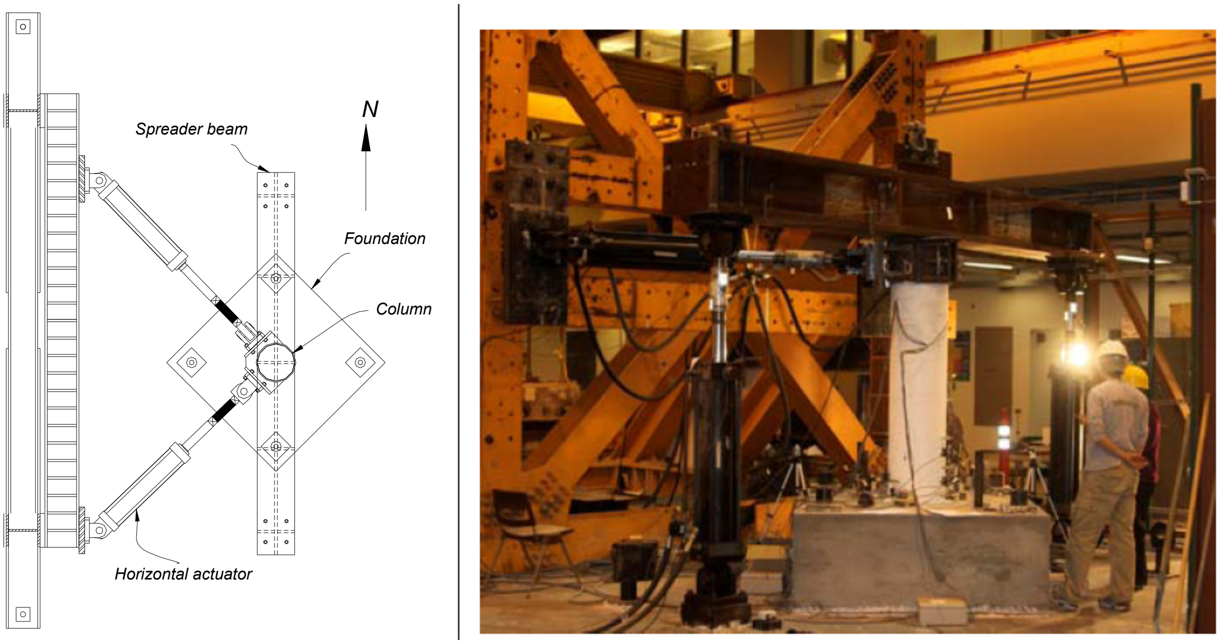

Figure 31. Plan and global views of the test configuration (Panagiotou et al. 2014).

3.3.2 Response to cyclic displacements

TS-1 and TS-2 were loaded with incrementally increasing positive and negative drifts up to a peak drift ratio of 11%. Figure 32(a) shows the response of TS-1, while Figure 32(b) shows the response of TS-2. Both columns retained over 90% of peak lateral strength up to drift ratios of 4.8% and maintained their vertical load resistance through the duration of the test.

The bonding condition of the bars in the two columns was the primary reason for variations in the force-displacement characteristics. Bonding of the bars in TS-2 led to more strain hardening in the plastic hinge and allowed the FRC material to contribute tensile resistance, even after cracking. As a result, the peak lateral strength of column TS-2 was 10% larger than that of column TS-1. In addition, the secant stiffness of TS-2 was 20% larger than TS-1 during displacement cycles of 1.2% and 1.8% drift ratio.

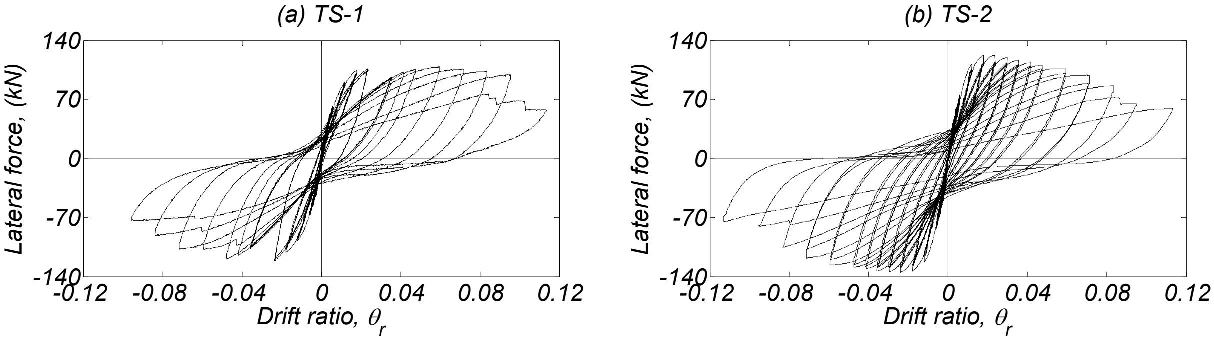

Figure 32. Measured lateral force-displacement responses; (a) TS-1 and (b) TS-2 (Panagiotou et al. 2014).

The response of the HyFRC shell (tube) column is shown in Figure 33 and is compared with the response of specimen TS-1. In both columns the longitudinal rebar was unbonded; however, there were four major differences:

1. The HyFRC in the shell column had 2.0% fibers by volume (1.8% steel, 0.2% PVA) while TS-1 had 1.5% fibers by volume (1.3% steel, 0.2% PVA).

2. The compressive strength of the HyFRC shell (f_c' = 66 MPa) was 78% higher than the SC-HyFRC in TS-1 (f_c' = 37 MPa).

3. The HyFRC shell had over twice the amount of transverse reinforcement ($\rho_t = 0.9\%$) compared to TS-1 ($\rho_t = 0.4\%$). The spacing was half.

4. The design clear cover in the HyFRC shell column was 25 mm, whereas in TS-1 the design cover was 13 mm but as low as 8 mm.

The response of the two columns at drift ratios less than 5% was nearly identical. The maximum shear force of the HyFRC shell column was 3.4% smaller than TS-1 for westward response (at -4.4% drift ratio) and 8.3% larger for eastward response (at 4.2% drift ratio). Shear force was taken as the maximum load applied in the west and east directions by the horizontal actuators. The hysteretic envelopes of the two columns begin to diverge during cycles of drift ratios larger than 5%. At these drift ratios, the differences in fiber content, compressive strength, and spiral confinement produced a noticeably better response in the HyFRC shell column. In the eastward direction (initial push direction), the HyFRC shell column retained 90% of its maximum load capacity at a drift ratio of 10.7% whereas TS-1 retained only 84% of its maximum capacity. At -10% drift ratio in the westward direction, the load resistance of the shell column was 98% of its maximum load while TS-1 retained only 61%.

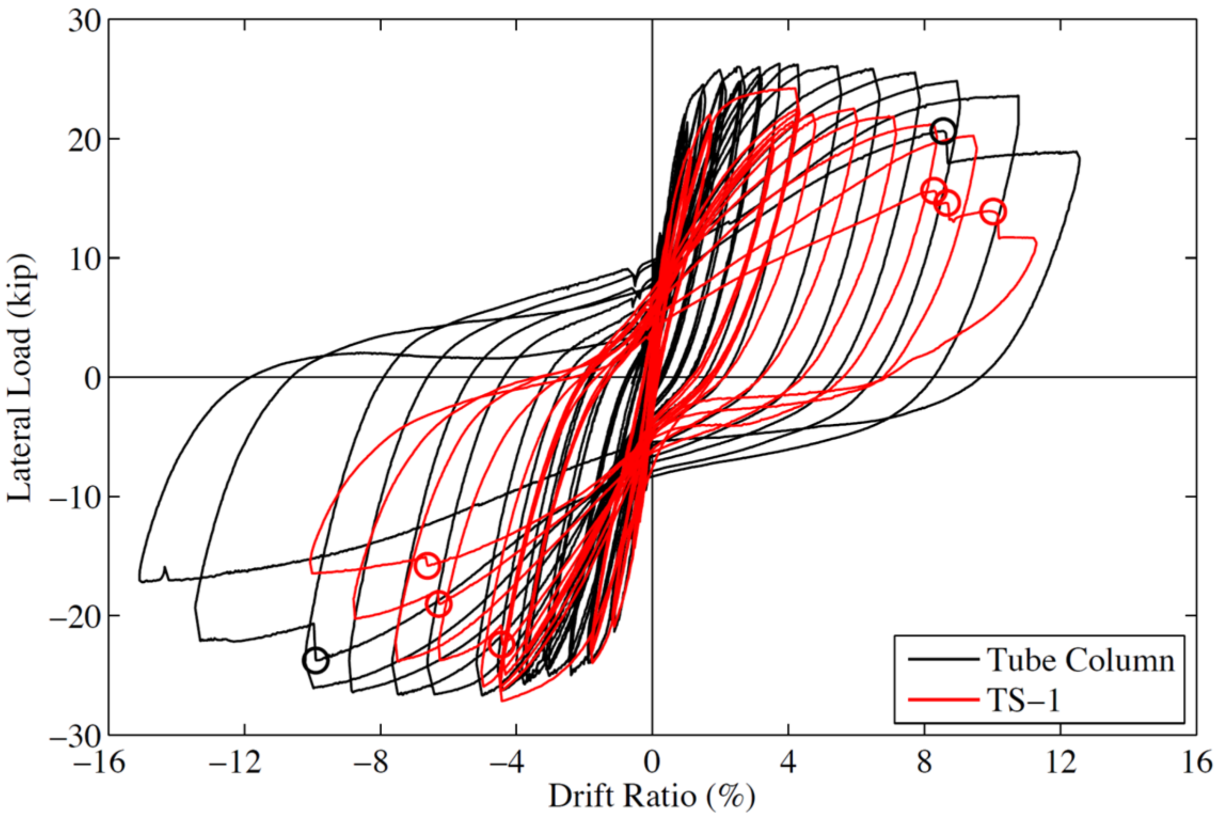

Figure 33. *Lateral force-displacement response of HyFRC shell (tube) column compared to TS-1 (1 kip = 4.45 kN) (Nguyen et al. 2014).*

3.3.3 Observed HyFRC column damage

The development of damage in the three columns varied but in all cases was less severe compared to the damage expected in a conventional R/C bridge column under equivalent displacement demands. Photos of each column at different drift ratios are shown in Figure 34.

Damage in column TS-1 initiated at a drift ratio of 2.4% when localized spalling occurred unexpectedly at a height of 356 mm above the foundation. This spalling occurred at a location with only 8 mm of cover over the spiral, which was less than the designed cover thickness of 13 mm for both TS-1 and TS-2. The longest fiber in SC-HyFRC is 30 mm long, thus the ability of fibers to flow into the cover material was restricted. A longitudinal bar buckled at the location of spalling [Figure 34(a)] at drift ratios of 3.6% and 4.8% and fractured at a drift ratio of 6.0%. Buckling of a second bar initiated at a drift ratio of 4.8%, followed by fracture of that bar at 8.3% drift ratio. A third bar fractured at a drift ratio of 9.5%, while three additional bars fractured during the final cycle of 11.3% drift.

Damage in column TS-2 was concentrated in three through-thickness cracks at heights of 32 mm, 76 mm, and 146 mm above the foundation, with localization occurring at the bottom crack [Figure 34(e)]. During the cycle at a drift ratio of 6.0%, one reinforcing bar buckled at a height 64 mm above the foundation after the spiral fractured there. Significant crushing of the SC-HyFRC occurred during cycles at 8.3% drift and four additional bars buckled. Two longitudinal bars fractured during drift ratios of 9.5%.

(a) East side – $\theta_r = 3.6\%$ (b) East side – $\theta_r = 4.8\%$ (c) West side – $\theta_r = 6.0\%$

(d) West side – $\theta_r = 3.6\%$ (e) East side – $\theta_r = 4.8\%$ (f) East side – $\theta_r = 6.0\%$

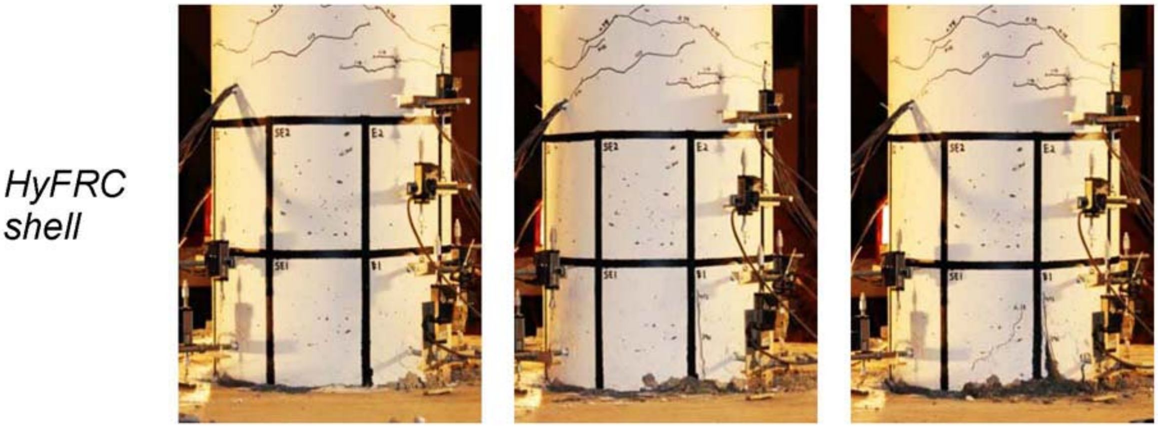

(g) SE side after $\theta_r = 3.5\%$ (h) SE side after $\theta_r = 7.3\%$ (i) SE side after $\theta_r = 11.2\%$

Figure 34. Damage observed in HyFRC columns; (a)-(c) TS-1, (d)-(f) TS-2, (g)-(i) HyFRC shell (Panagiotou et al. 2014, Nguyen et al. 2014).

The damage resistance of the HyFRC shell column was superior to both TS-1 and TS-2. Slight scaling of the HyFRC cover at the east side toe initiated at a drift ratio of 3.0% and propagated as splitting cracks between drift ratios of 3.5% to 7.3% [Figure 34(g) to (h)]. At a drift ratio of 9.5%, a noticeable splitting crack developed on the southeast face of the column. There was no spalling of cover in the HyFRC shell column. Aside from the splitting cracks, there was very little compression damage to the shell up to drift ratios of 11.2% [Figure 34(i)]. Examination of the interface between the corrugated steel pipe and the core after column demolition showed no sign of delamination. In addition, buckling of the longitudinal bars, which occurred in both TS-1 and TS-2, was not observed. Fracture of the longitudinal bars was delayed until drift ratios exceeding 11.3%, whereas fracture first occurred for TS-1 and TS-2 at drift ratios of 6.0% and 9.5%, respectively.

The damage in two similarly-reinforced conventional R/C columns tested under cyclic loading conditions is shown in Figure 35. The R/C columns had the code-required amount of transverse reinforcement (0.7%) which was twice that of TS-1 and TS-2 and the same amount as the HyFRC shell. Clearly, the spalling damage is more severe in the R/C columns at comparable drift ratios.

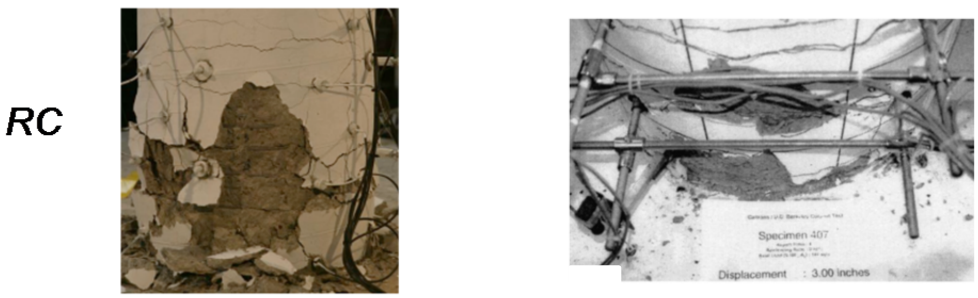

(g) Specimen Base45 – θ_r = 3.9%   (h) Specimen 407 – θ_r = 3.1%

Figure 35. Damage observed in conventional R/C columns (Terzic et al. 2010, Lehman et al. 2004).

3.3.4 Key observations from HyFRC column tests

Several important observations regarding the performance of previous columns built with HyFRC were considered in the design of the post-tensioned HyFRC column presented in this chapter. A summary of important observations is as follows:

1. Spalling was eliminated in all three columns for imposed drift ratios exceeding 10%.

2. Buckling occurred in columns TS-1 and TS-2 whereas no buckling occurred in the HyFRC shell column.

3. TS-1 and TS-2 had half the amount of confinement reinforcement as the shell column, which had a code-compliant amount (Caltrans 2010).

4. TS-1 and TS-2 had half the clear cover of the shell column. The design cover of the shell column was approximately equal to the length of the longest fiber in HyFRC.

5. Plastic hinges were avoided in columns designed with unbonded longitudinal reinforcement (TS-1 and the HyFRC shell column). In those columns, HyFRC contributed very little to the column response in tension.

6. Column TS-2, with bonded longitudinal reinforcement, had localized crack opening/closing at one to three flexural cracks, atypical of a plastic hinge.

One key consideration taken from these tests was the ability of HyFRC to provide ductility to the compression zone of columns. Based on points (1) through (4) and the compression results from Chapter 2, it was concluded that HyFRC can effectively control spalling in columns. Using a code-level quantity of confinement reinforcement along with HyFRC and providing a clear cover that is close to the length of the longest fiber can reduce or eliminate the possibility of bar buckling.

Points (5) and (6) show that HyFRC members may be less prone to crack localization if the longitudinal reinforcing bars are unbonded. Unbonding avoids crack localization at the expense of the flexural strength contribution provided by the material; however, the compression ductility is still superior to conventional R/C. Crack localization has been observed in several other studies of FRC flexural members with bonded reinforcement (Fischer and Li 2003, Saiidi et al. 2009, Kawashima et al. 2012, Haralddsson et al. 2013).

The tension stiffening tests presented in Chapter 2 support the notion that crack localization can be more severe in HyFRC compared to conventional R/C. In HyFRC, if the strength of the composite away from the crack has a greater capacity than that of the rebar and bridging fibers at the crack, localization will occur. In R/C, bond deterioration allows plasticity to spread in the rebar and keeps strains from localizing at the crack locations, although the tensile contribution of the concrete is minimal.

3.4 Design objectives

The broad design objective of the proposed PT HyFRC rocking column was to reduce column damage and prevent residual column displacements, even for low-probability, MCE-level demands. This requirement differentiated the column from most previous studies (see Section 3.2.1) which had lower design demands and often were not tested beyond drift ratios of 4.0%. An explanation of the prototype column, the design demands, and the specific target performance objectives are included in this section.

3.4.1 Prototype column

The PT HyFRC column was designed to have geometry and strength characteristics similar to a prototype reinforced concrete bridge column built in California. The prototype was a fixed-base column with a diameter (*D*) of 1.22 m. A single prototype column supports the roadway bridge superstructure at each bent. The height to the centroid of the superstructure mass (*H*) is 7.32 m, resulting in *M/VD* = 6 for the column in single curvature. Figure 36 shows the elevation and cross section of the prototype bridge bent. The prototype column was 75% smaller than the prototype selected in a prior test program of recentering bridge columns by Jeong et al. (2008). That column was tested under similar conditions as were used for the PT HyFRC column shake table test presented in Chapter 4.

The prototype was based on a Caltrans SDC design (2010) and included 36 longitudinal reinforcing bars with a diameter of 22 mm (No. 7) for a longitudinal reinforcement ratio of ρ_l = 1.2%. A steel spiral with a diameter of 16 mm (No. 5) and a pitch of 82 mm were specified for shear and confinement for a transverse reinforcement ratio of ρ_t = 0.9%. Both longitudinal and transverse reinforcement were expected to be Grade 420 steel, and the design compressive strength of concrete was specified as f_c' = 35 MPa. Clear cover was assumed to be equal to 38 mm.

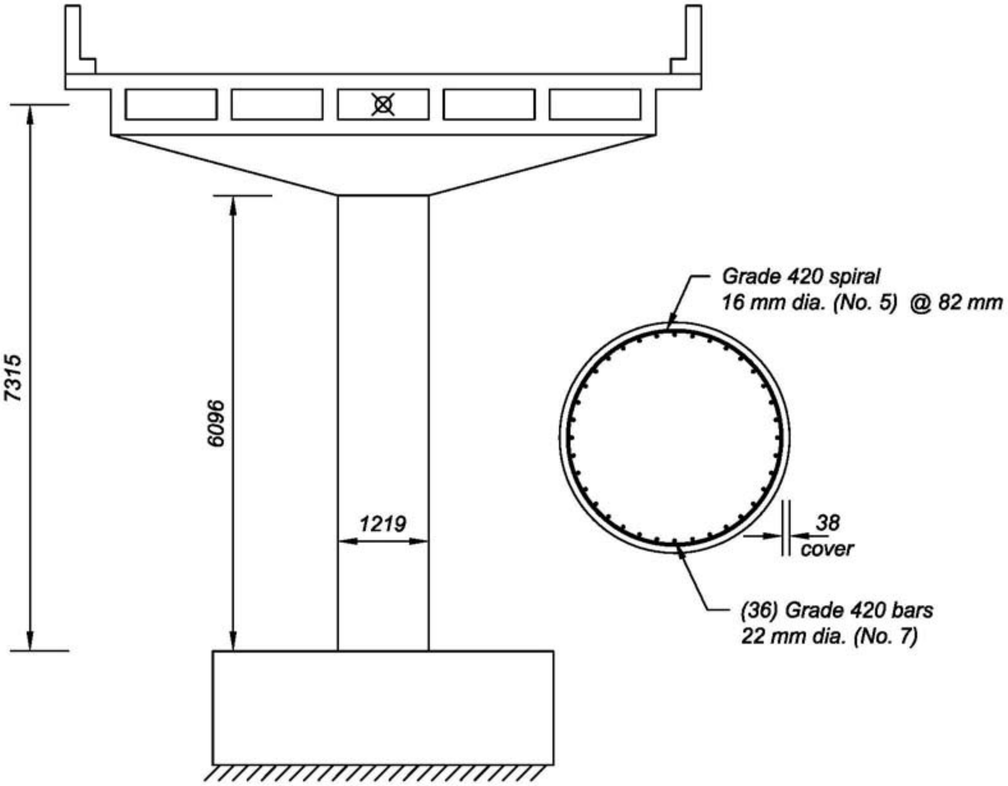

Figure 36. Elevation and cross section of the prototype R/C bridge bent (dimensions in mm).

3.4.2 Design demands

Caltrans SDC was used to define the design-level displacement demand for the column. For ordinary bridges, the Caltrans SDC design ductility demand, μ_D, cannot exceed four. The intention of this limit is to motivate designers to utilize flexible systems, thus reducing the required strength of ductile members and minimizing the demand to adjacent capacity protected components (Caltrans 2010). Therefore the design drift ratio for the rocking column was specified as the drift ratio corresponding to μ_D = 4 in the prototype R/C column. Given the fact that the geographic location of the prototype was not defined, the MCE-level ductility demand was arbitrarily chosen as $\mu_D = 8$ (two times the design level) which was the approach taken by Jeong et al. (2008).

An analytical model of the prototype R/C column was used to determine the drift ratios at various ductility demands. Nonlinear pushover analysis of the model resulted in a peak lateral strength of $0.3W$, a yield drift ratio of $\theta_y = 1.04\%$, and therefore design and MCE level drift ratios of 4.1% and 8.3% at $\mu_D = 4$ and 8, respectively. The pushover analysis also showed a ductility capacity of $\mu_c = 4.1$ at a drift ratio of 4.3% if capacity was defined as the point where the slope of the pushover curve became negative. The MCE-level ductility demand ($\mu_D = 8$) exceeded this capacity, but the model showed that bar fracture and core concrete crushing did not occur when the slope became negative and hence it is likely that collapse would not occur until much larger drift ratios.

3.4.3 Performance objectives

From a qualitative perspective, the rocking column was designed to have minimal spalling and no significant plastic hinging at both the design and MCE-level drift ratios. Under the design-level drift demand, the objective was to have zero damage to HyFRC (no required repairs or patching). At the MCE-level, cosmetic damage to HyFRC was expected, yet the objective was still to eliminate any need for extensive repairs. Rebar and strands were intended to remain intact and structurally sound under both levels of demand.

Several specific performance objectives were targeted for the rocking column at the MCE-level drift ratio of 8.3%:

1. The residual drift ratio after unloading to zero lateral force must be less than 0.5%.

2. The post-tensioned strands must remain elastic to prevent loss of recentering ability.

3. The energy dissipating rebar should be unbonded sufficiently to prevent strains from exceeding 5% to prevent fracture.

4. The depth of the compression zone of the column section should be less than 0.25 to prevent excessive compression damage.

In addition, the lateral strength of the rocking column was intended to be within 15% of the prototype column at the design-level drift ratio of 4.1%. The ability of the rocking column to meet these objectives was evaluated for many design variations using an analytical model described in the next section.

3.4.4 Preliminary column design concept

The column performance objectives were satisfied, in part, by considering the conclusions drawn from prior HyFRC column tests during design (Section 3.3.4). Unbonding of the longitudinal bars was aimed at avoiding the crack localization seen in other tests. A larger thickness of cover material was specified compared to TS-1 and TS-2 to allow more fiber infiltration, and a closer spiral spacing (equivalent to that of the HyFRC shell) was used to reduce bar buckling potential. A higher design f_c' was used for HyFRC in the rocking column compared to TS-1 or TS-2, but it was still smaller than that of the HyFRC shell. The other design details, such as the initial post-tension force (P_{pt}) and the reinforcement ratios of post-tensioning (ρ_{pt}), unbonded bars (ρ_d), and headed bars (ρ_b) were selected based on analysis of a nonlinear numerical model. Details of the model are included in the next section.

The column design also considered several salient characteristics of prior column tests described in Table 9. FRC and steel plate armoring were well-suited for resisting the high compression demands caused by post-tensioning, so HyFRC and discrete headed bars were used in order to armor the rocking plane. The bars yield in compression and dissipate energy while the distributed plate heads avoid the rigidity of continuous steel-on-steel interfaces. Also, in prior tests, unbonded energy dissipaters resulted in less damage than bonded dissipaters. Furthermore, high-strength strands were used for post-tensioning rather than bars. Strands have a higher yield strain than bars so the risk of yielding at large drift ratios was reduced.

The PT HyFRC rocking column was intended to be constructed in several parts. First, the portion of the column from the foundation up to a height of D would be precast with HyFRC and would contain the headed bars to reinforcing the compression zone during rocking. Second, the unbonded longitudinal bars would be cast into the footing and the precast portion would be installed after the footing cured, passing the unbonded bars through embedded ducts. Third, the upper portion of the column and the bridge bent would be cast as conventional R/C. Finally, the strands would be routed from the through the column and post-tensioned.

3.5 Description of the analytical model

An analytical model for the 1/3 scale rocking column test specimen was developed using the OpenSEES software framework (Mazzoni et al. 2006). A 2-D schematic representation of the model is shown in Figure 37. In actuality, the model was assembled in three dimensions and used several unique modeling techniques not used for typical R/C columns. These include the model’s representation of the rocking plane, the unbonded rebar, and the post-tensioning. The key components of the column are called out based on the materials intended for those regions, and the elements used to model them are defined in the legend.

This section first provides a brief description of the common modeling approaches used to capture the behavior of rocking columns. Next, the OpenSEES material, element, and analysis objects used in the model are described. Finally, a parametric study is presented which shows the effects of variations in several key column design parameters on the column response predicted by the model.

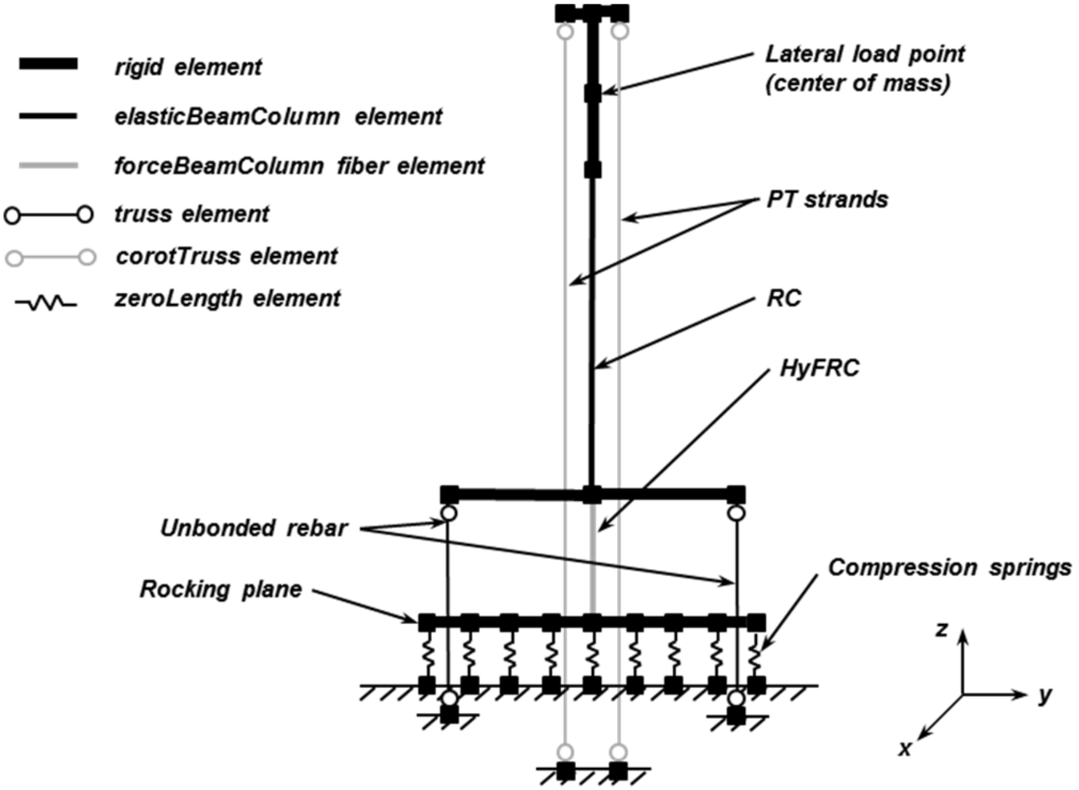

Figure 37. 2-D schematic representation of the PT HyFRC column analytical model developed in OpenSEES (not to scale).

3.5.1 Modeling approaches for post-tensioned columns

Housner (1963) first proposed the equations of motion for rigid blocks rocking on similarly rigid foundations. Since that time, numerous modeling techniques have been developed to predict the response of rocking structures to static and dynamic loading. Recent modeling techniques used for post-tensioned columns have varied in complexity and have included lumped plasticity elements (Palermo et al. 2007), fiber elements (Sakai and Mahin 2004), solid 3-D finite elements (Kwan and Billington 2003a,b, Lee and Billington 2009), and models with distributed contact springs (Marriot et al. 2008, Marriot et al. 2011, Guerrini and Restrepo 2013b).

The approach taken herein combines several of the above techniques for individual components of the PT HyFRC column. The unbonded post-tensioned strands and the unbonded rebar were modeled using springs (truss elements) and the bonded regions of the column were modeled using fiber elements, similar to the approach taken by Sakai and Mahin (2004). A bed of distributed contact (compression) springs was used to capture the response of the rocking plane, similar to the approach in Marriot et al. (2011). The following sections describe in detail the various components of the model as shown in Figure 37.

3.5.2 Compression springs

A bed of distributed vertical springs defined by *zeroLength* elements (Figure 37) was used to represent the rocking plane at the base of the column. Each spring connected two nodes (*i* and *j*) sharing the same (x, y, z) coordinates. Node *i* was fixed in all three directions, while node *j* was fixed only in the horizontal directions (x and y). A nonlinear force-deformation relationship was defined for each spring in the vertical (z) direction by scaling a material stress-strain model; stress coordinates were scaled by the effective spring area, A_{sp}, and strain coordinates were scaled by the effective spring length, L_{sp}. The material stress-strain models used for the springs were defined to have zero tensile resistance; therefore, the springs provided no resistance to uplift of the rocking plane.

Different springs were used to represent headed rebar and HyFRC at the rocking interface. For the HyFRC elements, the cross sectional area of the column was discretized by subdividing the area radially and circumferentially as shown in Figure 38. Each subsection was represented by a spring located at its radial and angular midpoint with unique area A_{sp}. The vertically free nodes of each spring were connected radially by rigid horizontal beam elements extending from a single node at the column centroid to the outermost spring (Figure 38). Different material stress-strain models were assigned to spring within the spiral (confined HyFRC) or outside the spiral (unconfined HyFRC).

Headed reinforcing bars which terminated at the rocking plane were used in the PT HyFRC column. These bars were modeled using compression springs with the effective length of the concrete springs and the area and position properties of each bar in the cross section. The vertically free nodes were also connected by rigid horizontal beam elements to a single node at the column centroid.

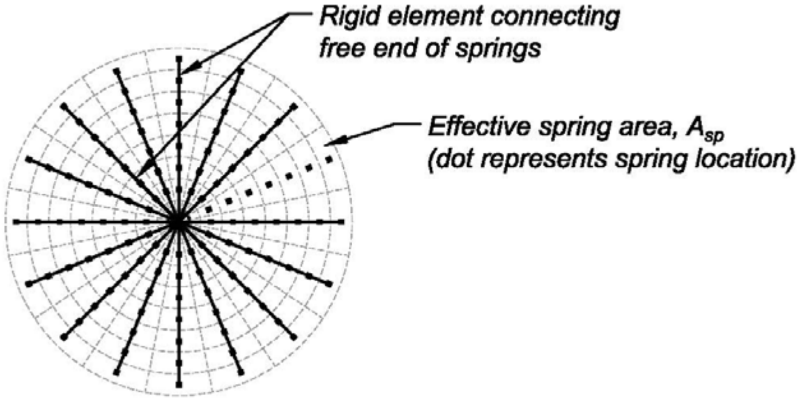

Figure 38. Planar discretization of the column cross section for HyFRC springs.

As mentioned, the force-deformation relationship for each HyFRC or rebar spring was defined by scaling a material stress-strain model by A_{sp} and L_{sp}. The effective length was taken to be equal to the theoretical depth of the compression zone at the rocking plane (i.e. neutral axis depth), c, under the MCE-level ductility demand. This assumption follows work by Restrepo and Rahman (2007) on rocking R/C walls where the inelastic strains that develop within the compression zone were assumed to be uniform over a distance c above the foundation. The values of c and L_{sp} were found, iteratively, to converge to $D/4$ at the MCE-level drift ratio of 8.3%. This value was used for L_{sp} in all model analyses.

3.5.3 Truss elements

The unbonded rebar and post-tensioned strands were modeled using truss elements that spanned over their actual unbonded lengths. In OpenSEES, the *truss* element, which considers only linear geometry, was chosen for the unbonded bars. The *corotTruss* element, which considers corotational (nonlinear) element geometry, was used for the post-tensioning. A nonlinear transformation was chosen for the post-tensioning because the strands will be inclined by an amount approximately equal to the base rotation as the column uplifts. Therefore, the nonlinear effects associated with the inclination of the truss element should be considered. Analyses showed that rotation at the rocking plane accounted for 80% of the MCE-level drift ratio of 8.3%, confirming the importance of the nonlinear transformation for the strands.

3.5.4 Beam-column elements

The column was modeling using two different types of beam-column elements. The first was a nonlinear *forceBeamColumn* element, which is based on an iterative force-based formulation. This element was used for the end region of the column which was designed to be cast with HyFRC. Integration points were included in the element only at its endpoints. The section force-deformation behavior was defined by aggregating discretized fibers of different materials, and the stress-strain characteristics of the fibers were defined using nonlinear material models for confined HyFRC, unconfined HyFRC, and reinforcing steel.

The R/C portion of the column above the HyFRC end region was modeled as elastic using the *elasticBeamColumn* element. These elastic elements were used above the unbonded region made of HyFRC (see Figure 37) where the column was expected to remain elastic. The transformed section approach used to define the elastic properties of the R/C cross section.

As shown in Figure 37, rigid elements extend from the top of the *elasticBeamColumn* element to the lateral load point (center of inertial mass), as well as from the load point to the height of the post-tensioning anchorage. These elements were included to mimic the PT HyFRC test column as it was configured during shake table testing, when the center of the inertial mass and the PT anchorage were well above the top of the actual column. Rigid elements were used to model the region above the column, and a more thorough description of the shake table test configuration will be presented in Chapter 4.

3.5.5 Coordinate transformations

The OpenSEES geometric transformation object (*geomTransf*) transforms beam element stiffness and resisting force from the basic system to the global-coordinate system, and different coordinate transformations were used for various elements used in the model. A *Linear* transformation was used for the rigid elements connecting the contact springs to the column centroid at the column base. A *Corotational* tranformation was used for the *forceBeamColumn* element and the *elasticBeamColumn* element used for the R/C portion of the column. A *PDelta* transformation was used for the *elasticBeamColumn* elements representing the inertial mass region above the column.

3.5.6 Material models

Previously developed *uniaxialMaterial* objects in OpenSEES defined the nonlinear stress-strain and loading/unloading relationships for the various elements within the column.

The stress-strain relationships of *zeroLength* elements and *forceBeamColumn* fibers representing HyFRC were modeled using *Concrete03* (nonlinear tension-softening concrete material), a model that was initially developed for FEDEAS/FEAP (Filippou 2007a). *Concrete03* is defined by ten parameters: the compressive strength and corresponding strain (f_c', ε_0), the crushing strength and corresponding strain (f_{cu}, ε_u), the ratio of the unloading slope at ε_u to the initial loading slope in compression ($\lambda_c = E_u/E_c$), the tensile strength (f_t), the tensile stress and strain at the transition from nonlinear to linear softening (f_{t1}, ε_{t1}), the exponent of the tension softening curve (β), and the tensile strain at zero tensile stress (ε_{tu}). The initial slope in compression is $E_c = 2f_c'/\varepsilon_0$. The envelope in compression is parabolic up to point (ε_0, f_c'), then linear softening occurs until (ε_u f_{cu}) when the slope is zero. In tension the envelope is linear up to f_t, following by nonlinear softening to (ε_{t1}, f_{t1}), then linear softening to (ε_{tu}, 0).

One benefit of this model over other OpenSEES concrete models is the ability to control the unloading slope with the λ_c parameter. Furthermore, the tensile behavior of HyFRC (see Figure 19) is well-represented by the nonlinear tension softening and the model parameters can effectively be tuned to represent any FRC material. The backbone curves for *Concrete03* in compression and tension are shown in Figure 39(a) and Figure 39(b), respectively. The hysteretic response of the material is shown in Figure 40. It should be noted that the values shown on the ordinate axis (i.e. stress) in Figure 39 and Figure 40 are not the values used in the model; the user can define the curve with any values.

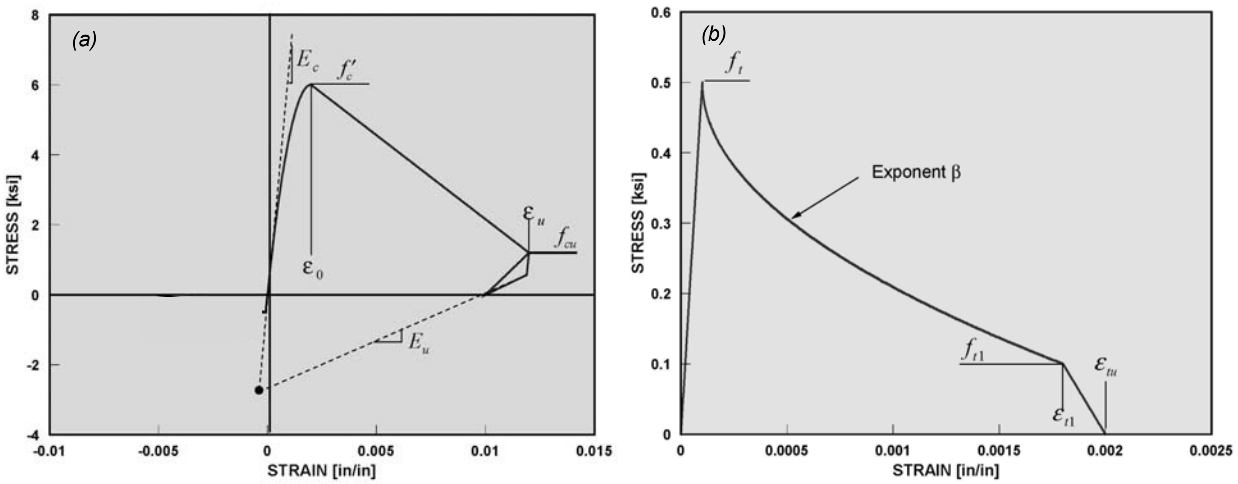

Figure 39. Backbone stress-strain curves for Concrete03; (a) in compression and (b) in tension (Filippou 2007a).

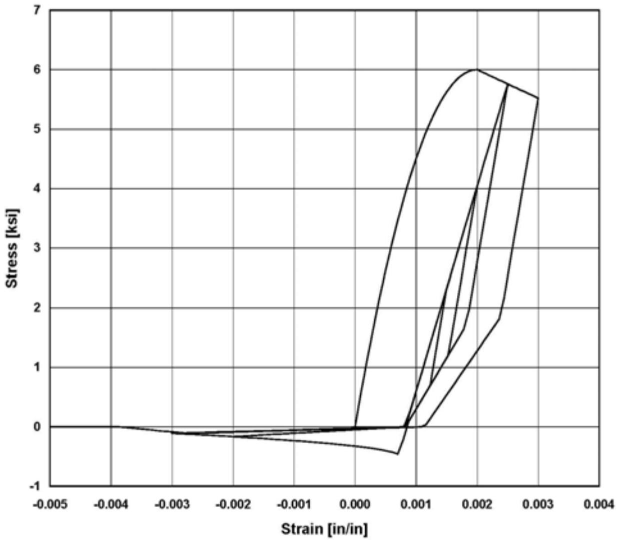

Figure 40. Hysteretic stress-strain response of the Concrete03 material model (Filippou 2007a).

The stress-strain relationship of *truss* elements representing the unbonded rebar was modeled using *Steel02* (Giuffre, Menegotto, and Pinto material with isotropic strain hardening, Filippou et al. 1983). *Steel02* was also used to define the stress-strain behavior of the steel fibers in the *nonlinearBeamColumn* element. This reinforcing steel model is defined by six parameters: the yield strength (f_y), the Young's modulus (E), the strain hardening ratio ($b = E_p/E$), the exponent that controls the transition between elastic and hardening branches (R), and two additional parameters that control the change in R with cyclic loading, (c_1 and c_2). Four additional parameters defining isotropic hardening are optional (a_1, a_2, a_3, a_4). Figure 41(a) shows the backbone tension curve and Figure 41(b) shows the hysteretic response. Again, the curves shown in these figures are not representative of the values used in the model.

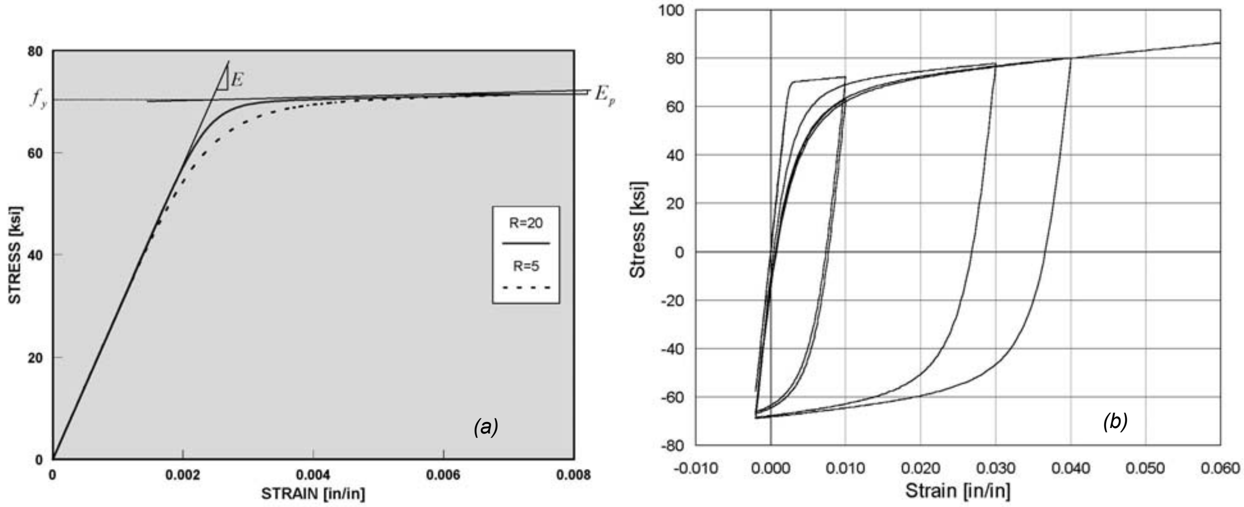

Figure 41. Response of Steel02; (a) backbone curve in tension and (b) hysteretic stress-strain response (Filippou 2007b).

The stress-strain relationship of the springs at the rocking plane representing the headed rebar was modeled using the *ElasticPPGap* material model rather than *Steel02*. *ElasticPPGap* is a bilinear hysteretic model defined by five parameters: the tangent, E, the stress when the material reaches the plastic state, F_y, the initial gap (the deformation when stress initiates), the hardening ratio, $b = E_p/E$, and an option for damage accumulation that causes the gap to grow based on the inelastic strain developed. *ElasticPPGap* allows load to accumulate in tension or compression only; the slope of the unloading path is E until the load is zero. At that point, the slope becomes zero until the material is reloaded to the "gap" deformation. Figure 42(a) shows the main parameters of *ElasticPPGap* and Figure 42(b) shows the hysteretic response with damage accumulation. In Figure 42(b), the blue curve represents the initial loading/unloading while the red curve represents reloading.

The *ElasticPPGap* material was also used in conjunction with the *InitStrainMaterial* to define the stress-strain relationship of the strands. *ElasticPPGap* defined the tensile stress-strain behavior of post-tensioning using no initial gap. The damage option was selected to allow a tension gap to grow if strand yielding occurred. Physically, yielding would result in a longer "slack" length of the strands. The post-tensioning force was modeled by defining an initial strain, ε_0, in the *ElasticPPGap* material model using the *InitStrainMaterial* object.

The *ElasticPPGap* material was well suited to capture the compression-only response of the discontinuous headed rebar and the tension-only response of the post-tensioning. No initial gap was used for the headed bars since they would initially develop compression at the rocking plane, but the damage accumulation option was used to create a compression gap if/when the headed bars yielded in compression. The parameters of *ElasticPPGap* (E, F_y, and b) were identical to the main parameters defining the *Steel02* envelope (E, f_y, and b, respectively) except that they were scaled by the area and length of the headed bar in order to represent force-displacement rather than stress-strain.

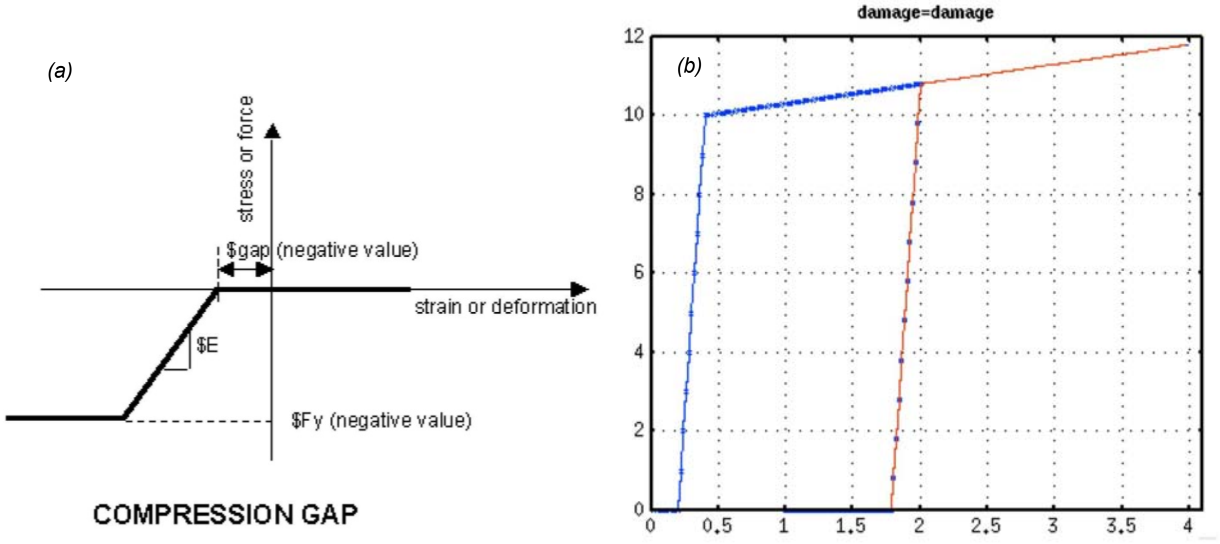

Figure 42. Response of ElasticPPGap; (a) backbone curve in compression and (b) hysteretic response with damage accumulation.

3.5.7 Material model parameters

Values for the parameters of the material models are provided in Appendix Table A. 1. The material properties of the rebar and post-tensioning strand were obtained from coupon tests of each material used in the PT HyFRC shake table test presented in Chapter 4. The *Concrete03* parameters f_c' and ε_0 for unconfined HyFRC were obtained from cylinder compression tests of the material used in the column. The model by Mander et al. (1988a) was used to estimate f_c' and ε_0 for confined HyFRC based on the effective confining stress provided by the transverse reinforcement.

The confinement tests presented in Chapter 2 were used to define the compression softening parameters of HyFRC. The stress and strain at the crushing point for the *Concrete03* models (f_{cu} and ε_u) were defined by [3.2] and [3.3], where α_1 and α_2 are dimensionless empirical factors.

$$\varepsilon_u = \alpha_1 \varepsilon_0 \tag{3.2}$$

$$f_{cu} = \alpha_2 f_c' \tag{3.3}$$

The factors α_1 and α_2 were estimated from the measured unconfined and confined stress-strain test responses from Chapter 2 (see Figure 11). The estimates were taken from the SC-HyFRC samples since they had the same fiber content as the HyFRC used in the column. The confined samples at $\rho_s = 1.0\%$ were used for the confined properties. The procedure for estimating the variables was as follows:

1. The crushing point for each test was taken as the point in the response when stress becomes approximately constant.

2. The peak point for each test was taken as the point of maximum stress.

3. The values of α_1 and α_2 were estimated for each test based on their respective definitions in [3.2] and [3.3].

4. The values were averaged for all test responses in Figure 11.

The tensile properties of HyFRC (f_t, ε_{t1}, f_{t1}, ε_{tu}) were based on results from the direction tension dogbone tests presented in Chapter 2 (see Figure 19). Tensile properties were only defined for HyFRC located within the *forceBeamColumn* element; for the compression springs the tensile properties were set to zero.

The initial strain in the post-tensioning was calculated using [3.4], where P_{pt} is the post-tensioning force, W is the weight of the inertial mass, K_0 is the axial stiffness of the column, and E_{pt}, A_{pt}, and L_{pt} are the elastic modulus, cross sectional area (total), and length of the post-tensioning, respectively.

$$\varepsilon_0 = \frac{W+P_{pt}}{K_0 L_{pt}} + \frac{P_{pt}}{E_{pt} A_{pt}} \tag{3.4}$$

The first term in [3.4] represents the strain expected to be lost due to elastic shortening of the column under load, while the second term represents the target strain in the post-tensioning after shortening occurs. The axial stiffness (K_0) was obtained from model analysis.

3.5.8 Analysis methods

Unidirectional pushover analysis was performed to estimate the lateral strength of the column and to predict the inelastic force-displacement response. Cyclic analysis was performed by imposing a displacement history which consisted of a unidirectional push to a specified peak drift ratio, a subsequent pull to the same peak drift ratio but in the negative direction, and finally a push back to zero lateral displacement. These static analyses were used to investigate the influence of different design parameters on the column hysteretic response.

Dynamic analyses were conducted using nonlinear response history analysis (NRHA). The accelerations imposed on the PT HyFRC test column were applied to the analytical model, and dynamic analysis results will be presented in Chapter 4 where they compared with the measured shake table test response.

The static analyses were displacement controlled (OpenSEES *DisplacementControl* integrator object) such that each successive analysis step targets an incremental displacement at one degree of freedom. For all static analyses the displacement increment was specified as 0.25 mm (0.01 inches) at the height of the inertial mass. The Newton-Raphson algorithm (OpenSEES *Newton* algorithm object) was employed to solve the nonlinear system of equations at each analysis step. The Newmark method (OpenSEES *Newmark* integrator object) was used in dynamic analyses to solve the equations of motion, with $\gamma = 1/2$ and $\beta = 1/4$ (average acceleration method). This method is conditionally stable and second order accurate.

3.6 Parametric model analysis

A series of model analyses were conducted prior to arriving at the final design of the PT HyFRC column described in Section 3.4.4. The column diameter, aspect ratio, and the weight of the inertial mass were identical for all analyses. The vertical coordinates (z) and the lengths of the various model elements described in Section 3.5 were also fixed. Table 10 summarizes the characteristics of the analytical model (see Figure 37) that were held constant in all analyses.

Several important aspects of the elements used in analyses should be noted with response to Table 10. First, identical model parameters for *Concrete03* were used to represent HyFRC in all analyses. Confinement effects were based on the spiral diameter, spacing, yield strength and concrete cover shown in Table 10. Furthermore, the number of elements representing unbonded rebar, headed rebar, and post-tensioned strands was held fixed for all analysis, although the reinforcement ratios were varied. The target reinforcement ratios for different analysis cases were achieved by scaling the area of individual elements of a given type.

The unbonded length of the longitudinal bars was kept equal to 1.25*D* based on satisfactory performance in specimens TS-1 and the HyFRC shell column, although a length of 2*D* has also been suggested (Sakai and Mahin 2004, Jeong et al. 2008). The length of the unbonded post-tensioning was held fixed to mimic the condition in shake table testing presented in Chapter 4.

Table 10. Geometric properties and loading conditions implemented in all parametric model analysis cases.

Column diameter, D, mm	406		
Effective height of lateral load, H, mm	2438		
Weight of inertial mass (dead load), W, kN	232.5		
Unconfined compressive strength, f_c', MPa			
HyFRC	44.6		
Concrete	34.5		
Spiral diameter, mm	5.7		
Spiral spacing, mm	32		
Spiral yield strength, MPa	480		
Concrete cover, mm	32		
Longitudinal reinforcement [a]	*number*	*radius, mm*	*start angle* [b]*, °*
headed rebar	10	159	31
unbonded rebar	5	151	7
post-tensioned strands	4	27	0
Vertical element geometry	*z_i, mm*	*z_j, mm*	*L, mm*
compression springs	0	0	102
HyFRC region	0	406	406
RC region	406	1346	940
unbonded rebar	-51	457	508
post-tensioned strands	-552	2915	3467
Section discretization for compression springs			
radial divisions	8		
circumferential divisions	16		
number of concrete springs	128		
number of headed bar springs	10		

[a] *Unbonded bars are located between every two headed rebar circumferentially (total 15 bars)*
[b] *Start angle refers to the angle from the major bending axis to the first bar. Unbonded bars are separated by 72°. Headed bars are separated by 24° or 48°.*

A 1/3 scale model of an R/C column was also analyzed in OpenSEES by Schoettler et al. (2013). The model was developed for the reference R/C specimen subjected to the shake table tests (to be presented in Chapter 4) and had a higher reinforcement ratio ($\rho_l = 1.6\%$) than the prototype R/C column ($\rho_l = 1.2\%$, Figure 36). The column was modeled with a single *forceBeamColumn* element defined by a nonlinear fiber section. Static lateral pushover analysis of the reference R/C column model was conducted to define the target lateral shear strength of the PT HyFRC test column. Based on that analysis, a shear strength of $0.3W$ was targeted (78 kN). Cyclic analyses were not conducted for the reference R/C column model.

3.6.1 Analysis case details

The details of the variables adjusted in 25 analysis cases are presented in Table 11, including the post-tension force (P_{pt}) and the reinforcement ratios of post-tensioning (ρ_{pt}), unbonded rebar (ρ_d), and headed rebar (ρ_b). These parameters were chosen as variable parameters primarily because they have the largest effect on the overall column response. They were also chosen because they dictate the quantities of rebar and post-tensioning to be used in the column as well as the post-tensioning force to apply. The reinforcement ratio of headed rebar directly controls the strength and stiffness of the compression zone (assuming the HyFRC properties are fixed). The values of P_{pt}, ρ_{pt}, and ρ_d influence the magnitude of the λ parameter for hybrid post-tensioned columns which describes their recentering ability.

The parameter λ given by [3.1] and the sum of the reinforcement ratios of unbonded rebar and post-tensioning ($\rho_d + \rho_{pt}$) are also given in Table 11. The moments used to calculate λ were taken at the design-level drift ratio of 4.2% during each analysis. The combined ratio ($\rho_d + \rho_{pt}$) was intended to be similar in magnitude to the longitudinal steel ratio of the prototype R/C column ($\rho_l = 1.2\%$) to have comparable strength and stiffness in both cases. For the cases presented, λ ranged between 0.52 and 7.06.

In Table 11, Cases 1-5 represent a variation in P_{pt}, Cases 6-10 represent a variation in ρ_{pt}, Cases 11-15 represent a variation in ρ_d, and Cases 16-20 represent a variation in ρ_b with all other parameters held constant in each set of cases. Cases 21-25 were specifically chosen to investigate the response when $\lambda < 1$; the only parameters varied in those cases were P_{pt} and ρ_d. Finally, Case R/C represents the details of the R/C reference column, and Case PT HyFRC represents the final optimized design parameters for the rocking column.

Each case was subjected to cyclic displacements with two different amplitudes. The amplitude of the first cycle was the design-level drift ratio of ±4.2%, and the amplitude of the second cycle was the MCE-level drift ratio of ±8.3%.

One objective of these analyses was to obtain a recentering force-displacement curve which unloaded as close to the origin as possible. A competing objective was to maximize hysteretic energy dissipation, evaluated qualitatively as the area encompassed by the hysteretic curve. Curves which softened at large drift ratios were undesirable as such behavior typically leads to structural instability. In recentering columns, instability is less likely because even if the structure softens as drift ratios increase, the recentering force still brings it back to its initial position.

Of course, practical limitations also dictated the final choice of parameters. It would be impractical to have a total reinforcement ratio of unbonded rebar and post tensioning ($\rho_d + \rho_{pt}$) significantly larger than the prototype R/C column longitudinal ratio of $\rho_l = 1.2\%$. In addition, a value of ρ_b that was too large would lead to congestion within the cross section. Finally, the specific combination of P_{pt} and ρ_{pt} had to result in initial post-tension stresses low enough to prevent yielding at large drift ratios. The most important consideration was to obtain a combination of P_{pt}, ρ_{pt}, ρ_d , and ρ_b that achieved the objectives yet was practical and feasible for actual column construction.

Table 11. Details of 25 analysis cases performed with the analytical model

Analysis case	*P_{pt}, kN*	*ρ_{pt}, %*	*ρ_d, %*	*ρ_b, %*	*$\rho_{pt}+\rho_d$, %*	*λ*
1	111	0.43	0.77	1.54	1.20	1.08
2	223					1.32
3	334					1.54
4	556					2.02
5	668					2.27
6	445	0.22	0.77	1.54	0.99	1.53
7		0.32			1.09	1.70
8		0.54			1.31	1.86
9		0.65			1.42	1.95
10		0.86			1.63	2.10
11	445	0.43	0.19	1.54	0.62	7.06
12			0.39		0.82	3.51
13			0.58		1.01	2.38
14			0.96		1.40	1.43
15			1.16		1.59	1.19
16	445	0.43	0.77	0.39	1.20	1.79
17				0.77		1.79
18				1.16		1.78
19				2.31		1.77
20				3.08		1.79
21	223	0.43	1.16	1.54	1.59	0.88
22	334		1.16		1.59	1.03
23	223		1.54		1.97	0.65
24	334		1.54		1.97	0.77
25	223		1.93		2.36	0.52
RC	-	-	-	1.60	-	-
PT HyFRC	445	0.43	0.77	1.54	1.20	1.79

3.6.2 Analysis case results

The lateral force-displacement responses of the 25 analysis cases are shown in Figure 43 and Figure 44 for the design-level and MCE-level analyses, respectively. The ordinate is the ratio of the column shear force to the weight of the inertial mass, *V/W*, and the abscissa is the column drift ratio, θ. The pushover response of the reference R/C column model is also superimposed in each figure for comparison.

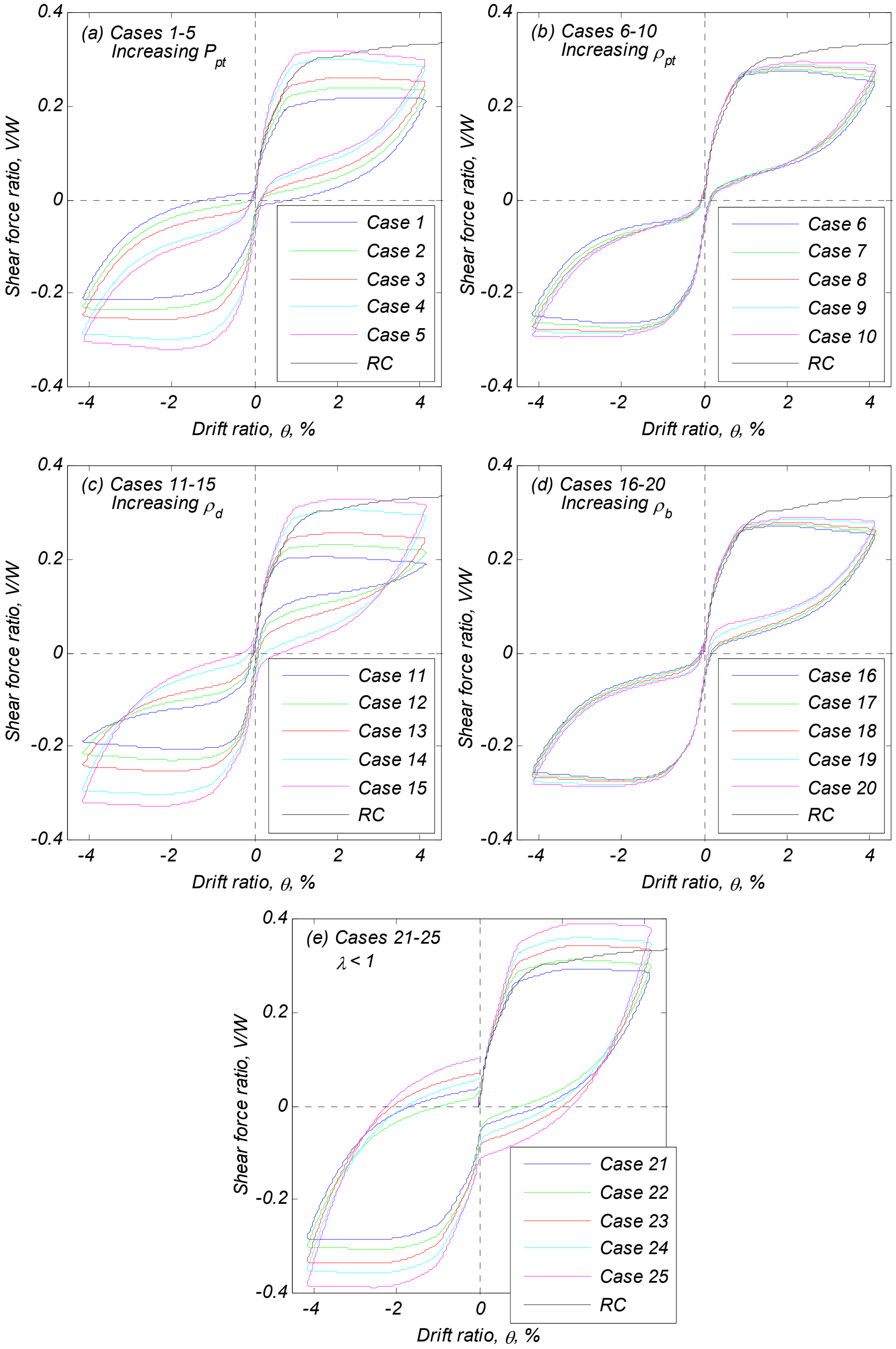

Figure 43. Results of parametric analysis at an amplitude of 4.2% drift ratio; (a) Cases 1-5, (b) Cases 6-10, (c) Cases 11-15, (d) Cases 16-20, and (e) Cases 21-25.

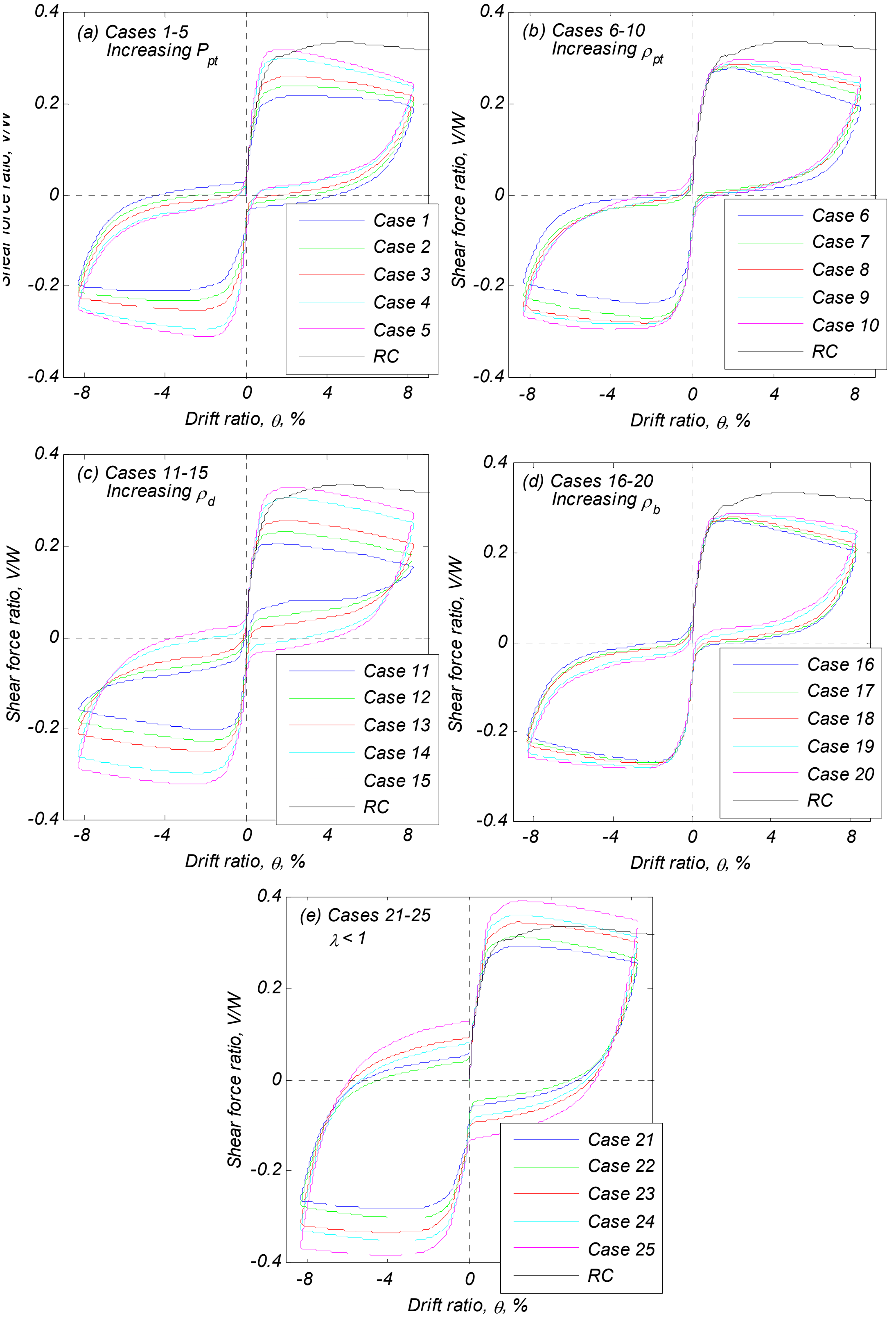

Figure 44. Results of parametric analysis at an amplitude of 8.3% drift ratio; (a) Cases 1-5, (b) Cases 6-10, (c) Cases 11-15, (d) Cases 16-20, and (e) Cases 21-25.

Table 12 and Table 13 provide a summary of model response parameters taken from the design-level and MCE-level analyses, respectively. For each analysis case, the tables include the maximum shear force (V/W_{max}), the ratio between the shear force at the peak drift ratio and the maximum shear force ($V_{4.2}/V_{max}$ or $V_{8.3}/V_{max}$), the residual drift ratio after unloading to zero load, the depth of the compression zone at the rocking interface (c), the maximum strain in compression ($\varepsilon_{c,max}$), the uplift during rocking (Δ_{up}), the maximum strain in the unbonded bars in tension ($\varepsilon_{d,max}$), and the ratio of the maximum strain in the post-tensioned strands to the yield strain, ($\varepsilon_{max,\, pt} / \varepsilon_{y,\, pt}$). The values of c, $\varepsilon_{c,max}$, Δ_{up}, $\varepsilon_{d,max}$, and $\varepsilon_{max,\, pt} / \varepsilon_{y,\, pt}$ are taken when the column is at the maximum drift ratio for each case.

The mean and coefficient of variation (*COV*) for the 25 values of each response parameter is also shown in Table 12 and Table 13. The coefficient of variation is the ratio of the standard deviation to the mean and is a measure of the dispersion for each parameter. Some of the model response parameters were affected by design variations moreso than others. For example, the residual drift ratio and $\varepsilon_{max,\, pt} / \varepsilon_{y,\, pt}$ had *COV*'s of 1.28 and 0.25 for cycles at 4.2% drift ratio (Table 12) while Δ_{up} and $\varepsilon_{d,max}$ had *COV*'s of 0.04 and 0.03. The latter two variables were practically unaffected by variations in the main design parameters with *COV*'s less than 0.04 for both amplitudes of drift ratio (Table 13). The *COV* of c and $\varepsilon_{c,max}$ was twice that of Δ_{up} and $\varepsilon_{d,max}$, indicating a stronger dependence on the design parameters.

Table 12. Key response parameters at an amplitude of 4.2% drift ratio.

Analysis case	*V/W_{max}*	*$V_{4.2}/V_{max}$*	*Residual drift ratio, %*	*c, mm*	*Δ_{up}, mm*	$\varepsilon_{c,max}$	$\varepsilon_{d,max}$	$\varepsilon_{max,\, pt} / \varepsilon_{y,\, pt}$
1	0.22	0.99	0.89	77.6	12.6	-2.92	2.06	0.34
2	0.24	0.98	0.14	80.0	12.3	-2.98	1.97	0.44
3	0.26	0.97	0.15	87.6	11.9	-3.23	1.91	0.54
4	0.30	0.95	0.16	100.5	11.3	-3.64	1.83	0.75
5	0.32	0.94	0.19	106.5	11.0	-3.83	1.78	0.86
6	0.28	0.91	0.13	87.6	11.9	-3.23	1.91	1.00
7	0.28	0.94	0.14	91.5	11.7	-3.36	1.89	0.80
8	0.29	0.96	0.15	96.8	11.5	-3.53	1.86	0.56
9	0.29	0.97	0.16	98.7	11.4	-3.59	1.85	0.50
10	0.30	0.98	0.18	102.2	11.2	-3.70	1.81	0.41
11	0.21	0.94	0.06	81.1	12.3	-3.03	1.94	0.66
12	0.23	0.95	0.08	85.4	12.1	-3.16	1.91	0.65
13	0.26	0.95	0.10	90.1	11.8	-3.31	1.89	0.65
14	0.31	0.96	0.25	98.3	11.4	-3.57	1.85	0.65
15	0.33	0.96	0.65	101.5	11.2	-3.66	1.84	0.65
16	0.27	0.93	0.22	107.7	11.2	-3.98	1.79	0.64
17	0.28	0.94	0.18	102.5	11.4	-3.77	1.83	0.64
18	0.28	0.95	0.16	98.9	11.5	-3.63	1.86	0.65
19	0.29	0.97	0.12	85.4	11.9	-3.11	1.89	0.65
20	0.29	0.98	0.09	79.3	12.1	-2.87	1.91	0.66
21	0.29	0.98	1.47	89.2	11.8	-3.28	1.91	0.43
22	0.31	0.97	0.99	95.7	11.5	-3.48	1.87	0.54
23	0.34	0.98	2.00	96.9	11.4	-3.51	1.87	0.43
24	0.36	0.98	1.75	102.5	11.1	-3.69	1.84	0.53
25	0.39	0.98	2.23	103.6	11.0	-3.71	1.84	0.42
Mean	0.29	0.96	0.51	93.88	11.61	-3.43	1.88	0.60
COV	0.14	0.02	1.28	0.09	0.04	0.09	0.03	0.25

Table 13. Key response parameters at an amplitude of 8.3% drift ratio.

Analysis Case	*V/W_{max}*	*$V_{8.3}/V_{max}$*	*Residual drift ratio, %*	*c, mm*	*Δ_{up}, mm*	$\varepsilon_{c,max}$	$\varepsilon_{d,max}$	$\varepsilon_{max,\,pt}/\varepsilon_{y,\,pt}$
1	0.22	0.89	4.41	89.1	25.1	-6.95	3.83	0.60
2	0.24	0.86	3.12	96.4	24.4	-7.48	3.76	0.71
3	0.26	0.83	1.58	101.5	23.9	-7.85	3.67	0.81
4	0.30	0.79	0.48	110.6	23.1	-8.49	3.46	1.00
5	0.32	0.76	0.58	113.4	22.8	-8.68	3.43	1.00
6	0.28	0.70	1.19	90.4	25.0	-7.04	3.84	1.01
7	0.28	0.78	0.40	101.9	23.9	-7.87	3.67	1.00
8	0.29	0.83	0.66	109.6	23.2	-8.42	3.47	0.80
9	0.29	0.84	0.87	112.8	22.9	-8.65	3.42	0.73
10	0.30	0.87	1.54	117.2	22.4	-8.95	3.29	0.63
11	0.21	0.76	0.11	94.0	24.7	-7.31	3.71	0.92
12	0.23	0.78	0.15	99.8	24.1	-7.73	3.68	0.91
13	0.26	0.79	0.24	102.9	23.8	-7.95	3.63	0.91
14	0.31	0.82	2.95	109.1	23.2	-8.38	3.56	0.91
15	0.33	0.83	4.37	111.2	23.0	-8.52	3.54	0.90
16	0.27	0.75	2.63	118.0	22.8	-9.16	3.36	0.86
17	0.28	0.77	1.64	115.2	22.9	-8.93	3.45	0.88
18	0.28	0.79	0.73	110.5	23.2	-8.54	3.49	0.89
19	0.29	0.84	0.33	99.4	23.9	-7.62	3.69	0.92
20	0.29	0.87	0.21	90.7	24.5	-6.93	3.77	0.93
21	0.29	0.87	5.33	102.7	23.8	-7.92	3.66	0.70
22	0.31	0.84	5.02	107.9	23.3	-8.30	3.58	0.80
23	0.34	0.87	5.98	108.8	23.2	-8.35	3.59	0.69
24	0.36	0.86	5.75	111.6	22.9	-8.54	3.55	0.79
25	0.39	0.89	6.21	112.0	22.9	-8.56	3.55	0.68
Mean	0.29	0.82	2.26	105.47	23.56	-8.13	3.58	0.84
COV	0.14	0.06	0.92	0.08	0.03	0.08	0.04	0.14

3.6.3 Effect of variation in P_{pt} and ρ_d

The two parameters having the largest effect on the lateral strength were P_{pt} and ρ_d since these parameters primarily define the amount of overturning resistance of the rocking column. Cases 1-5 show that increasing P_{pt} increased the lateral strength and decreased the residual drift ratio since λ increased with P_{pt} [Figure 43(a) and Figure 44(a)]. Cases 11-15 show that increasing ρ_d with a constant P_{pt} also increased the lateral strength [Figure 43(c) and Figure 44(c)]; however, the residual drift ratio also increased since λ decreased.

Higher P_{pt} in Cases 1-5 cause more hysteretic recentering as would be expected. The hysteretic loop widened and less recentering occurred as ρ_d increased in Cases 11-15, owing to the greater volume of yielding bars. Case 11, which represented the lowest analyzed value of ρ_d (0.19%) and the highest value of λ (7.06) had negligible residual drift ratio (0.06%) and the most "flag-shaped" hysteretic loop due to the low volume of energy dissipaters. In contrast, Case 15 had a low value of λ (1.19) and the residual drift ratio was larger at 0.65%.

The depth of the neutral axis (c) at the maximum drift ratio increased as P_{pt} and ρ_d increased; see Table 12 and Table 13. As a consequence, the uplift (Δ_{up}) decreased slightly while the compression strain demand at the extreme fiber ($\varepsilon_{c,max}$) increased (assumed to be spread uniformly over a height c).

Cases 21-25 were intended to have $\lambda < 1$ by combining a relatively low P_{pt} with a relatively high ρ_d. The recentering moment provided by the combination of post-tensioning and gravity loads was inadequate, resulting in large residual drift ratios [Figure 43(e) and Figure 44(e)]. Cases 23 and 25, with $\lambda = 0.65$ and 0.52, had the largest residual drift ratios of 2.00% and 2.23%, respectively.

3.6.4 Effect of variation in ρ_{pt} and ρ_b

The parameters ρ_{pt} and ρ_b did not have a large effect on the lateral strength when P_{pt} and ρ_d were held constant. However, ρ_{pt} and ρ_b did affect the inelastic portion of the force-displacement response. Increases in either parameter improved the post-yield column stiffness, especially at large drift ratios [Figure 44(b) and Figure 44(d)].

Table 12 and Table 13 show that the uplift was similar for all analysis cases at a given displacement amplitude ($COV \leq 0.04$); hence, as the area of post-tensioning increased, the change in post-tension force at large displacements increased for equivalent levels of uplift. This larger post-tension force resulted in more load resistance in the inelastic portion of the column response. Furthermore, as ρ_{pt} increased, the initial stress in the post-tensioning decreased proportionally when P_{pt} was held constant, reducing the chance of yielding. Case 6, which had the lowest $\rho_{pt} = 0.22\%$, had a post-tension force equal to 500 kN at 4.2% drift ratio. Case 10, which had the highest $\rho_{pt} = 0.86\%$, had a post-tension force equal to 754 kN at 4.2% drift ratio. Case 6 was the only case in which the strands yielded and also had the most strength degradation with $V_{4.2}/V_{max} = 0.91$. The ratio ρ_{pt} had little effect on the residual displacement since λ was greater than 1.5 for Cases 6-10.

As ρ_b increased (Cases 16-20), the post-yield strength degradation of the column decreased by a small margin. Greater ρ_b values increased the strength of the compression zone resulting greater flexural stiffness, less degradation of HyFRC, a shallower neutral axis depth, and more uplift (Table 13). The residual drift ratio also decreased, especially after the maximum drift ratio of 8.3% [Figure 44(d)]. Cases 19 and 20, which had the highest $\rho_b = 2.31\%$ and 3.08%, respectively, showed pronounced recentering due to the reduction in elastic compression damage.

The parametric study showed that increasing ρ_b or decreasing P_{pt} had opposite effects on the neutral axis depth (c) and column uplift (Δ_{up}). The former effectively decreased c and increased Δ_{up} while the latter increased c and decreased Δ_{up}. Both changes resulted in lower residual drift ratios. Given this outcome, the parametric study verified that the use of headed bars can lead to both minimal residual drift ratios and a reduction in compression damage (i.e. a reduction in c) compared to post-tensioned columns without headed bars.

3.7 PT HyFRC column design parameters

The parametric study was used to optimize the design of the PT HyFRC column to meet the specific performance objectives in Section 3.4.3. The optimized design parameters are provided in Table 11 as Case PT HyFRC. These parameters were the fixed values of the Case parameters considered in the study (P_{pt}, ρ_{pt}, ρ_d, and ρ_b) when a single parameter was varied. Using the chosen design parameters, the column had $\lambda = 1.78$.

The lateral response using these parameters is shown in Figure 45, while the key response parameters from the model are provided in Table 14. The design resulted in a lateral force-displacement response that recentered with practically no residual drift ratio after a maximum imposed drift ratio of 8.3%. The predicted maximum shear strength of the column was $V_{max} = 0.28W$ at a drift ratio of 2.16%. At this drift ratio, the strength of the PT HyFRC column model was 92% of the R/C column model. For larger drift ratios, the strength of the PT HyFRC column degraded as a result of inelastic compression damage. At drift ratios of 4.2% and 8.3%, the predicted strength of the PT HyFRC column was 81% and 71% of the R/C column strength, respectively.

Table 14. Key response parameters for the PT HyFRC column.

Analysis Case	*Peak drift ratio, %*	V_{max}	$V_{4.2}/V_{max}$	$V_{8.3}/V_{max}$	*Residual drift ratio, %*	*c, mm*	Δ_{up}, *mm*	$\varepsilon_{c,max}$	$\varepsilon_{d,max}$	$\varepsilon_{max,pt}/\varepsilon_{y,pt}$
Design-level	4.2	0.28	0.95	-	0.14	94.1	11.6	-3.44	1.87	0.65
MCE-level	8.3	0.28	0.95	0.80	0.50	106.8	23.5	-8.23	3.57	0.91

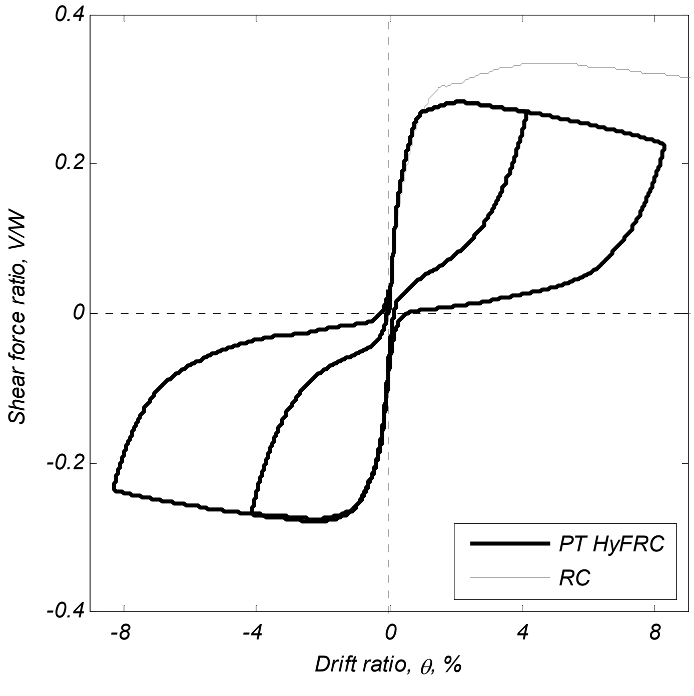

Figure 45. Predicted cyclic force-displacement response of the PT HyFRC column.

Based on the predicted response parameters in Table 14, the PT HyFRC test column satisfied the specific performance objectives listed in Section 3.4.3. The predicted residual drift ratio was 0.5% after sustaining maximum drift ratio of 8.3%, and the strands were only expected to reach 91% of their yield strain. In addition, the maximum predicted strain in the unbonded bars was $\varepsilon_{d,max} = 3.6\%$ and the depth of the compression zone was $c = 0.26D$, slightly higher than the targeted value of 0.25D. The model predicted that at the peak drift ratios of 4.2% and 8.3%, rotation at the column base would account for 89% and 94% of the total drift ratio (with rotation calculated as = $\frac{\Delta_{up}}{D-c}$).

3.8 Summary

In this chapter, an innovative post-tensioned HyFRC rocking column was designed and modeled to achieve specific performance criteria under design and MCE-level earthquake demands. The design-level drift ratio was chosen to correspond to the drift ratio in the prototype R/C bridge column at the maximum allowable Caltrans SDC displacement ductility demand (μ_D = 4). The MCE-level demand was chosen as two times the design demand. Performance criteria set for the column included limiting residual drift ratios to 0.5%, preventing yielding of the post-tensioning, limiting unbonded bar strains to 5.0%, and limiting the depth of the compression zone to 0.25D.

An analytical model was built in OpenSEES to evaluate the column performance while varying design parameters. The model utilized nonlinear material constitutive laws for steel and HyFRC, the latter being based on confinement results presented in Chapter 2. The rocking plane was modeled using a rigid column base supported by a distributed bed of compression-only springs. Unbonded post-tensioning and longitudinal bars were modeled using truss elements rigidly connected to the column centroid.

A set of parametric analyses were conducted were a single design variables (P_{pt}, $\rho_{pt,}$ $\rho_{d,}$ or ρ_b) was incrementally increased while holding the others fixed. The following is a summary of key findings of the parametric analyses:

- The column lateral strength was directly proportional to the parameters P_{pt} and ρ_d.

- Increasing P_{pt} reduced residual displacements, while increasing ρ_d increased residual displacements.

- Increasing P_{pt} and/or ρ_d increased the depth of the neutral axis which reduced uplift and increased compression strain demands.

- Varying ρ_{pt} and/or ρ_b had no influence on lateral strength.

- Increasing ρ_{pt} and/or ρ_b improved the post-yield column stiffness, especially at large drift ratios.

- Increasing ρ_b decreased the depth of the neutral axis and increased the uplift, resulting in lower compression strain demands.

The chosen PT HyFRC column design parameters resulted in the following anticipated performance:

- The maximum column shear strength was 0.28*W*. The strengths at drift ratios of 4.2% and 8.3% were 0.95*W* and 0.80*W*, respectively.

- The residual drift ratio would be 0.5% after unloading from a peak drift ratio of 8.3%.

- At a drift ratio of 8.3%: (1) the uplift was 0.06*D*, (2) the maximum compression strain demand was -8.2%, (3) the maximum strain in the unbonded bars was 3.6%, and (4) the maximum post-tensioning stress was 91% yield.

- The chosen reinforcement ratios were reasonable for practical implementation and did not congest the column cross section. Four post-tensioned strands, five unbonded rebars, and 10 headed rebars (all rebar the same size) resulted in the reinforcement ratios given in Table 11 for PT HyFRC.

4 Shake Table Test Response of a Low Damage Post Tensioned HyFRC Bridge Column

4.1 Introduction

Two 1/3 scale columns representing the prototype R/C bridge column (see Figure 36) were tested on a shaking table using historical ground motion records. Specimen PT HyFRC represented the proposed rocking/recentering column designed and modeled in Chapter 3. A reference R/C specimen having the conventional reinforcement details of the prototype column was tested for comparison. The PT HyFRC column was subjected to eleven earthquake ground motions. The reference column was subjected to seven ground motions before a substantial permanent residual displacement developed and testing was stopped.

This chapter presents experimental results of the shake table tests. Details of the experiment are explained first, followed by a comparison of test results for the two columns. The predictions of the analytical model developed in Chapter 3 are compared to the experimental results. OpenSEES was used to perform nonlinear time history analysis of the analytical model using the ground motions recorded during testing.

Test results will show that the PT HyFRC column successfully eliminated residual displacements (< 0.5%) under MCE-level ground motions. The other performance criteria defined in Chapter 3 were also satisfied. Damage was less severe in the PT HyFRC column than the reference column. Furthermore, the analytical model accurately predicted the dynamic response even after column damage had developed.

4.2 Description of test columns

The two test columns are shown in Figure 46. The diameter of the columns was $D = 406$ mm and height of the center of the inertial mass (from the top of footing) was $H = 2438$ mm. These dimensions corresponded to a shear span ratio $M/VD = 6$ considering the cantilevered, single-column bridge bent prototype. Figure 46(a) shows the column's vertical cross section. Figure 46(b) shows the horizontal cross sections at the column base (Section *A-A*) and also near mid-height (Section *B-B*) as well as a cross section of the reference column. The dimensions of the column, footing, and load stub were the same for both specimens.

The PT HyFRC column design parameters were optimized in Chapter 3. It was precast with HyFRC to a height of *D* above the footing [shown hatched in Figure 46(a)]. The design 28-day compressive strength of the HyFRC was f_c' = 48 MPa (6.2 ksi). The column contained a total of fifteen longitudinal reinforcing bars (ASTM A706 Gr. 420) with a 16-mm-diameter (No. 5). Five bars were unbonded over a length of 1.25*D* (508 mm) at the column base using tightly wrapped duct tape coated with lithium grease. These bars provided internal energy dissipation at ρ_d = 0.77%. The unbonding extended 51 mm into the footing to prevent concrete at the top of the footing from failing in tension.

The remaining ten bars had 51x51x13 mm steel plate heads and were precast in the HyFRC column base with no bond modification. These bars only resisted compression at ρ_b = 1.54% and did not extend into the footing. Ten identical bars with matching heads were cast in the footing in the same pattern to absorb the compression from the bars above.

Post-tensioning consisted of four seven wire steel strands (ASTM A416 Gr. 1860) with a 15-mm-diameter (0.6 in) for a reinforcing ratio of ρ_{pt} = 0.43%. The strands were passed through a 76-mm-diameter corrugated metal duct in the center of the column. They were unbonded between their anchorages over a length of 1.42*H* (3467 mm). A steel pipe was used to extend the unbonded length of the strands beyond the load stub. This extension allowed the strands to remain elastic at a drift ratio of 8.3% according to the analytical model. A hollow core pressure jack was placed above the steel pipe to measure the strand force and adjust it (if necessary) prior to testing. The strands were anchored by tapered conical wedge grips seated in a wedge plate.

The fixed base reference column was also modeled in Chapter 3 and was designed according to CalTrans Seismic Design Criteria (Schoettler et al. 2013). The longitudinal steel consisted of 16 bars (ASTM A706 Grade 420) with a 13-mm-diameter (No. 4) for ρ_l = 1.6% [see Figure 46(b)]. The design 28-day design compressive strength of concrete was f_c' = 28 MPa (4 ksi).

The transverse spiral reinforcement in the two columns was identical. Size W4 steel spiral (ASTM A82) with a 5.7-mm-diamter was spaced at 32 mm for a ratio of ρ_t = 0.85%. The spiral continued into the load stub and footing for the reference column. For the PT HyFRC column, the spiral was discontinuous at the top of the footing to allow uplift during rocking. Others have suggested that for post-tensioned columns, the spiral spacing should be one half of the value used here (Sakai and Mahin 2004) to provide higher confinement.

The reinforcement details of the footing and load stub for the two columns are included in Appendix Figure A. 1 to Figure A. 6. They were over-reinforced to remain elastic during testing so that the column response would be isolated.

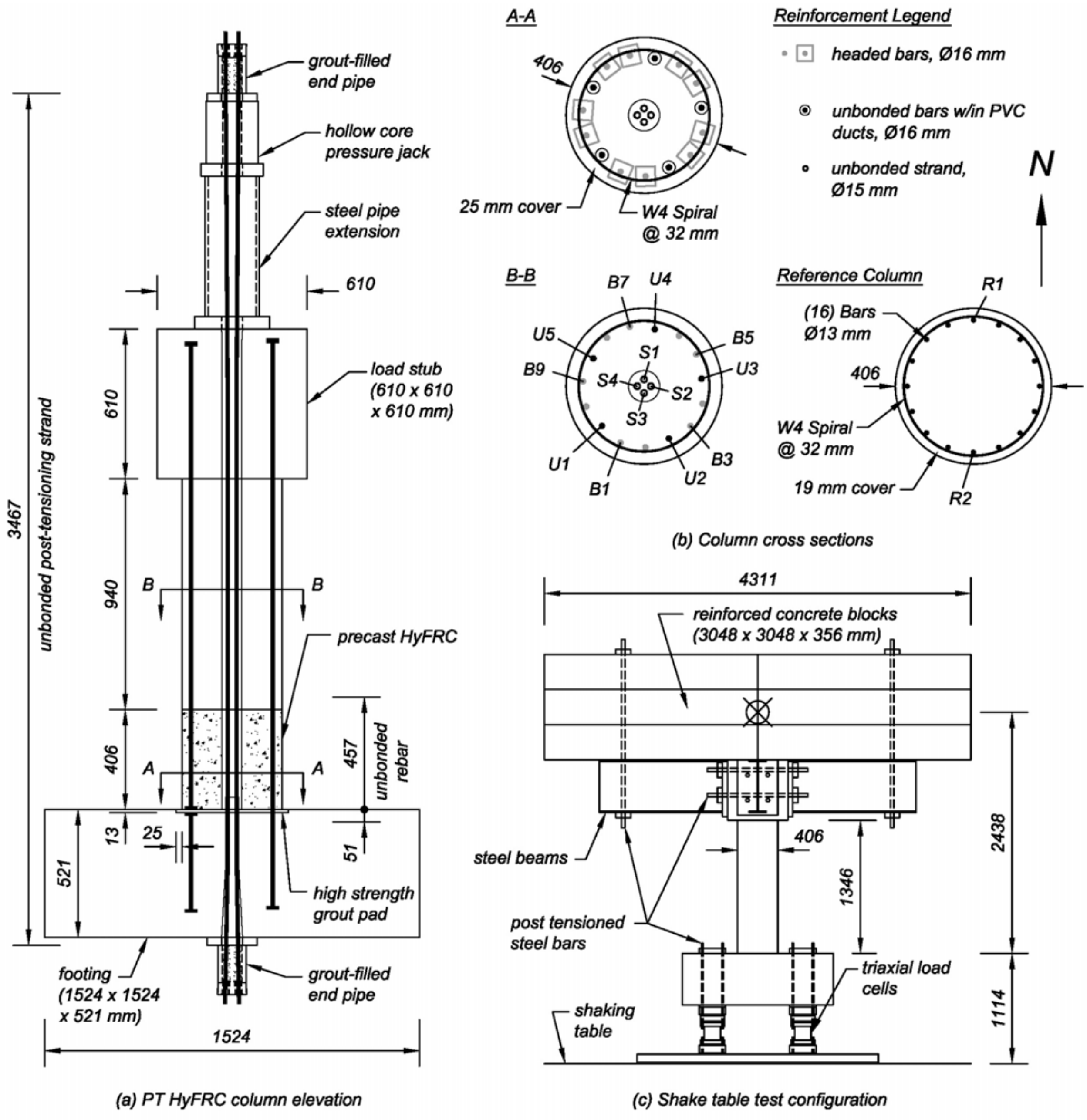

(a) PT HyFRC column elevation

(b) Column cross sections

(c) Shake table test configuration

Figure 46. Schematic of test columns; (a) PT HyFRC column elevation, (b) column cross sections, and (c) shake table test configuration.

4.2.1 Column construction

Construction of the PT HyFRC column consisted of five stages. The precast portion was formed and cast first. Spiral reinforcement was tied to 25 mm dia. PVC ducts and the headed longitudinal bars as shown in Figure 47. A section of 76-mm-diameter corrugated metal duct was placed in the center for the post-tensioning. HyFRC was mixed in the Concrete Laboratory at UC Berkeley and cast around the reinforcement cage. The HyFRC was allowed to cure for 38 days before it was installed.

The second stage consisted of forming and casting the column footing as shown in Figure 48. The unbonded and headed rebar were constructed in the footing to match the PVC ducts and headed rebar in the precast portion. Spiral reinforcement was wrapped and tied around the bars. A piece of 51-mm-diameter corrugated metal duct for the post tensioning was embedded. Concrete was cast flush with the circular piece of plywood shown in Figure 48. Removal of the plywood left a 13 mm deep by 457 mm diameter recession in the top of the footing. The headed bars were then flush to the top of the recession. The piece of corrugated duct extended 51 mm above the top of the footing.

In the third stage of construction the precast HyFRC portion of the column was installed. Figure 49 shows the precast block as it was lowered. The unbonded bars were passed through the embedded ducts. FiveStar® High Strength Precision Non-Shrink Grout mix was combined with 0.17 parts water (by weight) and was poured into the footing recession. The block was seated on 10 mm shims while the grout cured around it. Additional grout was poured into the void space in the PVC ducts to provide buckling resistance to the unbonded bars. Lastly, the spiral was continued from the precast portion upwards and tied to all 15 longitudinal bars.

The remainder of the column and the load stub were formed and case in the fourth stage of construction. Figure 50 shows a top view of the load stub where some of the longitudinal bars were diverted around the load stub reinforcement. These portions portion were cast monolithically with normal concrete. The spiral was continuous over the cold joint between the precast HyFRC and the upper portion of the column.

The last stage was to draw and stress the post-tensioned strands. The strands were drawn through the embedded ducts and were anchored using wedge plates. Wedges were seated in end plates set in specially-fabricated steel pipe sections shown in Figure 51. The four strands were individually stressed six days prior to testing. The end pipes were filled with 10 strand diameters (152 mm) of grout. Grouting eliminated stress concentrations at the wedge anchors that might lead to premature strand failure. The strand force increased from its initial value during rocking and was transferred to the grout through bond then to the pipe via weld beads on the inside surface.

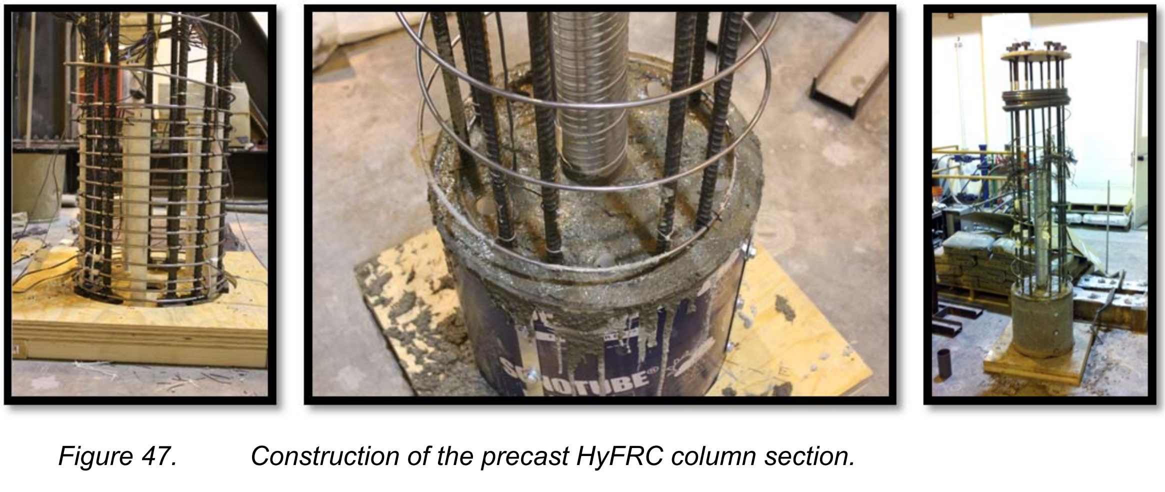

Figure 47. Construction of the precast HyFRC column section.

Figure 48.	*Construction of the footing.*

Figure 49.	*Installation of the precast HyFRC end portion.*

Figure 50. Construction of the upper portion of the column and the load stub.

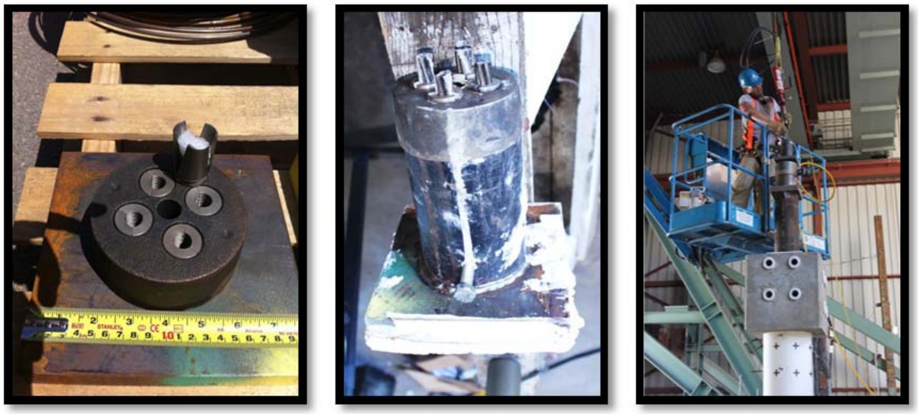

Figure 51. Strand anchorage and stressing.

The reference column was cast in two stages. The footing for the reference column was formed with the longitudinal bars and spiral and was cast first. The column and load stub were then cast monolithically. Hence, there was a cold joint at the top of the footing. In both columns, concrete and HyFRC surfaces were roughened at cold joints to improve the bond between separate castings.

4.2.2 Measurements taken during strand stressing

Several measurements were taken during strand stressing. Strain gages were used to record individual strand strains. The gages were located on opposite sides of each strand at mid-height of the column. The strain measurements are shown in Figure 52(a). As each strand (designated N, S, E, W) was stressed, the strain in the two gages (designated 51 or 52) increases. The strains relaxed as the wedge seated after each strand was released. The strain loss due to seating was approximately 2500 $\mu\varepsilon$, corresponding to a displacement of approximately 8.5 mm. The total force from all strands [Figure 52(b)] was measured by the pressure jack in series with the strands. The total force first increased as each strand was stressed then decreased as the wedge was seated, similar to the measured strains.

The main objective during stressing was to ensure that the strain (or load) in each strand was approximately equal. Large deviations in strain between strands could cause premature yielding or fracture during testing. After stressing was complete, measured strains were between 2500 and 3000 με and this small deviation was considered acceptable.

The total load provided by the four strands after stressing was 381 kN, 14% lower than the target load of P_{pt} = 445 kN. In addition, there was some loss of post-tension force between stressing and testing due to creep within the column. Consequently, the hydraulic jack was used to increase the load to the target value prior to testing under the assumption that the force (or strain) applied by the jack would be equally distributed among the four strands. After the target load was achieved, the jack was locked off. A pressure transducer was used to continuously monitor the load in the jack during testing.

(a) Strains in the strands during stressing

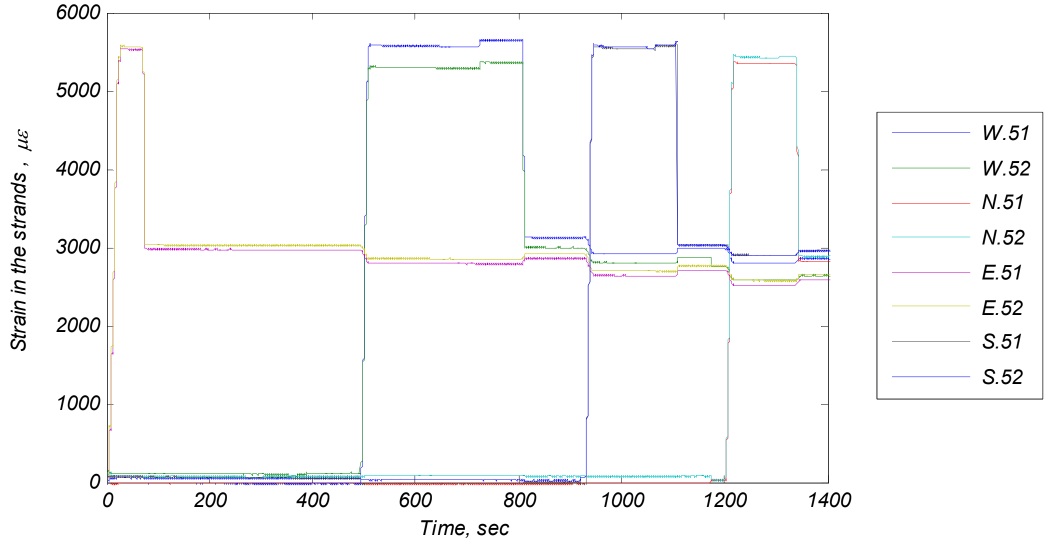

(b) Load measured by the hydraulic jack during stressing

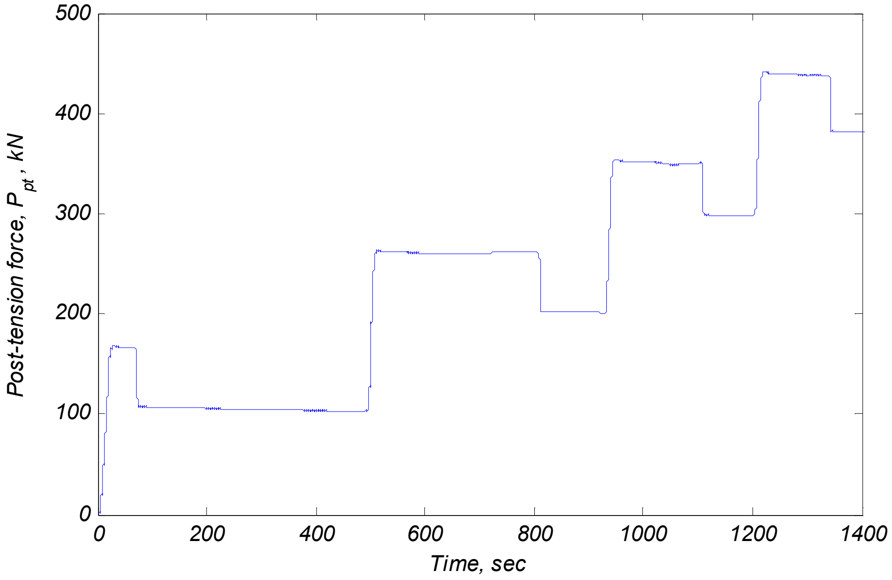

Figure 52. *Measurements taken during stressing; (a) strains in the strands, (b) load measured by the hydraulic jack.*

4.2.3 Material properties

The proportions of the HyFRC mix are given in Table 15. The HyFRC material contained hooked-end steel fibers at a volumetric ratio of 0.013 which had the properties of fiber S2 (Table 3) described in Chapter 2. It also contained polyvinyl alcohol (PVA) fibers at a volumetric ratio of 0.002 (fiber PVA1, Table 3). The ratios of fibers in the HyFRC were the same as were used in prior column tests (Kumar et. al. 2011). Compared to those tests, the water to binder ratio was reduced to 0.40 to target a higher compressive strength of 43 MPa. The same chemical admixtures (superplasticizer and viscosity modifying admixture) were used to improve the workability of the fresh mix. Due to the reduction in water content, some of the self-consolidating properties were lost.

The compressive strengths of the HyFRC and the normal weight concrete used in the columns and the footings are summarized in Table 16. Samples with a diameter of 152 mm and a height of 305 mm were crushed four days prior to the column test. The strength of the grout pad was obtained from 51 mm cubes. The 28-day strength is also provided in Table 16 for the concrete and HyFRC used in the columns.

The compressive stress-strain response of the HyFRC in the column is shown in Figure 53(a) up to the peak stress based on cylinder tests. Beam samples of the HyFRC (152x152x610 mm) were also tested in flexure. The flexural performance of the material did not contribute to the performance of the column since the longitudinal bars were unbonded. Regardless, Figure 53(b) shows that the HyFRC beams exhibited the characteristic deflection hardening behavior that would be expected for HPFRCC's.

The yield and ultimate stresses (f_y, f_{su}) and strains (ε_y, ε_{su}) for the spirals, rebar, and strands used in the columns are summarized in Table 17. The tensile stress-strain responses of coupon samples of the strand, the spiral, and the reinforcing bars are given in Figure 54. The spiral coupons were taken from the actual spiral after it was fabricated. The induced plastic deformation as part of the straightening used before testing the coupons may have caused the coupons to fracture at a lower tensile strain than expected.

Table 15. Mix proportions for the column HyFRC (SSD condition)

kg per cubic meter				*fiber volume %*	
Water	*Cement*[a]	*Fly Ash*[b]	*Gravel*[c]	*Steel*	*PVA*
219	413	136	418	1.3	0.2
Sand[d]	*SP*	*VMA*			
1044	2.3	5.6			
[a]ASTM C150 Type II; [b]ASTM C618 Type C; [c]pea gravel, 9.5 mm MSA; [d]coarse sand, FM = 3.2					

Table 16. Compressive strength of column materials.

	Sampled f_c', MPa (age)			
Specimen	*Column*	*Found.*	*HyFRC*	*Grout*
PT HyFRC	33.5 (29 days) 34.5[a] (52 days)	55.5[a] (66 days)	34.8 (28 days) 44.6[a] (101 days)	63.8[a] (64 days)
Reference	18.3 (27 days) 22.6[b,c] (139 days)	34.7[b] (143 days)	-	-
[a] *four days prior to testing;* [b]*on day of testing;* [c]*18% lower than design f_c' = 27.6 MPa*				

Table 17. *Tensile properties of reinforcing bars used in columns.*

Specimen	*Material*	f_y *, MPa*	ε_y *, %*	f_{su} *, MPa*	ε_{su} *, %*
PT HyFRC	W4 spiral	435^a	0.44	651	1.1
	D16 rebar	481^b	0.25	658	11.1
	D15 strand	1769^c	1.0	1874	2.5
Reference	W4 spiral	435^a	0.44	651	1.1
	D13 rebar	545^a	0.52	647	11.7

[a] 0.2% offset method; [b] onset of yield plateau; [c] stress at 1% elongation per ASTM A416

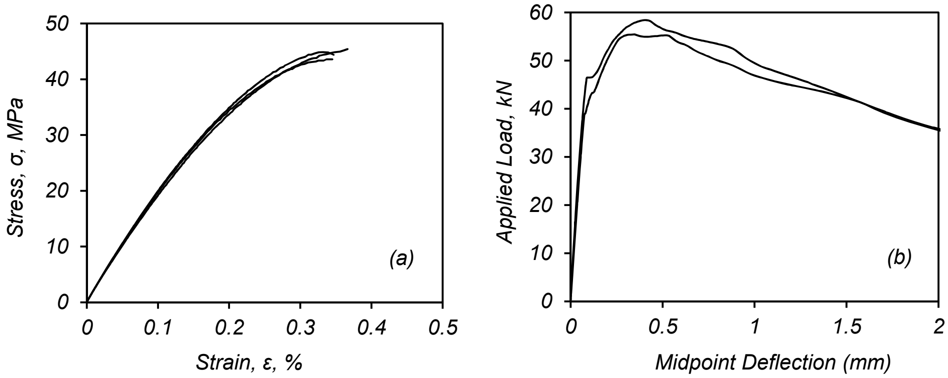

Figure 53. *Performance of HyFRC; (a) compression stress strain response and (b) flexural response.*

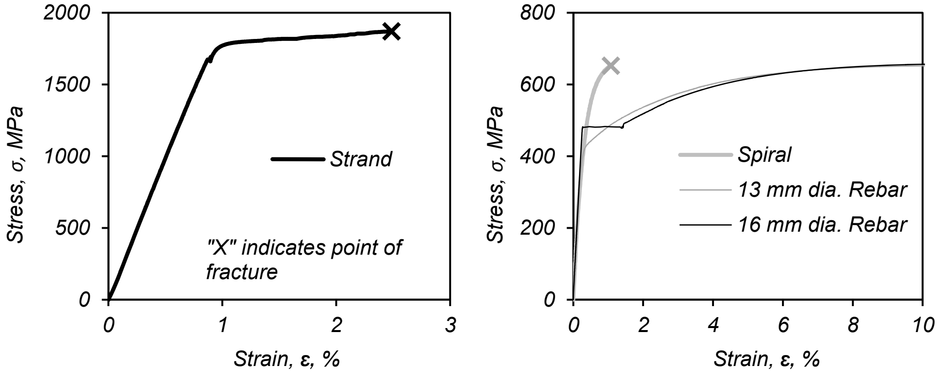

Figure 54. *Tensile stress strain response of steel strand, spiral, and reinforcing bars.*

4.2.4 Test configuration

The test configuration for both the PT HyFRC column and the reference column is shown in Figure 46(c). Three 3048 x 3048 x 356 mm reinforced concrete plates were used for inertial mass. Wide flanged steel cantilevered beams supported the plates and were fixed to the column load stub. The mass plates were fixed to the wide flange steel beams using post-tensioned bars.

The total mass of the test configuration was 23,700 kg (a gravity load $W = 232.5$ kN), and the total rotational mass moment of inertia (of the mass plates, beams, and load stub combined) was 20.5 kN-m-s^2 (Schoettler et al. 2013). The total axial force ratio ($\alpha_t = P_t/f_c'A_g$) varied for the two columns because of differences in concrete strength and the additional post-tensioning force in the PT HyFRC column. The reference column had a ratio $\alpha_t = 8.2\%$, while PT HyFRC column had α_t of 15.4%.

Figure 55(a) shows the RC mass plates being installed on the steel beams. Figure 55(b) shows the column in the final test configuration prior to the start of testing. Lifting slings were attached to the steel beams then to the shake table to prevent overturning of the column in the event of collapse.

Figure 55. Photos during test preparation; (a) installation of the RC mass plates, (b) final test configuration prior to testing.

Instrumentation for specimen PT HyFRC consisted of five load cells, 28 displacement transducers, and 38 internal strain gages. Four load cells, 32 displacement transducers, and 54 internal strain gages were used for the reference column. Thirty-five accelerometers and 21 wire potentiometers were common to both tests. All instruments sampled at 200 Hz. Recorded signals were processed using a high-order low-pass filter with a cutoff frequency of 25 Hz. Accelerometer signals were also high-pass filtered with a cutoff frequency of 0.25 Hz.

Each footing was supported by four triaxial load cells that measured horizontal force in two directions and vertical force [see Figure 46(c)]. The hollow core pressure jack of the PT HyFRC was used as a fifth load cell to measure the strand force during testing.

The accelerometers were fixed to the footing, column, and mass plates in both the horizontal and vertical directions at multiple locations. They were screwed to aluminum cubes which were then fixed to the specimen using epoxy adhesive. Each 51 mm cube had one accelerometer oriented vertically and one oriented horizontally. The locations of accelerometers on the mass blocks for the PT HyFRC column are shown in Appendix Figure A. 7. The locations of accelerometers on the PT HyFRC column and footing are shown in Appendix Figure A. 8.

Displacement transducers were fixed between threaded rods extending from the face of each column. The transducers measured the biaxial curvature profile, bar slip, and column uplift during testing. The rods were threaded into embedded coupling nuts. A hex bolt was screwed into the embedded end of the coupler for anchorage (Appendix Figure A. 9). The locations of displacement transducers in the PT HyFRC column are shown in Appendix Figure A. 10.

The steel rebar, spirals, and strands of each column were instrumented with strain gages. The locations of strain gages are provided in Appendix Table A. 2, which includes the height of each gage with respect to the footing. Locations of the spiral gages are shown in Appendix Figure A. 10. The name designations of the headed bars, unbonded bars, and strands are shown in Figure 46(b).

Finally, wire potentiometers tracked the 3-D displacement of seven targets on the specimen—three on the footing and four on the mass plates. These displacements were used to resolve three translations and three rotations at the center of mass using the procedure in Vithani and Gupta (2002). The locations of the wire potentiometer targets on the mass blocks and footing are shown in Figure A. 7 and Figure A. 8, respectively.

4.3 Ground motion test sequence

A common test sequence of nine scaled earthquake ground motion records, each with three directional components, was intended to be applied to both columns. The sequence started with a record expected to induce elastic response in the reference column ($\mu_D < 1$), followed by two tests at half the design level ($\mu_D = 2$), two tests at the design level ($\mu_D = 4$), one test at 1.5 times the design level ($\mu_D = 6$), one test at the MCE level ($\mu_D = 8$), one test at 2.5 times the design level ($\mu_D = 10$), and finally a repeat of one of the design level tests.

Testing of the reference column was stopped after the seventh test (MCE-level) due to the extreme residual drift ratio. The PT HyFRC column was subjected to 11 tests (two more than planned) since damage and residual drift ratios were minor after the original nine tests. The tenth test (GM10) was identical to GM8 although the polarity was reversed, while the eleventh test (GM11) was the same motion as GM6 but scaled 30% larger.

Table 18 gives details of all ground motion records including the amplitude scale factors. It also gives the peak drift ratios and μ_D targeted for the reference column. Although the horizontal components of each motion were identical for the two columns, the polarity of the vertical component was unintentionally reversed for the reference column. The axial responses of the columns may have been different as a result.

Table 18. Details of ground motion tests.

Test	Earthquake[a] *Station*	Acceleration amplitude scale factor	Target μ_D (ref. col.)	Target drift ratio (ref. col.)
GM1	Coalinga 1983/05/09 02:49 *46T07 Harris Ranch - Hdqtrs*	2.50	< 1	< 1%
GM2	Imperial Valley - 06 1979 *EC Meloland Overpass FF*	0.80	2	2.1%
GM3	Morgan Hill, 1984 *Coyote Lake Dam (SW Abut)*	0.70	2	2.1%
GM4[b]	Northridge - 01 1994 *Rinaldi Receiving Station*	0.56	4	4.2%
GM5[b]	Northridge - 01 1994 *Sylmar - Olive View Med FF*	-0.80	4	4.2%
GM6	Northridge - 01 1994 *Rinaldi Receiving Station*	0.90	6	6.3%
GM7[c]	Kobe, Japan, 1995 *Takatori*	0.77	8	8.3%
GM8	Kobe, Japan, 1995 *Takatori*	-0.90	9.6	10.0%
GM9	Northridge - 01 1994 *Sylmar - Olive View Med FF*	-0.80	4	4.2%
GM10	Kobe, Japan, 1995 *Takatori*	0.90	9.6	10.0%
GM11	Northridge - 01 1994 *Rinaldi Receiving Station*	1.17	-	-

[a] *from PEER Ground Motion Database (2000, 2012)*
[b] *design-level test;* [c] *MCE-level test*

Priority in ground motion selection was given to records that satisfied the following criteria:

1. They caused similar displacements when run through the analytical model of each column over the fundamental period range 0.4 to 0.7 seconds.
2. They contained near-fault velocity pulses likely to cause large column drift ratios.
3. They were generated by strike-slip fault mechanisms.

The time step of each record was multiplied by a factor of $1/\sqrt{3}$ to maintain a scale factor of unity for induced accelerations (the length scale factor, L, was 3). Each directional component for a given record was scaled by the factor given in Table 18.

The displacement ductility demand was predicted using nonlinear time history analysis of the OpenSEES model for the reference column, with the ground motion records run sequentially. The 1% damped elastic acceleration and displacement response spectra for the N-S, W-E, and vertical directional components of each ground motion are given in Figure 56(a) to (c). Tests consisting of the same ground motion record but different acceleration amplitude scale factors (e.g. GM4, GM6, and GM11) resulted in spectra with the same general shape as would be expected.

(a) N-S component

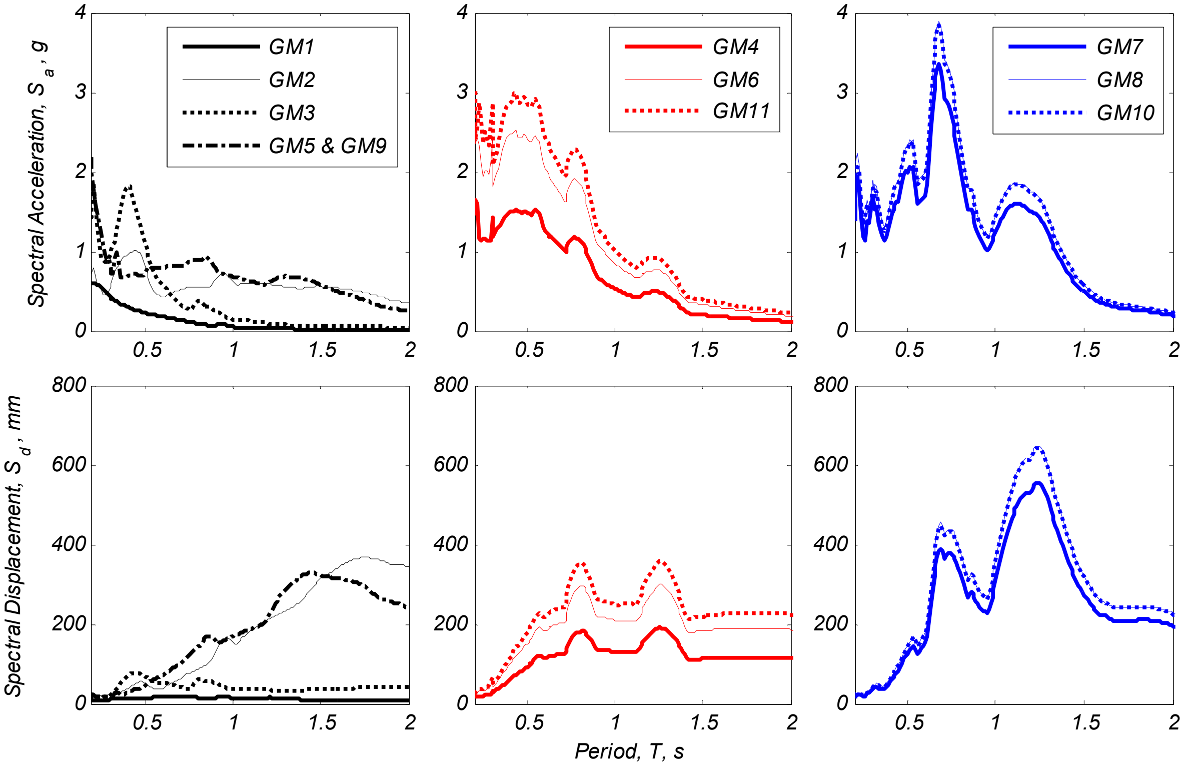

(b) W-E component

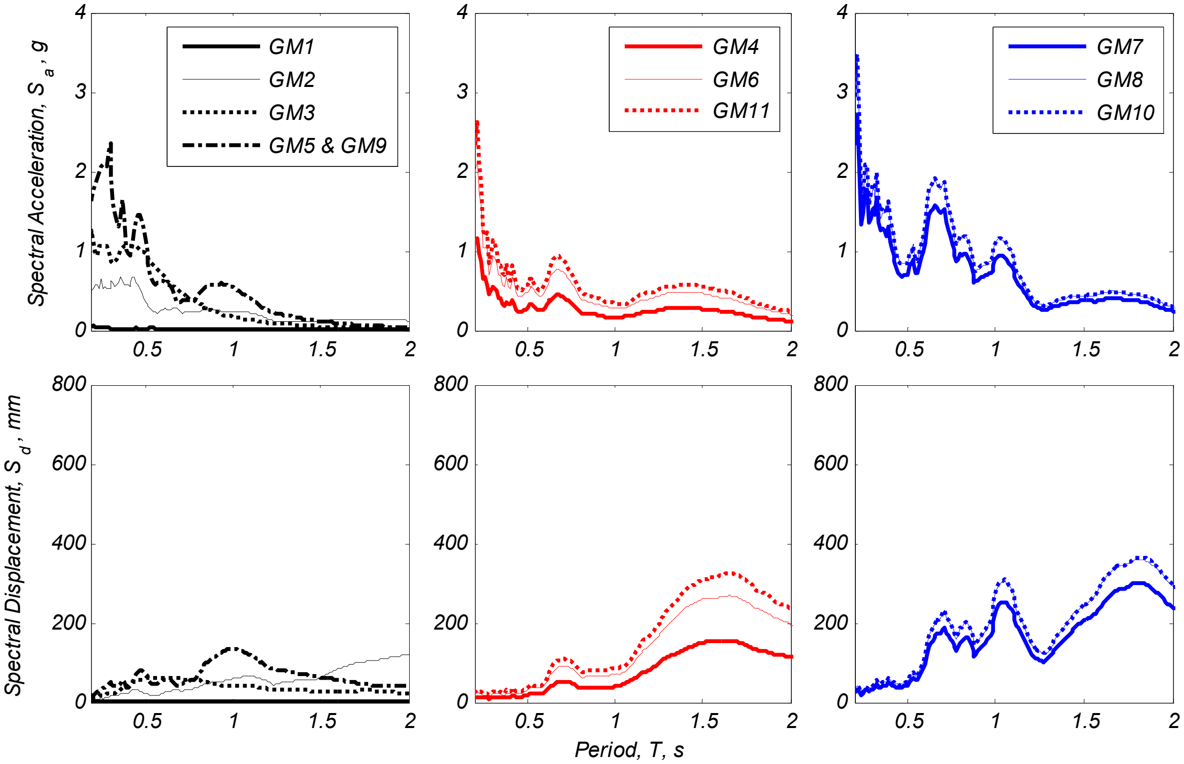

Figure 56. Elastic response spectra for imposed ground motions with $\zeta = 1\%$; (a) N-S component, (b) W-E component, and (c) vertical component.

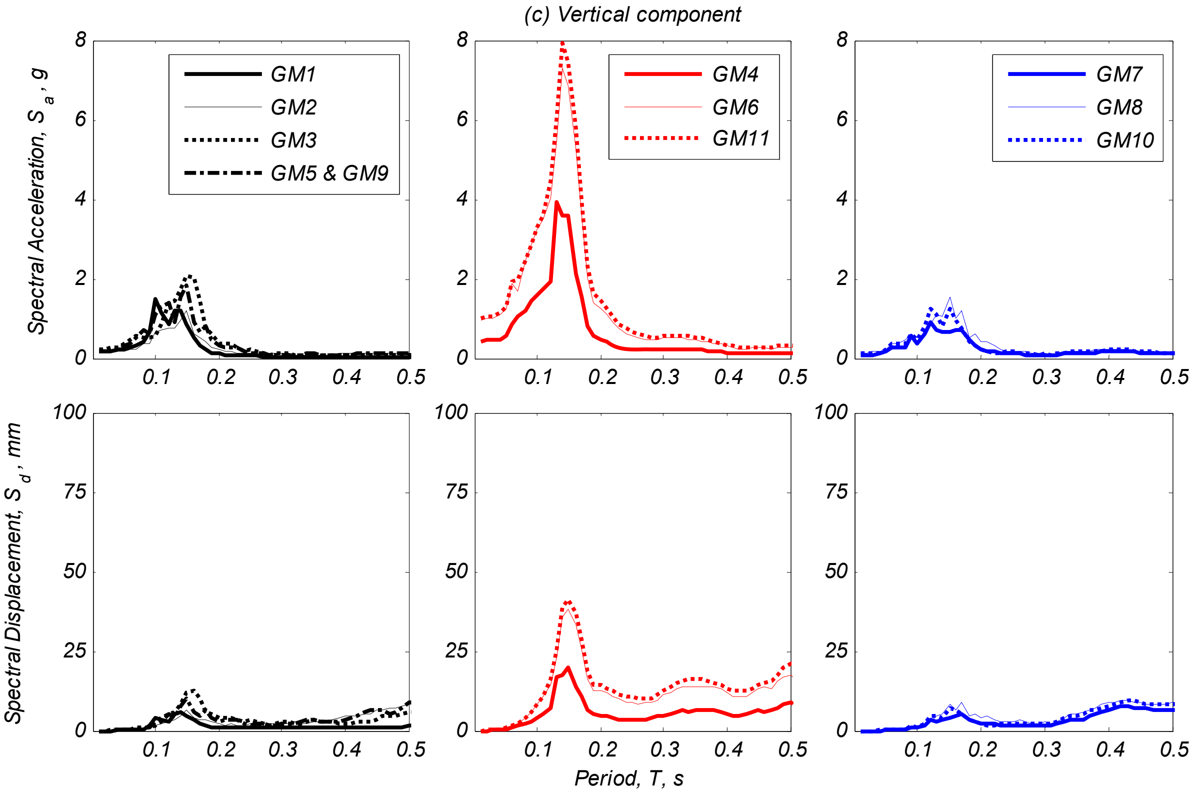

Figure 56. *Elastic response spectra for imposed ground motions with ζ = 1%, (a) N-S component, (b) W-E component, and (c) vertical component (cont.).*

4.4 Free vibration test results

A free vibration test was used to determine the fundamental period and damping ratio of each column. The test was conducted by applying a small static lateral load to the column, then quickly releasing it while recording the column displacement. The free vibration response of the two columns is shown in Figure 57, where the ordinate is the column displacement normalized by the initial displacement, u/u_0.

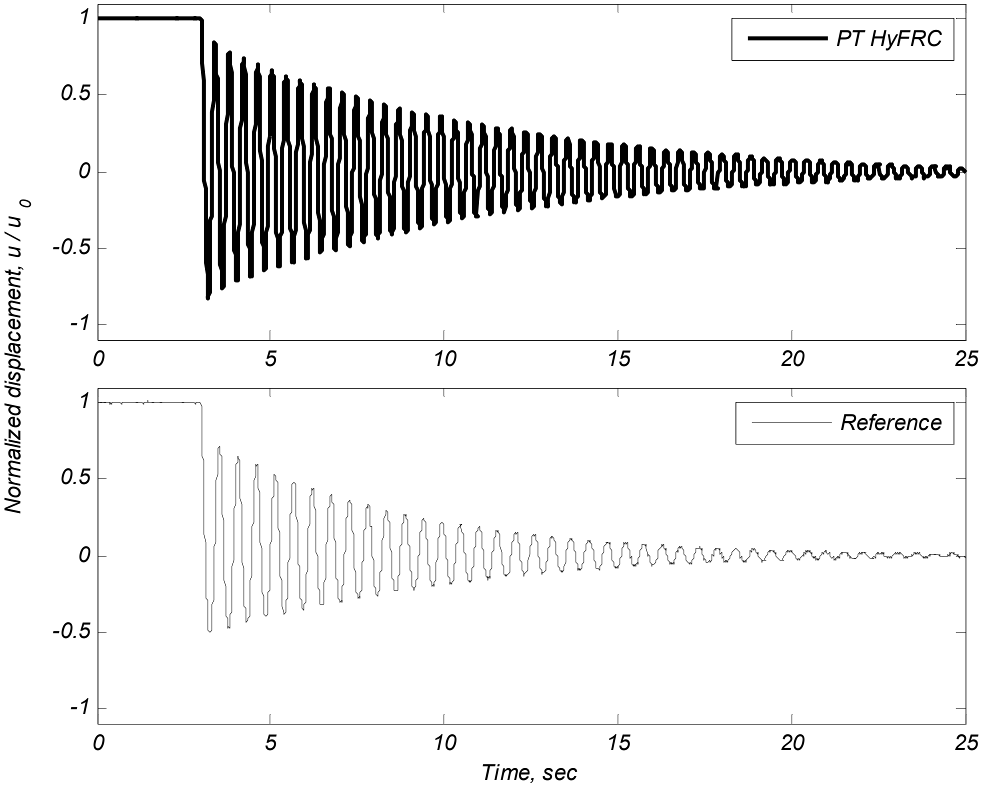

Figure 57. Free vibration response of the two columns.

The first mode fundamental period (T_1) was estimated using Fourier analysis of the free vibration response in the frequency domain. The damping ratio (ζ) was calculated using [4.1] from Chopra (2006),

$$\zeta = \frac{1}{2\pi j} ln\left(\frac{u_i}{u_{i+j}}\right) \qquad [4.1]$$

where u_i and u_{i+j} are the displacement amplitudes at cycle i and cycle $i+j$, respectively. The PT HyFRC column had a fundamental period of $T_1 = 0.40$ seconds and a damping ratio of $\zeta = 0.9\%$, while the reference column's fundamental period was $T_1 = 0.53$ seconds and the damping ratio was $\zeta = 1.3\%$.

4.5 Shake table test results

The PT HyFRC column effectively limited residual displacements for all tests, including the MCE-level earthquake (GM7). The column reached a drift ratio of 8.0% during that test, but the residual drift ratio was only 0.4%. The maximum measured strain in the unbonded bars was 3.4% and no fractures occurred. The force in the post-tensioned strands during testing remained well below the yield force. Spalling was prevented by the HyFRC through the duration of testing. During the eleventh test, two of the unbonded bars fractured.

The reference column behaved in a ductile manner during the design-level tests (GM4 and GM5) by forming a plastic hinge with distributed flexural cracking. Some spalling was observed. The residual drift ratio was 0.9% after reaching a peak drift ratio of 5.8% during GM5. During the MCE-level test (GM7), the peak drift ratio was 10.8% and the residual drift ratio increased to 6.8% making it unsafe to continue testing. Spalling was substantial on the north side of the column but no bars fractured.

4.5.1 Global displacement response

The peak and residual drift ratios measured during testing are provided in Table 19. The SRSS value represents the maximum resultant of the N-S and W-E vector components. Drift ratio was calculated as the ratio of the horizontal displacement of the center of mass in direction *i* to the height of the center of mass, *H*. All displacement measurements were taken relative to the footing and the datum was the position of the mass prior at the start of the first test. Residual drift ratios presented in Table 19 are the drift ratio of the column at the end of the test. Figure 58 compares the peak and residual drift ratios (SRSS) of the two columns for GM1 to GM7.

Table 19. Measured peak and residual column drift ratios.

	PT-HyFRC Column							Reference Column						
	Peak drift ratio, %			*Residual drift ratio, %*			*Peak drift ratio, %*			μ_D	*target* μ_D	*Residual drift ratio, %*		
Test	*N-S*	*W-E*	***SRSS***	*N-S*	*W-E*	***SRSS***	*N-S*	*W-E*	***SRSS***			*N-S*	*W-E*	***SRSS***
GM1	0.46	0.05	**0.46**	0.02	0.00	**0.02**	-0.40	-0.40	**0.44**	0.42	< 1	0.00	0.00	**0.00**
GM2	2.05	-1.05	**2.11**	0.05	-0.03	**0.06**	3.48	-1.22	**3.49**	3.35	2	0.36	-0.08	**0.37**
GM3	1.74	-2.08	**2.08**	0.06	-0.04	**0.08**	1.51	-0.44	**1.51**	1.45	2	0.38	-0.08	**0.39**
GM4	-4.26	-1.70	**4.32**	0.02	-0.05	**0.05**	-3.63	-1.69	**3.65**	3.50	4	-0.29	-0.05	**0.29**
GM5	5.89	-2.02	**6.22**	0.08	-0.06	**0.10**	5.55	2.22	**5.75**	5.52	4	0.88	-0.02	**0.88**
GM6	-4.91	-2.96	**5.03**	0.17	-0.14	**0.22**	6.06	-3.27	**6.10**	5.85	6	1.56	-0.39	**1.61**
GM7	7.83	-3.14	**7.96**	0.35	-0.17	**0.39**	10.74	3.19	**10.75**	10.32	8	6.74	0.56	**6.76**
GM8	6.61	-5.15	**6.77**	0.24	-0.33	**0.41**	-	-	-			-	-	-
GM9	7.10	-2.81	**7.18**	0.51	-0.31	**0.59**	-	-	-			-	-	-
GM10	6.93	-5.91	**7.20**	0.39	-0.51	**0.64**	-	-	-			-	-	-
GM11	8.01	-7.09	**8.84**	0.59	-0.68	**0.90**	-	-	-			-	-	-
	**N, W directions are positive* ***SRSS refers to the resultant of the N-S and W-E directional components*													

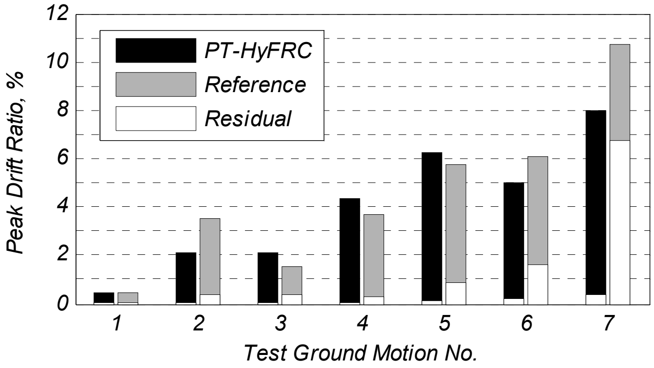

Figure 58. Comparison of peak and residual drift ratios (SRSS).

The residual drift ratio of the PT HyFRC column was under 0.5% for all tests up to and including GM7. The column reached peak drift ratios (SRSS) of 4.3%, 6.2%, 5.0%, and 8.0% during GM4, GM5, GM6, and GM7, respectively. The column sustained peak drift ratios over 6.5% in all tests beyond GM7, but the cumulative residual drift ratio was only 0.9% at the end of testing. The final position of the PT HyFRC column at the end of testing is shown in Figure 59(a).

The reference column began developing appreciable residual drift ratios after test GM5. During that test, the peak drift ratio was 5.8%. The residual drift ratio increased from 0.3% before the test to 0.9% after the test. The peak drift ratio was 6.1% during GM6 and the residual drift ratio nearly doubled to 1.6%. During GM7, the peak drift ratio was 10.8% and the residual drift ratio increased by a factor of four to 6.8%. Ratcheting of the plastic hinge occurred as the residual drift ratio increased in the N direction and was exacerbated by the P-Δ effect on the inertial mass. The final position of the reference column at the end of testing is shown in Figure 59(b). One reason the reference column peak drift ratio was substantially larger than PT HyFRC for GM7 was because of the 1.6% residual drift ratio which existed prior to the test. Relative to their initial position, the two column achieved similar drift ratios during GM7.

The actual ductility demands imposed on the reference column (based on the analytical θ_y = 1.04%) are also included in Table 19. The largest deviation from the target ductility demand occurred during GM2, GM5, and GM7 when the imposed ductility demands were 68%, 38%, and 47% higher than the target values.

The time history of drift ratio in the N-S and W-E directions (N, W positive) for the PT HyFRC and reference columns are shown in Figure 60 for GM1 to GM7. Figure 61 shows the time history of drift ratio of the PT HyFRC column for GM8 through GM11. The peak displacement responses of the two columns were aligned in time for tests GM3 to GM6, especially at the points of largest displacement demand. Test GM7 caused significant damage in the reference column; hence, the peak points in the response did not align thereafter.

The orbital displacement responses of the two columns are shown in Figure 62 for GM1 to GM6 and Figure 63 for GM7 to GM11. Typically, the maximum drift ratio in the N-S direction was larger than the maximum drift ratio in the W-E direction. The paths of the orbital responses were similar for the two columns for all tests through GM6. Figure 63 shows the substantial residual drift ratio of the reference column following GM7.

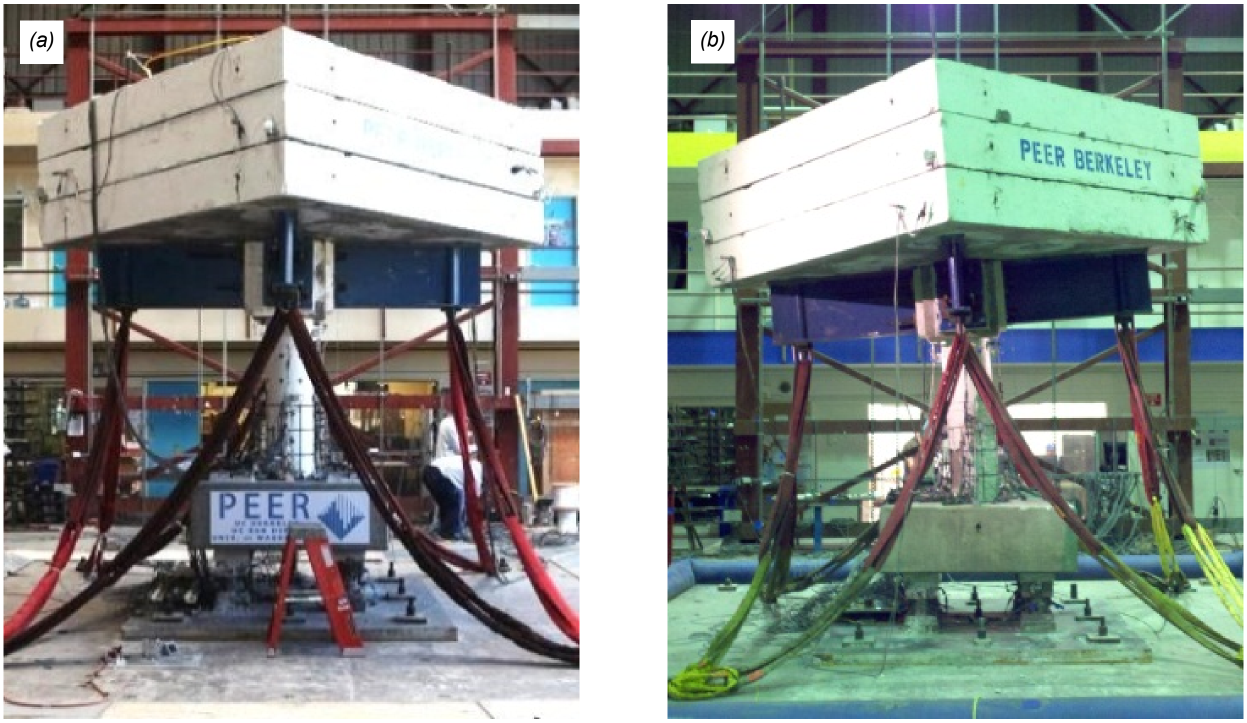

Figure 59. Elevation of columns at the end of testing; (a) PT HyFRC column with a residual drift ratio of 0.9% and (b) reference column with a residual drift ratio of 6.8%.

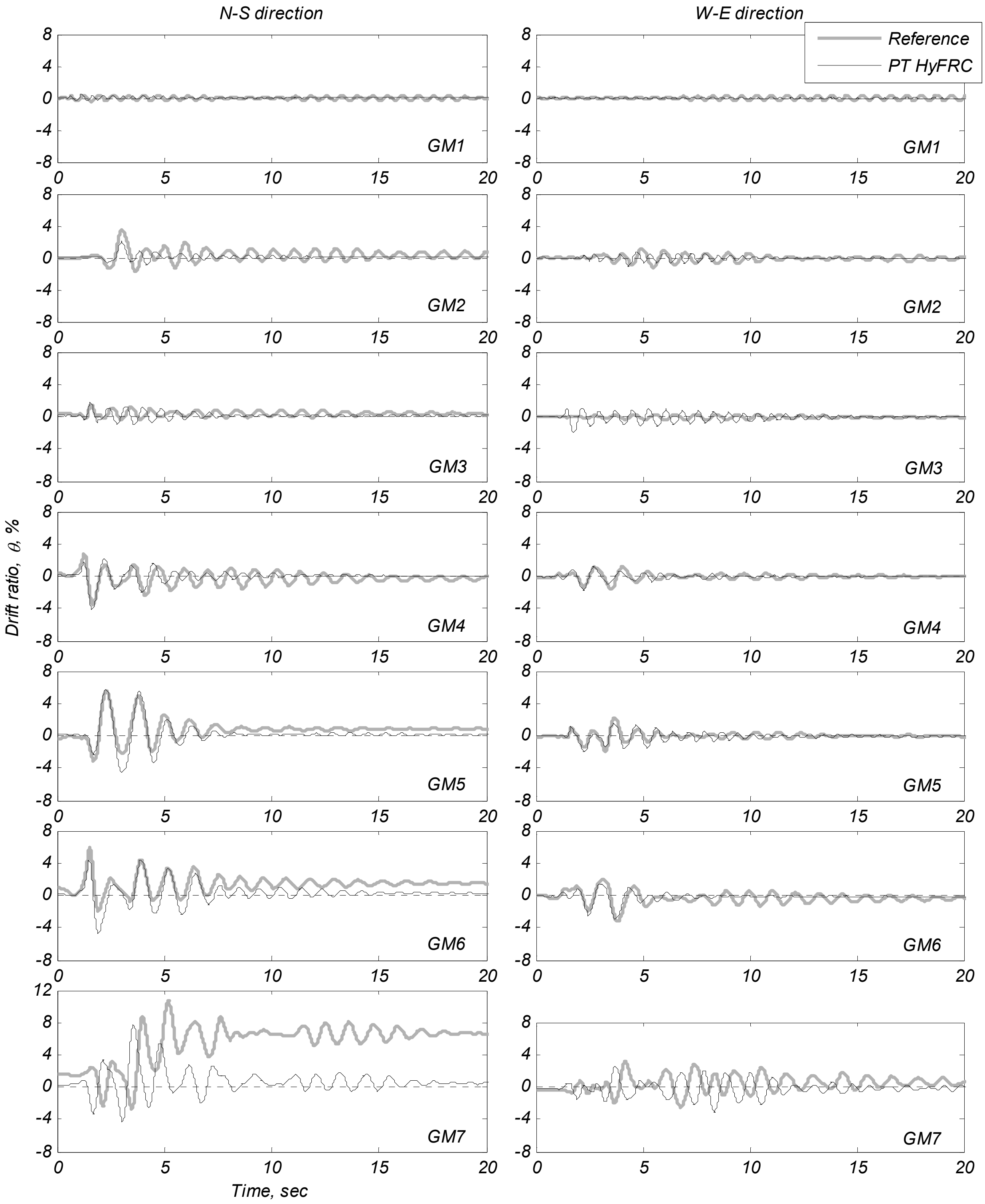

Figure 60. Time history of column drift ratio in the N-S and W-E direction for tests GM1 to GM7.

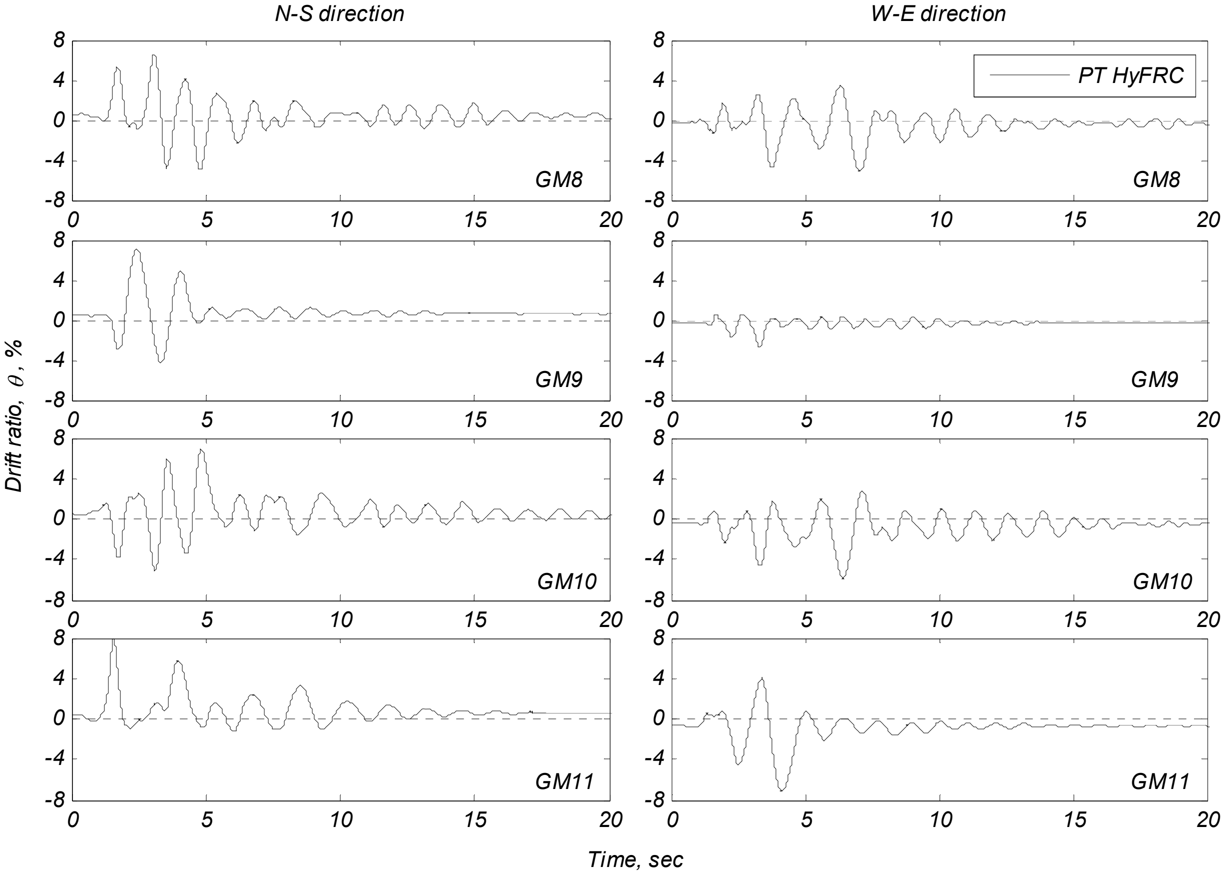

Figure 61. Time history of column drift ratio in the N-S and W-E direction for GM8 to GM11.

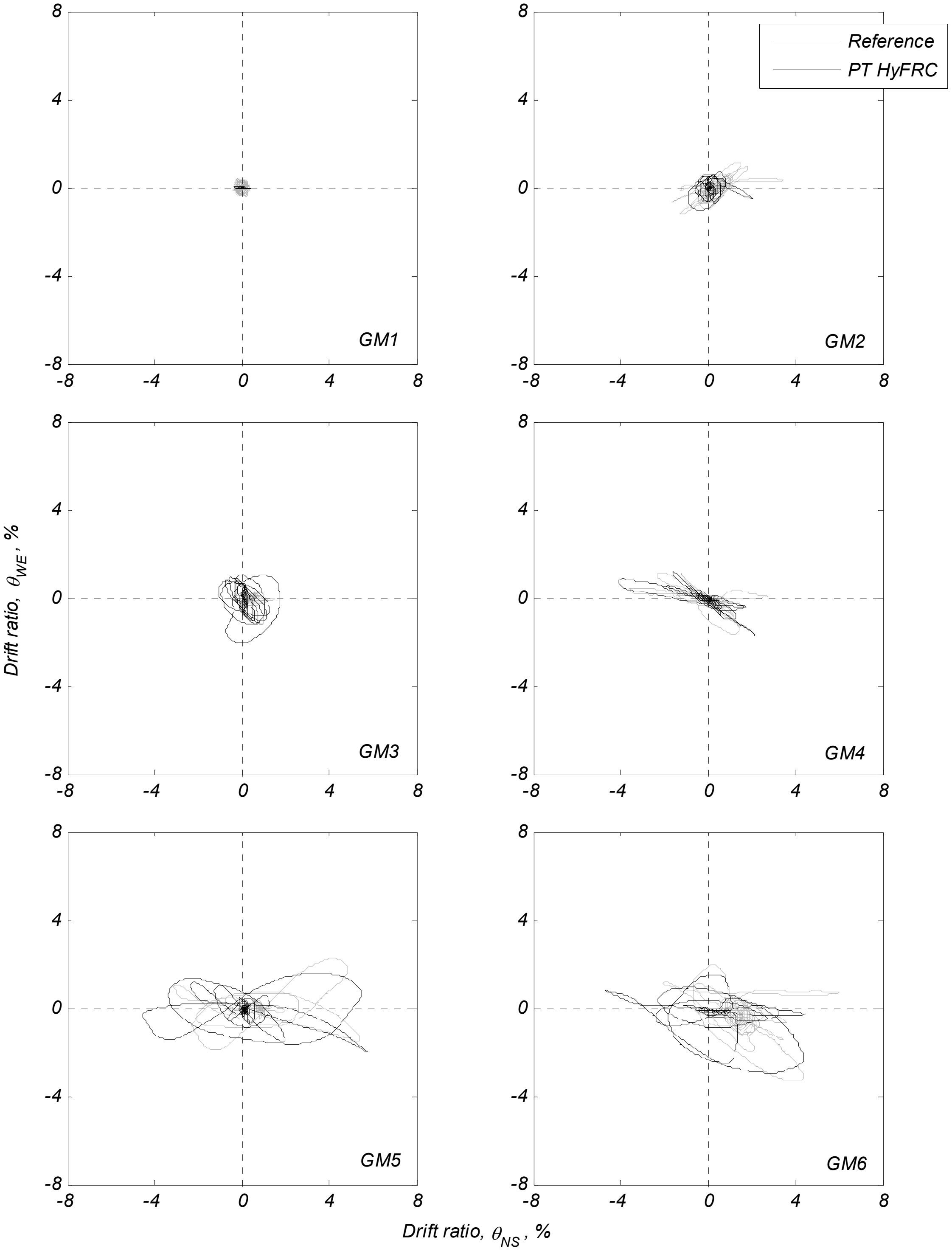

Figure 62. Orbital displacement response of the columns for GM1 to GM6.

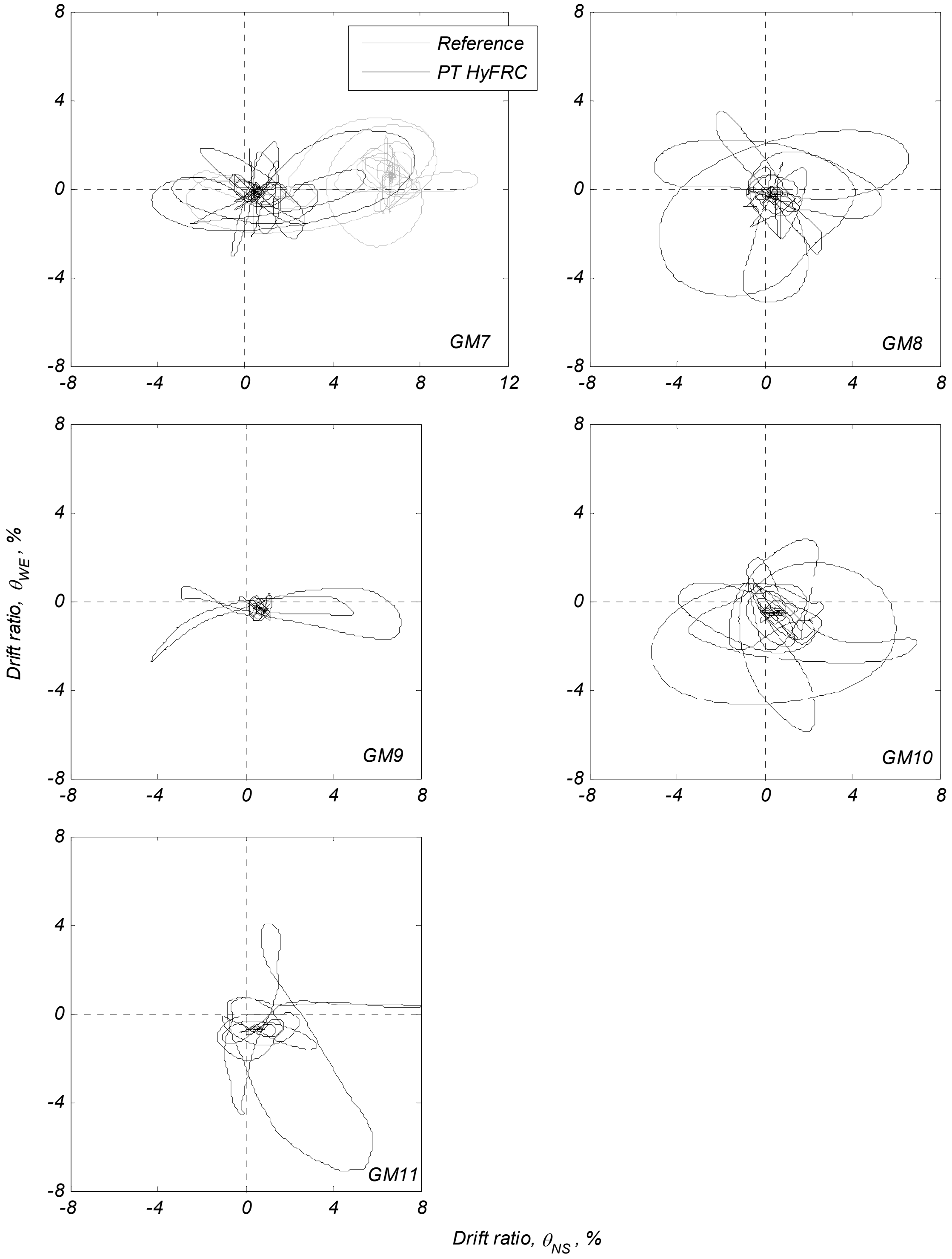

Figure 63. Orbital displacement response of the columns for GM7 to GM11.

4.5.2 Change in period of vibration

The fundamental periods of the columns in the N-S and W-E directions are given in Table 20. These periods were obtained from two white noise tests (three components of excitation each) with durations of 90 seconds and 0.02 g root-mean-square (RMS) amplitude of acceleration. The white noise tests were run before each ground motion test, and the fundamental periods were computed using Fourier analyses (Fast Fourier transform) of the displacement response. White noise tests predicted an initial fundamental period of $T_1 = 0.43$ and $T_1 = 0.58$ seconds for the PT HyFRC and reference columns, respectively. These periods were 8% and 9% higher than the periods obtained from free vibration testing.

Figure 64 compares the periods of the two columns in the N-S direction (the predominant direction of response) for GM1 to GM7. A longer initial fundamental period may explain why the peak drift ratio of the reference column during test GM2 was 65% larger than that of the PT HyFRC column. The period of the reference column was two times its initial period before GM3. The period of the PT HyFRC column increased only marginally through GM5, indicating that more lateral stiffness was preserved compared to the reference column. Yielding of the reference column longitudinal bars reduced their effective stiffness with each test due to the development of plastic tensile strains. The PT HyFRC column retained stiffness because the strands remained elastic through the duration of testing.

Table 20. Fundamental period of columns in the N-S and W-E directions

Test	*Fundamental period, T, sec*			
	PT HyFRC column		*Reference column*	
	N-S direction	*W-E direction*	*N-S direction*	*W-E direction*
GM1	0.43	0.42	0.58	0.57
GM2	0.43	0.43	0.66	0.66
GM3	0.46	0.46	1.01	0.90
GM4	0.49	0.50	0.99	1.00
GM5	0.58	0.50	1.01	1.01
GM6	0.69	0.57	1.14	1.07
GM7	0.74	0.59	1.11	1.12
GM8	0.81	0.67	-	-
GM9	0.83	0.78	-	-
GM10	0.91	0.74	-	-
GM11	1.06	0.84	-	-
End	1.15	0.89	-	-
**Periods were obtained from white noise tests run before the start of each GM test*				

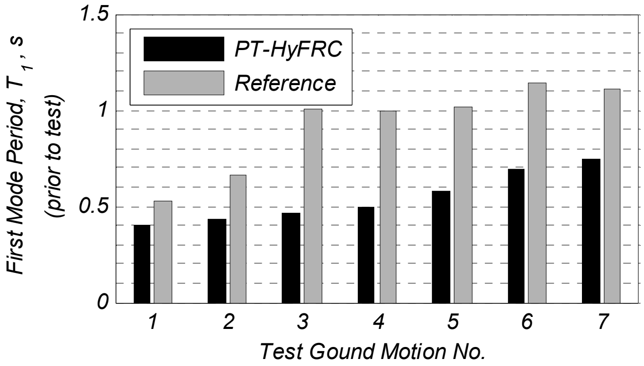

Figure 64. Comparison of first mode periods of the two columns in the N-S direction at the start of each test.

4.5.3 Local column deformations

The PT HyFRC column sustained global displacement demands by uplifting and rocking at the interface with the footing. During rocking, compressive forces caused inelastic deformations in the HyFRC and headed rebar near the rocking plane. The unbonded rebar yielded in tension during column uplift. A small amount of elastic deformation also occurred within the column.

Table 21 shows the column base rotation at the points of maximum drift ratio for each test. Base rotation (θ_B) was estimated as the difference in opposite displacement transducer measurements divided by the horizontal distance between the transducers. The bottom level of transducers that spanned between the column and the footing were used for this calculation. Rocking caused the peak drift ratio and base rotations to be quite similar. The base rotation comprised over 78% of the peak drift ratio when drift ratios exceeded 4%.

Figure 65 and Figure 66 show the base rotation in the N-S and W-E directions, respectively, plotted against the column drift ratio. Elastic deformation within the column accounted for the difference between the measured response and the case of pure rigid body rotation represented by the dashed line. During GM1, column displacements were primarily accommodated by elastic response of the column and rocking did not occur.

Table 22 shows the maximum measured uplift and compression strain on each column face during each test. Several steps were needed to find the uplift and strain at the column face since the transducers were offset from it by varying distances. First, each displacement measurement was divided by its gage length (see Appendix Figure A. 10) to estimate average strain over that length. Second, a planar surface was fit to the four strain measurements in a least squares sense. The strain value at the column face was then interpolated from the planar surface. Uplift was calculated by multiplying the tension strain at the face by the average of the gage lengths on each side. The values were calculated with respect to the measurement at the beginning of each test since damage caused compression strains to accumulate.

The maximum uplift in the N-S direction was 17.5 mm (S face) during GM7, and the corresponding compression strain on the N face was -9.43%. The maximum uplift in the W-E direction was 19.5 mm (W face) during GM11, and the corresponding compression strain on the E face was -11.83%. HyFRC and the headed reinforcing bars allowed the column to sustain these extreme compression strains with no cover spalling or bar buckling.

Table 21. Rotation at the column base at points of maximum drift ratio.

	N-S direction		*W-E direction*	
	Peak drift ratio, %	*Base rotation, $\theta_{B,}$ %*	*Peak drift ratio, %*	*Base rotation, $\theta_{B,}$ %*
GM1	0.46	0.17	0.05	0.00
GM2	2.05	1.37	-1.05	-0.66
GM3	1.74	1.14	-2.08	-1.48
GM4	-4.26	-3.59	-1.70	-1.23
GM5	5.89	4.60	-2.02	-1.51
GM6	-4.91	-4.38	-2.96	-2.30
GM7	7.83	6.37	-3.14	-2.43
GM8	6.61	5.44	-5.15	-4.30
GM9	7.10	6.25	-2.81	-2.31
GM10	6.93	6.01	-5.91	-4.79
GM11	8.01	7.05	-7.09	-5.98
**N, W directions are positive*				

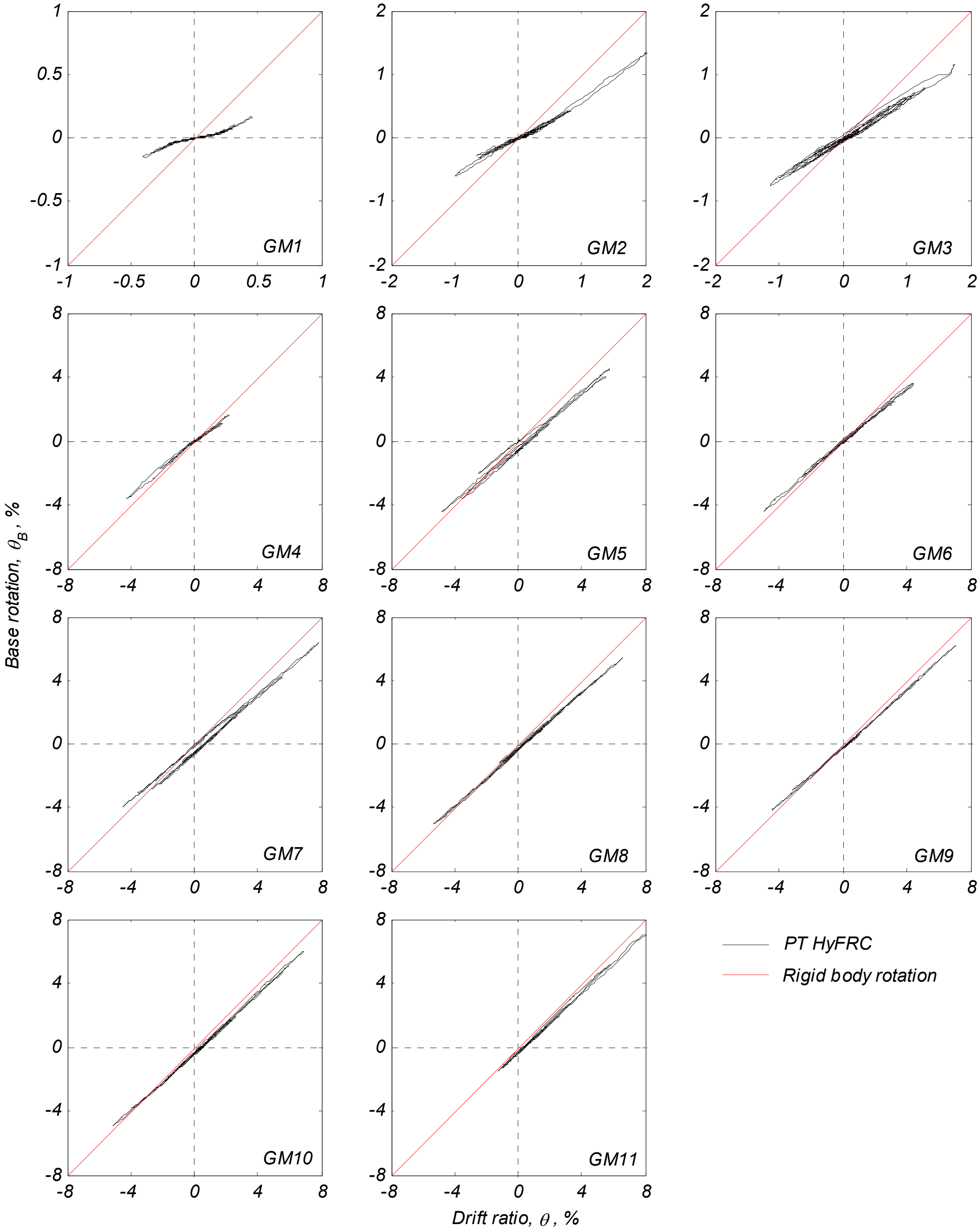

Figure 65. Rotation at the column base versus drift ratio in the N-S direction

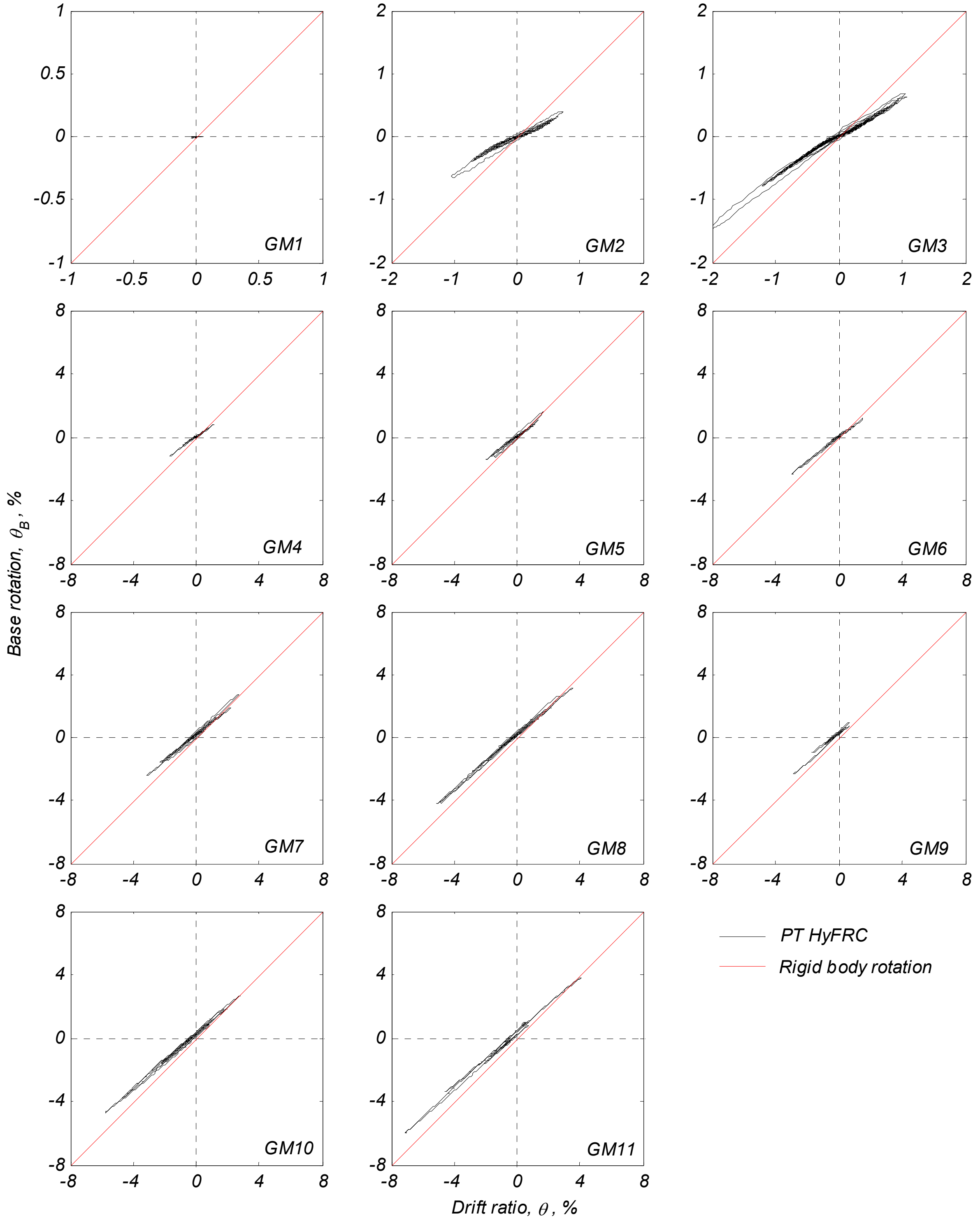

Figure 66. Rotation at the column base versus drift ratio in the W-E direction

Table 22. Maximum uplift and compression strain on the N, S, W, and E column faces.

	Maximum uplift, mm				*Maximum compression strain, $\varepsilon_{c,max}$, %*			
	N face	*S face*	*W face*	*E face*	*N face*	*S face*	*W face*	*E face*
GM1	0.5	0.4	0.2	0.1	-0.34	-0.27	-0.01	-0.01
GM2	2.4	4.1	2.6	1.4	-1.36	-0.29	-0.32	-0.70
GM3	2.8	3.3	5.4	2.3	-1.42	-0.61	-0.69	-2.09
GM4	13.2	5.4	5.2	6.2	-0.85	-3.05	-0.24	-0.56
GM5	15.9	14.2	9.7	7.2	-3.62	-4.10	0.39	-0.24
GM6	15.4	10.3	8.4	6.8	-6.47	-4.75	-1.69	-3.78
GM7	13.5	**17.5**	9.3	10.4	-9.43	-4.74	-1.86	-2.54
GM8	**17.0**	13.4	15.6	10.6	-11.52	-6.69	-4.79	-7.67
GM9	14.3	15.2	11.0	4.0	-13.98	-5.23	-1.68	-1.09
GM10	16.2	14.5	15.1	7.3	-13.75	**-7.03**	-5.50	-9.75
GM11	4.8	16.8	**19.5**	**11.0**	**-16.52**	-2.32	**-6.49**	**-11.83**

** **bold** values are the maximum for each face*

4.5.4 Lateral force-displacement response

The maximum lateral forces measured in each column and the corresponding drift ratios are provided in Table 23. Force is represented by the base moment ratio, defined as the moment at the base of the column divided by the product of the weight and height of the inertial mass, M/WH. The base moment was calculated from the vertical force measurements of the four load cells beneath the footing based on their respective distance from the column centroid in each direction. Moment caused by rotational inertia of the mass blocks contributed to the base moment; hence, the value M/WH is not equivalent to the shear force ratio, V/W. The moment caused by horizontal inertia of the footing below the column was removed from M/WH.

The peak moment strengths of the reference column in the N-S and W-E directions (N, W positive) were -0.34WH and -0.27WH at drift ratios of -3.17% and -2.99%, respectively. The same values for the PT HyFRC column were -0.36WH and -0.31WH at drift ratios of -2.99% and -1.96, respectively.

The shape of the force-displacement response affects the magnitude of the residual lateral displacement a column may develop after an earthquake ground motion. Figure 67 through Figure 70 compare the lateral force-displacement response histories of the two columns. The subplot on the left in each row is the N-S direction, while the subplot on the right is the W-E direction. The PT HyFRC column showed characteristic recentering hysteretic loops for all tests up to GM5. During GM4 (Figure 68), the hysteretic loop in the S direction is wide but the column unloads through zero drift ratio. The reference column hysteretic loops were wider and rarely crossed through the origin.

The PT HyFRC column practically eliminated residual drift ratios, but the residual was measured at the end of each test. The drift ratio at the points when the columns unloaded to zero moment was larger starting at GM5. The reason the drift ratio at unloading was different than the drift ratio at the end of the test was because the recentering continued as the ground motion subsided and cycles of large displacements damped out. In a way, the ground motion helped to restore the column to its original position—a phenomena that was also observed in the reference column.

The drift ratio after unloading from the peak displacement to $M = 0$ may be a better indicator of the column recentering ability than the residual drift ratio. These values can be compared to static testing results, and the restorative effects of the tail-end of the ground motions are neglected. These values of drift ratio ($\theta_{M=0}$) are listed for the two columns in Table 24 as are the drift ratios at the point of unloading (θ_{max}).

These results show that the PT-HyFRC column experienced a nearly complete recentering behavior for motions up to and including GM4 (4.1% peak drift ratio) for which $\theta_{M=0}$ = 0.2%. The value of $\theta_{M=0}$ increased to 0.6% during GM5 after unloading from a peak drift ratio of 5.9%, and then increased to 3.5% after unloading from the peak drift ratio of 7.8% during GM7. The measured M-θ response of the reference column in the N-S direction shows larger values of $\theta_{M=0}$ equal to 1.3%, 2.7%, and 7.9% after unloading from peak drift ratios of 3.6%, 5.6%, and 10.7%, respectively for GM4, GM5, and GM7.

The drift ratio at zero moment increased for the PT HyFRC column in the tests beyond GM7, likely as a result of damage to the column base at the rocking plane as well as significant inelastic deformation of the unbonded longitudinal bars. Still, at the end of each test the residual drift ratio was under 1%.

Table 23. Maximum moments during each test in the N-S and W-E directions.

	PT HyFRC column				*Reference column*			
	N-S direction		*W-E direction*		*N-S direction*		*W-E direction*	
Test	$(M/WH)_{max}$	θ, %	$(M/WH)_{max}$	θ, %	$(M/WH)_{max}$	θ, %	$(M/WH)_{max}$	θ, %
GM1	-0.20	-0.38	-0.02	-0.05	-0.12	-0.38	-0.10	-0.40
GM2	0.33	1.63	-0.23	-1.03	0.32	3.13	0.17	1.16
GM3	0.31	1.74	**-0.31**	**-1.96**	0.23	1.45	-0.07	-0.18
GM4	**-0.36**	**-2.99**	0.20	1.16	**-0.34**	**-3.17**	-0.22	-1.67
GM5	0.34	5.52	-0.19	-1.51	0.33	5.09	-0.20	-1.60
GM6	-0.34	-4.39	0.28	1.48	0.30	5.32	**-0.27**	**-2.99**
GM7	0.31	7.05	-0.27	-3.05	0.33	10.62	-0.23	-2.38
GM8	-0.30	-4.95	0.29	3.33	-	-	-	-
GM9	0.29	6.94	-0.14	-2.68	-	-	-	-
GM10	-0.28	-4.47	0.26	2.53	-	-	-	-
GM11	0.28	5.99	0.28	4.04	-	-	-	-

**N, W directions are positive*
Maximum over all tests shown in* ***bold

Table 24. Drift ratio at zero moment after unloading from the peak displacement in each direction.

Test	*PT HyFRC column*				*Reference column*			
	N-S direction		*W-E direction*		*N-S direction*		*W-E direction*	
	θ_{max} , %	$\theta_{M=0}$, %	θ_{max} , %	$\theta_{M=0}$, %	θ_{max} , %	$\theta_{M=0}$, %	θ_{max} , %	$\theta_{M=0}$, %
GM1	0.46	0.02	0.05	0.01	-0.40	0.03	-0.40	0.00
GM2	2.05	0.17	-1.05	-0.07	3.48	1.40	-1.22	-0.23
GM3	1.74	0.27	-2.08	-0.33	1.51	0.67	-0.44	-0.06
GM4	-4.26	-0.19	-1.70	-0.09	-3.63	-1.28	-1.69	-0.43
GM5	5.89	0.61	-2.02	-1.16	5.55	2.70	2.22	1.02
GM6	-4.91	-0.59	-2.96	-1.15	6.06	3.30	**-3.27**	**-1.75**
GM7	**7.83**	**3.54**	-3.14	-0.32	**10.74**	**7.90**	3.19	0.94
GM8	6.61	3.32	-5.15	-0.98	-	-	-	-
GM9	7.10	2.27	-2.81	-1.26	-	-	-	-
GM10	6.93	2.24	-5.91	-1.58	**-**	**-**	-	-
GM11	8.01	1.99	**-7.09**	**-2.75**	-	-	**-**	**-**

**N, W directions are positive*
******bold*** *values correspond to maximum of $\theta_{M=0}$ over all tests for each direction*

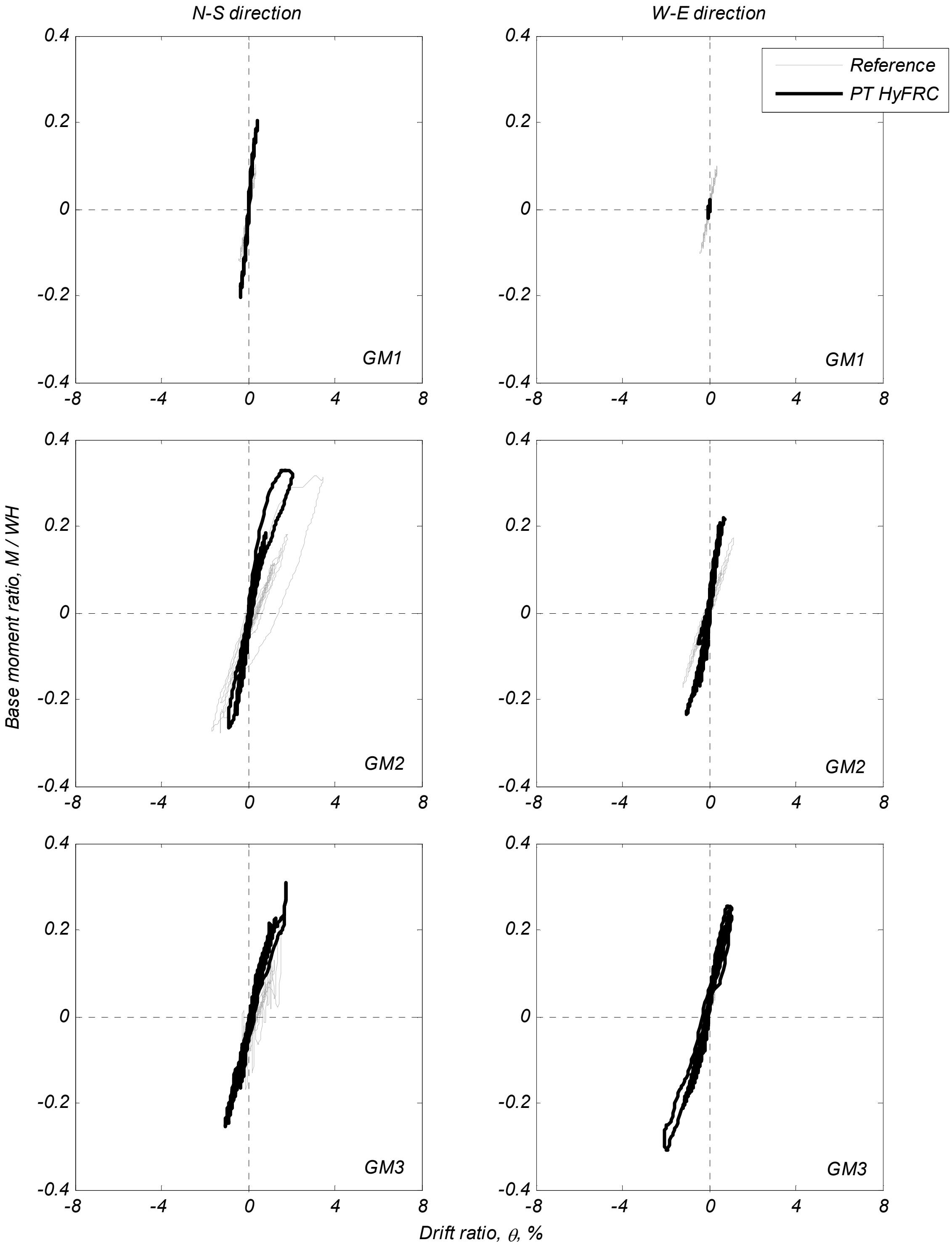

Figure 67. Measured overturning moment vs. drift ratio in the N-S and W-E directions (N, W positive) for GM1, GM2, and GM3.

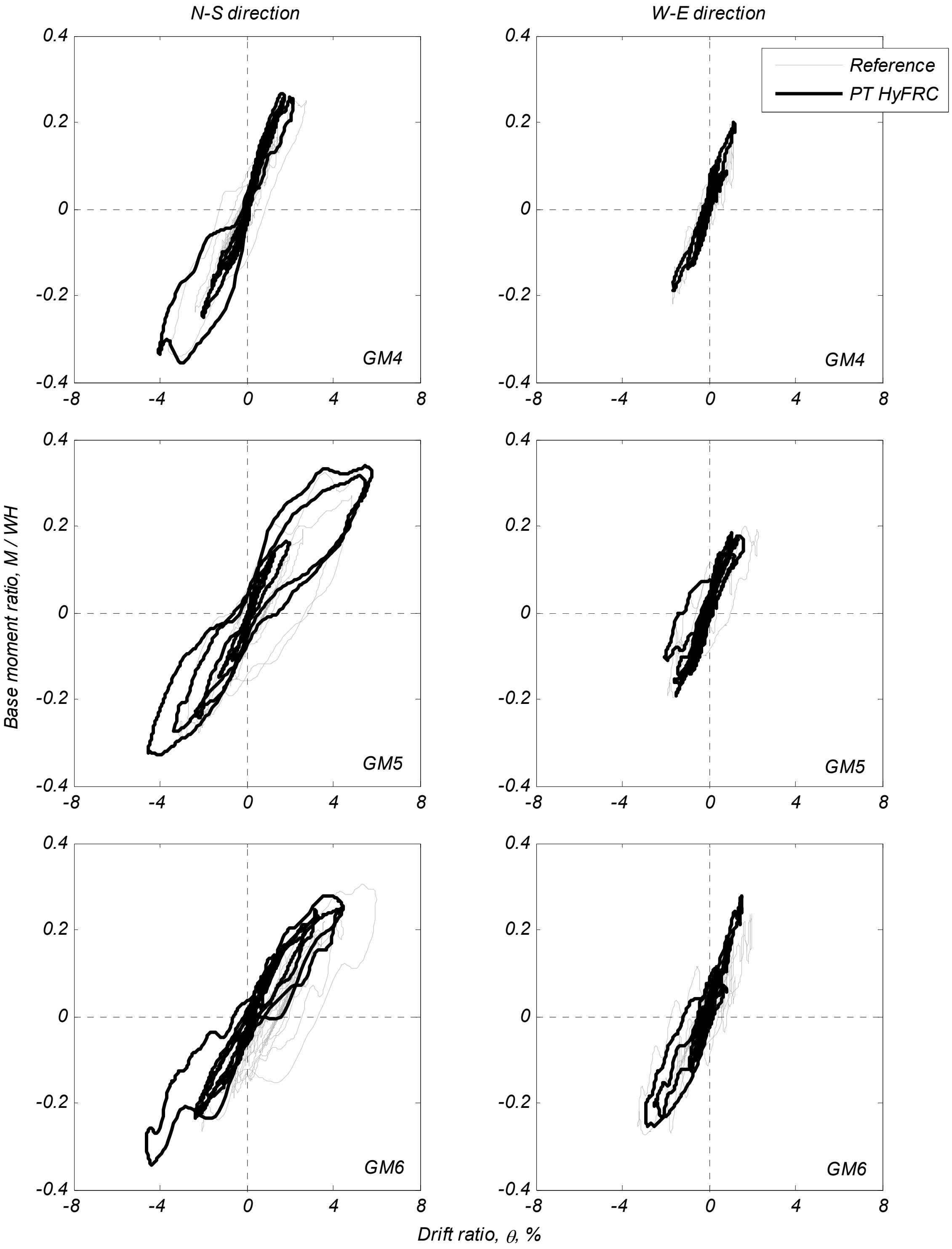

Figure 68. Measured overturning moment vs. drift ratio in the N-S and W-E directions (N, W positive) for GM4, GM5, and GM6.

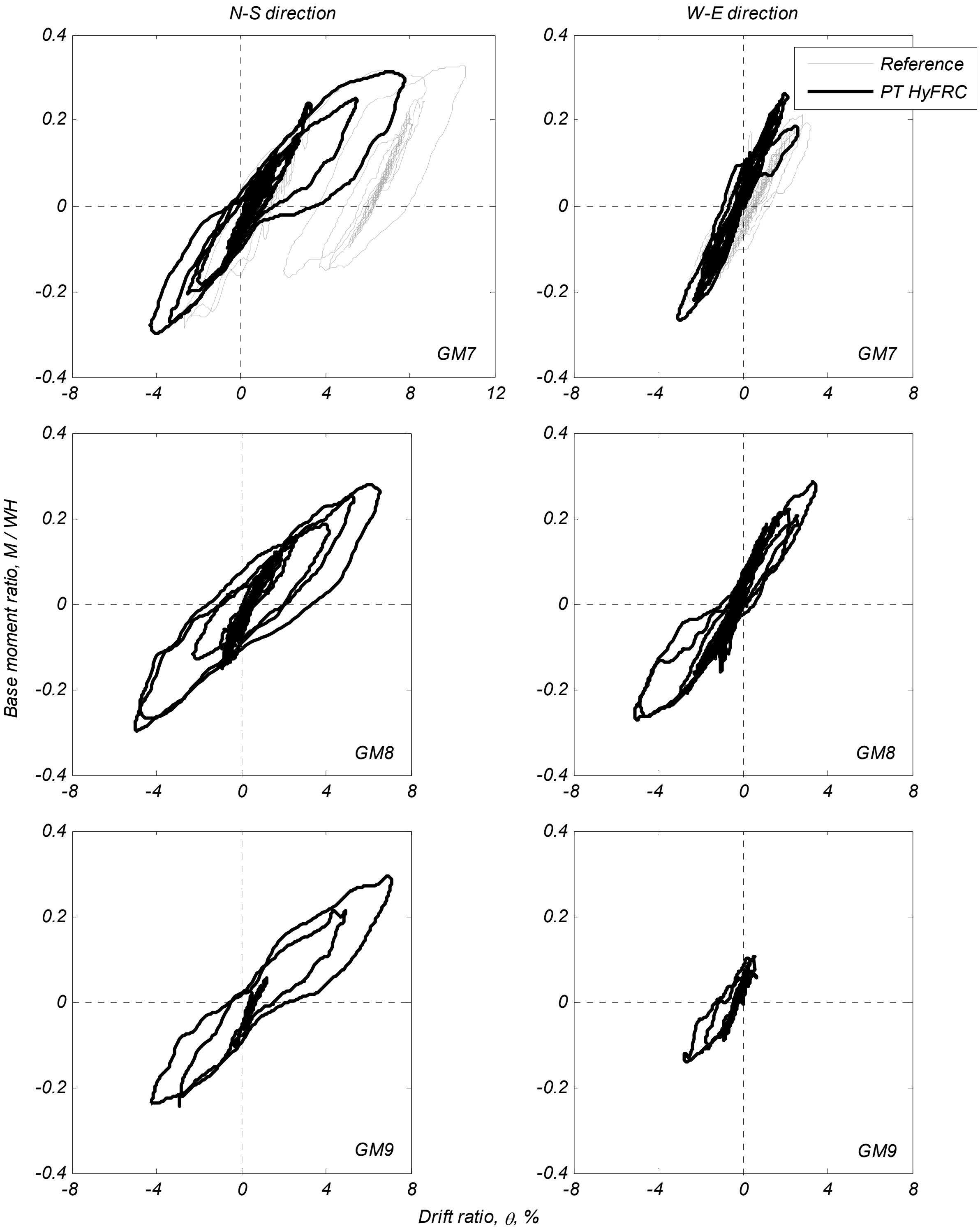

Figure 69. Measured overturning moment vs. drift ratio in the N-S and W-E directions (N, W positive) for GM7, GM8, and GM9.

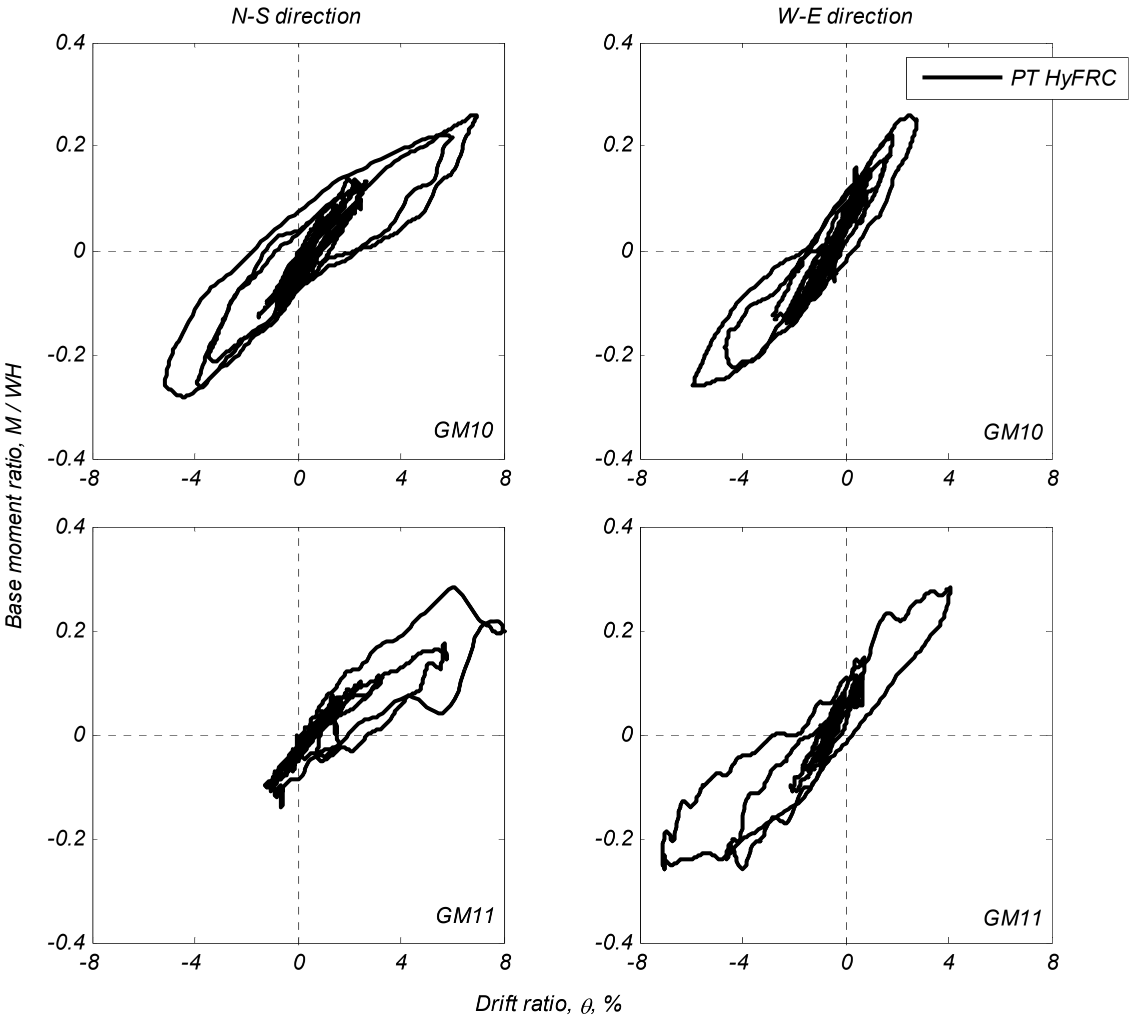

Figure 70. Measured overturning moment vs. drift ratio in the N-S and W-E directions (N, W positive) for GM10 and GM11.

4.5.5 Measured force in the post-tensioning

Table 25 shows the post-tension force at the start and end of each test as a raw value and as a percent of yield force. It also shows the maximum force measured during the test and the net change. Prior to the first test, the post-tensioning force was 48% of the yield force (or 455 kN) in the PT HyFRC column. The post-tensioning force was 45% of the yield force (or 429 kN) after test GM11 for an accumulated loss of only 5.7% of the initial force through the duration of testing. The maximum force was measured during test GM7 when the force reached 62% of the yield force (or 589 kN) at a drift ratio of 8.0%. Based on these results, a shorter length of unbonded strand may have been sufficient to prevent yielding under the MCE-level displacement demand.

Table 25. Post-tension force measured during testing.

Test	Start of test		Maximum		End of test		Net change
	P_{pt} , kN	% yield	P_{pt} , kN	% yield	P_{pt} , kN	% yield	ΔP_{pt}
GM1	455	47.6	455	47.7	454	47.5	-1
GM2	453	47.5	474	49.6	452	47.3	-1
GM3	453	47.5	474	49.6	452	47.4	-1
GM4	453	47.4	541	56.7	450	47.1	-3
GM5	451	47.2	575	60.2	448	47.0	-2
GM6	448	47.0	548	57.4	446	46.8	-2
GM7	445	46.6	589	61.7	444	46.5	-1
GM8	443	46.4	548	57.4	438	45.9	-4
GM9	438	45.9	527	55.2	437	45.8	0
GM10	434	45.5	515	53.9	431	45.1	-3
GM11	432	45.3	552	57.9	429	45.0	-3

4.5.6 Strain gage measurements

Appendix Table A. 3 provides the initial and maximum values of strain measured in the post-tensioned strands for each test. The same values for the gages on the unbonded rebar, headed rebar, and spiral are provided in Appendix Table A. 4, Table A. 5, and Table A. 6. The locations of all the strain gages were given in Table A. 2.

Based on strain measurements, none of the strands yielded. The maximum strain in the strands was 0.507% in gage GSS.52 located on strand S3 (south strand). This was well below the strain at the onset of yielding of 0.9%. The smallest and largest losses of initial strain were -4.2% and -6.2% of the initial strains measured by gages SW.51 and SE.51, respectively. These losses were consistent with the loss of initial post-tension force measured by the load cell.

The grouted end anchorages were inspected after column demolition and no slip of the strands or grout damage was observed. Therefore, the losses in strain were assumed to be a result of axial shortening of the column by between 0.51 mm and 0.71 mm based on the unbonded length of the strands (3467 mm) and the magnitude of losses mentioned above.

The unbonded bars remained elastic during the first test (GM1) as intended. Appendix Table A. 4 shows that yielding was measured by at least one strain gage on unbonded bars U1, U2, and U5 during GM2. Peak strains exceeding the yield strain are shown in bold in Table A. 4. During GM2, the maximum strain of the unbonded bars was 1.80%. This strain was recorded on two different bars by gages located 76 and 89 mm above the footing. After bars yielded during GM2, the plastic strains increased with each subsequent test as shown by the starting strain values. Yielding was delayed until GM4 for bar U3 since it was located near the W-E axis and the largest displacements were in the N-S direction.

The maximum strains recorded in the unbonded bars U1, U2, U3, and U5 were 3.62%, 1.80%, 0.97%, and 1.66%, respectively. The maximum strains recorded by each gages are shown in red. The objective of limiting these strains to 5% was achieved using the unbonded length of 1.25*D*.

The strains measured in the unbonded bars were larger in gages closer to the footing. Gage LU1.2 was 76 mm above the footing while gage LU1.1 was 175 mm above the footing, both on bar U1. The strains during each test were larger in the lower gage. The same pattern was present in bars U2 and U5. Gages LU2.1 and LU5.1 were located approximately 100 mm lower than gages LU2.2 and LU5.2 and the strains were larger.

The gage measurements show that strains over the unbonded length were non-uniform. If the bars were 100% unbonded, one would expect constant strain over the unbonded length. Although chemical bond between the bars and the grout within the PVC ducts was avoided, the discrepancy arises because there could have been friction and mechanical interlock between the bars and the surrounding grout which increased the effective bond.

The headed rebar remained elastic until GM3, when bar B5 yielded in compression as shown in Table A. 5. Bar B1 yielded during GM4, bar B3 and B7 yielded during GM5, and bar B9, which was closest to the W-E axis, yielded during GM7. After yielding, all the bars developed significant plastic compression strains. The headed bar F3 within the footing remained elastic through the duration of testing indicating that damage within the footing was minimal. That maximum compression strain over all headed bars was -5.95% in bar B5 during GM11.

Strain measurements in Table A. 6 show that the spiral on the N column face yielded during GM5 when gage TN.22 measured a strain of 0.45%. Yielding was also measured during GM8 on the W and E faces by gages TW.22 and TE.2 with maximum strains of 0.56% and 0.55%, respectively. These three gages were located at heights of 76, 64, and 83 mm above the footing on the outside face of the spiral, and the approximate circumferential location is shown in Appendix Figure A. 10. Gage TN.22 recorded the maximum spiral strain of 1.21% during GM11. The strains in the spiral at the start of each test increased as testing progressed; however, they rarely exceeded the yield strain of 0.44%. Hence, the starting strains were elastic in nature and were caused by expansion of the confined HyFRC core.

Several factors may have contributed to the overall lack of significant spiral yielding. First, the ratio of the spiral spacing to longitudinal bar diameter was $s/d_b = 2$, well below the ratio in the prototype column of $s/d_b = 5$. The tight spiral spacing reduces the likelihood of bar buckling which might cause localized spiral strains. In addition, fibers in HyFRC provide added confinement and likely resisted some expansion of the core.

4.5.7 Observed column damage

The crack at the rocking plane opened during the first test (GM1). The crack was only captured in real-time by video cameras mounted on the footing; it closed after the test was complete. During test GM2, the uplift increased and light compressive scaling/cracking of the HyFRC and grout pad on the NE face of the column was observed approximately 25 mm above the footing as shown in Figure 71(a). This cracking progressed slightly during test GM3 as shown in Figure 71(b). Some vertical splitting cracks initiated during test GM3, branching off the compressive cracks on the NE face.

The uplift at the rocking interface during the first design-level test (GM4) is shown in the photo of the NE face of the column in Figure 71(c). This photo was taken from video at the instant the specimen was at a drift ratio of 4.3%. There was no evidence of spalling after either of the design-level tests (GM4 and GM5). Crack propagation was minimal as shown in Figure 71(c).

The HyFRC did not lose integrity during the MCE-level earthquake (GM7) as shown in Figure 71(d), although vertical splitting cracks that had initiated in prior tests propagated upward. These cracks did not extend higher than 200 mm above the footing. Slight outward bulging of the column base was observed. Neither spiral fracture nor bar buckling were evident on any face.

Fracture of the unbonded longitudinal bars was delayed until the last test (GM11) when bars U1 and U4 fractured; however, the column residual drift ratio was still only 0.9%. Figure 71(e) shows the damage state of the N face of the column after the last test. The HyFRC material did not spall from the column face during testing. The fibers helped resist opening of the splitting and compression cracks that were observed. Figure 71(f) shows the N column face after damaged HyFRC was removed manually with a hammer and chisel. Cracking penetrated through the cover to the depth of the spiral up to a height of 200 mm above the footing but did not penetrate into the confined core.

Figure 72 shows the recessed grout pad on the top of the footing after the column was removed for demolition. Some of the grout was damaged and the footing headed bars are visible, but the demolition process could have exacerbated any damage incurred during testing.

The reference column formed a plastic hinge with distributed flexural cracks. Early damage consisted of cracks at a spacing of between 51 and 127 mm which formed up to a height of approximately 1.5*D* (610 mm) above the footing after GM2 [see SW column face in Figure 73(a)]. Spalling initiated during the first design-level test (GM4) and became more pronounced in subsequent tests with a larger affected area and deeper penetration. Spalling on the NE column face is shown in Figure 73(b) after GM5.

After the test GM6, vertical splitting cracks and spalling increased to a height of *D* (406 mm) above the footing on the NW face of the column. After GM7, this spalling and compressive damage was severe as shown in Figure 73(c) and the spiral reinforcement was exposed. Although the residual drift ratio was 6.8% after this test, the ductile reinforcement detailing prevented bar fracture, spiral fracture, and bar buckling. The N face of the column at the end of testing is shown in Figure 73(d) showing the full extent of spalling.

Figure 74 provides a side-by-side comparison of each column’s damage on the NE face after ground motions GM4, GM5, GM7, and at the end of testing. The peak drift ratios sustained during each test in the N direction are also provided.

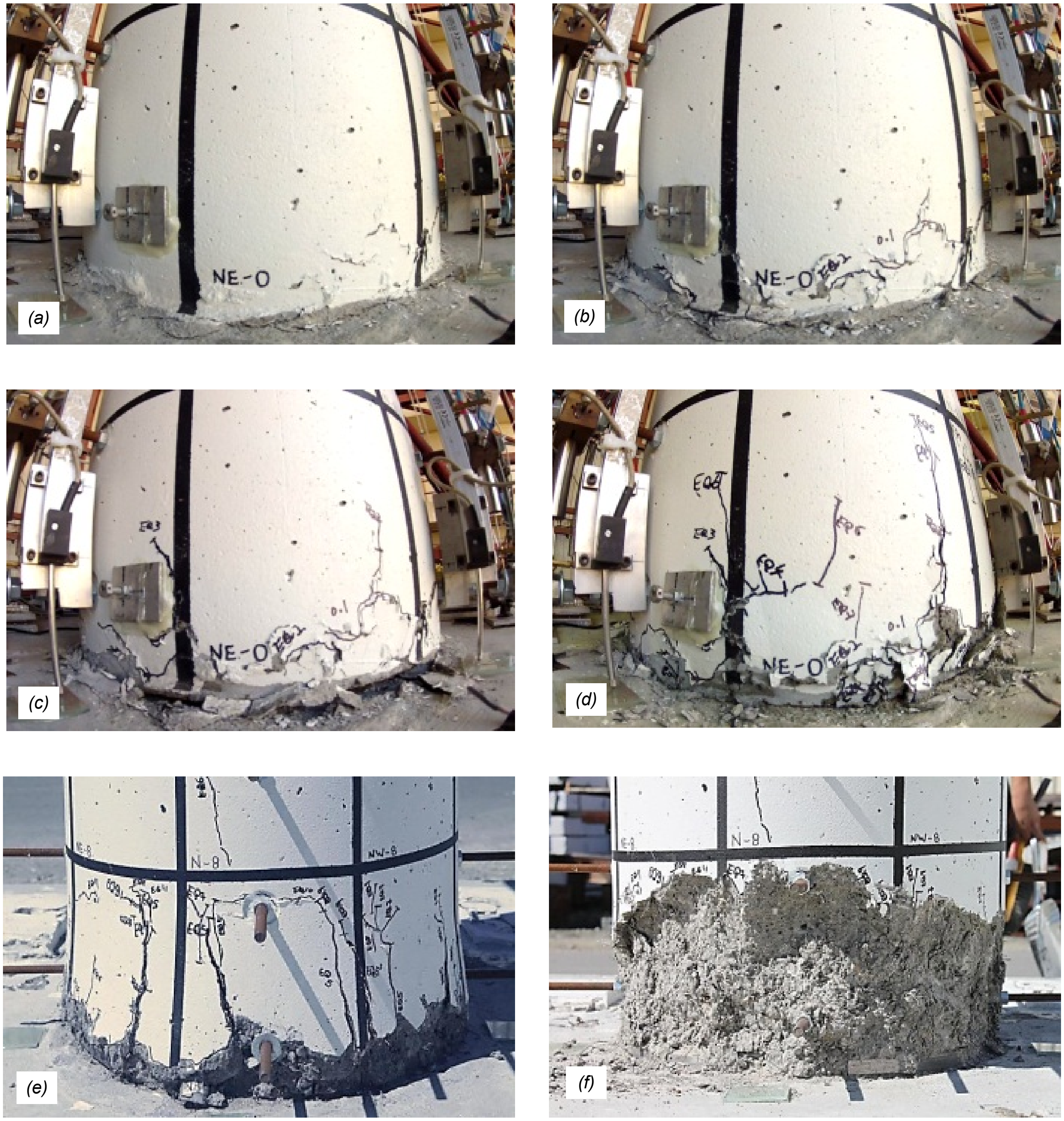

Figure 71. Damage to the PT HyFRC column; (a) NE face after GM2, (b) NE face after GM3, (c) NE face at 4.3% drift ratio during GM4, (d) NE face after GM7, (e) N face at the end of testing, and (f) N face after removal of damaged HyFRC.

Figure 72. *Grout pad after column demolition.*

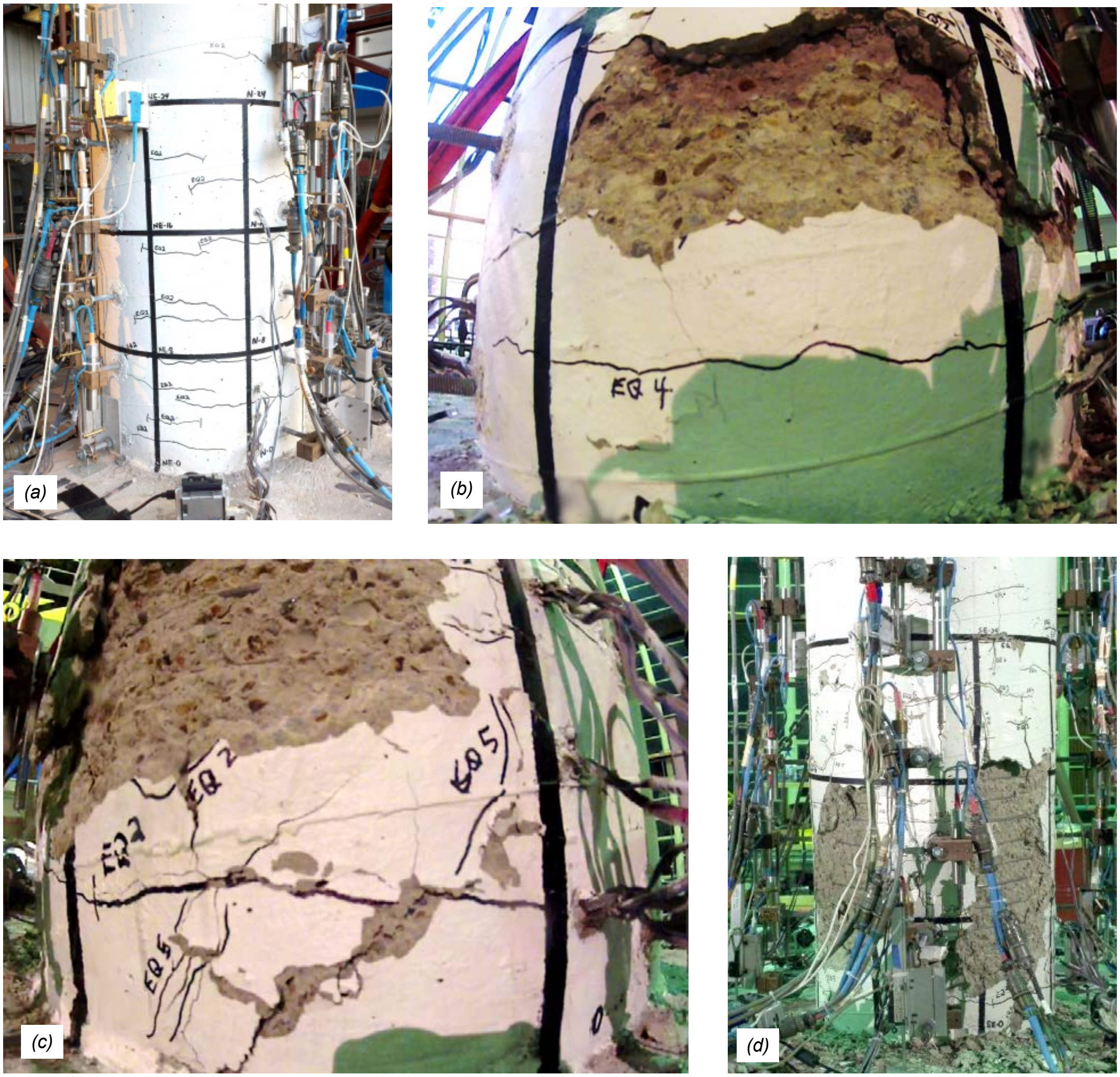

Figure 73. Damage to the reference column; (a) SW face after GM2, (b) NE face after GM5, (c) NW face after GM7, and (d) N face after GM7.

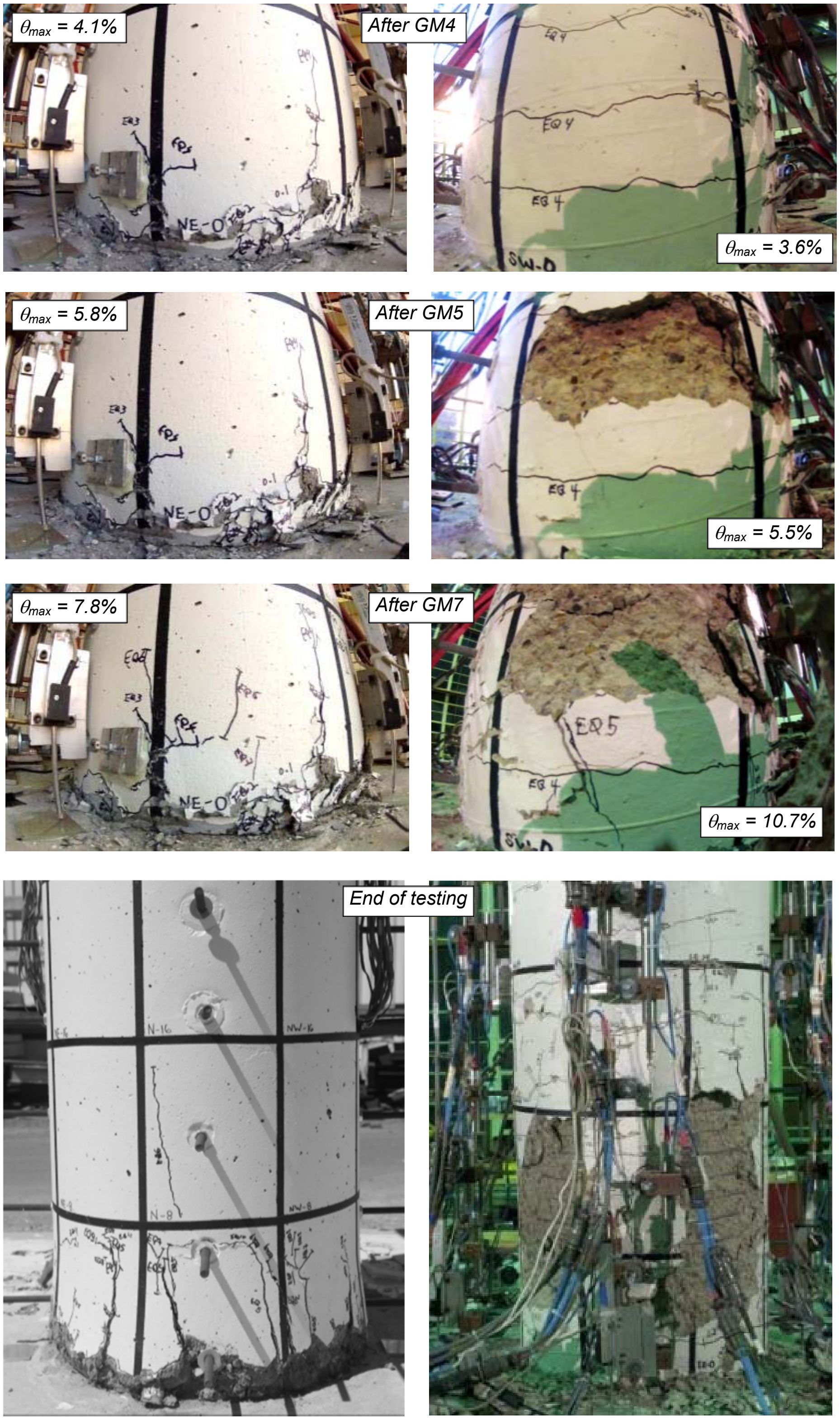

PT-HyFRC **Reference**

Figure 74. Side-by-side comparison of column damage.

4.6 Damage reduction using headed rebar and HyFRC

The damage in the PT-HyFRC column was less severe than the damage in a similar specimen, PRC-U2, tested by Jeong et al. (2008). Details of the two specimens are provided in Table 26. The primary difference between the specimens was that PT HyFRC had headed longitudinal rebar as well as HyFRC at the base while PRC-U2 had no headed rebar and contained only conventional concrete.

PRC-U2 contained 12 longitudinal bars ($\rho_d = 0.7\%$) that were unbonded at the base over a length of $2D$ (812 mm) as well as a single high strength steel bar ($\rho_{pt} = 0.7\%$) that was post-tensioned. Confinement was provided by spiral reinforcement at $\rho_t = 0.8\%$. The two columns had practically the same diameter (D), shear span ratio (M/VD), and gravity load (P_g). PRC-U2 had a 22% smaller post-tension force (P_{pt}), a 15% smaller ratio of unbonded rebar (ρ_d), and a 20% smaller transverse reinforcement ratio (ρ_t) compared to PT HyFRC.

Table 26. Comparison of columns PT HyFRC and PRC-U2

Specimen	*Test type*	*D, mm*	*M/VD*	*P_g, kN*	*P_{pt}, kN*	*ρ_{pt}, %*	*ρ_d, %*	*ρ_b, %*	*ρ_t, %*	*Peak drift ratio, %*	*Residual drift ratio, %*
PRC-U2	Biaxial shake table	406	6.2	232.5	346	0.7	0.7	-	0.8	4.7 10.0	0.1 0.9
PT HyFRC	Triaxial shake table	406	6	232.5	445	0.4	0.8	1.5	0.9	4.3 (GM4) 8.0 (GM7)	0.1 0.4

Different ground motions were applied to the two columns, but the peak drift ratios imposed on PRC-U2 in design-level and MCE-level tests were 4.7% and 10.0%. The residual drift ratios were 0.1% and 0.9%, respectively. PT HyFRC attained peak drift ratios of 4.3% during the design-level test (GM4) and 8.0% during the MCE-level test (GM7). The residual drift ratios were comparable at 0.1% and 0.4%.

Although the recentering abilities were comparable, PRC-U2 had more severe damage than was observed for the PT HyFRC column. After reaching 4.7% drift ratio, there was significant concrete spalling as shown in Figure 75(a). The spiral fractured and six bars buckled when the column reached 10.0% drift ratio as shown in Figure 75(b). This type of compression damage was not observed in PT HyFRC, presumably because of the HyFRC and headed rebar in the column base.

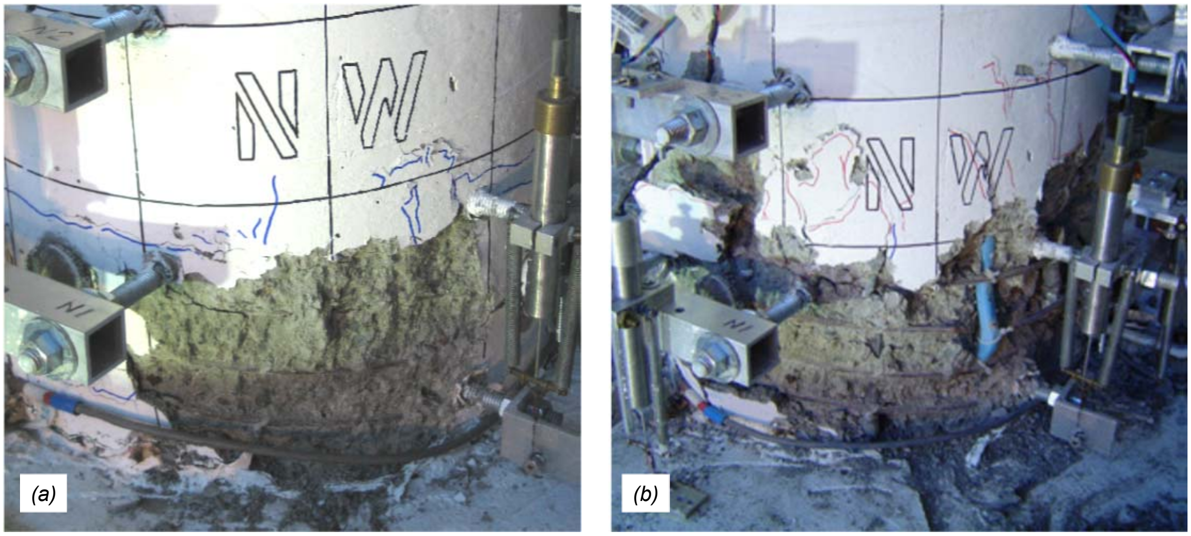

Figure 75. Damage observed in specimen PRC-U2; (a) after a drift ratio of 4.7% and (b) after a drift ratio of 10.0% (Jeong et al. 2008).

4.7 Response predicted by the analytical model

The analytical model discussed in Chapter 3 was subjected to the ground motions measured during column testing to validate the modeling technique. This section will describe the dynamic analysis procedure and the model predictions will be compared with the measured test results. The comparison will show that the model accurately predicted the column response, including displacements, forces, the local rocking mechanism, and associated damage.

4.7.1 Dynamic analysis procedure

Nonlinear response history analysis (NRHA) was conducted using the analytical model presented in Chapter 3. Inertial mass was lumped at a single node at the center of mass in the model. The mass of 23,700 kg was assigned to the translational degrees of freedom (DOFs) in the x, y, and z directions. The rotational mass of 20.5 kN-m-s^2 was assigned to the rotational DOFs about x and y at the same point.

Rayleigh damping was assigned to all non-rigid column elements to have a modal damping ratio, ζ, of 1.0% in the first and second modes. Damping was neglected in the rigid elements because the stiffness proportional component would be excessive. The modal damping ratio (1.0%) was matched to the free vibration test result.

The model had the properties specified in Table 10 in Chapter 3, except that the number of compression springs representing HyFRC at the rocking plane was increased by a factor of four. Increasing the number of springs allowed for a more accurate calculation of the overturning moment at the base of the column.

Accelerometers measurements of the footing during testing provided the input ground motions for dynamic analysis. Each time history was successively applied to the model in the three translational directions. The analysis sequence did not include the white noise tests run between each ground motion. The timestep of each acceleration time series was 0.005 seconds as was the dynamic analysis timestep.

The state of the model at the end of each test was saved as the initial state for the next ground motion. This allowed damage to accumulate as the sequence progressed that same way that it would have accumulated during testing.

4.7.2 Predicted global displacement response

The predicted and measured peak and residual drift ratios of the column are listed in Table 27. The table also shows the absolute and percent error in the predicted peak drift ratio (SRSS). Figure 76 compares the predicted and measured drift ratios of the column side-by-side. The error in the peak drift ratio prediction was under 10% for all tests except for GM9 when the error was 12.2%.

The prediction for peak drift ratio remained accurate well into the inelastic range of column response. The percent errors were only 0.3% and -0.2% during EQ6 and EQ7 when the column reached peak drift ratios of 5.03% and 7.96%, respectively.

The model prediction for residual drift ratios was less accurate than for peak drift ratios. This was primarily because the magnitude of the residual values was so small. The only discrepancy in model analysis was that the model predicted that the column would be permanently displaced to the NW. During testing, it was permanently displaced to the NE.

Figure 77 compares the predicted and measured time history of drift ratio for GM1 to GM7, while Figure 78 shows the same comparison for GM8 to GM11. The model predicted the time history in both directions for tests GM1 to GM7 with practically no error. After GM7, the model prediction in the W-E direction was slightly offset. As mentioned, the model predicted that a residual drift ratio would develop in the W direction while the test showed the opposite. The peaks in the time history were aligned despite the offset.

Figure 79 and Figure 80 compare the predicted and measured orbital response of the column. For GM1 to GM6 the predicted orbital path was again practically identical to the measured response. The rolling motion during testing was more significant than the model predicted. The general shape of the predicted path for GM7 to GM11 was also very close to the measured response except for the model offset to the W.

Table 27. Predicted and measured peak and residual drift ratios.

Test	*Measured values*						*Predicted values*						*Error in peak drift ratio*	
	Peak drift ratio, %			*Residual drift ratio, %*			*Peak drift ratio, %*			*Residual drift ratio, %*				
	N-S	*W-E*	**SRSS**	*N-S*	*W-E*	**SRSS**	*N-S*	*W-E*	**SRSS**	*N-S*	*W-E*	**SRSS**	*absolute*	*percent*
GM1	0.46	0.05	**0.46**	0.02	0.00	**0.02**	0.48	-0.04	**0.48**	0.00	0.00	**0.00**	0.02	3.6
GM2	2.05	-1.05	**2.11**	0.05	-0.03	**0.06**	1.90	-0.64	**1.96**	0.05	-0.02	**0.06**	-0.15	-7.1
GM3	1.74	-2.08	**2.08**	0.06	-0.04	**0.08**	1.82	-2.05	**2.06**	0.03	-0.04	**0.05**	-0.03	-1.3
GM4	-4.26	-1.70	**4.32**	0.02	-0.05	**0.05**	-4.23	-1.34	**4.26**	-0.01	-0.01	**0.02**	-0.06	-1.3
GM5	5.89	-2.02	**6.22**	0.08	-0.06	**0.10**	6.07	1.87	**6.10**	0.07	-0.03	**0.08**	-0.13	-2.0
GM6	-4.91	-2.96	**5.03**	0.17	-0.14	**0.22**	5.04	-2.14	**5.04**	0.14	-0.03	**0.14**	0.02	0.3
GM7	7.83	-3.14	**7.96**	0.35	-0.17	**0.39**	7.44	4.32	**7.94**	0.57	0.24	**0.62**	-0.02	-0.2
GM8	6.61	-5.15	**6.77**	0.24	-0.33	**0.41**	-6.69	5.36	**7.06**	0.53	0.77	**0.94**	0.28	4.2
GM9	7.10	-2.81	**7.18**	0.51	-0.31	**0.59**	6.29	2.29	**6.30**	0.41	0.92	**1.01**	-0.88	-12.2
GM10	6.93	-5.91	**7.20**	0.39	-0.51	**0.64**	6.22	4.94	**6.71**	0.28	0.82	**0.87**	-0.48	-6.7
GM11	8.01	-7.09	**8.84**	0.59	-0.68	**0.90**	7.87	5.32	**8.15**	0.41	0.75	**0.85**	-0.69	-7.8

**N, W directions are positive*
***SRSS refers to the resultant of the N-S and W-E directional components*

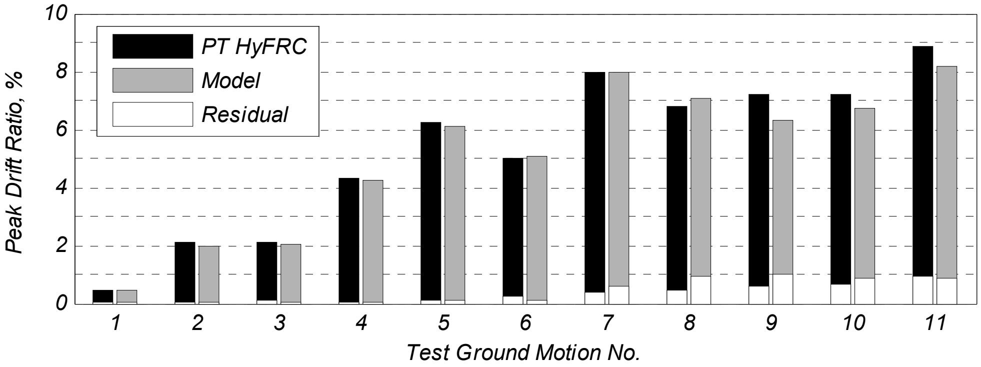

Figure 76. Comparison of predicted and measured peak and residual drift ratios.

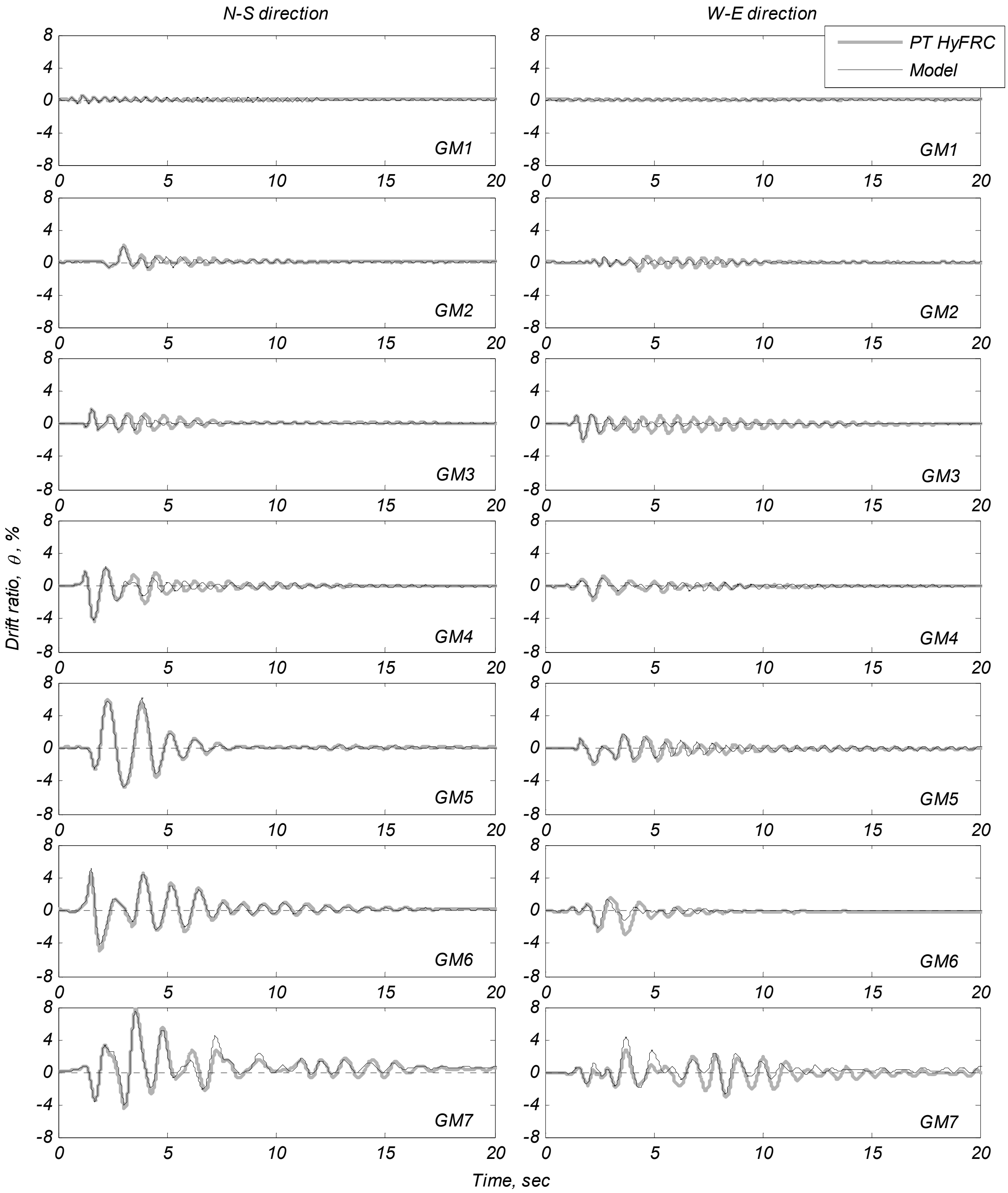

Figure 77. Predicted and measured time history of drift ratio for GM1 to GM7 in the N-S and W-E directions (N, W positive).

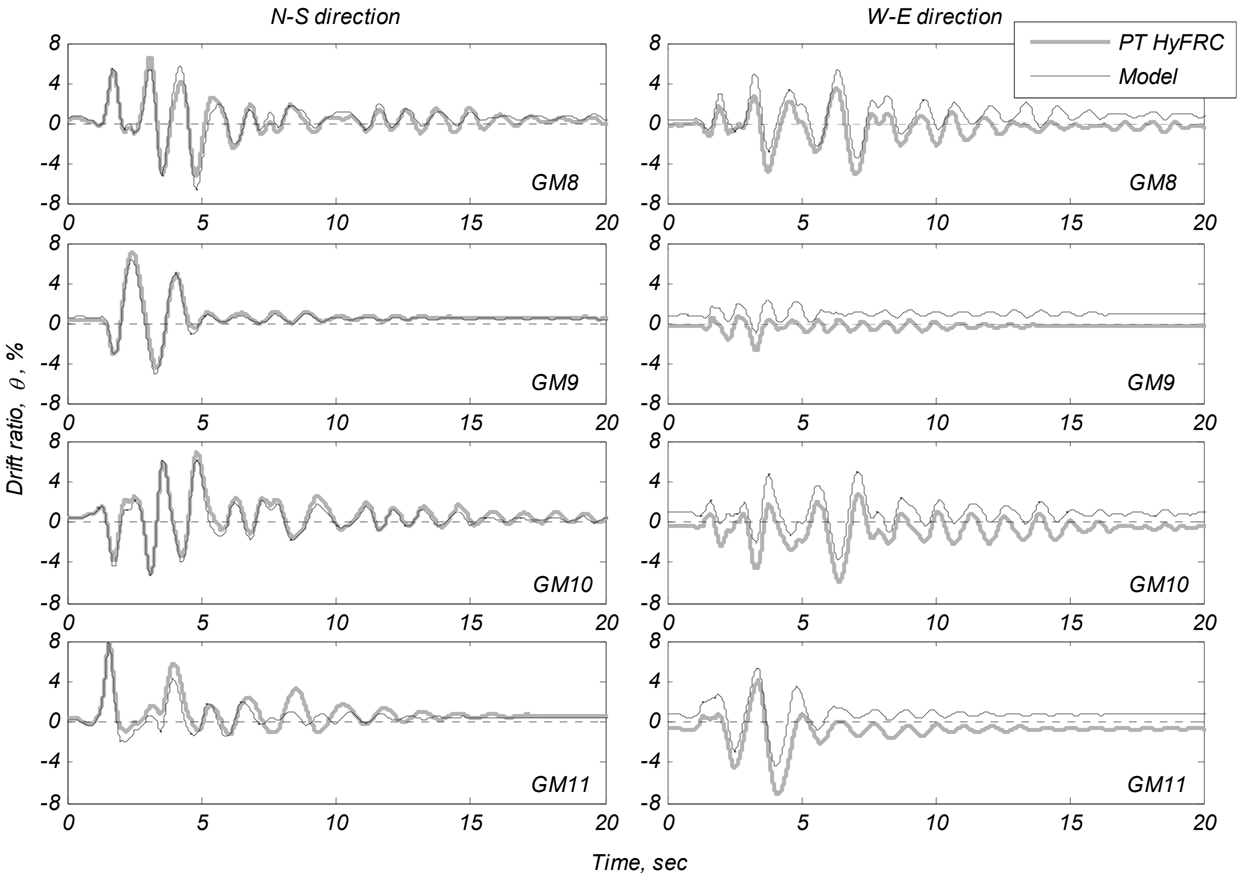

Figure 78. Predicted and measured time history of drift ratio for GM8 to GM11 in the N-S and W-E directions (N, W positive).

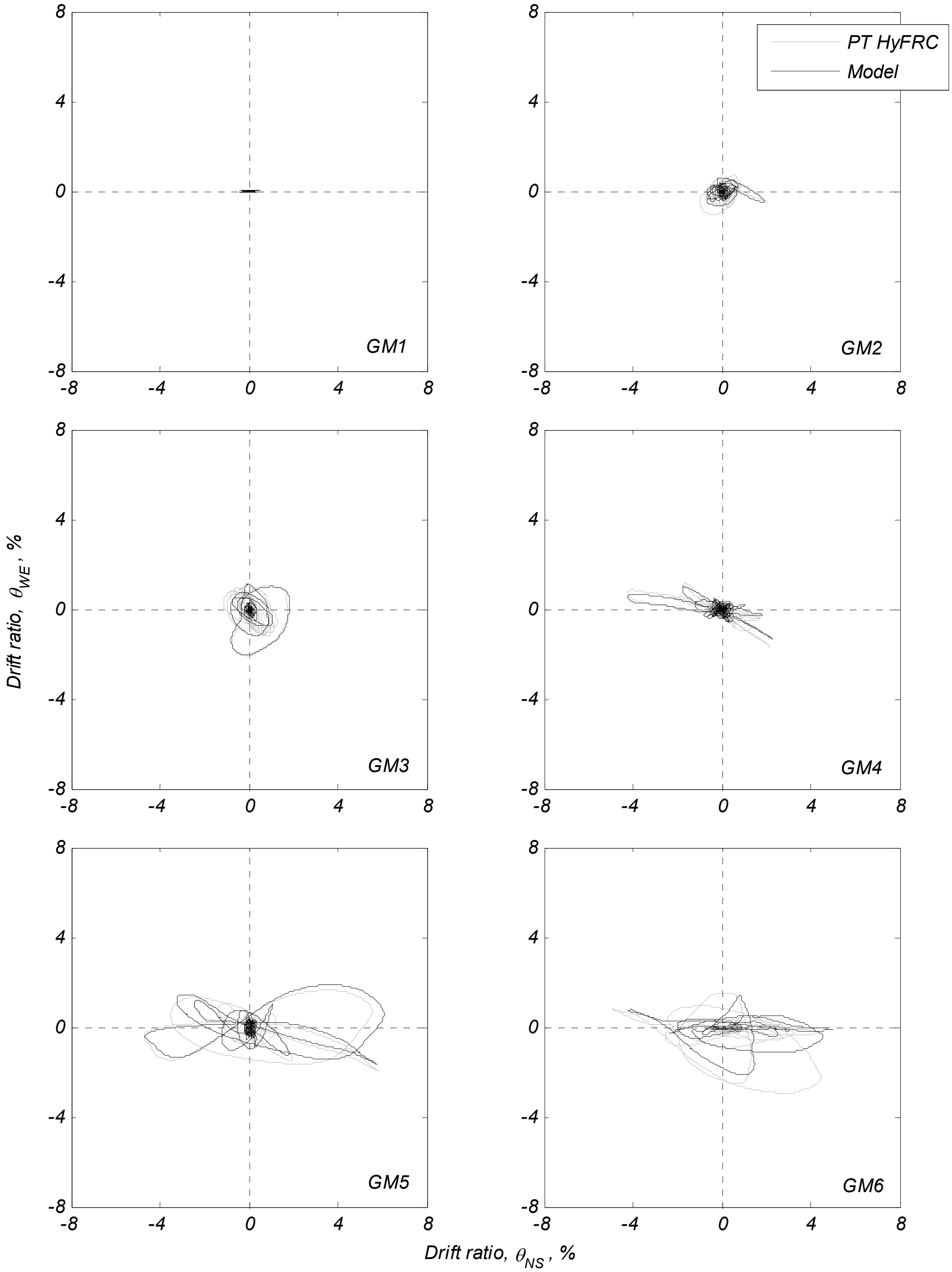

Figure 79. Predicted and measured orbits for GM1 to GM6.

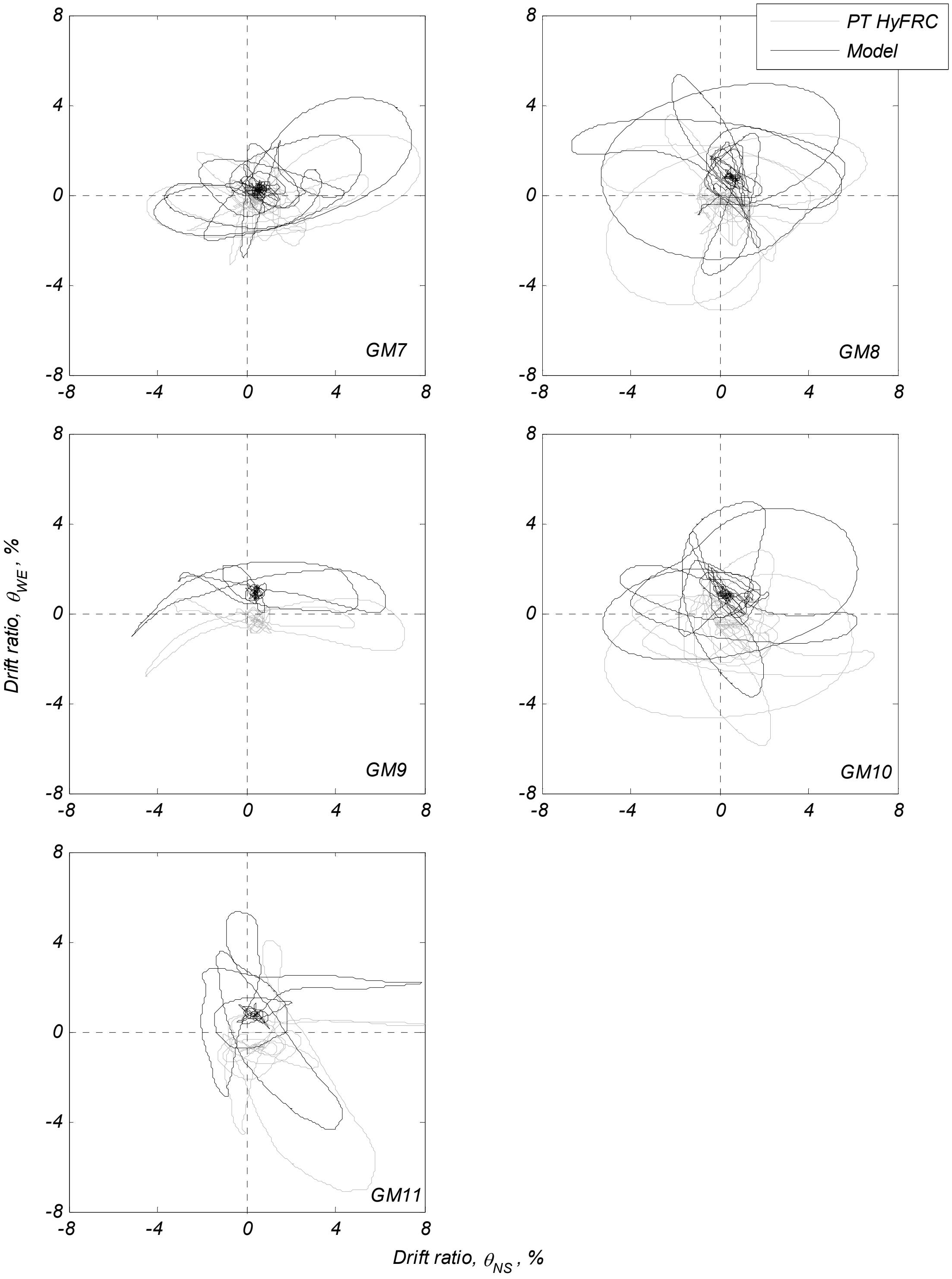

Figure 80. Predicted and measured orbits for GM7 to GM11.

4.7.3 Predicted changes in period of vibration

The fundamental periods predicted by the model in the first and second modes were equivalent and equal to T_1, $T_2 = 0.43$ seconds. The mode shapes consisted of displacement of the lumped mass in the two horizontal directions. The period of the third mode was $T_3 = 0.33$ seconds. The first two modes of the model correspond to translations of the lumped mass in two perpendicular directions, while the third mode corresponds to a torsional rotation of the column about the vertical axis and did not vary. The first two mode shapes are shown in Figure 81. The squares in the figure correspond to the nodes on the column axis. The top node is the anchorage of the PT while the second node from the top represents the location of the center of mass.

Table 28 and Figure 82 compare the predicted model periods with the measured periods obtained by white noise testing. The model periods were obtained by eigenvalue analysis of the stiffness and mass matrices at the start of each test. The model accurately predicted the elongation of the modal periods up to GM4. After GM4, the model tended to overestimate the period and the associated stiffness degradation compared to what occurred during testing.

The model's mode shapes likely changed direction as the column stiffness degraded in different directions. However, the white noise test periods were always calculated about the N-S and W-E axes. This discrepancy could in part explain the variability between the tested and predicted periods after GM4.

Table 28. Predicted and measured periods of vibration.

Test	*Fundamental period, T, sec*				
	*Measured values**		*Predicted values*		
	N-S direction	*W-E direction*	T_1	T_2	T_3
GM1	0.43	0.42	0.43	0.43	0.33
GM2	0.43	0.43	0.43	0.43	0.33
GM3	0.46	0.46	0.47	0.44	0.33
GM4	0.49	0.50	0.54	0.53	0.33
GM5	0.58	0.50	0.63	0.55	0.33
GM6	0.69	0.57	0.79	0.59	0.33
GM7	0.74	0.59	0.87	0.64	0.33
GM8	0.81	0.67	0.98	0.80	0.33
GM9	0.83	0.78	0.92	0.91	0.33
GM10	0.91	0.74	0.98	0.85	0.33
GM11	1.06	0.84	0.92	0.84	0.33
End	1.15	0.89	-	-	-
**Periods were obtained from white noise tests run before the start of each GM test*					

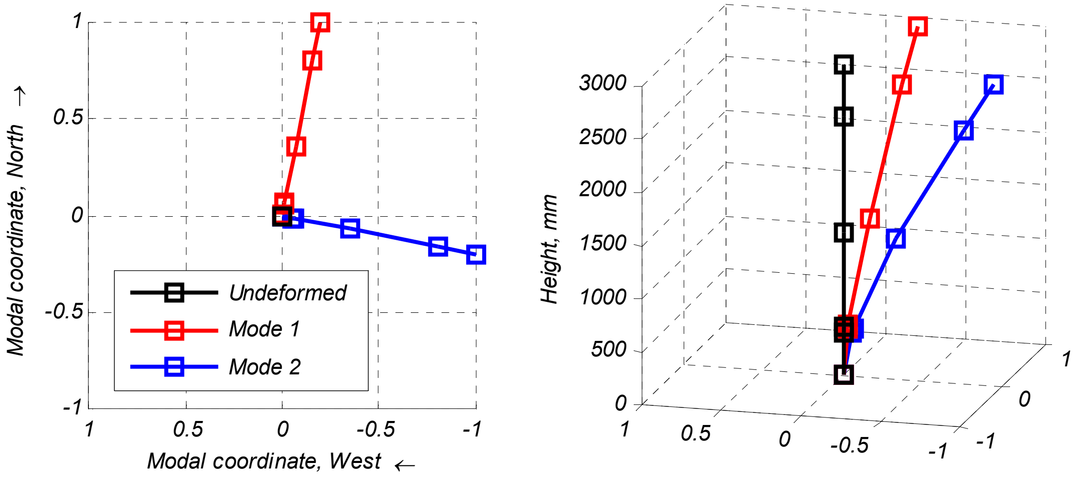

Figure 81. First two modes shapes of the analytical model.

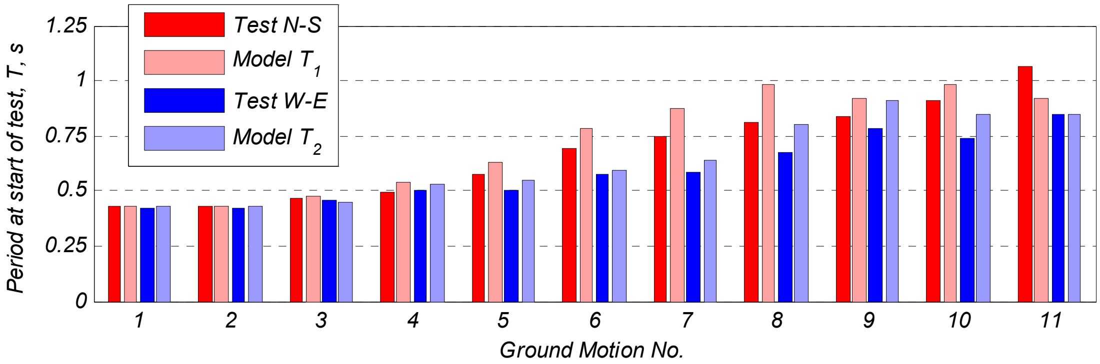

Figure 82. Comparison of predicted and measured period of vibration in two directions.

4.7.4 Predicted local column deformations

The predicted and measured uplift at the rocking plane on each side of the column are compared in Table 29. The error in the model relative to the test is also shown. These errors were consistent in magnitude with those of the peak drift ratios. Therefore, the correlation between uplift and drift ratio during testing was consistent in the model.

The uplift predictions were highly accurate, thus validating the modeling approach for the rocking plane. During GM4, the predictions were 91%, 118%, 90%, and 90% of the measured values on the N, S, W, and E faces, respectively. The predicted peak drift ratios in those directions were 106%, 99%, 86%, and 79% of the measured peak drift ratios. During GM5 and GM7 the uplift predictions were between 82% and 133% of the measured values while the peak drift ratios were 84% to 161% of the measured values.

The model tended to under-predict the uplift on the N and W sides and over-predict the uplift on the S and E sides. In the later tests, uplift was consistently over-predicted on the E face and under-predicted on the W face which agreed with the overestimation of displacements to the W.

The maximum compression strain predictions are shown in Table 30. The predicted compression strains were less accurate than the uplift predictions for several reasons. One reason is because the transducer measurements might not have been as accurate in compression. Localized compression damage affected the displacement transducer rod position and they became inclined from the horizontal as the HyFRC bulged outward during GM7 to GM11. Also, a least squares plane was fitted to the four transducer measurements to estimate the strains on the column faces. Hence, actual strains at a face may have been larger or smaller than reported in Table 30.

Figure 83(a) shows the predicted position of the rocking plane at the point of maximum drift ratio during GM5. Figure 83(b) shows the position measured during testing using the least-squares planar fit described previously. Figure 83(c) shows the measured position using the *Matlab* surface fitting function *griddata.m* (Matlab 2011). This function fits a smooth surface which passes through the transducer measurements rather than a least square plane. The circles represent the location of the transducers on the rods, and the transparent plane is located at zero uplift.

By fitting the surface through the transducer measurements, the neutral axis becomes curved and the uplift/strain profile is non-planar. This technique may provide a more accurate estimate of the real uplift/strain profile than fitting a least squares plane through the data. It forgoes a plane-sections-remain-plane (PSRP) assumption and instead allows the estimated rocking plane to deform according to the actual measurements. The PSRP assumption was forced in the model by the rigid connections of the compression springs. Hence, the neutral axis was always linear.

The orbit of the column was often circular in shape, and such displacement would imply that the edges of the column base would be more highly strained than the center. Regardless of method for fitting the test data, the model prediction and the planar fit of the measured data show strong agreement in terms of the depth and orientation of the neutral axis.

Figure 84 shows the predicted and measured uplift during GM7. The model overestimated the neutral axis depth and compressive deformation compared to the least squares fit of the measured data.

Table 29. Predicted and measured uplift at the column face.

Test	*Maximum uplift, mm*											
	N face			*S face*			*W face*			*E face*		
	PT HyFRC	*Model*	*Relative error, %*	*PT HyFRC*	*Model*	*Relative error, %*	*PT HyFRC*	*Model*	*Relative error, %*	*PT HyFRC*	*Model*	*Relative error, %*
GM1	0.5	0.5	-1	0.4	0.6	38	0.2	0.2	-17	0.1	0.2	24
GM2	2.4	1.3	-45	4.1	4.7	15	2.6	2.5	-5	1.4	1.1	-17
GM3	2.8	2.8	0	3.3	4.4	34	5.4	5.1	-5	2.3	2.9	24
GM4	13.2	12.0	-9	5.4	6.3	18	5.2	4.7	-10	6.2	5.6	-10
GM5	15.9	13.0	-18	14.2	16.6	17	9.7	9.2	-6	7.2	7.8	8
GM6	15.4	11.5	-25	10.3	12.7	23	8.4	5.5	-35	6.8	5.2	-23
GM7	13.5	11.1	-18	**17.5**	**20.4**	16	9.3	6.9	-26	10.4	**13.8**	33
GM8	**17.0**	**18.9**	11	13.4	13.0	-3	15.6	9.5	-39	10.6	13.0	23
GM9	14.3	14.4	1	15.2	15.0	-1	11.0	7.1	-36	4.0	4.9	22
GM10	16.2	14.1	-13	14.5	15.0	3	15.1	11.3	-25	7.3	10.2	39
GM11	4.8	5.3	12	16.8	20.1	20	**19.5**	**14.4**	-26	**11.0**	11.6	5

** **bold** values are the maximum for each face*

Table 30. Predicted and measured compression strains at the column faces.

Test	*Maximum compression strain, $\varepsilon_{c,max}$, %*											
	N face			*S face*			*W face*			*E face*		
	PT HyFRC	*Model*	*Relative error, %*	*PT HyFRC*	*Model*	*Relative error, %*	*PT HyFRC*	*Model*	*Relative error, %*	*PT HyFRC*	*Model*	*Relative error, %*
GM1	-0.34	-0.25	-26	-0.27	-0.23	-16	-0.01	-0.02	41	-0.01	-0.02	48
GM2	-1.36	-1.16	-15	-0.29	-0.36	21	-0.32	-0.33	2	-0.70	-0.38	-46
GM3	-1.42	-1.24	-13	-0.61	-0.52	-15	-0.69	-0.67	-3	-2.09	-1.34	-36
GM4	-0.85	-1.23	45	-3.05	-2.83	-7	-0.24	-0.35	49	-0.56	-0.49	-12
GM5	-3.62	-5.65	56	-4.10	-3.56	-13	0.39	-0.67	-273	-0.24	-0.92	289
GM6	-6.47	-5.02	-22	-4.75	-3.64	-23	-1.69	-1.13	-33	-3.78	-1.62	-57
GM7	-9.43	-6.52	-31	-4.74	-3.96	-16	-1.86	-3.23	74	-2.54	-2.48	-2
GM8	-11.52	-5.75	-50	-6.69	**-7.67**	15	-4.79	**-5.50**	15	-7.67	-3.97	-48
GM9	-13.98	-5.97	-57	-5.23	-6.37	22	-1.68	-2.19	30	-1.09	-1.28	18
GM10	-13.75	-6.35	-54	**-7.03**	-6.64	-6	-5.50	-4.46	-19	-9.75	**-5.31**	-46
GM11	**-16.52**	**-7.56**	-54	-2.32	-3.54	53	**-6.49**	-4.51	-30	**-11.83**	-4.98	-58

** **bold** values are the maximum for each face*

(a) Predicted uplift during GM5

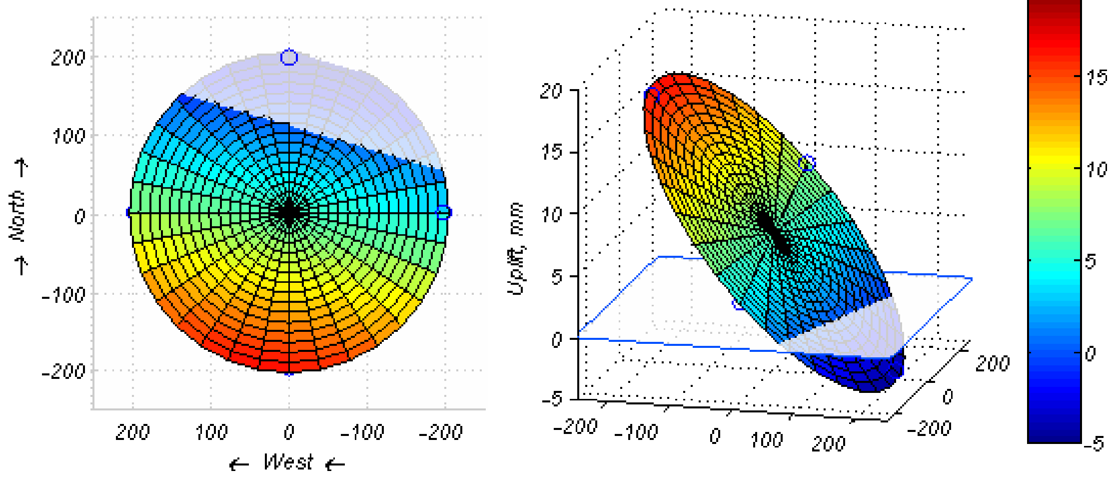

(b) Measured uplift during GM5 using least squares planar fit

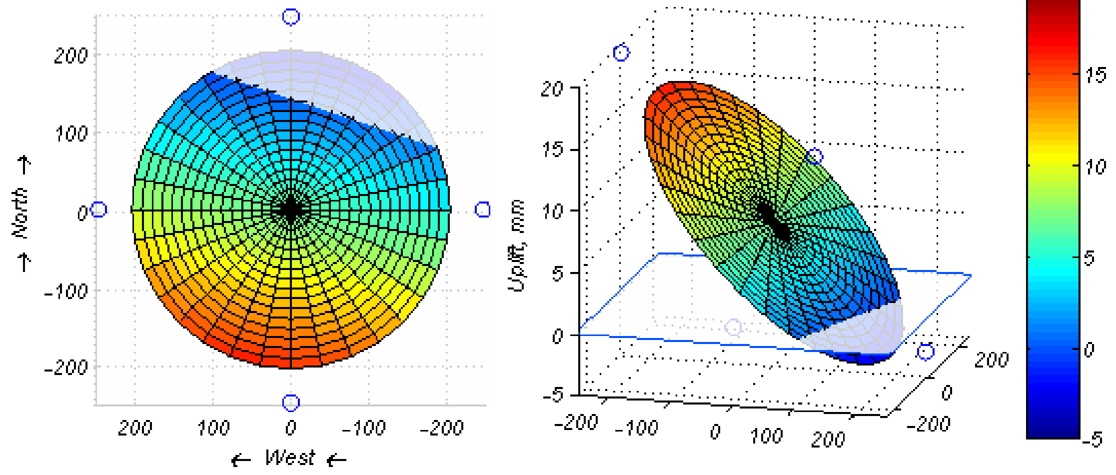

(c) Measured uplift during GM5 using surface fitting

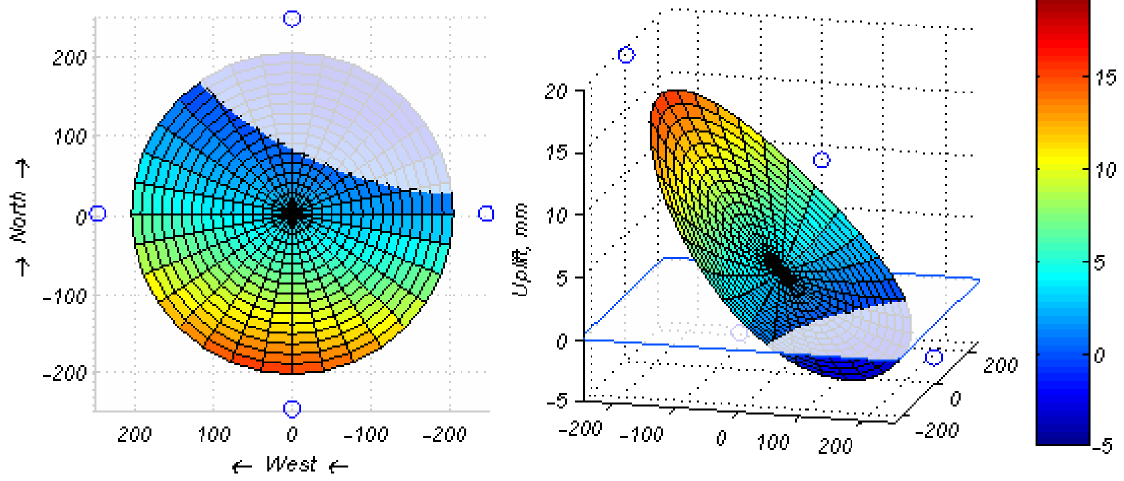

Figure 83. Uplift of the rocking plane at the peak drift ratio during GM5; (a) model prediction, (b) measured uplift using least squares planar fit, (c) measured uplift using surface fit.

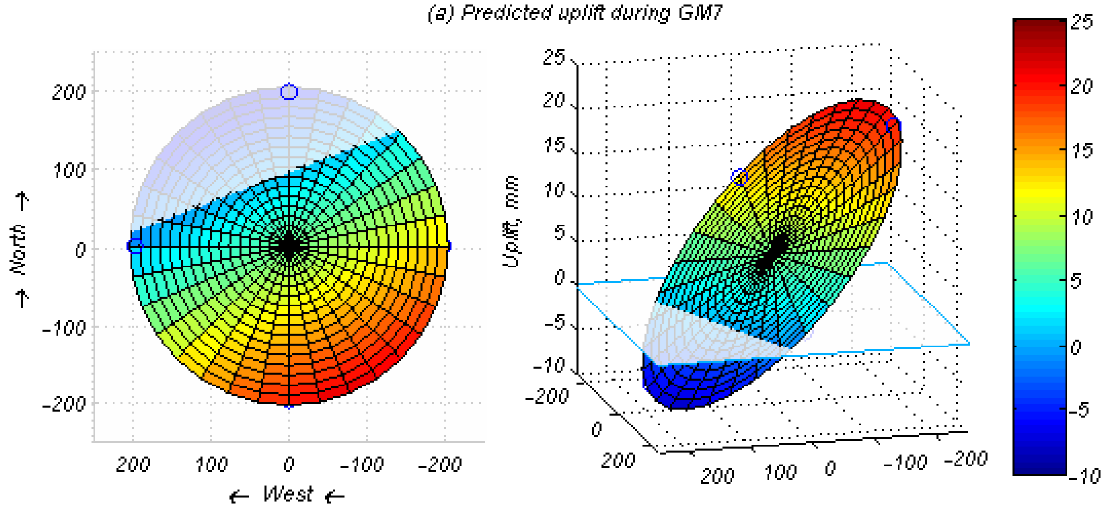
(a) Predicted uplift during GM7

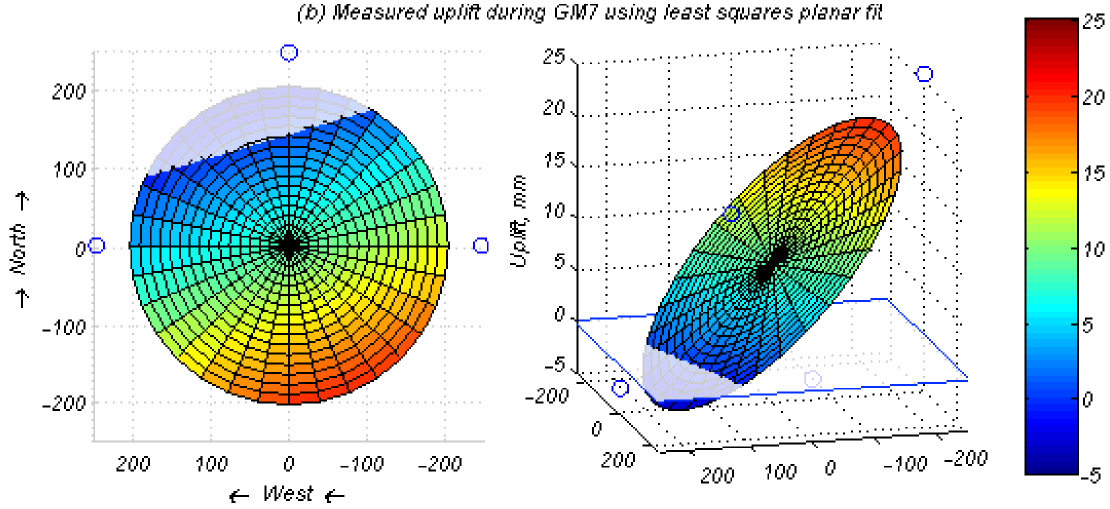
(b) Measured uplift during GM7 using least squares planar fit

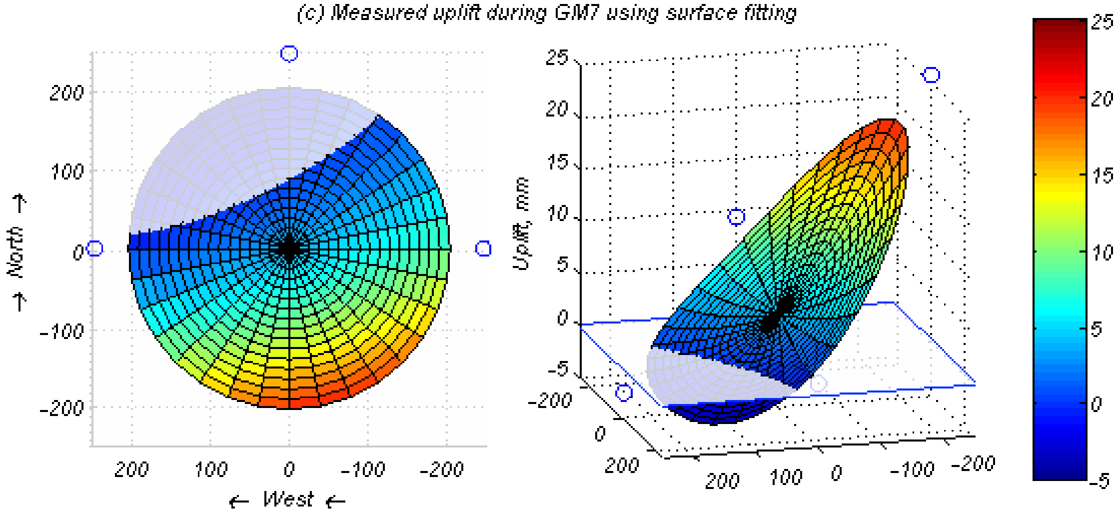
(c) Measured uplift during GM7 using surface fitting

Figure 84. *Uplift of the rocking plane at the peak drift ratio during GM7; (a) model prediction, (b) measured uplift using least squares planar fit, (c) measured uplift using surface fit*

4.7.5 Predicted lateral force-displacement response

The predicted and measured force-displacement response of the column are compared in Figure 85 through Figure 88. Table 31 gives the ratio of the predicted to measured maximum moments for each test. The predictions were between 80% and 124% of the measured values.

The model accurately predicted the lateral strength of the test column. The maximum predicted overturning moment in the N-S direction was -0.33WH at a drift ratio of -3.28% during GM4. This prediction was only 7% less than the maximum test moment which was equal to -0.36WH at a drift ratio of -2.99% during GM4. In the W-E direction, the maximum predicted moment was 0.30WH at a drift ratio of 5.33% during GM8. During testing, the maximum W-E moment occurred during GM3 and was equal to -0.31WH.

The predicted hysteretic response very closely followed the tested response. During GM4 and GM5 (see Figure 86) the predicted response in the N-S direction follows essentially the same path as the measured response over multiple reversing cycles of displacement, and the maximum predicted moments to the N and S directions were within 4% of the measured values. The curves also practically overlap for GM5 through GM11 in the N-S direction.

The model also accurately captured the drift ratios at zero moment after unloading ($\theta_{M=0}$) which were tabulated in Section 4.5.4. The model was able to accurately predict that the drift ratio at zero moment progressively increased during testing.

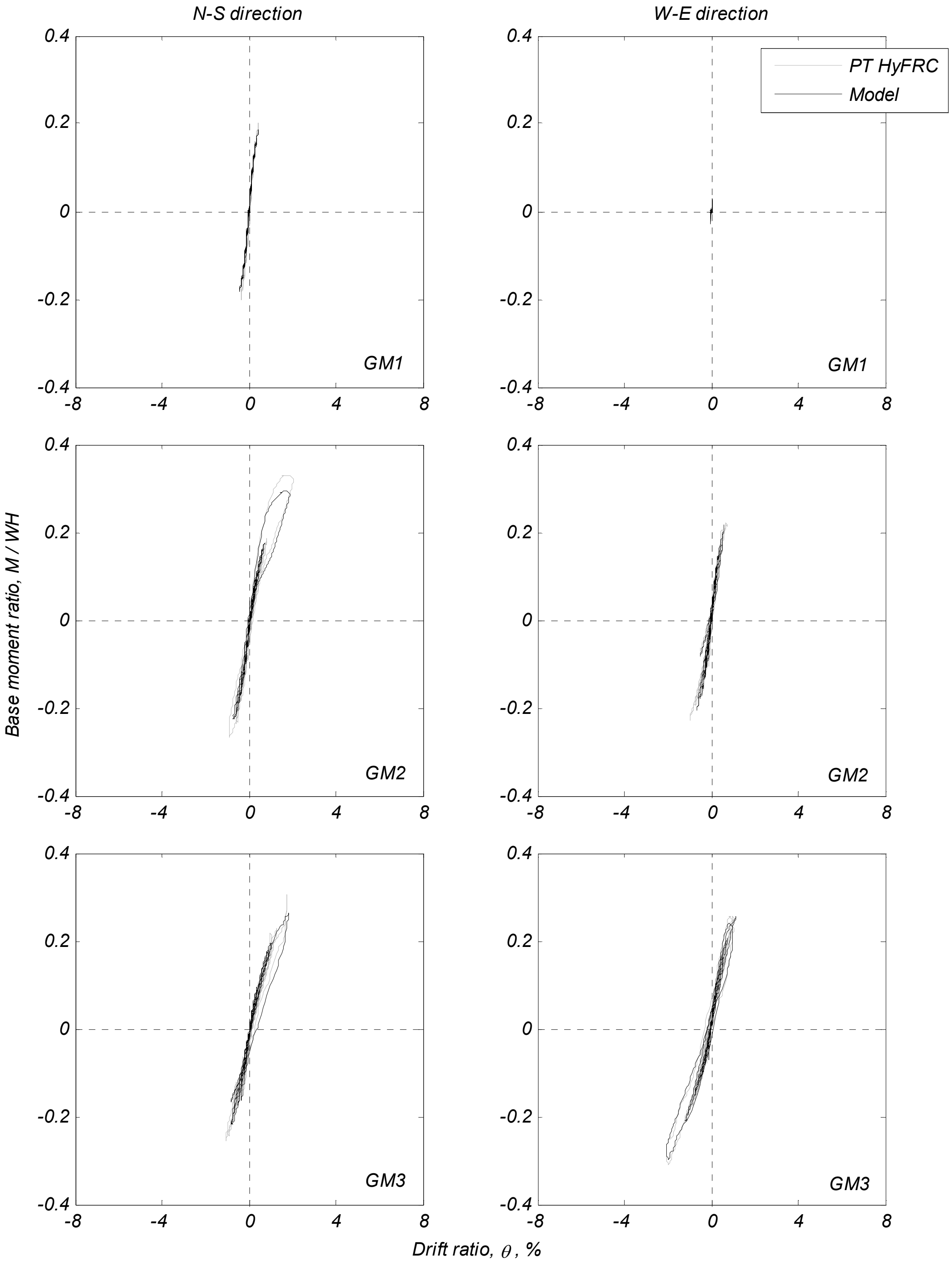

Figure 85. Predicted and measured overturning moment vs. drift ratio in the N-S and W-E directions (N, W positive) for GM1, GM2, and GM3.

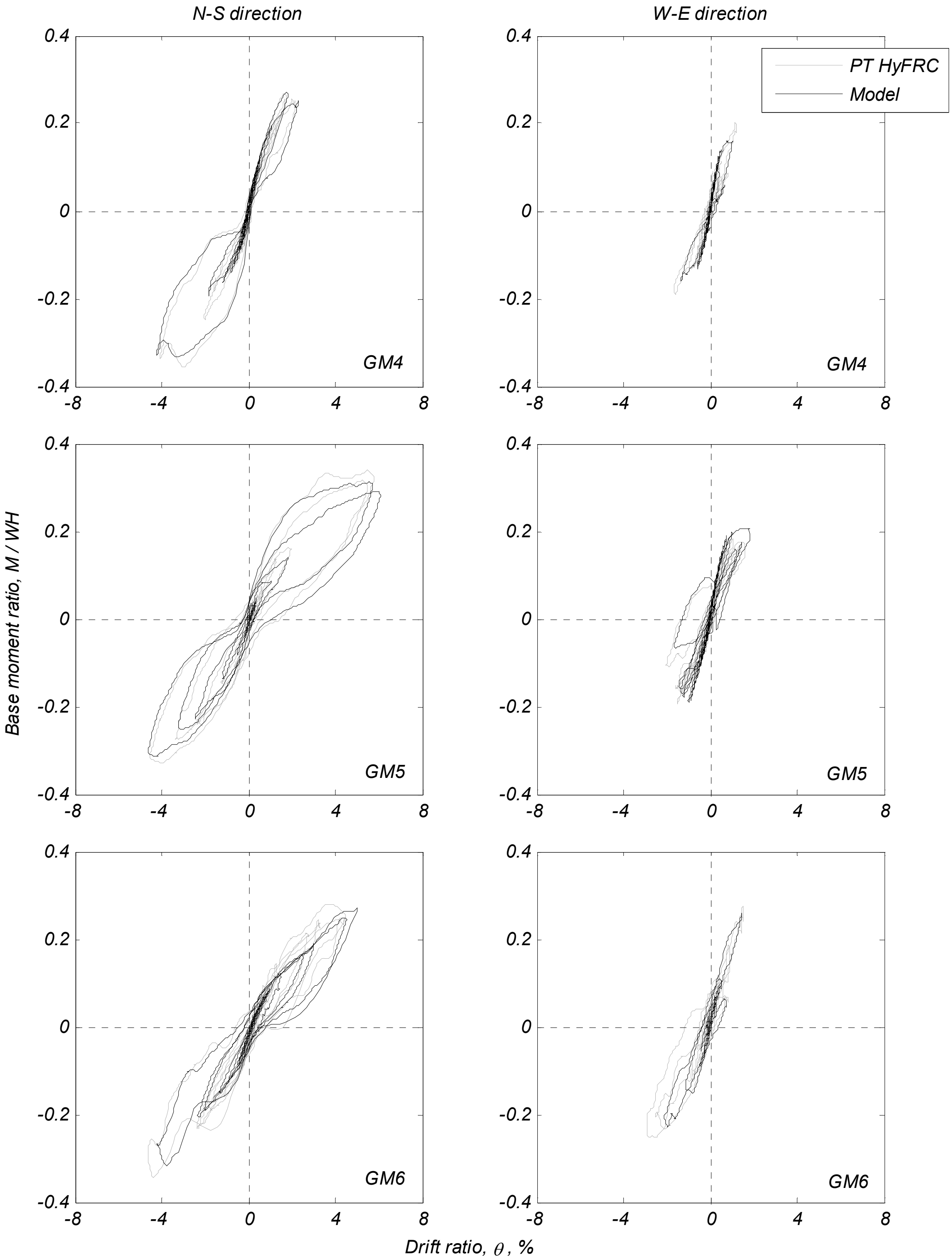

Figure 86. Predicted and measured overturning moment vs. drift ratio in the N-S and W-E directions (N, W positive) for GM4, GM5, and GM6.

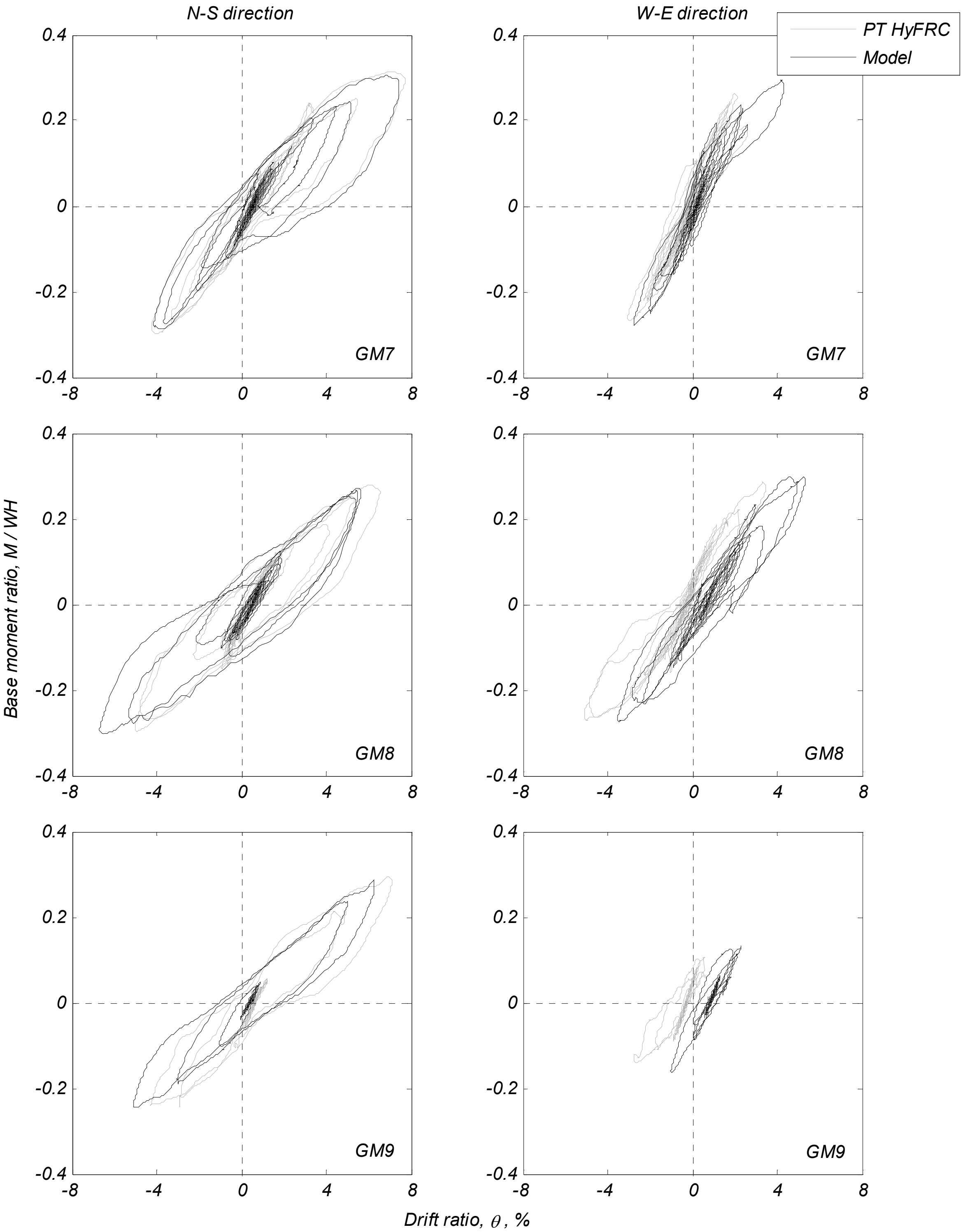

Figure 87. *Predicted and measured overturning moment vs. drift ratio in the N-S and W-E directions (N, W positive) for GM7, GM8, and GM9.*

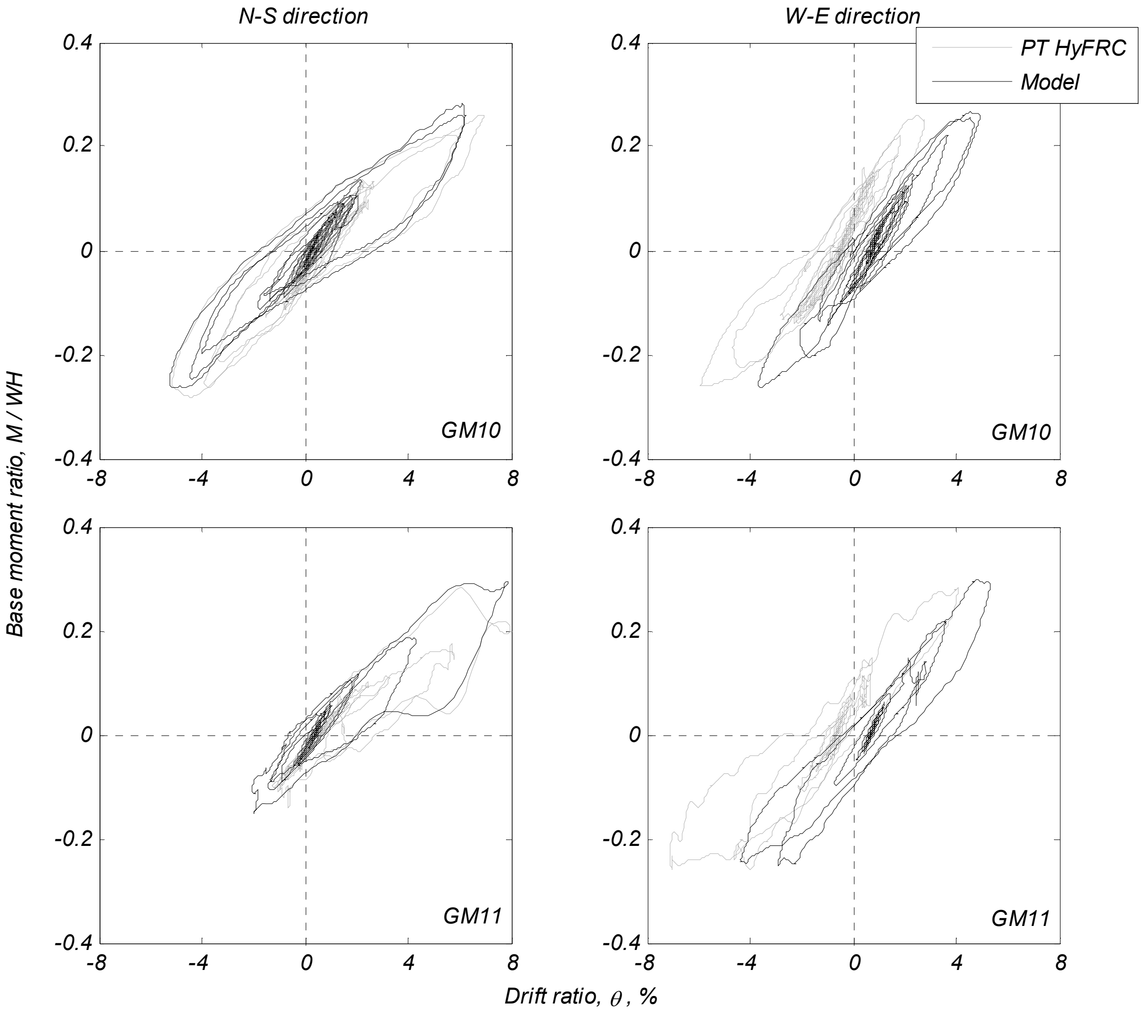

Figure 88. Predicted and measured overturning moment vs. drift ratio in the N-S and W-E directions (N, W positive) for GM10 and GM11

Table 31. Ratio of maximum predicted and measured moments in each direction .

Test	Ratio of maximum predicted moment to measured moment			
	N direction	S direction	W direction	E direction
GM1	0.93	0.90	1.24	1.21
GM2	0.90	0.85	0.99	0.88
GM3	0.86	0.85	1.00	0.96
GM4	1.01	0.94	0.80	0.84
GM5	0.92	0.96	1.13	1.00
GM6	0.97	0.93	0.94	0.90
GM7	0.98	0.97	1.12	1.04
GM8	0.98	1.02	1.04	1.01
GM9	0.97	1.00	1.23	1.17
GM10	1.07	0.94	1.03	1.02
GM11	1.05	1.08	1.06	0.97

4.7.6 Predicted post-tensioning force and strains

The predicted and measured post-tensioning forces for each ground motion are shown in Figure 89. The model post-tension force was calculated as the sum of the force in the four truss elements representing the strands while the measured test values are taken from the hydraulic pressure jack. The model overestimated the maximum PT force for all tests. The predictions were 107%, 109%, and 114% of the measured value for GM2, GM3, and GM4, respectively. The largest error was during GM7 when the model prediction was 131% of the measured value.

The model also predicted greater losses in PT force than were measured during testing. The PT force predicted by the model at the start of GM11 was 8% less than the measured value. The model's overestimation of the PT force may explain why the model's neutral axis depth was over-predicted during GM5 and GM7.

Figure 90 compares the strand strain gage measurements with the strains predicted using the analytical model. The model generally underestimated the strain at the start of each test and overestimated the peak strains during testing. The predicted starting strains were between 105% and 122% of the measured values and the predicted peak strains were between 113% and 160% of the measured values. The model's overestimation of peak strains was in line with the general overestimation in PT forces.

One potential source of discrepancy between the measured starting strain values and the model values was that the gages on the strands were oriented along the axis of the individual wires. The seven helical wires were inclined from the axis of the strand by approximately 10° on the surface. Strain along the strand axis would therefore be lower than the strain on the inclined axis. A second effect not considered in the model is the presence of slip between individual strands.

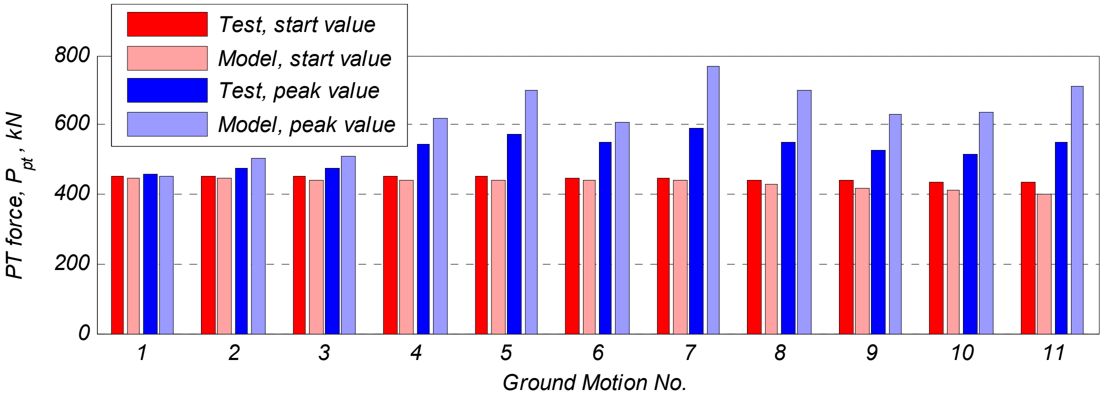

Figure 89. Predicted and measured post-tensioning forces

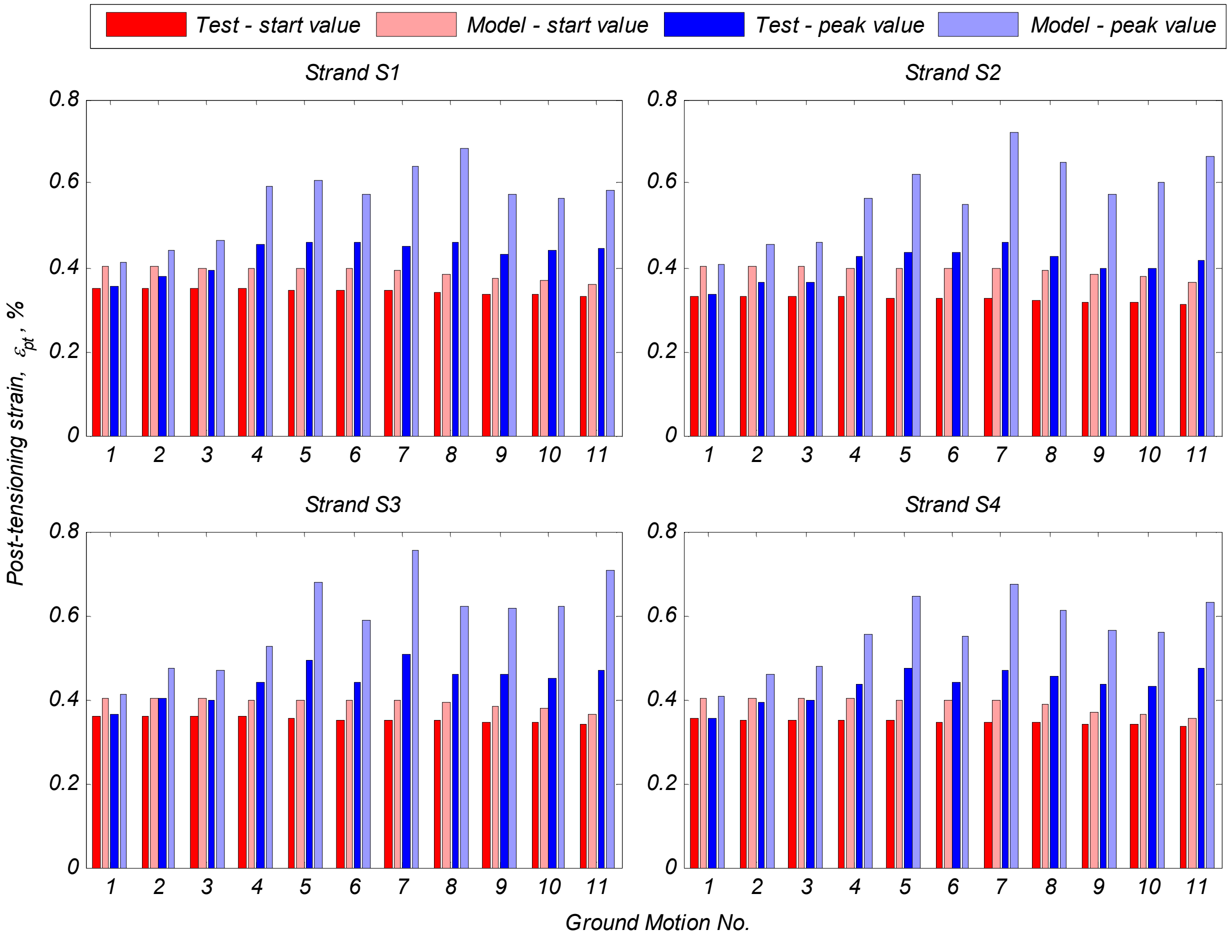

Figure 90. Predicted and measured strains in the PT strands.

4.8 Summary

This chapter presented shake table test results of the PT HyFRC column and compared them to a conventionally designed reference column. Performance was compared in terms of measured test quantities as well as observed damage.

The reference column exhibited ductile plastic hinging with no evidence of catastrophic failure mechanisms (e.g. bar rupture, spiral rupture) despite the significant residual drift ratio after GM7. The Caltrans seismic design criteria resulted in an adequately ductile response and the residual drift ratio was under 1.0% after the column achieved $\mu_D = 3.6$ and 5.6 during GM4 and GM5; the code indeed prevented collapse at these levels of demand. The spalling damage after GM5 would likely require significant repair in the form of grout patching and epoxy injecting of cracks. Re-plumbing of the column/bridge could also be required. The residual drift ratio of 1.6% after GM6 ($\mu_D = 5.9$) could require complete column replacement based on column demolitions conducted after the Kobe earthquake. Either scenario would lead to significant bridge downtime.

The PT HyFRC column experienced pronounced recentering and avoided formation of a plastic hinge. The combined reinforcement ratio of unbonded rebar and post-tensioning was less than the reference column's longitudinal reinforcement ratio, and a lateral strength nearly equivalent to the reference column was achieved by tuning the post-tensioned force in the analytical model used for design. Minor repairs would be required for continuous bridge functionality after the drift ratios of 4.3% to 8.0% achieved during GM4 to GM7. There would likely be no need to recenter the column and no traffic disruption since column integrity was preserved.

The following is a summary of key test results and observations:

- The lateral strength of the two columns was practically identical. The overturning resistance of PT HyFRC was 0.36*WH* while that of the reference column was 0.34*WH*.

- PT HyFRC had minimal residual displacement after the design-level (GM4, GM5) and MCE-level (GM7) earthquakes. The peak drift ratios during those tests were 4.3%, 6.2%, and 8.0% while the residual drift ratios were only 0.05%, 0.1%, and 0.4%.

- During the same ground motions, the reference column had peak drift ratios 3.7%, 5.8%, and 10.8% with residuals of 0.3%, 0.9%, and 6.8%. Testing was halted after the MCE-level test.

- Base rotation (caused by uplift) comprised over 78% of PT HyFRC's peak drift ratio when it exceeded 4%.

- During the MCE-level earthquake: (1) the maximum PT HyFRC column uplift was 17.5 mm, (2) the corresponding compression strain was -9.4%, (3) the maximum post-tension stress was 62% of yield, and (4) the maximum unbonded bar strain was 3.4%.

- No spalling was observed in the PT HyFRC column during any test. Spalling initiated in the reference column during the design-level test (GM4).

- The surface of the footing under the column base was undamaged after testing.

- Two unbonded bars fractured in PT HyFRC during the final test (GM11), but the residual drift ratio was only 0.9%.

- No bar buckling or spiral fracture was observed in either column during testing.

- Damage in PT HyFRC was less than PRC-U2 under similar displacement demands. PRC-U2 was post-tensioned with unbonded bars but had no HyFRC or headed bars.

The PT HyFRC column model was validated by comparing the results of dynamic analysis (using the ground motions recorded during testing) with the actual test results. The model was found to be highly accurate at predicting the column response. The following is a summary of key model results:

- The model error in predicted lateral strength was only 7%.
- The model error in predicting peak drift ratio was under 8% for the first eight ground motions.
- The model error in predicting residuals was larger due to their small magnitude.
- The model predicted that a residual drift ratio would develop in the W direction while the test showed the opposite.
- Except for that error, the time histories of drift ratio and the orbital paths predicted by the model align with the test response.
- The model's initial period was identical to the period measured by white noise testing.
- The model reproduced the lateral-force displacement response nearly identically and captured the drift ratio at unloading ($M_{\theta=0}$).
- For the MCE-level earthquake, the model predicted the following: (1) the maximum uplift was 17.5 mm, (2) the corresponding compression strain was -9.4%, (3) the maximum post-tension stress was 62% of yield, and (4) the maximum unbonded bar strain was 3.4%.
- The model over-predicted the force and strain demands in the post-tensioned strands by up to 60%.

5 Summary and Conclusions

The purpose of this dissertation was to investigate new materials and design methods that can increase the longevity of bridge structures while reducing or eliminating damage caused by earthquakes.

HPFRCC materials can increase bridge longevity by controlling deterioration processes (e.g. rebar corrosion or ASR) that degrade conventional concrete. Their performance in bridge columns under severe earthquake loading was also presumed to be superior based on prior tests. Modern R/C bridge columns provide adequate displacement ductility at the expense of significant damage and residual displacements during severe earthquakes. Advanced bridge column designs which avoid plastic hinging and encourage bridge recentering can ensure that bridges remain functional following earthquakes. Thus, bridges in California can be more durable and more earthquake resistant by combining HPFRCC materials with advanced design methods for bridge columns.

The research showed that reinforced HyFRC was more damage resistant than conventional concrete in compression and tension (Chapter 2). Furthermore, the advanced column design remained nearly plumb and showed only minimal damage after a representative California maximum considered earthquake (Chapter 4). This chapter will discuss the implications for seismic design using HyFRC and advanced bridge columns as well as recommendations for future research in these areas.

5.1 Considerations for the design of HyFRC columns

The results of this dissertation provided considerable insight into the benefits and potential drawbacks of HyFRC for seismically designed bridge columns. The material was shown to be beneficial for resisting large compression demands, but the tensile response revealed that the material may actually reduce the ductility of rebar during earthquakes.

5.1.1 Design for compression

In uniaxial compression, reinforced HyFRC was shown to retain more strength than conventional concrete at equal levels of post-peak deformation. Both unconfined and confined HyFRC had gradual post-peak softening responses. Increasing the transverse reinforcement ratio tended to increase confined concrete strength, but the softening response was consistent across all ratios including unconfined specimens. Cover spalling did not occur and cracking was distributed.

In contrast, unconfined concrete experienced a brittle failure (i.e. cover spalling) after the peak load. Confined concrete specimens had more abrupt softening than HyFRC. Increasing the transverse ratio improved the peak strength and the softening response. Post-peak behavior similar to HyFRC was achieved only at the highest tested transverse ratios. Spalling occurred in concrete specimens and cracks localized to one dominant shear plane.

These response characteristics were also observed in tests of HyFRC columns (Chapter 3) as well as the shake table test of the PT HyFRC column (Chapter 4). Specimens TS-1 and TS-2 were designed with half the amount of transverse reinforcement required by Caltrans SDC; however, spalling did not develop in those columns until a drift ratio of 4.8%. The spalling was significantly less severe than that of R/C columns with twice the transverse reinforcement at the same drift ratio. The HyFRC shell and the PT HyFRC columns had code-compliant levels of transverse reinforcement, and spalling and bar buckling were completely avoided. These columns were tested to drift ratios in excess of 12% and 8%, respectively.

The damage resistance of HyFRC in compression was particularly well-suited for the PT HyFRC column. Post-tensioning causes a higher axial force than in conventional columns, and, consequently, the compressive demands are larger. The PT HyFRC column had a total axial load (P_t) three times that of the reference column (α_t was larger by a factor of 1.83). The PT HyFRC column avoided spalling and buckling despite having an axial load ratio that was twice that of TS-1, TS-2, and the HyFRC shell.

The spalling resistance and compression ductility of HyFRC are both well suited for seismic design situations. Considerations for the design of HyFRC columns in compression are summarized in the following:

- HyFRC columns can achieve a ductile compression response (in terms of spalling and bar buckling) with lower levels of transverse reinforcement.

- HyFRC columns retain strength in the extreme compression fibers at large deformations by preventing spalling. This strength should be considered in nonlinear M-φ analysis.

- HyFRC was able to sustain compression strains of over 10% in the post-tensioned column.

- HyFRC may influence bar buckling and provide more resistance than concrete which can spall. It may be particularly effective in columns where transverse reinforcement is widely spaced.

- Adequate spiral and bar spacing should be provided to allow free ingress of the largest fibers into cover material.

5.1.2 Design for tension

In uniaxial tension, reinforced HyFRC attained significantly higher strength than the bare reinforcing bar well beyond its yield strain. The strength of the concrete samples never exceeded the yield strength of the rebar. The strength enhancement was due to crack bridging by fibers.

The composite fracture strain in HyFRC at a reinforcing ratio typical of reinforced concrete columns ($\rho_l = 1.2\%$) was comparable to concrete at the same ratio. Several crack localizations occurred at different instances during the response. For HyFRC at a lower reinforcing ratio ($\rho_l = 0.6\%$), the fracture strain was significantly reduced because localization occurred at a single crack.

In the former case, strain hardening of the rebar at the dominant crack caused the composite load to increase. This forced strain hardening to occur at other cracks to maintain equilibrium. Consequently, multiple cracks opened simultaneously as fiber load resistance (due to crack opening) degraded and rebar load resistance increased (due to strain hardening) at each crack. In the latter case, strain hardening of the rebar at the dominant crack was not large enough to cause cracks to open elsewhere. Once the fiber contribution degraded at the dominant crack, the load resistance of the rebar alone at that crack was less than the rebar plus fibers at other cracks.

This tension strain localization effect was observed to some extent in specimen TS-2 (Panagiotou et al. 2014), which had a longitudinal ratio of $\rho_l = 1.2\%$ and was made of HyFRC. The column tested by Haralddsson et al. (2013), which had HyFRC bonded to longitudinal rebar at $\rho_l = 0.8\%$, suffered a single, severe crack localization at the column base with minimal cracking elsewhere. That localization was not surpising given these test results. Columns made from other HPFRCC's showed similar localization (Aviram et al. 2014, Kawashima et al. 2012, Fischer and Li 2003, Saiidi et al. 2009), yet all of those columns had reinforcing ratios of at least $\rho_l = 1.2\%$.

Hence, the question arises as to why the multiple-cracking behavior observed in the uniaxial tension specimens did not occur in the columns with the same reinforcing ratio. The answer lies in the loading method for each situation. The columns were subjected to lateral loads which would have caused a triangular moment distribution at the base; hence, the tensile force resultant would decrease over column height. The uniaxial specimens experienced a uniform tension force. Thus, localization occurred in the columns because the tensile force resultant above the localization was not large enough to cause additional cracks to open. Hence, the localization effect observed in the uniaxial tests is exacerbated for columns under lateral load.

Tensile strain localization was avoided in columns with unbonded bars—TS-1, the HyFRC shell, and PT HyFRC. In those columns, the majority of tensile deformation was concentrated at the footing interface where uplift occurred.

Considerations for the design of HyFRC columns in tension are summarized in the following:

- Column lateral strength can be significantly enhanced by HyFRC in tension when longitudinal bars are bonded.

- The strength enhancement continues after bars yield and should be considered in nonlinear *M*-φ analysis.

- Localization of deformation at a single crack may occur when rebar is bonded. This can result in bar fracture at lower tensile strains than for R/C columns.

- Unbonding the longitudinal bars can circumvent the localization effect; however, doing so eliminates the lateral strength contribution of the HyFRC in tension.

5.2 Bridge resilience using PT HyFRC columns

The PT HyFRC column was shown to be more earthquake resilient than a conventionally designed reference column having the same strength and geometry (Chapter 4). The reference column performed adequately under the design-level earthquake, but damage developed as would be expected. Under the MCE-level earthquake, the residual drift ratio of the reference column would require complete bridge demolition and replacement to bring the roadway back in to service.

The PT HyFRC column had practically no damage or residual displacement at both the design and MCE-levels. A bridge designed with such columns could remain in full service following the earthquake, and only minor cosmetic repairs would be required, if any. The ability the column to remain in service was further confirmed by the fact that the post-tensioned strands did not yield and the unbonded bars did not fracture. Reinforcement of the rocking plane with both HyFRC and headed rebar was shown to provide excellent ductility under the large compression forces that resulted from post-tensioning and gravity forces.

One potential objection to such columns may be the uncertainty in modeling and the lack of general code-based design guidelines. The design and modeling used for the test column represented a simplified performance-based approach which proved adequate in this situation. Prescriptive design methods are less appropriate for this type of system due to its complexity and were not explored in this dissertation.

The modeling technique proposed here (Chapter 3) produced accurate predictions of column strength and ductility capacity. In fact, the model likely predicted the inelastic response of the column better than existing models could predict the behavior of R/C columns when drift ratios exceeded 3-4%.

5.3 Recommendations for future research

Some aspects of the seismic performance of HyFRC in bridge columns might be better understood by conducting additional experimental or investigations. Such investigations are explained in the following:

- The confinement tests were conducted on specimens that were quite small compared to full-scale bridge columns. Fibers could not be scaled. Full-scale compression tests similar to those of Mander et al. (1988a) would be more appropriate for deducing the properties of confined HyFRC in bridge columns.

- The assumptions for the load carried by longitudinal rebar and concrete in prior confinement tests should be re-visited as they can significantly affect the resulting confined concrete stress-strain curves. Optimal confinement tests would also attempt to measure the load in the longitudinal bars as well as slip.

- The tension stiffening/strengthening effects were explored using uniaxial tests (direct tension) rather than flexural tests. Therefore, the tests were not designed to simulate the localization behavior observed in columns. A series of flexural tests of specimens with varying reinforcing ratios might provide more insight into how the quantity of rebar affects localization in HyFRC.

- The ability of HyFRC to resist bar buckling is not well understood and could be explored by experimental testing.

- The application and understanding of unbonded reinforcement could be improved through additional experimental testing. Complete unbonding (i.e. constant strains) are typically assumed for design and modeling, yet strains over the unbonded length varied in PT HyFRC based on gage measurements. Furthermore, recommendations for unbonding techniques would likely be required by practitioners before such designs could be implemented.

Some additional topics were outside the scope of this investigation but are reasonable extensions of the work presented here. Relevant topics that were not specifically addressed in this research include:

- Development of confinement models for HPFRCC's based on full-scale tests. Such models would target predictive stress-strain equations that are a function of cross section shape, matrix strength, fiber quantities and properties, and the properties of the transverse reinforcement ties or spirals.

- Development of better installation and connection details for the PT HyFRC column including a cap beam connection.

- Analytical or experimental evaluation of the column performance in multi-column bents with stiff cap beams (i.e. columns in double curvature).

- Analytical or experimental investigation of the column in multi-bent bridge structures with spatial and temporal variations in ground motion attenuation.

- A performance-based earthquake engineering assessment of the column, compared to conventional designs.

- Investigation of the corrosion risk to the unbonded rebar and strands in the PT HyFRC column (both before and after earthquakes).

- Investigation of the feasibility to mix HPFRCC materials in large batches in the field (e.g. in ready-mix trucks) or in a manufacturing setting (e.g. precast concrete plant).

- Analytical or experimental investigation of flexure-shear interactions in HyFRC.

6 References

Abrishami, H., and Mitchell, D. (1997). “Influence of steel fibers on tension stiffening.” *ACI Structural Journal*, America Concrete Institute, 94(6), 769-776.

American Concrete Institute (2010). “Building Code Requirements for Structural Concrete.” *ACI Committee 318-10*, American Concrete Institute, Farmington Hills, MI.

American Society of Civil Engineers (2013). “Bridges: Investment and Funding.” *2013 Report Card for America’s Infrastructure*, Retrieved: April 18, 2014, <http://www.infrastructurereportcard.org/a/#e/bridge-repair-costs>.

Antonellis, G. and Panagiotou, M. (2013). “Seismic Response of Bridges with Rocking Foundations Compared to that of Fixed-base Bridges at a Near-fault Site.” *Journal of Bridge Engineering*, American Society of Civil Engineers, accepted for publication Oct. 2013.

Ardakani, S. and Saiid, M. (2013). "Design of Reinforced Concrete Bridge Columns for Near-fault Earthquakes," *Report No. CCEER-13-13*, Center for Civil Engineering Earthquake Research, Department of Civil and Environmental Engineering, University of Nevada, Reno, NV.

Aviram, A., Stojadinovic, B., Parra-Montesinos, G., and Mackie, K. (2010). “Structural Response and Cost Characterization of Bridge Construction Using Seismic Performance Enhancement Strategies.” *PEER Report 2010/01*, Pacific Earthquake Engineering Research Center, University of California, Berkeley, CA.

Beck, J. L. and Skinner, R., I. (1974). “The Seismic Response of a Reinforced Concrete Bridge Pier Designed to Step.” *Earthquake Engineering and Structural Dynamics*, John Wiley and Sons, Vol. 2, 343-358.

Belleri, A., Schoettler, M. J., Restrepo, J. I., and Fleischman, R. B. (2013). “Dynamic Behavior of Rocking and Hybrid Cantilever Walls in a Precast Concrete Building.” *ACI Structural Journal*, American Concrete Institute, accepted for publication Jan. 2013.

Billington, S. L. and Yoon, J. K. (2004). “Cyclic Response of Unbonded Posttensioned Precast Columns with Ductile Fiber-Reinforced Concrete.” *Journal of Bridge Engineering*, American Society of Civil Engineers, 9(4), 353-363.

Bischoff, P. (2003). “Tension stiffening and cracking of steel fiber-reinforced concrete.” *Journal of Materials in Civil Engineering*, America Society of Civil Engineering, 15(2), 174-182.

Blunt, J. and Ostertag, C. P. (2009). “Deflection Hardening and Workability of Hybrid Fiber Composites.” *ACI Materials Journal*, American Concrete Institute, 106(3), 265-272.

Buckle, I., Constantinou, M., Dicleli, M., and Ghasemi, H. (2006). “Seismic Isolation of Highway Bridges.” *Special Report MCEER-06-SP07*, MCEER, University at Buffalo, The State University of New York, Buffalo, NY.

California Department of Transportation (2010). “Caltrans Seismic Design Criteria Version 1.6.” Sacramento, CA.

Campione, G., Mindess, S., & Zingone, G. (1999). “Compressive stress-strain behavior of normal and high-strength carbon-fiber concrete reinforced with steel spirals.” *ACI Materials Journal*, American Concrete Institute, 96(1), 27-36.

Cheng, C. T. (2008). “Shaking table tests of a self-centering designed bridge substructure.” *Engineering Structures*, Elsevier, 30, 3426-3433.

Choi, H., Saiidi, M., and Somerville, P. (2007). "Effects of Near-Fault Ground Motion and Fault-Rupture on the Seismic Response of Reinforced Concrete Bridges." *Report No. CCEER-07-06*, Center for Civil Engineering Earthquake Research, Department of Civil Engineering, University of Nevada, Reno, NV.

Choi, H., Saiidi, M., Somerville, P., and El-Azazy, S. (2010). “Experimental Study of Reinforced Concrete Bridge Columns Subjected to Near-Fault Ground Motions.” *ACI Structural Journal*, American Concrete Institute, 107(1), 3-12.

Chopra, A. (2006). *Dynamics of Structures, 3rd Edition*. Prentice Hall, Upper Saddle River, NJ.

Chou, C. and Chen, Y. (2006). “Cyclic tests of post-tensioned precast CFT segmental bridge columns with unbonded strands.” *Earthquake Engineering and Structural Dynamics*, Wiley InterScience, 35, 159-175.

ElGawady, M., Booker, A. J., and Dawood, H. M. (2010). “Seismic Behavior of Posttensioned Concrete-Filled Fiber Tubes.” *Journal of Composites for Construction*, American Society of Civil Engineers, 14(5), 616-628.

Fantilli, A., Mihashi, H., Vallini, P., and Chiaia, B. (2011). “Equivalent Confinement in HPFRCC Columns Measured by Triaxial Test.” *ACI Materials Journal*, American Concrete Institute, 108(1), 159-167.

Fantilli, A., Vallini, P., and Chiaia, B. (2011). “Ductility of fiber-reinforced self-consolidating concrete under multi-axial compression.” *Cement & Concrete Composites*, 33, 520-527.

FEMA (2000). “Prestandard and Commentary for the Seismic Rehabilitation of Buildings.” *FEMA 356*, Federal Emergency Management Agency, Washington, D.C.

Filippou, F. C. (2007a). FEDEAS: Materials: Concrete material models. Retrieved: April 18, 2014, <http://www.ce.berkeley.edu/~filippou/Research/Fedeas/concrete.pdf>.

Filippou , F. C. (2007b). FEDEAS: Materials: Reinforcing steel material models. Retrieved: April 18, 2014, <http://www.ce.berkeley.edu/~filippou/Research/Fedeas/steel.pdf>.

Filippou, F. C., Popov, E. P., Bertero, V. V. (1983). "Effects of Bond Deterioration on Hysteretic Behavior of Reinforced Concrete Joints." *Report EERC 83-19*, Earthquake Engineering Research Center, University of California, Berkeley.

Fischer, G. and Li, V. (2002). “Effect of matrix ductility on deformation behavior of steel reinforced ECC flexural members under reversed cyclic loading conditions.” *ACI Structural Journal*, American Concrete Institute, 99(6), pp. 781-790.

Fischer, G., and Li, V. (2003). “Deformation Behavior of Fiber-Reinforced Polymer Reinforced Engineered Cementitious Composite (ECC) Flexural Members under Reversed Cyclic Loading Conditions.” *ACI Structural Journal*, American Concrete Institute, 100(1), 25-35.

Foster, S. J., & Attard, M. M. (2001). “Strength and ductility of fiber-reinforced high-strength concrete columns.” *Journal of Structural Engineering*, American Society of Civil Engineers, 127(1), 28-34.

Ganesan, N., & Murthy, J. V. (1990). “Strength and behavior of confined steel fiber reinforced concrete columns.” *ACI Materials Journal*, American Concrete Institute, 87(3), 221-227.

Grupp, J., Blunt, J., Ostertag, C. P., and Devine, T. (2007). “Effect of steel microfibers on corrosion of steel reinforcing bars.” *Cement and Concrete Research*, 37(7), 1115-1126.

Guerrini, G. and Restrepo, J. (2013a). “Seismic Response of Composite Concrete-Dual Steel Shell Columns for Accelerated Bridge Construction.” *Proceedings, Seventh National Seismic Conference on Bridges & Highways*, Paper No. B5-1, Oakland, CA.

Guerrini, G. and Restrepo, J. (2013b). “Seismic Response of Recentering Precast Composite Concrete-Dual-Shell-Steel Columns.” *Proceedings, 10th International Conference on Urban Earthquake Engineering*, Tokyo Institute of Technology, Tokyo, Japan.

Haraldsson, O., Schoettler, M., Finnsson, G., Davis, P., Stanton, J., and Eberhard, M. (2013). “Seismic Resistance of Precast Concrete Bridge Columns Made with Unbonded Pre-

Tensioning and Hybrid Fiber Reinforced Concrete," *Proceedings, Seventh National Seismic Conference on Bridges & Highways*, Paper No. B4-4, Oakland, CA.

Hewes, J. T. and Priestley, M. J. (2002). "Seismic Design and Performance of Precast Concrete Segmental Bridge Columns." *Report No. SSRP-2001/25*, University of California, San Diego.

Housner, G. W. (1963). "The Behavior of Inverted Pendulum Structures During Earthquakes," *Bulletin of the Seismological Society of America*, 53(2), 403-417.

Hsu, L. S., & Hsu, C.-T. T. (1994). "Stress-strain behavior of steel-fiber high-strength concrete under compression." *ACI Structural Journal*, American Concrete Institute, 91(4), 448-457.

Japan Road Association (2002). "Design specification of highway bridge: part V – seismic design." Japan.

Jen, G. and Ostertag, C. P. (2012). "Resistance to Corrosion Induced Cracking in Self Consolidating Hybrid Fiber Reinforced Concrete." *Proceedings, 6th Conference on High Performance Fiber Reinforced Cement Composites*, University of Michigan, Ann Arbor, MI, 163-170.

Jeong, H. I., Sakai, J., and Mahin, S. A. (2008). "Shaking Table Tests and Numerical Investigation of Self-Centering Reinforced Concrete Bridge Columns." *PEER Report 2008/06*, Pacific Earthquake Engineering Research Center, University of California, Berkeley, CA.

Kawashima, K., MacRae, G., Hoshikuma, J., and Nagaya, K. (1998). "Residual Displacement Response Spectrum." *Journal of Structural Engineering*, American Society of Civil Engineers, 124(5), 523-530.

Kawashima, K., Zafra, R., Sasaki, T., Kajiwara, K., Nakayama, M., Unjoh, S., Sakai, J., Kosa, K., Takahashi, Y., and Yabe, M. (2012). "Seismic Performance of Full-Size Polypropylene Fiber-Reinforced Cement Composite Bridge Column Based on E-Defense Shake Table Experiments." *Journal of Earthquake Engineering*, Taylor and Francis Group, 16(4), 463-495.

Kumar, P., Jen, G., Trono, W., Panagiotou, M., and Ostertag, C. P. (2011). "Self Compacting Hybrid Fiber Reinforced Composites for Bridge Columns." *PEER Report 2011/106*, Pacific Earthquake Engineering Research Center, University of California, Berkeley, CA.

Kwan, W., and Billington, S. (2003a). "Unbonded Posttensioned Concrete Bridge Piers. I: Monotonic and Cyclic Analyses." *Journal of Bridge Engineering*, American Society of Civil Engineers, 8(2), 92-101.

Kwan, W., and Billington, S. (2003b). “Unbonded Posttensioned Concrete Bridge Piers. II: Seismic Analyses.” Journal of Bridge Engineering, American Society of Civil Engineers, 8(2), 102-111.

Lee, W., and Billington, S. (2009). “Simulation and Performance-Based Earthquake Engineering Assessment of Self-Centering Post-Tensioned Concrete Bridge Systems.” *PEER Report 2009/109*, Pacific Earthquake Engineering Research Center, University of California, Berkeley, CA.

Lehman, D. E., Moehle, J. P., and Mahin, S. (2004). “Experimental Evaluation of the Seismic Performance of Reinforced Concrete Bridge Columns.” *Journal of Structural Engineering*, American Society of Civil Engineers, 130(6), 869-879.

Li, V. and Leung, C. (1992). “Steady-State and Multiple Cracking of Short Random Fiber Composites.” *Journal of Engineering Mechanics*, American Society of Civil Engineers, 118(11), 2246-2264.

Mazzoni, S., McKenna, F., Scott, M., Fenves, G., et al. (2006). “OpenSees Command Language Manual, *Open System for Earthquake Engineering Simulation (OpenSees)*, University of California, Berkeley, CA.

Mander, J. B. and Cheng, C. T. (1997). “Seismic design of bridge piers based on damage avoidance design.” *NCEER 97-0014*, National Center for Earthquake Engineering Research, University at Buffalo, State University of New York, Buffalo, NY.

Mander, J. B., Priestley, M. N., and Park, R. (1988a). “Theoretical Stress-Strain Model for Confined Concrete.” *Journal of Structural Engineering*, American Society of Civil Engineers, 114(8), 1804-1826.

Mander, J. B., Priestley, M. N., and Park, R. (1988b). “Observed Stress-Strain Behavior of Confined Concrete.” *Journal of Structural Engineering*, American Society of Civil Engineers, 114(8), 1827-1849.

Marriott, D., Pampanin, S., and Palermo, A. (2008). “Quasi-static and pseudo-dynamic testing of unbonded post-tensioned rocking bridge piers with external replaceable dissipators.” *Earthquake Engineering and Structural Dynamics*, Wiley InterScience, 38, 331-354.

Marriott, D., Pampanin, S., and Palermo, A. (2011). “Biaxial testing of unbonded post-tensioned rocking bridge piers with external replaceable dissipators.” *Earthquake Engineering and Structural Dynamics*, Wiley InterScience, 40(15), 1723-1741.

Matlab (2011). MATLAB Release 2011a. The MathWorks, Inc., Natick, MA.

Moreno, D., Trono, W., Jen, G., Ostertag, C. P., and Billington, S. L. (2014). “Tension stiffening in reinforced high performance fiber reinforced cement-based composites.” *Cement & Concrete Composites*, Elsevier, 50, 36-46.

Naaman, A. and Reinhardt, H. (2006). “Proposed classification of HPFRC composites based on their tensile response.” *Materials and Structures*, 39, 547-555.

Nguyen, W., Trono, W., and Ostertag, C. P. (2014). “Hybrid Fiber Reinforced Concrete Composites for Accelerated Bridge Column Construction.” *PEER Report (in progress)*. Pacific Earthquake Engineering Research Center, University of California, Berkeley, CA.

Panagiotou, M., Trono, W., Jen, G., Kumar, P., and Ostertag, C. P. (2014). “Experimental Response of HyFRC Bridge Columns with Novel Longitudinal Reinforcement Detailing.” Manuscript under review, *Journal of Bridge Engineering*, American Society of Civil Engineers.

Palermo, A. (2004). “The Use of Controlled Rocking in the Seismic Design of Bridges.” Ph.D. Thesis, Structural Engineering Department, Technical University of Milan, Italy.

Palermo, A., Pampanin, S., and Calvi, G. (2005). “Concept and Development of Hybrid Solutions for Seismic Resistant Bridge Systems.” *Journal of Earthquake Engineering*, Imperial College Press, 9(6), 899-921.

Palermo, A. Pampanin, S., and Marriott, D. (2007). “Design, Modeling, and Experimental Response of Seismic Resistant Bridge Piers with Posttensioned Dissipating Connections.” *Journal of Structural Engineering*, American Society of Civil Engineers, 133(11), 1648-1661.

Parra-Montesinos, G. (2005). “High-Performance Fiber-Reinforced Cement Composites: An Alternative for Seismic Design of Structures.” *ACI Structural Journal*, American Concrete Institute, 102(5), 668-675.

PEER (2010). Concrete Column Blind Prediction Contest 2010. PEER/NEES, Retrieved: April 18, 2014, <http://nisee2.berkeley.edu/peer/prediction_contest/?page_id=25>.

Phan, V., Saiidi M. S., Anderson, J. and Ghasemi, H. (2007). “Near-Fault Ground Motion Effects on Reinforced Concrete Bridge Columns,” *Journal of Structural Engineering*, American Society of Civil Engineers, 133(7), 982-989.

Priestley, M. N., Sritharan, S., Conley, J. R., and Pampanin, S. (1999). “Preliminary results and conclusions from the PRESSS five-story precast concrete test-building.” *PCI Journal*, Precast/Prestressed Concrete Institute, 44(6), 42-67.

Ramesh, K., Seshu, D. R., & Prabhakar, M. (2003). “Constitutive behavior of confined fibre reinforced concrete under axial compression.” *Cement & Concrete Composites*, 25(3), 343-350.

Restrepo, J., and Rahman, A. (2007). “Seismic Performance of Self-Centering Structural Walls Incorporating Energy Dissipators.” *Journal of Structural Engineering*, American Society of Civil Engineers, 133(11), 1560-1570.

Richart, F., Brandtzaeg, A., and Brown, R. (1928). “A Study of the Failure of Concrete under Combined Compressive Stresses.” *Bulletin No. 185, Engineering Experiment Station*, University of Illinois Bulletin, 26(12), University of Illinois, Urbana, IL.

Richart, F., Brandtzaeg, A., and Brown, R. (1929). “The Failure of Plain and Spirally Reinforced Concrete in Compression.” *Bulletin No. 190, Engineering Experiment Station*, University of Illinois Bulletin, 26(31), University of Illinois, Urbana, IL.

Saiidi, M. S., O’Brien, M., and Sadrossadat-Zadeh, M. (2009). “Cyclic Response of Concrete Bridge Columns Using Superelastic Nitinol and Bendable Concrete.” ACI Structural Journal, American Concrete Institute, 106(1), 69-77.

Sakai, J. and Mahin, S. A. (2004). “Analytical Investigations of New Methods for Reducing Residual Displacements of Reinforced Concrete Bridge Columns.” *PEER Report 2004/02*, Pacific Earthquake Engineering Research Center, University of California, Berkeley, CA.

Schoettler , M., Eberhard, M., Mahin, S., Mosalam, K., Ostertag, C., Panagiotou, M., Restrepo, J., Stanton, J., and Terzic, V. (2013). “Advancing the Performance of Bridge Columns: Overview of a Shake Table Test Program.” *Proceedings, Seventh National Seismic Conference on Bridges & Highways*, Paper No. B3-4, Oakland, CA.

Schoettler, M., Restrepo, J., Guerrini, G., Duck, D., and Carrea, F. (2012). “A Full-Scale, Single-Column Bridge Bent Tested by Shake-Table Excitation.” Retrieved: April 18, 2014. Center for Civil Engineering Earthquake Research, Department of Civil Engineering, University of Nevada, Reno, NV, < http://nees.org/resources/6868>.

Sheikh, S. (1982). “A Comparative Study of Confinement Models.” *ACI Journal*, American Concrete Institute, July-August 1982, 296-306.

Shoup, L., Donohue, N., and Lang, M. (2013). “The Fix We’re In For: The State of California’s Bridges.” Transportation for America. Retrieved: April 18, 2014, <http://t4america.org/docs/bridges_state/bridgereport-california.pdf>.

Solberg, K., Mashiko, N., Mander, J., and Dhakal, R. (2009). “Performance of a Damage-Protected Highway Bridge Pier Subjected to Bidirectional Earthquake Attack.” *Journal of Structural Engineering*, American Society of Civil Engineers, 135(5), 469-478.

Terzic, V. and Stojadinovic, B. (2010). “Post-Earthquake Traffic Capacity of Modern Bridges in California.” *PEER Report 2010/103*, Pacific Earthquake Engineering Research Center, University of California, Berkeley, CA.

Trono, W., Jen, G., Moreno, D. M., Billington, S. L., and Ostertag, C. P. (2011). "Confinement and Tension Stiffening Effects in High Performance Self-consolidated Hybrid Fiber Reinforced Concrete Composites." *Proceedings, Sixth International Workshop on High Performance Fiber Reinforced Cement Composites*, Rilem, 245-252.

Trono, W., Jen, G., Ostertag, C., and Panagiotou, M. (2013). "Tested and Modeled Seismic Response of a Rocking, Post-tensioned HyFRC Bridge Column." *Proceedings, Seventh National Seismic Conference on Bridges & Highways*, Paper No. C3-5, Oakland, CA.

Vithani, A. R. and Gupta, K. C. (2002). "Estimation of Object Kinematics from Point Data." *Proceedings of DETC'02*, American Society of Mechanical Engineers, Montreal, Canada.

Yamashita, R. and Sanders, D. (2009). "Seismic Performance of Precast Unbonded Prestressed Concrete Columns." *ACI Structural Journal*, American Concrete Institute, 106(6), 821-830.

Yi, C. K. and Ostertag, C. P. (2005). "Mechanical approach in mitigating alkali-silica reaction." *Cement and Concrete Research*, 35(1), 67-75.

Yuguang, Y., Walraven, J., and Uijl, J. (2009). "Combined effect of fibers and steel rebars in high performance concrete." *HERON*, 54(2/3), 205-224.

7 Appendix

Table A. 1. OpenSEES uniaxialMaterial parameters.

Concrete03	f_c', *ksi (MPa)*	ε_0	f_{cu}, *ksi (MPa)*	ε_u	λ	f_t, *ksi (MPa)*	ε_{t1}	f_{t1}, *ksi (MPa)*	β	ε_{tu}
HyFRC cover	-6.47 (-44.6)	-0.00345	-3.24 (-22.3)	-0.01877	0.5	**0.45 (3.1)**	**0.00024**	**0.45 (3.1)**	**0.5**	**0.05**
HyFRC core	-7.43 (-51.2)	-0.00949	-5.57 (-38.4)	-0.04744	0.5	**0.45 (3.1)**	**0.00057**	**0.45 (3.1)**	**0.5**	**0.05**

Note: Values in ***bold*** *were set equal to zero when used for HyFRC cover and core contact springs at the rocking plane*

Steel02	f_y, *ksi (MPa)*	*E, ksi (MPa)*	*b*	*R*	c_1	c_2
Unbonded rebar	69.8 (481)	28527 (196687)	0.0139	18	0.925	0.15

ElasticPPGap	*E, kips/in (kN/mm)*	F_y, *kips (kN)*	*gap*	*b*	*damage*
Headed rebar	2211 (387)	-21.64 (-96.3)	0	0.0139	yes

Note: Parameters defined in force and displacement units for implementation in zeroLength elements based on $A_s = 0.31\ in^2$ *and* $L_s = 4$ *inches.*

ElasticPPGap	*E, ksi (MPa)*	F_y, *ksi (MPa)*	*gap*	*b*	*damage*
Post-tensioning	28653 (197555)	258 (1782)	0	0.027611	yes

InitStrainMaterial	ε_0
Post-tensioning	0.00411651

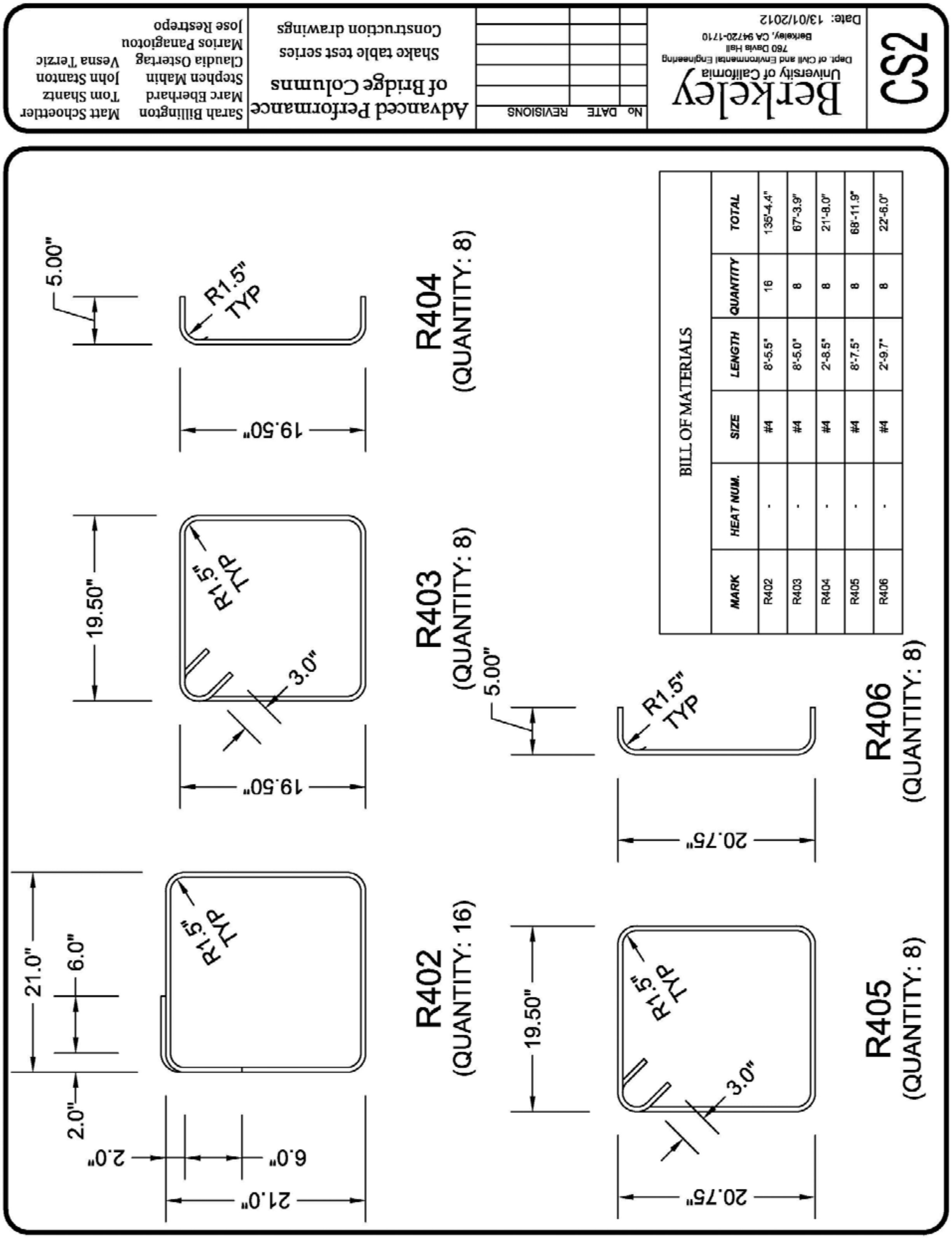

BILL OF MATERIALS

MARK	HEAT NUM.	SIZE	LENGTH	QUANTITY	TOTAL
R402	-	#4	8'-5.5"	16	135'-4.4"
R403	-	#4	8'-5.0"	8	67'-3.9"
R404	-	#4	2'-8.5"	8	21'-8.0"
R405	-	#4	8'-7.5"	8	68'-11.9"
R406	-	#4	2'-9.7"	8	22'-6.0"

Figure A. 1. *Reinforcement for column load stubs and footings.*

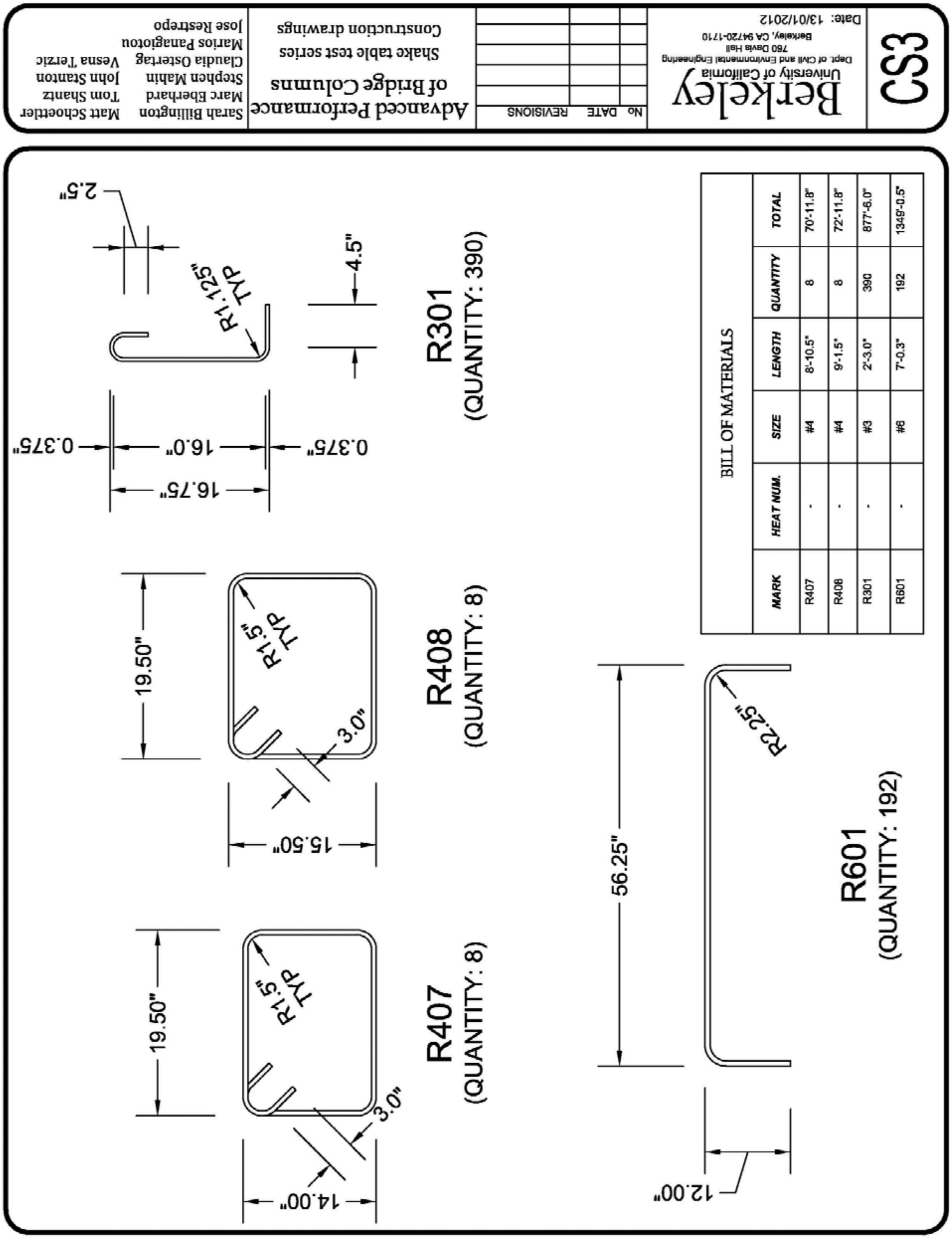

BILL OF MATERIALS

MARK	HEAT NUM.	SIZE	LENGTH	QUANTITY	TOTAL
R407	-	#4	8'-10.5"	8	70'-11.8"
R408	-	#4	9'-1.5"	8	72'-11.8"
R301	-	#3	2'-3.0"	390	877'-6.0"
R601	-	#6	7'-0.3"	192	1349'-0.5"

Figure A. 2. Reinforcement for column load stubs and footings (cont.).

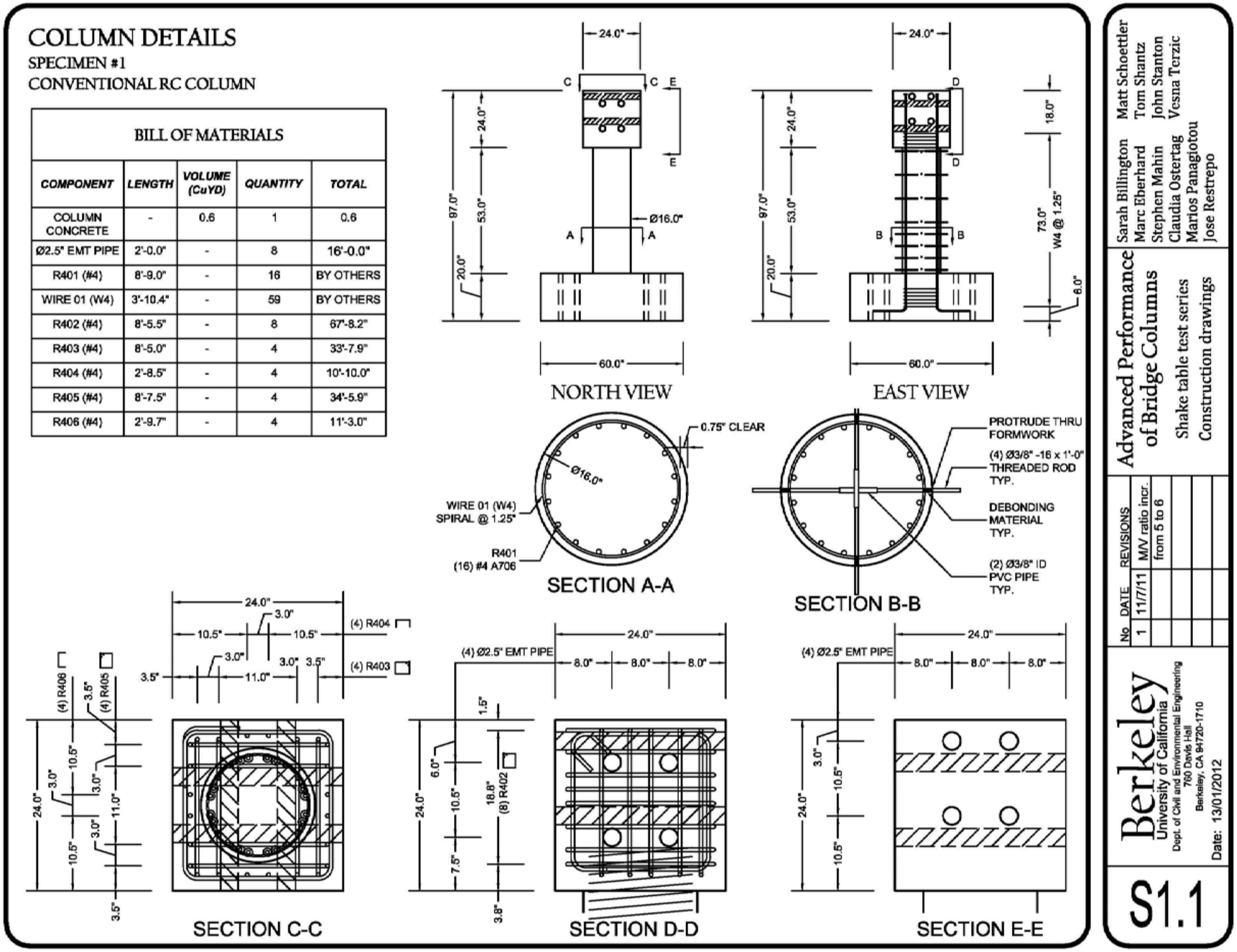
COLUMN DETAILS

SPECIMEN #1

CONVENTIONAL RC COLUMN

BILL OF MATERIALS

COMPONENT	LENGTH	VOLUME (CuYD)	QUANTITY	TOTAL
COLUMN CONCRETE	-	0.6	1	0.6
Ø2.5" EMT PIPE	2'-0.0"	-	8	16'-0.0"
R401 (#4)	8'-9.0"	-	16	BY OTHERS
WIRE 01 (W4)	3'-10.4"	-	59	BY OTHERS
R402 (#4)	8'-5.5"	-	8	67'-8.2"
R403 (#4)	8'-5.0"	-	4	33'-7.9"
R404 (#4)	2'-8.5"	-	4	10'-10.0"
R405 (#4)	8'-7.5"	-	4	34'-5.9"
R406 (#4)	2'-9.7"	-	4	11'-3.0"

Advanced Performance of Bridge Columns

Shake table test series

Construction drawings

Sarah Billington
Marc Eberhard
Stephen Mahin
Claudia Ostertag
Marios Panagiotou
Jose Restrepo

Matt Schoettler
Tom Shantz
John Stanton
Vesna Terzic

No	DATE	REVISIONS
1	11/7/11	M/V ratio incr. from 5 to 6

Berkeley
University of California
Dept. of Civil and Environmental Engineering
760 Davis Hall
Berkeley, CA 94720-1710

Date: 13/01/2012

S1.1

Figure A. 3. Reinforcement for column load stubs and footings (cont.).

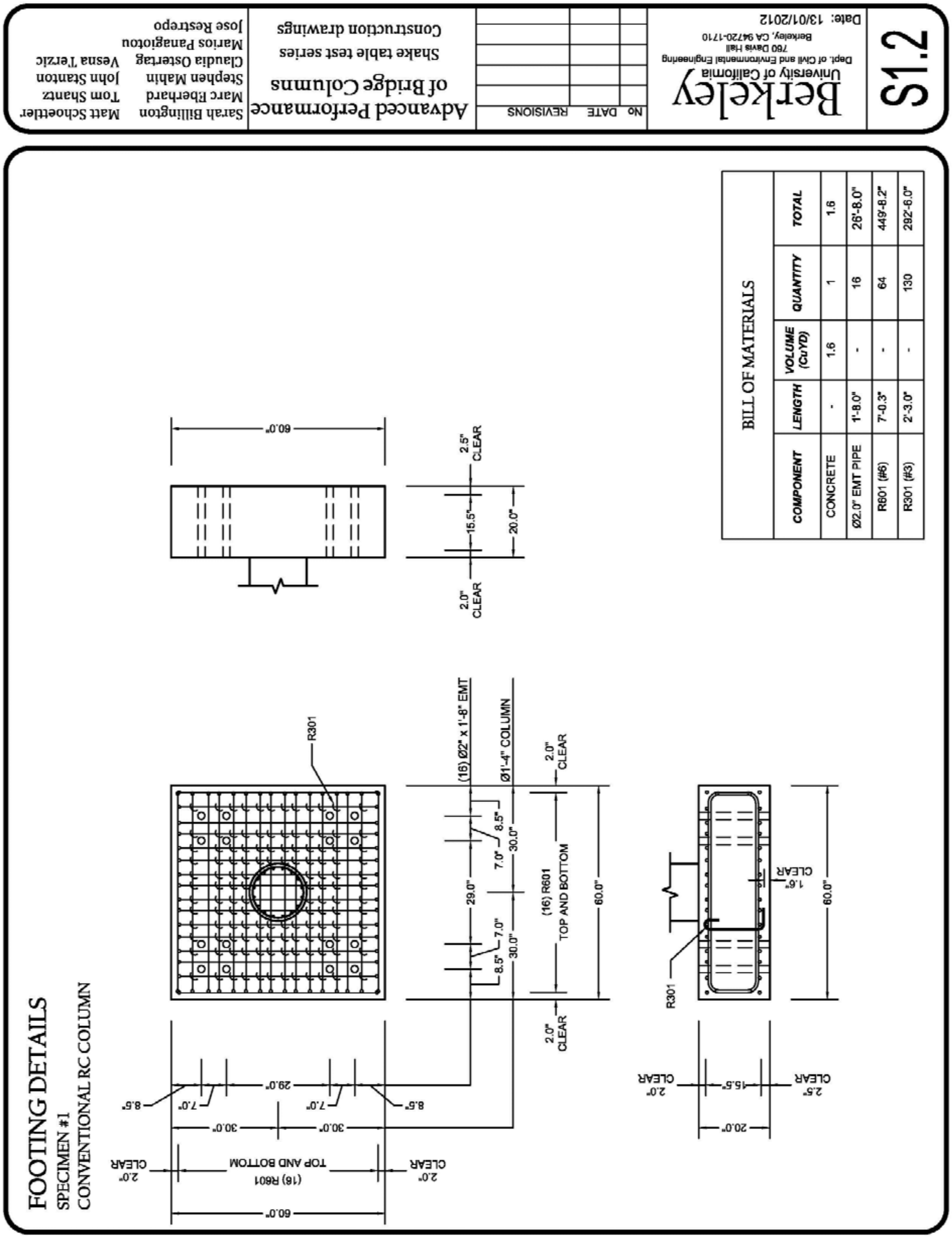

BILL OF MATERIALS

COMPONENT	LENGTH	VOLUME (CuYD)	QUANTITY	TOTAL
CONCRETE	-	1.6	1	1.6
Ø2.0" EMT PIPE	1'-8.0"	-	16	26'-8.0"
R601 (#6)	7'-0.3"	-	64	449'-8.2"
R301 (#3)	2'-3.0"	-	130	292'-6.0"

Figure A. 4. Reinforcement for column load stubs and footings (cont.).

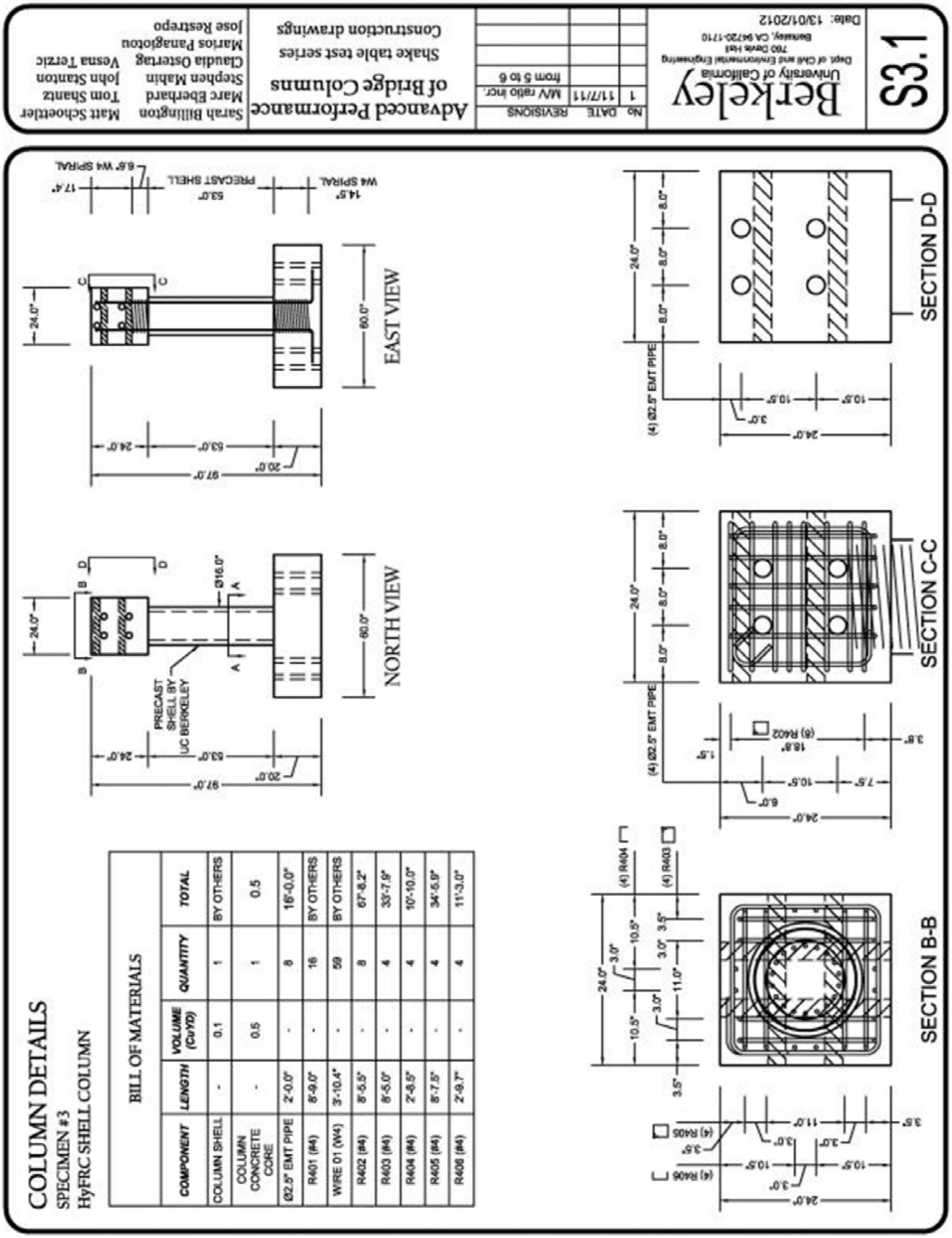

BILL OF MATERIALS

COMPONENT	LENGTH	VOLUME (CuYD)	QUANTITY	TOTAL
COLUMN SHELL	-	0.1	1	BY OTHERS
COLUMN CONCRETE CORE	-	0.5	1	0.5
Ø2.5" EMT PIPE	2'-0.0"	-	8	16'-0.0"
R401 (#4)	8'-9.0"	-	16	BY OTHERS
WIRE 01 (W4)	3'-10.4"	-	59	BY OTHERS
R402 (#4)	8'-6.5"	-	8	67'-8.2"
R403 (#4)	8'-5.0"	-	4	33'-7.9"
R404 (#4)	2'-8.5"	-	4	10'-10.0"
R405 (#4)	8'-7.5"	-	4	34'-5.9"
R406 (#4)	2'-9.7"	-	4	11'-3.0"

Figure A. 5. Reinforcement for column load stubs and footings (cont.).

FOOTING DETAILS

SPECIMEN #3
HyFRC SHELL COLUMN

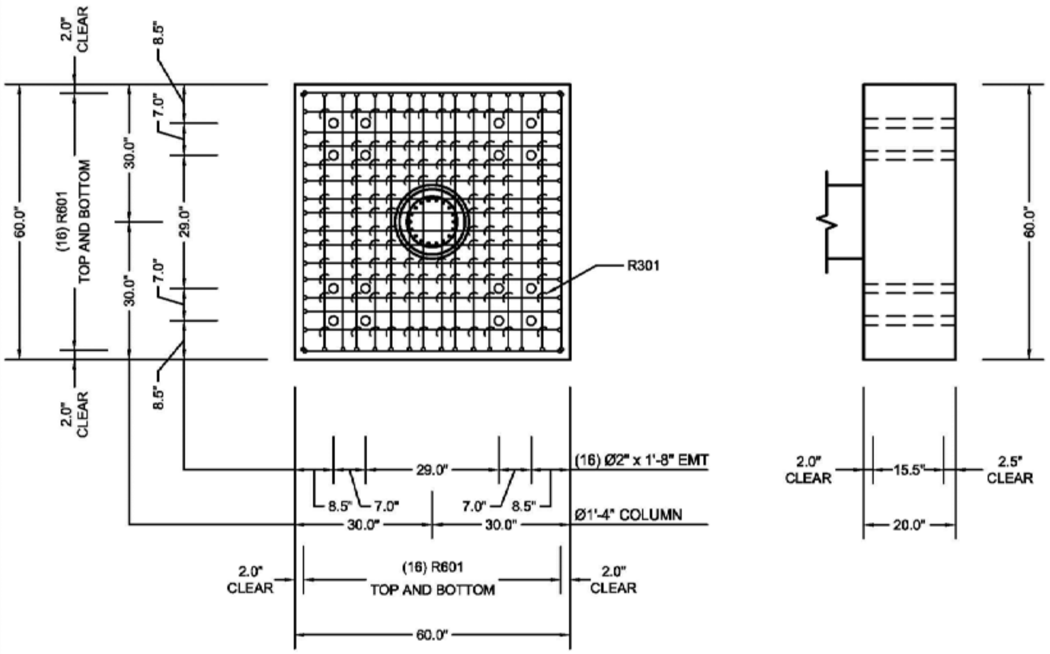

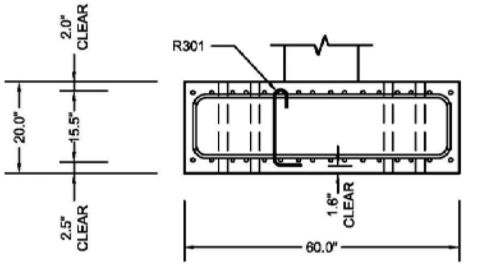

BILL OF MATERIALS

COMPONENT	LENGTH	VOLUME (CuYD)	QUANTITY	TOTAL
CONCRETE	-	1.6	1	1.6
Ø2.0" EMT PIPE	1'-8.0"	-	16	26'-8.0"
R601 (#6)	7'-0.3"	-	64	449'-8.2"
R301 (#3)	2'-3.0"	-	130	292'-6.0"

Sarah Billington
Marc Eberhard
Stephen Mahin
Claudia Ostertag
Marios Panagiotou
Jose Restrepo

Matt Schoettler
Tom Shantz
John Stanton
Vesna Terzic

Advanced Performance of Bridge Columns
Shake table test series
Construction drawings

No	DATE	REVISIONS

Berkeley
University of California
Dept. of Civil and Environmental Engineering
760 Davis Hall
Berkeley, CA 94720-1710
Date: 13/01/2012

S3.2

Figure A. 6. Reinforcement for column load stubs and footings (cont.).

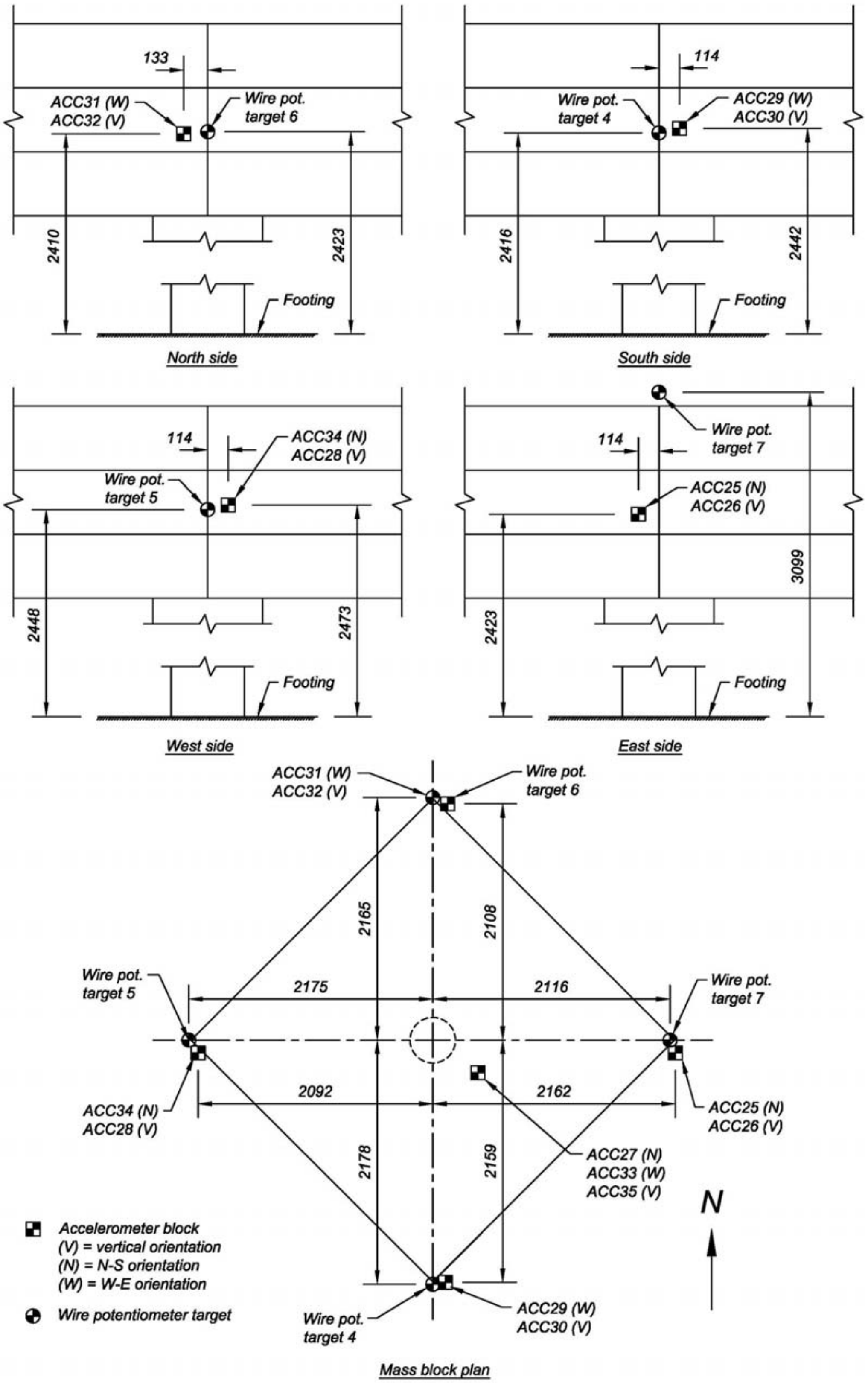

Figure A. 7. *Locations of accelerometers and wire potentiometer targets on the mass blocks.*

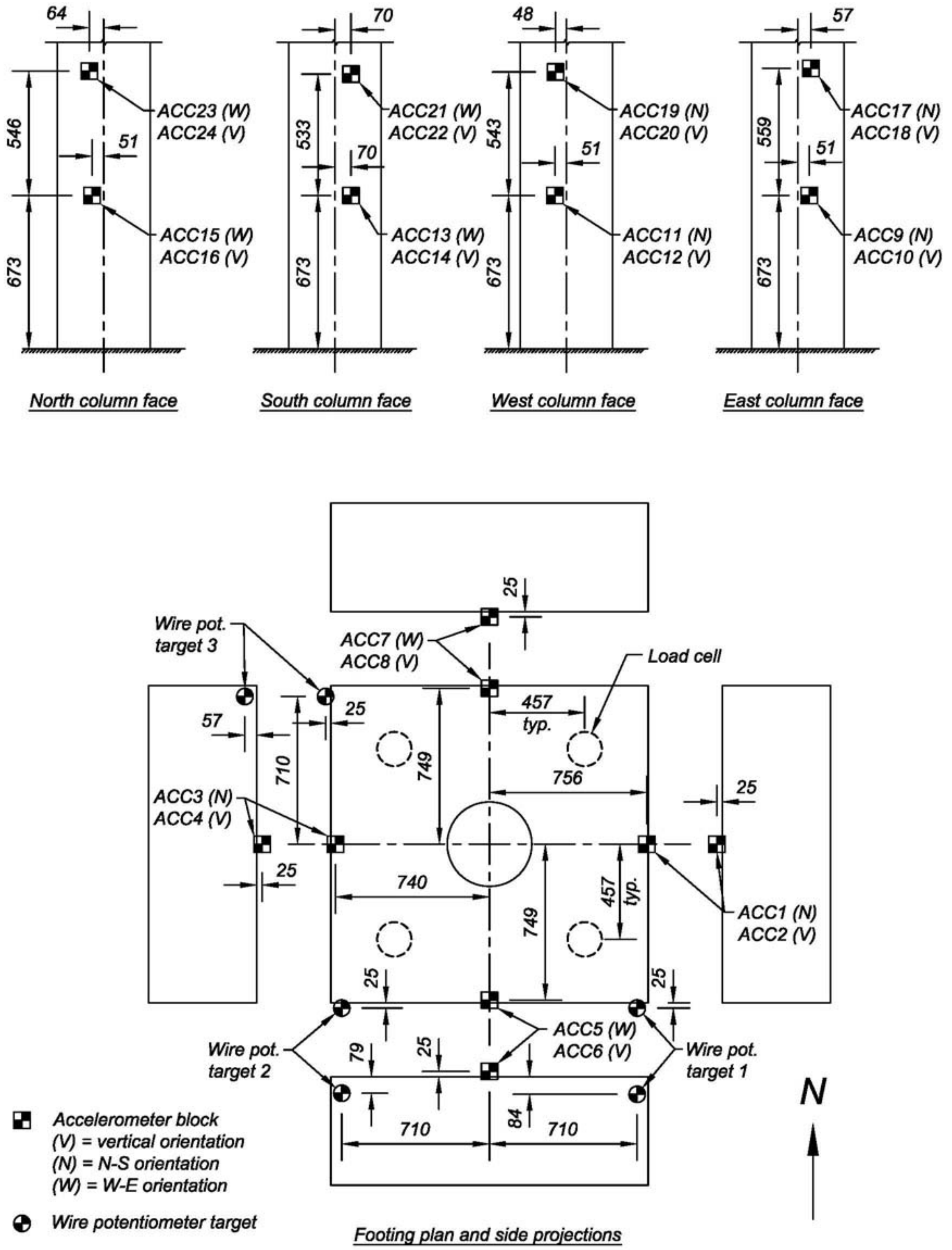

Figure A. 8. *Locations of accelerometers and wire potentiometer targets on the column and footing.*

Figure A. 9. Coupler embedded in the column for threaded rods.

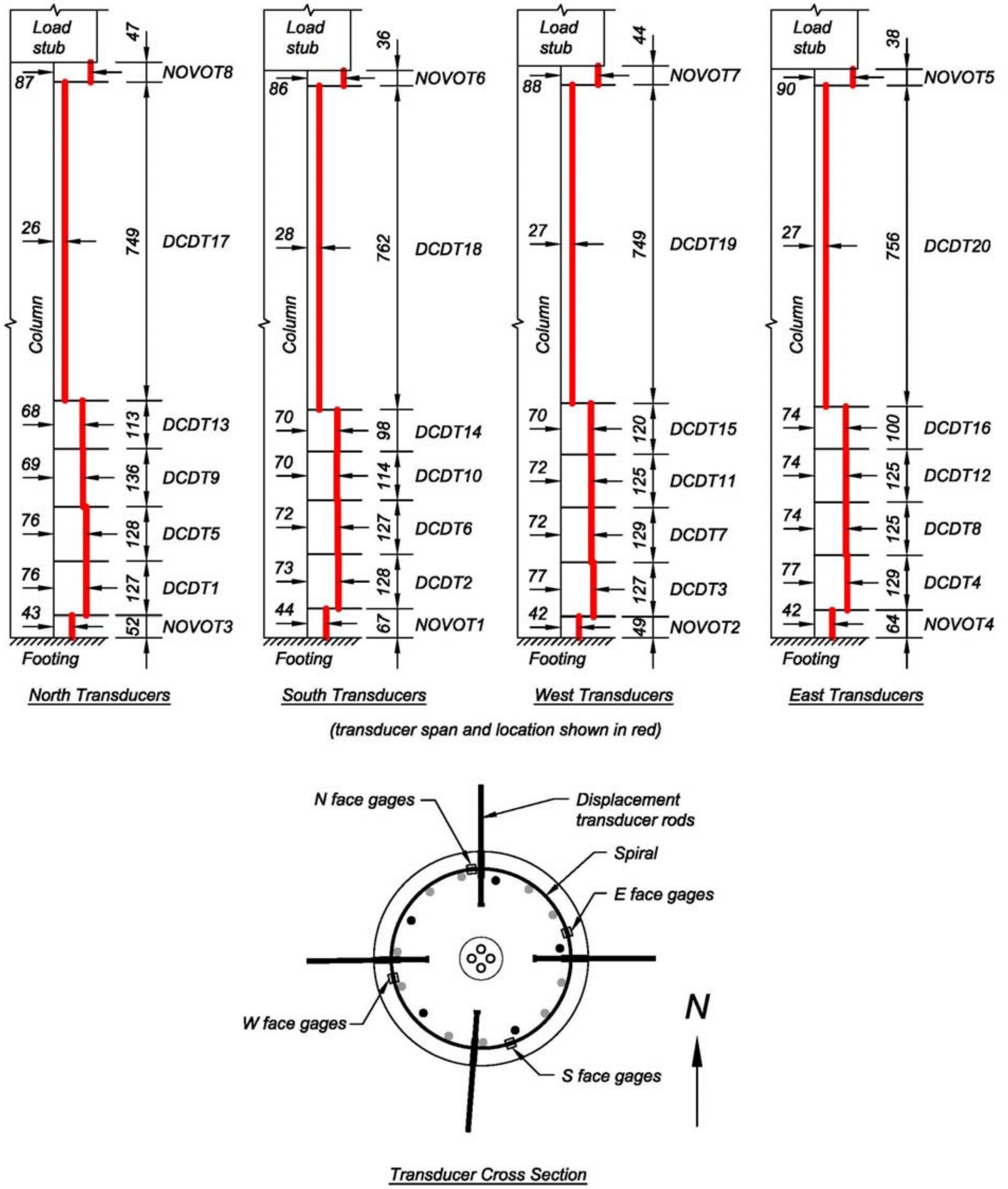

Figure A. 10. Locations of displacement transducers and spiral strain gages.

Table A. 2. Locations of strain gages on PT HyFRC column reinforcing bars.

Location	*Bar designation*[a]	*Label*	*Strain gage number*	*Elevation from top of footing (mm)*	*Bar face*[b]
Strand	S1	SN.51	7	*	**
		SN.52	8	*	**
	S2	SE.51	9	*	**
		SE.52	10	*	**
	S3	SS.51	11	*	**
		SS.52	12	*	**
	S4	SW.51	5	*	**
Unbonded rebar	U1	LU1.1	19	175	outer
		LU1.2	20	76	outer
		LU1.3	21	76	inner
		LU1.4	22	-178	outer
	U2	LU2.1	23	191	outer
		LU2.2	24	89	outer
	U3	LU3.1	26	186	outer
		LU3.2	27	83	outer
		LU3.3	28	83	inner
		LU3.4	29	-171	outer
	U5	LU5.1	30	181	outer
		LU5.2	31	76	outer
Headed rebar	B1	LB1	33	38	inner
	B3	LB3	34	38	inner
	B5	LB5	35	38	inner
	B7	LB7	36	38	inner
	B9	LB9	37	38	inner
Spiral[c]	N face	TN.11	39	108	outer
		TN.12	40	108	inner
		TN.21	45	76	outer
		TN.22	46	76	inner
	E face	TE.1	41	83	outer
		TE.2	48	83	inner
	S face	TS.1	42	89	outer
		TS.2	47	89	inner
	W face	TW.11	43	95	outer
		TW.12	44	95	inner
		TW.21	49	64	outer
		TW.22	51	64	inner
Headed rebar (within footing)	F3[d]	LF3	52	-64	inner

**PT strain gages were located between 450 mm and 900 mm from the top of the footing*

***two gages were placed on opposite sides of the strand on individual wires, oriented on the axis of the wires*

[a] *see Figure 46(b) for location of corresponding bars*

[b] *inner faces the concrete core; outer faces the concrete cover*

[c] *for circumferential location on spiral see Appendix Figure A. 10*

[d] *bar F3 lies immediately below bar B3 in Figure 46(b)*

Table A. 3. Strain gage measurements in the post-tensioned strands.

Test	*Point during test*	*Strand strain measurement, ε_{pt} , %*						
		Strand S4	*Strand S1*		*Strand S2*		*Strand S3*	
		SW.51	*SN.51*	*SN.52*	*SE.51*	*SE.52*	*SS.51*	*SS.52*
GM1	start	0.352	0.345	0.353	0.333	0.330	0.358	0.360
	peak	0.357	0.351	0.359	0.337	0.334	0.363	0.365
GM2	start	0.352	0.345	0.353	0.333	0.329	0.358	0.359
	peak	0.394	0.376	0.384	0.368	0.365	0.404	0.405
GM3	start	0.351	0.344	0.353	0.332	0.328	0.357	0.358
	peak	0.398	0.387	0.395	0.368	0.364	0.398	0.399
GM4	start	0.351	0.344	0.352	0.332	0.328	0.357	0.358
	peak	0.438	0.449	0.459	0.431	0.426	0.439	0.442
GM5	start	0.348	0.342	0.350	0.328	0.324	0.355	0.357
	peak	**0.474**	0.456	0.466	0.437	0.431	0.493	0.496
GM6	start	0.346	0.341	0.348	0.328	0.324	0.351	0.353
	peak	0.440	**0.457**	**0.467**	0.439	0.433	0.440	0.444
GM7	start	0.346	0.339	0.347	0.326	0.323	0.350	0.352
	peak	0.470	0.444	0.455	**0.463**	**0.457**	**0.505**	**0.507**
GM8	start	0.344	0.336	0.345	0.323	0.319	0.348	0.350
	peak	0.455	0.456	0.466	0.426	0.423	0.459	0.461
GM9	start	0.341	0.333	0.342	0.318	0.315	0.345	0.346
	peak	0.435	0.429	0.438	0.403	0.397	0.459	0.460
GM10	start	0.341	0.332	0.340	0.318	0.315	0.345	0.346
	peak	0.431	0.436	0.444	0.402	0.397	0.447	0.449
GM11	start	0.338	0.328	0.336	0.313	0.310	0.340	0.341
	peak	0.472	0.440	0.448	0.418	0.414	0.468	0.469

** maximum strain over all tests shown in* ***bold*** *for each gage*

Table A. 4. Strain gage measurements in the unbonded bars.

Test	*Point during test*	*Unbonded bar strain measurement, ε_d , %*											
		Bar U1				*Bar U2*		*Bar U3*				*Bar U5*	
		LU1.1	*LU1.2*	*LU1.3*	*LU1.4*	*LU2.1*	*LU2.2*	*LU3.1*	*LU3.2*	*LU3.3*	*LU3.4*	*LU5.1*	*LU5.2*
GM1	Start	0.00	0.00	0.00	0.00	0.00	0.00	0.00	0.00	0.00	0.01	0.00	0.00
	Peak	0.08	0.08	0.08	0.01	0.08	0.10	0.02	0.03	0.03	0.01	0.02	0.05
GM2	Start	0.00	0.00	0.00	0.00	0.01	0.00	0.00	0.00	0.00	0.01	0.00	0.00
	Peak	**0.32**	**1.80**	**1.44**	0.04	0.25	**1.80**	0.15	0.22	0.08	0.03	0.06	**1.30**
GM3	Start	0.02	0.50	0.47	-0.03	-0.02	0.21	0.00	-0.01	0.02	0.00	-0.01	0.49
	Peak	**0.26**	**1.66**	**1.32**	0.05	0.24	**1.31**	0.20	-	0.18	0.04	**0.48**	**1.56**
GM4	Start	0.05	0.44	0.45	-0.04	-0.01	0.21	-0.01	-	0.05	-0.01	0.12	0.15
	Peak	**0.88**	**1.97**	**1.56**	0.07	**0.27**	**1.52**	**0.94**	-	0.09	0.05	-	**1.57**
GM5	Start	0.14	0.36	0.41	-0.04	-0.01	0.19	0.10	-	0.04	-0.03	-	-0.04
	Peak	**1.67**	**3.28**	**2.69**	0.08	-	-	**0.97**	-	0.06	0.06	-	**1.66**
GM6	Start	0.29	0.47	0.25	-0.05	-	-	0.10	-	0.05	-0.03	-	-0.40
	Peak	**1.23**	**2.74**	**2.04**	0.09	-	-	-	-	0.08	0.06	-	**1.35**
GM7	Start	0.31	0.53	0.33	-0.05	-	-	-	-	0.05	-0.04	-	-0.41
	Peak	**1.52**	**3.37**	**2.68**	0.10	-	-	-	-	0.14	0.07	-	**1.58**
GM8	Start	0.35	1.10	0.06	-0.05	-	-	-	-	0.05	-0.04	-	-1.06
	Peak	**1.05**	**2.87**	**1.88**	0.10	-	-	-	-	0.09	0.07	-	-
GM9	Start	0.40	1.45	-0.15	-0.05	-	-	-	-	-0.03	-0.03	-	-
	Peak	**1.65**	**3.62**	**2.66**	0.10	-	-	-	-	0.11	0.06	-	-
GM10	Start	0.45	1.98	-0.12	-0.05	-	-	-	-	-0.08	-0.03	-	-
	Peak	**1.78**	-	**2.71**	0.11	-	-	-	-	0.03	0.07	-	-
GM11	Start	0.51	-	-0.72	-0.05	-	-	-	-	-0.02	-0.03	-	-
	Peak	**2.44**	-	-	**0.12**	-	-	-	-	0.15	0.08	-	-

** maximum strain over all tests shown in red for each gage*
*** strains exceeding the yield strain of 0.25% shown* ***bold***
**** hyphen represents gage failure*

Table A. 5. Strain gage measurements in the headed rebar.

Test	*Point during test*	*Headed rebar strain measurement, ε_b , %*					
		Bar B1	*Bar B3*	*Bar B5*	*Bar B7*	*Bar B9*	*Bar F3*
		LB1	*LB3*	*LB5*	*LB7*	*LB9*	*LF3*
GM1	start	0.00	0.00	0.00	0.00	0.00	0.00
	peak	-0.04	-0.03	-0.02	-0.05	0.00	-0.01
GM2	start	0.00	0.00	0.00	0.00	0.00	0.00
	peak	-0.07	-0.10	-0.09	-0.11	-0.04	-0.04
GM3	start	0.03	0.01	-0.01	0.00	0.02	0.00
	peak	-0.07	-0.09	**-0.29**	-0.16	-0.06	-0.05
GM4	start	0.04	0.02	-0.13	0.02	0.02	0.00
	peak	**-0.98**	-0.08	**-0.62**	-0.13	-0.02	-0.03
GM5	start	-0.72	0.00	-0.45	0.03	0.03	0.00
	peak	**-1.35**	**-1.41**	**-1.33**	**-1.79**	-0.07	-0.07
GM6	start	-1.02	-1.09	-1.03	-1.31	0.03	0.01
	peak	**-1.86**	**-1.61**	**-2.09**	**-1.92**	-0.17	-0.07
GM7	start	-1.46	-1.25	-1.74	-1.47	0.00	0.01
	peak	**-1.81**	**-2.25**	**-2.33**	**-3.14**	**-0.79**	-0.08
GM8	start	-1.46	-1.86	-1.95	-2.61	-0.50	0.01
	peak	**-2.44**	**-4.14**	**-3.15**	**-3.64**	**-1.29**	-0.08
GM9	start	-1.98	-3.66	-2.75	-3.07	-0.93	0.01
	peak	**-2.34**	**-5.04**	**-3.00**	**-4.04**	**-1.05**	-0.06
GM10	start	-1.99	-4.50	-2.78	-3.56	-0.93	0.01
	peak	**-2.35**	**-5.71**	**-5.13**	**-4.10**	**-1.77**	-0.08
GM11	start	-1.97	-5.19	-4.71	-3.62	-1.35	0.01
	peak	**-2.07**	**-5.35**	**-5.95**	**-4.49**	**-1.99**	-0.03

** maximum strain over all tests shown in red for each gage*

*** strains exceeding the yield strain of 0.25% shown* ***bold***

Table A. 6. Strain gage measurements in the spiral.

Test	*Point during test*	*Spiral strain measurement, ε_t , %*											
		N face				*S face*		*W face*				*E face*	
		TN.11	*TN.12*	*TN.21*	*TN.22*	*TS.1*	*TS.2*	*TW.11*	*TW.12*	*TW.21*	*TW.22*	*TE.1*	*TE.2*
GM1	start	0.00	0.00	0.00	0.00	0.00	0.00	0.00	0.00	0.00	0.00	0.00	0.00
	peak	0.01	0.02	0.01	0.02	0.01	0.01	0.00	0.00	0.00	0.00	0.00	0.00
GM2	start	0.00	0.00	0.00	0.00	0.00	0.00	0.00	0.00	0.00	0.00	0.00	0.00
	peak	0.01	0.05	0.02	0.06	0.01	0.03	0.01	0.02	0.01	0.03	0.02	0.05
GM3	start	0.01	0.01	0.00	0.02	0.01	0.01	0.00	0.01	0.01	0.01	0.00	0.03
	peak	0.01	0.07	0.03	0.12	0.02	0.05	0.02	0.05	0.03	0.07	0.04	0.12
GM4	start	0.01	0.02	0.01	0.04	0.01	0.02	0.01	0.02	0.01	0.03	0.00	0.04
	peak	0.01	0.06	0.03	0.12	0.04	0.14	0.02	0.06	0.04	0.08	0.02	0.09
GM5	start	0.01	0.03	0.01	0.05	0.01	0.04	0.01	0.03	0.02	0.06	0.00	0.06
	peak	0.06	0.23	0.14	**0.45**	0.06	0.17	0.04	0.11	0.10	0.20	0.08	0.24
GM6	start	0.01	0.06	-0.01	0.26	0.01	0.09	0.03	0.07	0.06	0.15	0.01	0.14
	peak	0.03	0.17	0.06	**0.43**	0.05	0.18	0.05	0.13	0.11	0.21	0.09	0.28
GM7	start	0.02	0.06	-0.01	0.27	0.01	0.09	0.03	0.09	0.07	0.19	0.00	0.20
	peak	0.13	0.23	0.12	**0.66**	0.06	0.20	0.07	0.17	0.13	0.33	0.06	0.35
GM8	start	0.07	0.05	-0.04	0.51	0.02	0.13	0.04	0.12	0.06	0.26	-0.01	0.23
	peak	0.14	0.16	0.07	**0.71**	0.09	0.27	0.10	0.25	0.16	**0.56**	0.08	**0.55**
GM9	start	0.08	0.06	-0.03	0.56	0.00	0.19	0.04	0.15	0.01	0.48	-0.04	0.39
	peak	0.13	0.19	0.05	**0.83**	0.05	0.25	0.05	0.19	0.04	**0.54**	-0.01	**0.49**
GM10	start	0.07	0.07	-0.07	0.63	-0.01	0.16	0.04	0.16	0.02	0.50	-0.04	0.44
	peak	0.12	0.19	0.02	**0.85**	0.05	0.28	0.07	0.23	0.08	**0.59**	0.02	**0.69**
GM11	start	0.08	0.10	-0.06	0.70	0.00	0.20	0.04	0.18	0.00	0.49	-0.09	0.52
	peak	0.17	0.23	0.12	**1.21**	0.03	0.24	0.09	0.25	0.13	**0.58**	-	**0.99**

** maximum strain over all tests shown in red for each gage*
*** strains exceeding the yield strain of 0.44% shown **bold***
**** hyphen represents gage failure*